Field Measurement of the Fate of Atmospheric H_2 in a Forest Environment:
from Canopy to Soil

by

Laura Kelsey Meredith

B.S., California Polytechnic State University, San Luis Obispo (2005)

Submitted to the Department of Earth, Atmospheric and Planetary Science
in partial fulfillment of the requirements for the degree of

Doctor of Philosophy in Climate Physics and Chemistry

at the

MASSACHUSETTS INSTITUTE OF TECHNOLOGY

February 2013

Author . . . .
Department of Earth, Atmospheric and Planetary Science
October 31, 2012

Certified by . . . .
Ronald G. Prinn
TEPCO Professor of Atmospheric Science
Thesis Supervisor

Accepted by . . . .
Robert D. van der Hilst
Schlumberger Professor of Earth and Planetary Sciences
Head, Department of Earth, Atmospheric and Planetary Sciences

Field Measurement of the Fate of Atmospheric H_2 in a Forest Environment:

from Canopy to Soil

by

Laura Kelsey Meredith

Submitted to the Department of Earth, Atmospheric and Planetary Science
on October 31, 2012, in partial fulfillment of the
requirements for the degree of
Doctor of Philosophy in Climate Physics and Chemistry

Abstract

Atmospheric hydrogen (H_2), an indirect greenhouse gas, plays a notable role in the chemistry of the atmosphere and ozone layer. Current anthropogenic emissions of H_2 are substantial and may increase with its widespread use as a fuel. The H_2 budget is dominated by the microbe-mediated soil sink, and although its significance has long been recognized, our understanding is limited by the low temporal and spatial resolution of traditional field measurements. This thesis was designed to improve the process-based understanding of the H_2 soil sink with targeted field and lab measurements.

In the field, ecosystem-scale flux measurements of atmospheric H_2 were made both above and below the forest canopy for over a year using a custom, automated instrument at the Harvard Forest. H_2 fluxes were derived using a flux-gradient technique from the H_2 concentration gradient and the turbulent eddy coefficient. A ten-fold improvement in precision was attained over traditional systems, which was critical for quantifying the whole ecosystem flux from small H_2 concentration gradients above the turbulent forest canopy. Soil uptake of atmospheric H_2 was the dominant process in this forest ecosystem. Rates peaked in the summer and persisted at reduced levels in the winter season, even across a 70 cm snowpack. We present correlations of the H_2 flux with environmental variables (*e.g.*, soil temperature and moisture). This work is the most comprehensive attempt to elucidate the processes controlling biosphere-atmosphere exchange of H_2. Our results will help reduce uncertainty in the present-day H_2 budget and improve projections of the response of the H_2 soil sink to global change.

In the lab, we isolated microbial strains of the genus *Streptomyces* from Harvard Forest and found that the genetic potential for atmospheric H_2 uptake predicted H_2 consumption activity. Furthermore, two soil *Actinobacteria* were found to utilize H_2 only during specific lifecycle stages. The lifecycle of soil microorganisms can be quite complex as an adaptation to variable environmental conditions. Our results indicate that H_2 may be an important energetic supplement to soil microorganisms under stress. These results add to the understanding of the connections between the environment, organismal life cycle, and soil H_2 uptake.

Thesis Supervisor: Ronald G. Prinn
Title: TEPCO Professor of Atmospheric Science

Acknowledgments

I have many people to thank for guidance, inspiration, and opportunities. First and foremost, I thank my advisor Ron Prinn for his support, advice, and good humor. I am ever grateful for the freedom and opportunities you've provided me to explore my scientific interests.

In addition to serving on my committee, the following individuals have helped me tremendously along the way. A special thanks to Bill Munger for all the hours he has spent over email, in meetings, and in the field. I have no idea how I would have accomplished these measurements without your mentoring. Thank you to Steve Wofsy for linking me to Harvard Forest, for your scientific guidance, for being unrelentingly supportive, and for making me feel so welcome in your group. Thank you to Colleen Hansel for your ideas, feedback, and optimism, without which I don't think I would have pursued the microbiology component of my thesis. Thank you to Tanja Bosak and Shuhei Ono for welcoming me into your the dynamic, fun, and collaborative labs. Thank you to Dianne Newman helping on my committee and for suggesting the MBL course.

A big thank you to Deepa Rao for embarking on a scientific tangent into the microbial realm with me. I never imagined our work together to go as far as it did, and I owe it to your hard work, dependability, and talent. Thank you for your friendship and for making it fun!

I am grateful for help from colleagues at the Harvard Forest EMS site: Josh McLaren, Mark VanScoy, Emery Boose, Ben Lee, Leland Werden, and the Harvard Forest department. In particular, thank you to Roisin Commane for her eternal willingness to collaborate in the field and at the desk. Thank you to Elaine Gottleib for help with CO_2 calibrations. I am grateful for the instrumentation I was able to use as a result of the hard work of Allison Dunn, Alfram Bright, and Bruce Daube.

I would like to recognize help from collaborators in the AGAGE network. A special thanks to Peter Salameh for providing GCwerks to this study and for troubleshooting help even at very inconvenient times. Thank you to Andrew Crotwell for a crash

course in gas chromatography, and to Brad Hall, Paul Novelli, and Duane Kitzis for their generous assistance with my project.

Attending the MBL Microbial Diversity Course gave me the skills, confidence, and inspiration to pursue the microbial component of my thesis. Thank you so much to Dan Buckley and Steve Zinder for the opportunity, and to the class of 2010. I would like to thank the Bosak-Ono lab members for their help along the way, and Paula Welander in particular for her patient answers to my questions in the lab.

I am so appreciative of the wonderful friendships I've made in Cambridge. Your support in both the fun and the uncomfortable times made all the difference for me. Thank you Ryan Abernathey, Anita Ganesan, Diane Ivy, Valerie Karplus, Chiara Lepore, Matt Rigby, Cim Wortham, and so many more. Thank you to Robens Joseph for your support. Bikram yoga has been my outlet for restoring my sanity and health in grad school - thank you to the Koontzes.

More than anything, I am grateful for the love and support of my parents Mike and Barbara. Thank you for fostering my interest in science from an early age all while allowing me the space to be a kid when I was a kid. I want to thank my three beautiful sisters Lisa, Amy, and Kelly for the love, friendship, and fun we have together. I am blessed with a wonderful family to ground me through all endeavors.

I am grateful for assistance from the following funding sources: NSF Graduate Research Fellowship, multiple grants from NASA to MIT for the Advanced Global Atmospheric Gases Experiment (AGAGE), MIT Center for Global Change Science, MIT Joint Program on the Science and Policy of Global Change, MIT EAPS-PAOC Henry Houghton Fund, MIT Martin Family Society of Fellows for Sustainability, MIT Ally of Nature Research Fund, MIT William Otis Crosby Lectureship, and MIT Warren Klein Fund. I also appreciate the institutional resources provided by MIT, EAPS, PAOC, Harvard University, Harvard Forest, and the Marine Biological Laboratory.

Contents

List of Figures

List of Tables

Chapter 1

Introduction

1.1 Background

1.1.1 Motivation

The viability of hydrogen as a "clean" energy alternative to fossil fuels has undergone much public and private debate. Early efforts toward complete transition to a hydrogen economy have faced challenges in development, deployment, and policy. Today, there is renewed interest in hydrogen as both a mobile and stationary energy carrier. California already hosts a fleet of fuel cell cars and H_2 fueling stations, and its plans to diversify its fuel supply to meet its recent Low Carbon Fuel Standards[1] include ramping-up H_2 production from natural gas, gassification of biomass wastes and fossil-derived H_2 with carbon capture and storage (Farrell and Sperling, 2007). Storage of energy in chemical bonds by electrolysis[2] is an attractive solution to the intermittency problem inherent to renewable energy sources, such as wind and solar

---

[1] The initial Low Carbon Fuel Standard goal is to reduce the carbon intensity of California's passenger vehicle fuels by at least 10 percent by 2020.

[2] Hydrogen is produced in an electrolyzer from water by passing an electric current through an anode and cathode in contact with water ($2H_2O_l$ + electricity $\rightarrow 2H_2 + O_2$) and can even be performed on saline water, thus a candidate technology for anticipated shortages of drinking water. Fuel cells are used to re-harvest that energy. Advances in the development of efficient water-splitting catalysts in the electrolyzer (Kanan and Nocera, 2008) and cheaper materials for the fuel cell (Winther-Jensen et al., 2008) increase the feasibility of large-scale utilization of wind and solar (or nuclear) to reduce emissions of greenhouse gases and local pollutants such as NO_x, O_3, soot and sulfur.

(Levene et al., 2006).

Historically, little attention has been paid to the global budget of atmospheric H_2, despite having potentially important climate impacts in Earth's oxic atmosphere as the second-most abundant reducing gas after methane. The renewed interest in hydrogen as an energy carrier, has inspired a commitment to understanding the natural hydrogen budget[3]. As emphasized in a recent review by Ehhalt and Rohrer (2009), the response of the poorly constrained, yet dominant, soil sink for atmospheric H_2 must be assessed in light of potential leaks[4] from widespread hydrogen energy use, continued emissions from fossil fuel use, and environmental changes due to projected climate change.

1.1.2 Literature review

Atmospheric H_2 Global Budget

Molecular hydrogen (H_2) is present in today's atmosphere at a global average mole fraction of approximately 530 parts per billion (ppb) (Novelli et al., 1999). This average value oscillates between clear minima and maxima caused by the superimposed seasonal cycles of H_2 sources and sinks. The seasonal cycle is evident in Figure 1-1, where the time-series of H_2 (*upper*) and CO (*lower*) mole fractions are compared from 1994 to 2007. These measurements were recorded at Mace Head, Ireland (*green*) and Cape Grim, Tasmania (*black*) Advanced Global Atmospheric Gases Experiment (AGAGE) stations (Prinn et al., 2000). Mole fraction anomalies (*i.e.*, much higher or lower than background levels arriving from over the Atlantic Ocean) are superimposed on the seasonal cycles. H_2 and CO are reduced products of incomplete combustion

---

[3] In 2007, the European Commission funded a multi-year project, EUROHYDROS, to investigate the natural and anthropogenic mechanisms behind the atmospheric H_2 budget in recognition of the candidacy of H_2 as a future energy carrier. http://www.meteor.uni-frankfurt.de/eurohydros/

[4] Reasonable estimates of H_2 loss to the atmosphere due to leaks in from delivery and end-use systems in a large-scale hydrogen economy (including pipelines, storage systems, compressors, pumps and vehicles) range from about 1 to 10%, with the most conservative estimates coming from industry and reported ranges for the existing H_2 distribution grid in Germany (Bond et al., 2008). Estimates of impacts vary widely, from transition to a large-scale hydrogen economy actually reducing H_2 emissions by replacing fossil fuels, to the transition resulting in a tripling of atmospheric H_2 mole fractions (Lovins, 2003; Warwick, 2004; Tromp et al., 2003).

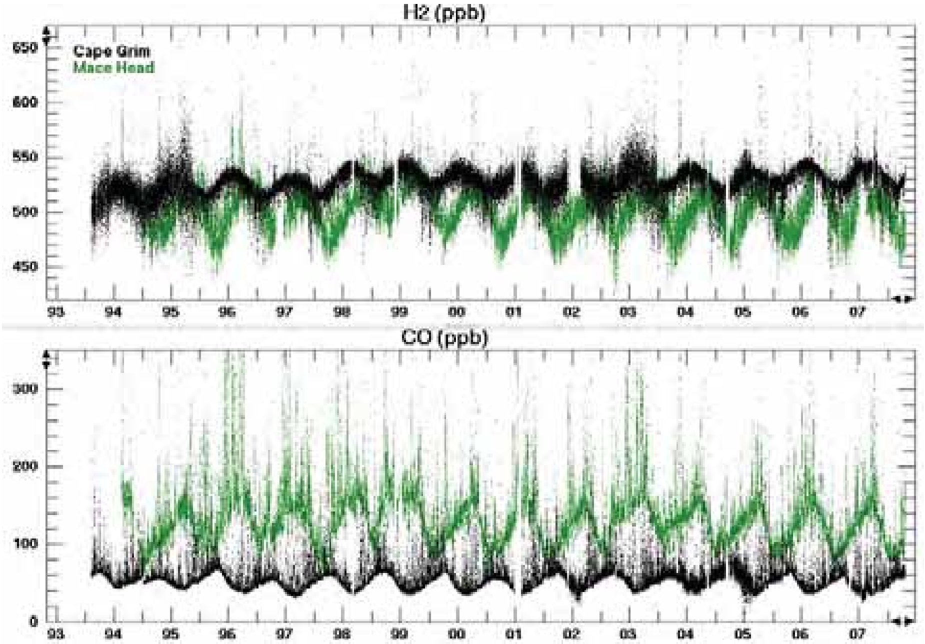

Figure 1-1: Multi-year, high-frequency H_2 (top) and CO (bottom) measurements at the Mace Head, Ireland (green) and Cape Grim, Tasmania (black) Advanced Global Atmospheric Gases Experiment (AGAGE) stations (Prinn et al., 2000). H_2 and CO have strong seasonal cycles in the Northern Hemisphere. Mole fraction anomalies (*i.e.*, much higher or lower than background levels arriving from over the Atlantic Ocean) were positive (above background levels) for both H_2 and CO and negative anomalies (below background levels) for H_2 only as a result of local emissions and uptake processes. Concentrations of H_2 are lower in the Northern Hemisphere due to the large soil sink.

and pollution anomalies above the background seasonal cycle are evident for both. However, only H_2 shows sharp depletion anomalies where mole fractions fall far below the seasonal cycle. Atypical for trace gases emitted anthropogenically, average H_2 mole fractions are lower in the Northern Hemisphere (*green*) than in the Southern Hemisphere (*black*). Curiously, the H_2 seasonal cycle is also only three months out of phase between hemispheres, whereas most other gases that undergo photochemical and biological conversions exhibit six-month phase shifts across the equator (*e.g.*, CO). These peculiar characteristics are largely the result of the dominant soil sink for atmospheric hydrogen, which has been estimated to comprise 62% to 92% of total loss, and is a relatively stronger component of the H_2 budget in the Northern Hemisphere (Conrad and Seiler, 1985; Novelli et al., 1999; Gerst, 2001; Hauglustaine, 2002).

Table 1.1: Average Global Budget of H_2 in the Troposphere (Novelli et al., 1999; Rhee, 2006; Xiao et al., 2007)

Budget Term **[Tg yr^{-1}]**	**Novelli et al. [1999]**	**Rhee et al. [2006]**	**Xiao et al. [2007]**
HCHO photolysis	40 ± 11	64 ± 12	76 ± 9
Biomass Burning	16 ± 5	16 ± 3	12 ± 3
Fossil Fuel	15 ± 10	15 ± 6	15 ± 10
Total Sources	77 ± 16	107 ± 15	103 ± 10
Oxidation by OH	19 ± 5	19 ± 3	18 ± 3
Soil Uptake (**% of Total Sink**)	56 ± 41 **(75%)**	88 ± 11 **(82%)**	84 ± 8 **(81%)**
Stratospheric Sink	–	–	1.9 ± 0.3
Sink Total	75 ± 41	107 ± 11	104 ± 8
Tropospheric Mass [Tg]	155 ± 10	155 ± 2	149 ± 23
Tropospheric Lifetime [yr]	2.1	1.4	1.4

Sources & Sinks

The H_2 budget[5] has been determined using "bottom-up", "top-down" and inverse-model approaches, and a few examples are given in Table 1.1 (Novelli et al., 1999; Rhee, 2006; Xiao et al., 2007). The largest source of H_2 is via photodissociation

---

[5] Minor sources, such as oceanic and terrestrial N_2 fixation and sinks (3 to 6 Tg yr^{-1}) are not listed, but are included in the table totals.

or oxidation of methane and nonmethane hydrocarbons (NMHCs) to formaldehyde (HCHO) and the subsequent photolysis of HCHO[6] to H_2 and CO. Secondly, combustion of fossil fuels and biomass burning is a major, direct source of atmospheric H_2 that can often be tracked by characteristic H_2:CO ratios. The H_2 sinks include uptake by soils, which will be discussed in detail, and its reaction with the OH[7] "cleansing radical". Diffusion of H_2 from the troposphere to the stratosphere is a minor loss term for tropospheric H_2 (Table 1.1); in fact, some of these hydrogen atoms are ultimately lost to space (Hunten and Strobel, 1974).

H_2 Impacts

It is prudent to assess the impact of changes to future H_2 emissions that might arise from energy use and climate change. H_2 emissions could increase under future energy use scenarios, either by increased fossil fuel combustion or leakage during use of H_2 as an energy carrier. Climate change may cause increased H_2 emissions from increased wildfire emissions or increases in H_2 precursor emissions (*e.g.*, methane and NMHCs.) Though hydrogen itself is not radiatively active, its reaction with the ·OH radical influences the global atmospheric oxidizing capacity. H_2 competes with other reduced atmospheric trace gases (*e.g.*, carbon monoxide (CO) and methane (CH_4)) for oxidation reactions with the ·OH radical, thereby increasing the residence time of potent greenhouse gas CH_4 in the atmosphere. H_2 is therefore considered to be an indirect greenhouse gas. Increased levels of H_2 may decrease the average ·OH level and thus the ability of ·OH to scavenge direct greenhouse gases like CH_4 from the atmosphere, thereby increasing their lifetimes and radiative impacts (Derwent et al., 2006). Elevated levels of hydrogen may also increase urban levels of ozone which is a greenhouse gas with negative health impacts[8]. Furthermore, H_2 diffuses into the

---

[6] There are two competing pathways for HCHO photolysis - Reaction 1: $HCHO + hv \rightarrow HCO + H$, Reaction 2: $HCHO + hv \rightarrow H_2 + CO$ - where Reaction 2 is more dominant in the troposphere. The competing reaction for HCHO is reaction with OH, that will produce CO but no H_2.

[7] OH Sink Reaction: $H_2 + OH \rightarrow H + H_2O$

[8] H_2 is an ozone precursor: $H_2 + OH \rightarrow H + H_2O$, $H + O_2 \rightarrow HO_2$, $HO_2 + NO \rightarrow NO_2 + OH$, $NO_2 + uv + O_2 \rightarrow NO + O_3$

upper atmosphere and forms stratospheric water vapor[9] and ice crystals. This can result in increased rates of catalytic ozone destruction in the ozone layer because those reactions occur on ice surfaces.

There is no consensus on the long term trend of H_2 mole fractions in the atmosphere; published include -2.3 ± 0.1 ppb yr^{-1} (Novelli et al., 1999), +1.2 ± 0.8 ppb yr^{-1} (Simmonds et al., 2000), +1.4 ± 0.5 ppb yr^{-1} (Langenfelds et al., 2002), and +3.2 ± 0.5 ppb yr^{-1} (Khalil and Rasmussen, 1990). Long-term observation of H_2 began in 1985, but have not been carried out for much more than 20 years at one location, and issues with drifting calibration standards and detector response challenge confidence in the ability to compare long-term observations, although new best practices have been described (Jordan and Steinberg, 2011). It is not clear whether anthropogenic combustion emissions have increased atmospheric H_2 mole fractions since preindustrial times or whether the soil H_2 and OH sinks have responded accordingly to keep mole fractions relatively stable relative to the pre-industrial levels. The OH sink is well constrained, but a more mechanistic understanding of the soil sink is necessary to understand its response to the expected increase in H_2 emissions.

Hydrogen Soil Sink

Earth's soils are responsible for the removal of ~50 to 90 Tg yr^{-1} of H_2 from the atmosphere via a microbe-mediated process that remained elusive even three decades after its discovery (Schmidt, 1974). Field and lab measurements have established a range of observed hydrogen uptake rates, which are typically represented by a dry deposition velocity, v_d, where the loss flux of hydrogen to the soil, Φ_{loss}, is expressed as $\Phi_{loss} = v_d[H_2]$. The range of reported values for the H_2 deposition velocity from the literature are shown in Figure 1-2, which vary quite widely (Conrad and Seiler, 1980, 1985; Yonemura et al., 1999, 2000; Gerst, 2001; Rahn, 2002; Sanderson et al., 2003; Steinbacher et al., 2007; Lallo et al., 2008; Constant et al., 2008a; Smith-Downey et al., 2008).

---

[9] Stratospheric water vapor formation from H_2 and water cycling reactions: $H_2 + O(^1D) \rightarrow OH + H$, $OH + HO_2 \rightarrow H_2O + O_2$, $H_2O + O(^1D) \rightarrow 2OH$

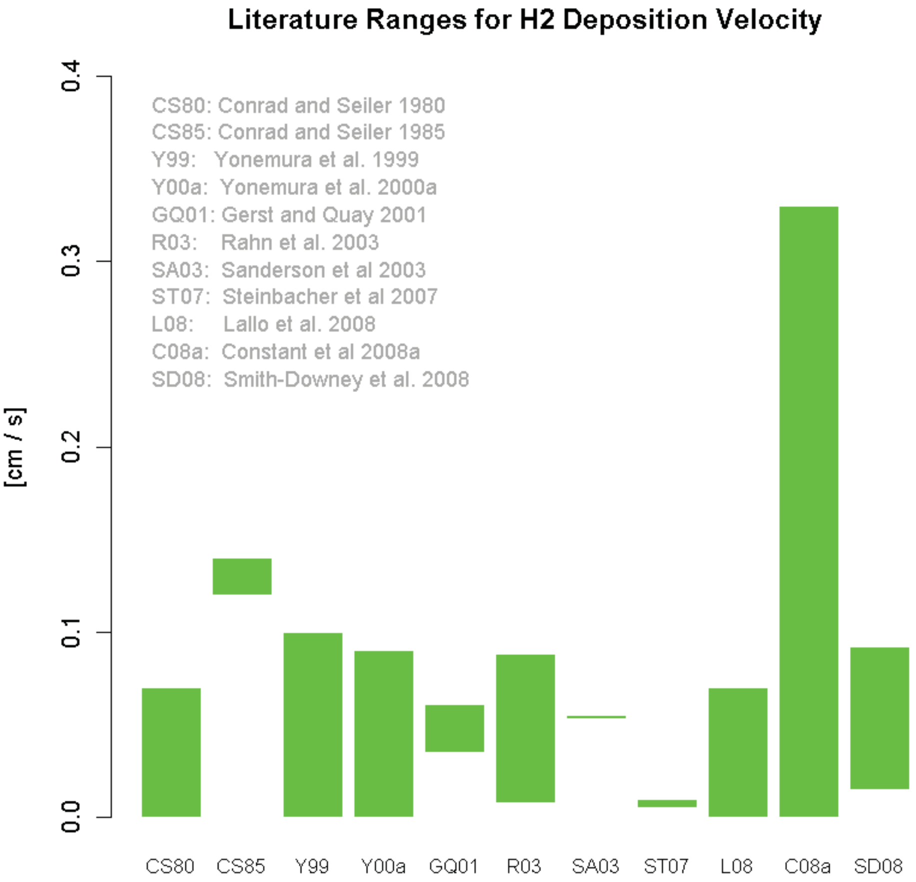

Figure 1-2: Literature values for the H_2 deposition velocity.

Soil factors that have been observed to influence H_2 uptake include water content, temperature, pH, and organic matter. Soil water content is an important control on H_2 uptake: high levels can strongly inhibit diffusion of H_2 into soil, but there may be a minimum moisture content required for biological activation of H_2 utilizing microorganisms (Smith-Downey et al., 2008; Conrad and Seiler, 1985; Fallon, 1982; Conrad and Seiler, 1981). Temperature has been reported to have mixed effects on H_2 uptake, with different studies reporting either inhibition of H_2 uptake below 10°C (Constant et al., 2008a), optimal uptake between 10°C and 30°C, and significant uptake even down to -4°C (Smith-Downey et al., 2006), or no temperature effect at all (Conrad and Seiler, 1985; Yonemura et al., 2000). The effect of soil pH and soil organic matter are even less certain. Field studies showed either no strong relationship with pH or that variation in soil moisture content confounded measurements (Schuler and Conrad, 1991; Goedde et al., 2000). Soil organic carbon and H_2 uptake were correlated in volcanic soils and boreal forests (King, 2003; King and Weber, 2008; Rahn, 2002), but not in subtropical soils (Conrad and Seiler, 1985). Variations in methodology, calibration scales and field sites may contribute to the different absolute values of these soil variables, yet the need for a more mechanistic description of soil processes is clear.

Recent research has found that the difference between H_2 uptake in forest, desert and marsh ecosystems was a function of diffusion (soil moisture and soil porosity controlling diffusion of H_2 to microbial communities) and of the vertical distribution of microbiological activity (Smith-Downey et al., 2008). Diffusion of trace-gases through soils and its dependence on soil moisture and temperature has been represented for other trace gas species (Liu et al., 1995). Future research should thus aim to describe the mechanisms by which soil variables affect the vertical distribution and activity of atmospheric H_2-consuming soil microorganisms.

Soil Microorganisms Utilizing H_2

Microorganisms utilize H_2 as an energy source with hydrogenase enzymes that catalyze the reversible oxidation of hydrogen[10]. Hydrogenases are classified by the metal ion and cofactors in their catalytic centers: [NiFe]-, [FeFe]- and [iron sulfur cluster free]-hydrogenases (Constant et al., 2009). Nearly all research on hydrogenases and microorganisms utilizing H_2 as an energy source belong to the low-affinity (Km $\sim$ 100 ppm), high-threshold (0.5 to 8 ppm) class that are unable to utilize atmospheric levels of H_2 (Conrad, 1996). These microorganisms are found in environments with H_2 levels of hundreds of parts per million and higher, including soil and sediment layers, where fermenting bacteria and methanogens exchange H_2 in symbiotic substrate degradation, or around legume nodules, where N_2-fixation releases relatively high levels of H_2. In whole soil samples, two different pH and temperature optima were observed: one for the low-affinity, high-threshold hydrogenases and the other corresponding to the high-affinity (Km $\sim$ 5-90 ppm), low-threshold (less than 0.1 ppm) hydrogenases which are able to utilize atmospheric levels of H_2 (Schuler and Conrad, 1991).

The first microbial strain demonstrating the ability to consume atmospheric levels ($\sim$ 500 ppb) of H_2 was isolated in recent years, *Streptomyces* sp. PCB7 (Constant et al., 2008b). This organism grown in monoculture demonstrated H_2 uptake rates up to 60% that of the whole soil H_2 uptake rates. Clearly other uncultured microorganisms or exoenzymes also contribute to the net H_2 uptake rates measured in soils. Early studies attributed soil H_2 oxidation entirely to extracellular hydrogenase enzymes (Conrad and Seiler, 1981), though attempts to extract those exoenzymes have only recovered less than 2% of the whole soil uptake activity (Guo and Conrad, 2008). Recent inhibition experiments suggest that intact microorganisms are responsible for 60-80% of uptake (King, 2003). The hydrogenase of *Streptomyces* sp. PCB7 has been classified as the [NiFe]- type because nickel amendments to that strain increased H_2 uptake rates. In recent years, the work of Constant et al. (2008b, 2010, 2011a,b) has shown that active metabolic consumption of atmospheric H_2 is the driving force

---

[10] H_2 Oxidation: $H_2 \leftrightarrow 2H^+ + 2e^-$

behind the significant soil sink. This finding contrasts strongly with the previous assumptions of H_2 uptake by free exoenzymes. More detail on the exiting advances in this field is given in Chapter 5, where results from the lab-based component of this thesis are presented.

Ecosystem-Scale H_2 Uptake

The strength of an ecosystem's H_2 sink has been inferred from the rates of decline in trace gas concentrations at one height at times when the boundary layer is most 'box-like' - at nighttime, with low winds and a capping inversion (Simmonds et al., 2000; Steinbacher et al., 2007). This method greatly simplifies the boundary layer micrometeorology, typically neglecting both advection and vertical exchange, which is not reliable with low sampling frequency or high surrounding surface heterogeneity. In fact, in fulfillment of requirements for the PAOC General Exam, I applied a one-dimensional vertical eddy diffusion model to select cases of H_2 drawdown during fairly stagnant, nocturnal inversions using extensive meteorological data from measurement campaigns at the AGAGE Mace Head station in Ireland. The H_2 uptake was assessed, but confidence in the results was limited by low sampling frequency (40 min) and nonzero horizontal advection on that breezy peninsula.

The need for measurements of higher-frequency atmospheric H_2 *fluxes* to truly measure the vertical exchange of H_2 due to the soil sink was made clear by that research. Only one study has actually measured the atmospheric *fluxes* of H_2. These measurements were obtained over a grassland in Quebec using a manufactured Bowen Ratio System® from Campbell Scientific and a Trace analytical RGA5 system for measurement of H_2 concentration gradients (Constant et al., 2008a). The system was used to derive the sensible heat eddy diffusivity coefficient from the temperature gradient, net radiation, ground heat flux, and the water vapor concentration gradient (to derive the Bowen ratio, which is the ratio of the sensible heat flux to the latent heat flux). Their method does not use a sonic heat flux and forces closure of the surface energy balance. The measurements show that soil uptake dominates H_2 soil-atmosphere exchange during most of the year and that soil temperature was correlated with uptake rates. The Constant et al. (2008a) study is the only extant H_2 flux study that was obtained using a flux-gradient approach, and not using flux chambers. Goals of this thesis include to add a novel set of measurements of ecosystem-scale H_2 fluxes performed in a forest ecosystem and to quantify correlations of the flux measurements with concurrent measurements of environmental, soil, and microbiological variables relevant to the soil sink process.

1.2 Thesis goals and approach

The overarching goal of this thesis is to contribute to the process-based understanding of the H_2 soil sink with targeted field and laboratory measurements. To accomplish this goal, a strategy was adopted with two main components that address the thesis goal by different approaches:

Field component (H_2 fluxes): To measure fluxes of H_2 in a temperate forest to determine the strength, seasonality, and variability of the soil sink for atmospheric H_2. To utilize concurrent measurements of possible process-relevant environmental and chemical variables to deduce correlative relationships with H_2 fluxes.

Laboratory component (H_2 microbiology): To contribute to the fundamental understanding of the soil microorganisms that drive the dominant sink for atmospheric H_2 by isolating soil microorganism and studying their H_2 uptake behavior.

The motivation and approach framework are discussed separately for each component in this section.

1.2.1 Field component: H_2 fluxes

Motivation:

As discussed in the introduction, it is important to understand the strength, seasonality, and controlling factors of the soil sink of atmospheric H_2. This aim has been plagued by the high spatial variability of soils and the low measurement frequency of traditional flux-chamber methods. In contrast, automated measurements of the fluxes of atmospheric H_2 made both at canopy- and ground-level on a flux tower can provide higher frequency information on the ecosystem-scale fate of H_2 with a larger footprint than flux chambers. Additionally, correlations of the H_2 fluxes with environmental variables (*e.g.*, air temperature, soil temperature, soil moisture) measured at the field site will be tested. The atmospheric flux component of this thesis was designed to answer the following questions:

1. How do atmospheric fluxes of H_2 vary diurnally and seasonally?
2. Do ecosystem-scale flux measurements of the H_2 soil sink agree with traditional flux chamber and modeling methods?
3. Which environmental variables and trace gases are observed to correlate with H_2 fluxes?

Approach

This component addresses the primary goal of this thesis, which is to contribute to the understanding of the significant soil sink of atmospheric H_2, by making automated measurements of the H_2 flux in a natural ecosystem for at least one full year. Gas chromatography with a detector sensitive to low levels of H_2, such as the HgO reduction or helium pulsed discharge detector, is the only readily available tool for measuring H_2 at atmospheric mole fractions. However, the analysis time is far too slow for eddy covariance flux measurements. Traditional H_2 soil uptake studies either do not directly measure fluxes (mole fraction time series) or disturb soil-atmosphere gas exchange when they do (flux chambers). Flux-gradient techniques can be used to target vertical fluxes over a relatively large footprint with little sampling disturbance (Dunn et al., 2009; Goldstein et al., 1996; Goldstein, 1998; Pielke Sr., 1984; Businger et al., 1971; Baldocchi et al., 1988; Liu and Foken, 2001; Meyers et al., 1996); therefore, in this project a tower-based H_2 flux-gradient instrument was designed as a targeted approach for studying the H_2 soil sink.

In the flux-gradient technique, atmospheric fluxes of trace gases, heat, and momentum, denoted by C, are described by a Fick's diffusion relation, where the vertical flux, F, is equal to the vertical gradient of C, dC/dz, times a constant of proportionality, K, which describes the action of turbulent atmospheric eddies: $F = -K \times dC/dz$. The method relies on the assumption that eddies mix chemicals, heat, and momentum uniformly within the atmospheric boundary layer.

The first method for inferring K assumes similarity between fluxes of trace gases at the forest (Dunn et al., 2009; Goldstein et al., 1996; Goldstein, 1998). This should be applied over vertical distances where both trace gases are conserved (*i.e.*, within a level of the forest where no significant sources or sinks are active). The flux and concentration gradient of a comparative chemical can be used to calculate K. Using this K value, the flux of a more slowly measured quantity, such as H_2, can then be calculated from its concentration gradient. This method is denoted "trace gas similarity" and is illustrated in Figure 1-3 for comparative chemicals CO_2 and H_2O. The flux of CO_2 and H_2O (*e.g.*, F_{CO2}) can be measured directly by an eddy covariance method and their concentration gradients (*e.g.*, $\Delta\chi_{CO2}/\Delta z$) can be measured at the same inlet heights as the H_2 concentration gradient ($\Delta\chi_{H2}/\Delta z$). The quantities measured in or available to this study at both the above- and below-canopy level are shown in Figure 1-3. As shown in that figure, eddy fluxes of CO_2 and H_2O are available only above the canopy, so the trace gas similarity method can only be applied at that location.

A second method for inferring K is by assuming similarity between the fluxes of sensible heat, H, and of chemicals, like H_2 (Dunn et al., 2009; Liu and Foken, 2001; Meyers et al., 1996). For this method, the sonic heat flux is corrected using a modified Bowen ratio approach, and the temperature gradient ($\Delta T/\Delta z$) is measured at the

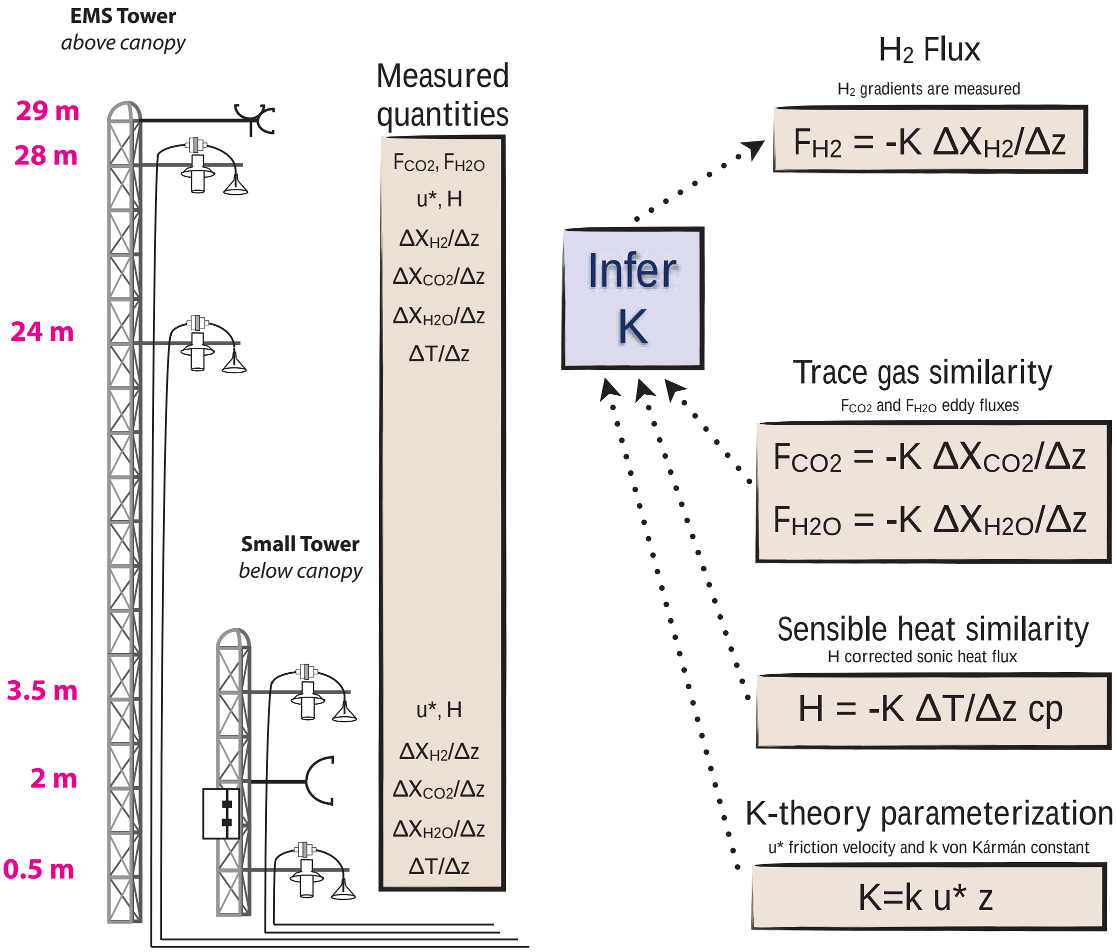

Figure 1-3: Schematic illustrating the approach for obtaining the flux of H_2 above and below the forest canopy by inferring the turbulent eddy coefficient, K, by one of three methods. K can be inferred by a trace gas similarity approach, where the flux and concentration gradient of another gas like CO_2 or H_2O are measured. Similarity to the sensible heat flux and temperature gradient can also be used. Finally, K can be parameterized from other measured quantities, such as the friction velocity u_* shown here. The measured and available quantities above and below the canopy for the calculation of H_2 fluxes are shown in the "measured quantities" list.

same heights as the H_2 concentration gradient (Liu and Foken, 2001; Dunn, 2006; Dunn et al., 2009). The available measurements (Figure 1-3) allow for sensible heat similarity to be applied to calculate H_2 fluxes both above and below the canopy.

The last method for inferring the turbulent eddy coefficient is by parameterizing K by one of a number of theories (Pielke Sr., 1984; Businger et al., 1971; Baldocchi, 2012). Figure 1-3 is a simple parameterization based on the friction velocity, u_*, which an indication of the shear stress created by the wind flow that can be calculated from 3D sonic measurements (Section 3.2.3).

In this study, an instrument was designed to measure the concentration gradient of H_2 to high precision for the flux-gradient calculation. Instrument design and performance is discussed in Chapter 2. The methods for calculating fluxes are discussed in detail and annual H_2 fluxes are presented in Chapter 3. Wintertime fluxes are investigated in detail in Chapter 4.

1.2.2 Laboratory component: H_2 microbiology

Motivation

Laboratory studies were conducted in this thesis work to contribute to the the fundamental understanding microbiology behind the H_2 soil sink.

Approach:

Questions this laboratory study is designed to answer:

1. Is the presence of the pertinent hydrogenase predictive of an organism's tendency to consume atmospheric H_2 in the environment?
2. Is atmospheric H_2 consumption tied to organismal lifestyle?

The laboratory work was performed both in the Torrey Lab at the Harvard Forest Long Term Ecological Research site in Petersham, MA and in the Bosak-Ono Lab at MIT. The approach and detailed work related to the microbiology is only described in Chapter 5, and the approach will not be described in detail in this introduction.

Further information can be found in the senior thesis of Ms. Deepa Rao (B.S., MIT, 2012), entitled “Exploring the microbe-mediated soil H_2 sink: A lab-based study of the physiology and related H_2 consumption of isolates from the Harvard Forest LTER”, from the Department of Earth, Atmospheric and Planetary Sciences at MIT (Rao, 2012). Her thesis contains detailed methods and analysis sections with supplemental information to what is presented in this thesis.

Chapter 2

Instrument for atmospheric H_2 flux-gradient measurements

Objective

This chapter is concerned with the design and construction of an instrument for measuring atmospheric H_2 fluxes by a flux-gradient approach (Section 1.2). Instrument performance is critically evaluated to ensure that 1) H_2 concentration gradients above and below the forest canopy can be measured to high precision, 2) sample streams are physically averaged sufficiently to account for sampling time mismatch, and 3) there is no systematic bias in the mole fraction measurements between each inlet of a concentration gradient pair.

Results

- An automated and continuous instrument system was designed and constructed that synchronized a gas chromatograph (H_2), infrared gas analyzers (CO_2 and H_2O), meteorological sensors (temperature and wind), devices for the selection and control of sample gas streams, and two data logging devices.

- The instrument worked!

- Compared to the traditional mercuric oxide reduced gas detector (HgORD), a ten-fold improvement in H_2 mole fraction measurement precision was attained with a helium ionization pulsed discharge detector (HePDD)[1].

- Over the study period, the linearity of the HePDD response was stable and the calibration standard had no significant drift; therefore, the H_2 mole fractions in this study can be reported with confidence.

- Infrared gas analyzer measurements of CO_2 and H_2O were made to satisfactory precision (0.025 to 0.043% and 0.04 to 0.05% for CO_2 and H_2O, respectively) for measuring ambient concentration gradients.

- Integrating volumes, used to physically average the air, were found to be a key instrument feature for calculating concentration gradients from mole fraction measurements staggered in time.

- No significant mole fraction bias between the gas sample lines of a given concentration gradient pair (*e.g.* the 24 m versus 28 m inlets) was found for H_2 measurements. Summertime condensation within sample stream tubing compromised the nulling procedure for CO_2 and H_2O bias assessment, but convincing evidence for bias between the sampling lines was not found.

- The instrument system was found to meet the stated performance objectives over its deployment at Harvard Forest during the 2010 - 2012 period.

2.1 Instrument design

A primary goal of this thesis is to contribute to the understanding of the significant soil sink of atmospheric H_2 by making automated measurements of the H_2 flux in a natural ecosystem for at least one full year. To achieve this goal, multiple measurements were conducted to enable the calculation of the vertical flux of H_2; therefore, a major

---

[1] To our knowledge, this is the first application of the HePDD to an ecosystem-scale study with the goal of quantifying local H_2 sources and sinks.

part of this work was the integration of the instruments into a flux-gradient system. The philosophy and manifestation of the integrated instrument design is discussed in Section 2.1 (overall instrument schematic Figure 2-1) and its installation in the field is described in Section 2.1.1 (field installation). A detailed presentation of the individual components for measuring H_2, CO_2 and H_2O, and meteorological variables are discussed in Sections 2.1.2 (gas chromatograph for H_2), 2.1.3 (spectrophotometric analyzer for CO_2 and H_2O), and 2.1.4 (meteorological measurements), respectively.

Instrument philosophy

As discussed in Section 1.2, a single flux-gradient calculation requires two gas inlets separated by some vertical distance, z, and an early consideration was the number and location of concentration gradient measurements. A CO_2 flux-gradient infrared gas analyzer (IRGA) instrument system, referred to henceforth as the *IRGA rack*, was generously lent to this study by the Wofsy-Munger group at Harvard University (described in detail in Section 2.1.3). The IRGA rack was built for simultaneous sampling of two concentration gradient pairs, for a total of four gas inlets each. The instrument was designed to utilize all four IRGA rack inlet streams and to sample H_2 from the same air samples.

The above and below canopy environment were assessed to determine where to install gas inlets. Concentration gradients of the H_2 mole fraction below the forest canopy are expected to be larger than above the canopy because of the proximity to the soil sink and reduced atmospheric turbulence. However, it can be difficult to measure fluxes below a certain threshold of turbulence (*e.g.*, Gu et al. (2005)). Above the canopy, there is generally sufficient turbulence; however, well-mixed air farther from the soil sink will have much smaller concentration gradients. The height of the Harvard Forest tower limited increasing the distance over which concentration gradients were measured, which could have improved the signal-to-noise of the above canopy concentration gradient measurements. Even if the tower was higher, the flux gradient method would not work if it spanned nocturnal inversions, which could limited analysis of data on a higher tower. Depending on the instrumental precision these small concentration gradients may limit the ability to calculate a flux above the canopy. Both locations for flux-gradient measurements present challenges and advantages; we decided to set up two flux-gradient sets, one above and one below the canopy, to test the different methods and to have the opportunity to rely more heavily on one location if needed. Additionally, measuring the H_2 flux above and below the canopy enabled us to diagnose the canopy environment as a H_2 source, sink, or neutral zone. Henceforth, the four gas inlets are referred to as 1T, 1B, 2T, and 2B, where "1" and "2" indicate the above and below canopy environment, respectively, and "T" and "B" refer to the top or bottom gas inlet of a given concentration gradient pair, respectively. The 1T, 1B, 2T, and 2B inlets are installed at 28, 24, 3.5, and 0.5 m heights on the tower, respectively.

Calculating a concentration gradient from mole fraction measurements that are staggered in time requires the air samples to be physically averaged long enough to span the analysis time of both inlet streams in the concentration gradient pair (Dunn et al., 2009). Furthermore, concentrations gradients within the canopy can be quite variable, and flux-gradient theory is more applicable to mean gradients than to the instantaneous gradient. This is especially important when concentration gradients are small because high-frequency perturbations in the mole fraction gradients could result in artificially large calculated concentration gradients and fluxes. The time-limiting step of the system was H_2 quantification by gas chromatography that, even with accelerated chromatography, could only sample one inlet every four minutes. In contrast, the IRGA rack, containing two gas analyzers dedicated to one concentration gradient pair each, required only one minute of sampling for each averaged measurement and could sample two inlets at a time. Integrating volumes (flow-through reservoirs) were used to physically average an inlet stream with an averaging timescale of $\tau = V/Q$, where V is the integrating volume and Q is the flow rate. The integrating volumes can be thought of as applying an exponential filter to the raw inlet stream with an e-folding time equal to τ. As a conceptual exercise, we can imagine introducing a 45 ppb spike above a background 500 ppb H_2 mole fraction to the gas inlet for one minute. If the integrating volume is 2 L and the flow rate is 250 mL/min through that volume, the H_2 spike will decay inside the well-mixed integrating volume with an e-folding time of $\tau = V/Q = 8$ min such that the perturbation decreases from 505.6 to 502.1 ppb over 8 minutes, which is a 63% reduction in the perturbation (1 e-folding timescale).

Measuring potentially small concentration gradients through different inlet lines can be prone to systematic biases due to leaks or physical interactions. Offsets between inlet streams were designed to be routinely checked by a nulling procedure, where all inlet streams sample a common reservoir of air. This allows any offsets to be quantified and instrumental issues to be diagnosed.

In summary, the goals of the instrument design were four-fold: 1) two sets of flux-gradient measurements (four gas inlets), 2) fluxes both above and below the canopy, 3) inlet streams physically averaged over an appropriate time (τ), and 4) a nulling procedure to test for systematic biases.

Instrument design

A schematic of the final instrument design is shown in Figure 2-1. The system can be divided into three main parts: 1) the gas chromatograph (GC, H_2 measurements), 2) the infrared gas analyzers (IRGA, CO_2 and H_2O measurements), and 3) the gas stream selection system (coordinates gas flow for desired sampling routine). The gas chromatograph and IRGA components are discussed in depth in Sections 2.1.2 and 2.1.3. A brief overview of the gas stream selection system is given here, and it is described in much more detail in Appendix A.1.1.

During the normal sampling routine, air samples were drawn through the sample line and four four-minute duration GC measurements were made in the following order over a 16 minute cycle: top of the EMS tower (1T, 1B) to the bottom of the small tower (2T, 2B)[2]. Meanwhile, continuous gas streams from each inlet were drawn through the IRGA rack and at any given time either the 1T/2B or 1B/2T inlets were

---

[2] The four gas inlets are referred to as 1T, 1B, 2T, and 2B, where "1" and "2" indicate the above and below canopy environment, respectively, and "T" and "B" refer to the top or bottom gas inlet of a given concentration gradient pair. The 1T, 1B, 2T, and 2B inlets are installed at 28, 24, 3.5, and 0.5 m heights on the tower, respectively

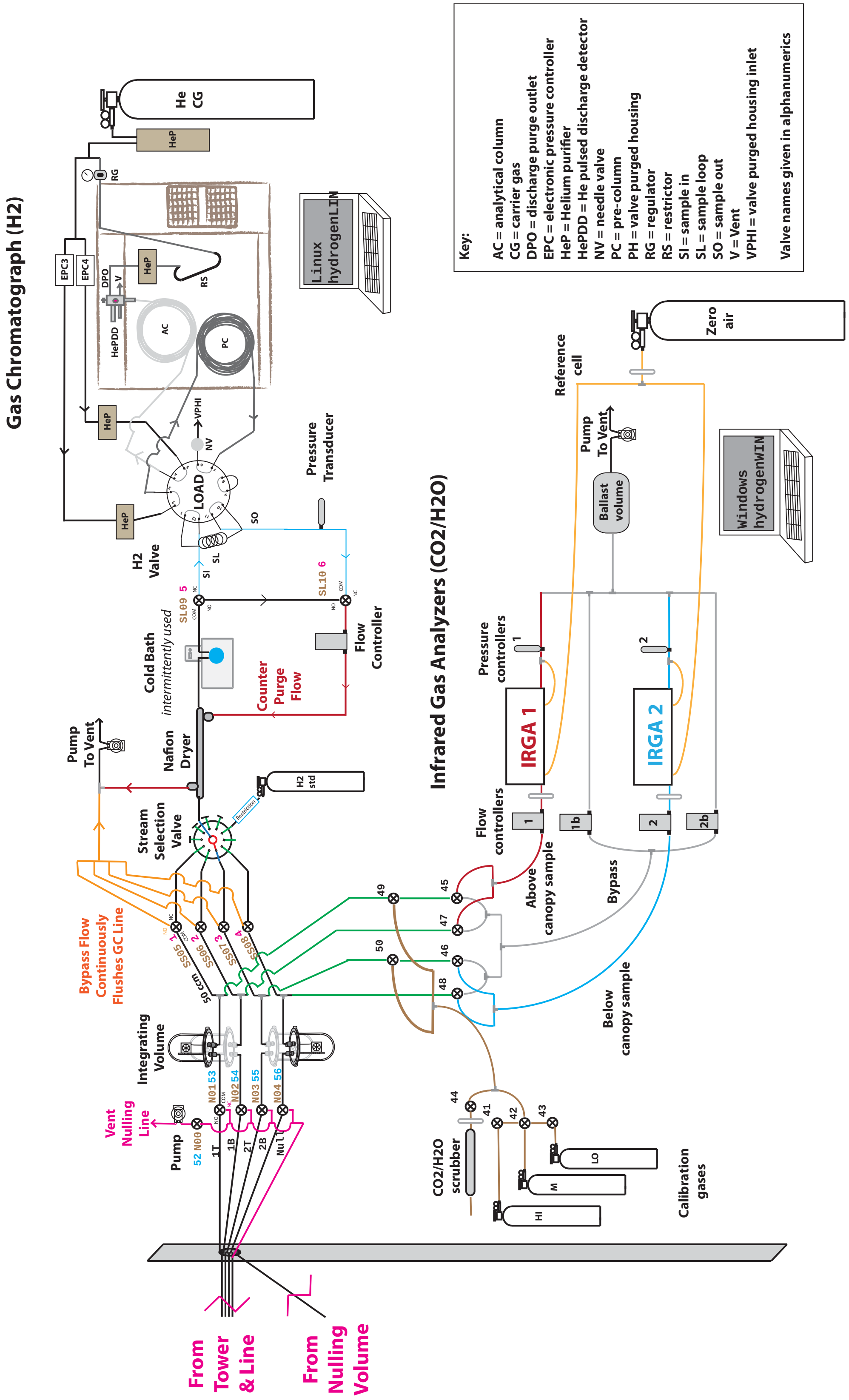

Figure 2-1: Flux-gradient instrument components installed inside the Environmental Measurement Site (EMS) shed at Harvard Forest.

sampled for a minute each before switching.

Calibrations were performed approximately every 1.5 and 3 hours for H_2 and CO_2, respectively. The H_2 calibration was performed by bypassing all tower inlet gas streams to the GC pump and sampling a calibration tank via the stream selection valve (SSV). An automated nulling routine, which samples the same volume of air to test for biases between the gas inlet streams of the instrument, was performed three times per week. Biases were tested between the 3-way solenoid nulling valves (N01 - N04) to the instrument detectors. The nulling volumes (1 L to 2 L depending on measurement period) had a residence time of 1 to 8 minutes depending on the flow rate in a given measurement period. Where the residence time is approximated by $\tau = V/F$, where V is the reservoir volume and Q is the flow rate. Details on the nulling procedure and nulling volumes are given in Appendix A.1.2. Biases were diagnosed by calculating offsets from the average concentration trend in the volume as discuss in Section 2.2.3.

As discussed in detail in Appendix A.1.3, the flux-gradient system was controlled by two computers: 1) a Fedora 11 Linux computer running GCwerks (Version 3.02-2, Peter Salameh, Scripps Institute of Oceanography, http://gcwerks.com) to control the gas chromatograph and 2) a WindowsXP machine running LoggerNet (Campbell Scientific, Logan, UT) to communicate with Campbell Scientific CR10X data loggers.

2.1.1 Field installation at Harvard Forest

The flux-gradient system was deployed and run at the Harvard Forest EMS tower instrument shed starting on 29 August 2010. The IRGA rack, GC, and upstream rack were installed in an instrument room. All gases were stored in the neighboring gas tank room except the H_2 secondary standard, which was stored in the instrument room. The IRGA rack pump was installed in a dedicated pump room to minimize the heat load to the instrument room.

Gas inlets were installed at four heights: at 24 and 28 m (1B and 1T) on the 29 m EMS tower and at 0.5 and 3.5 m (2B and 2T) on a smaller tower erected near the EMS tower over undisturbed soils as shown in Figure 2-2. A bird's eye view of

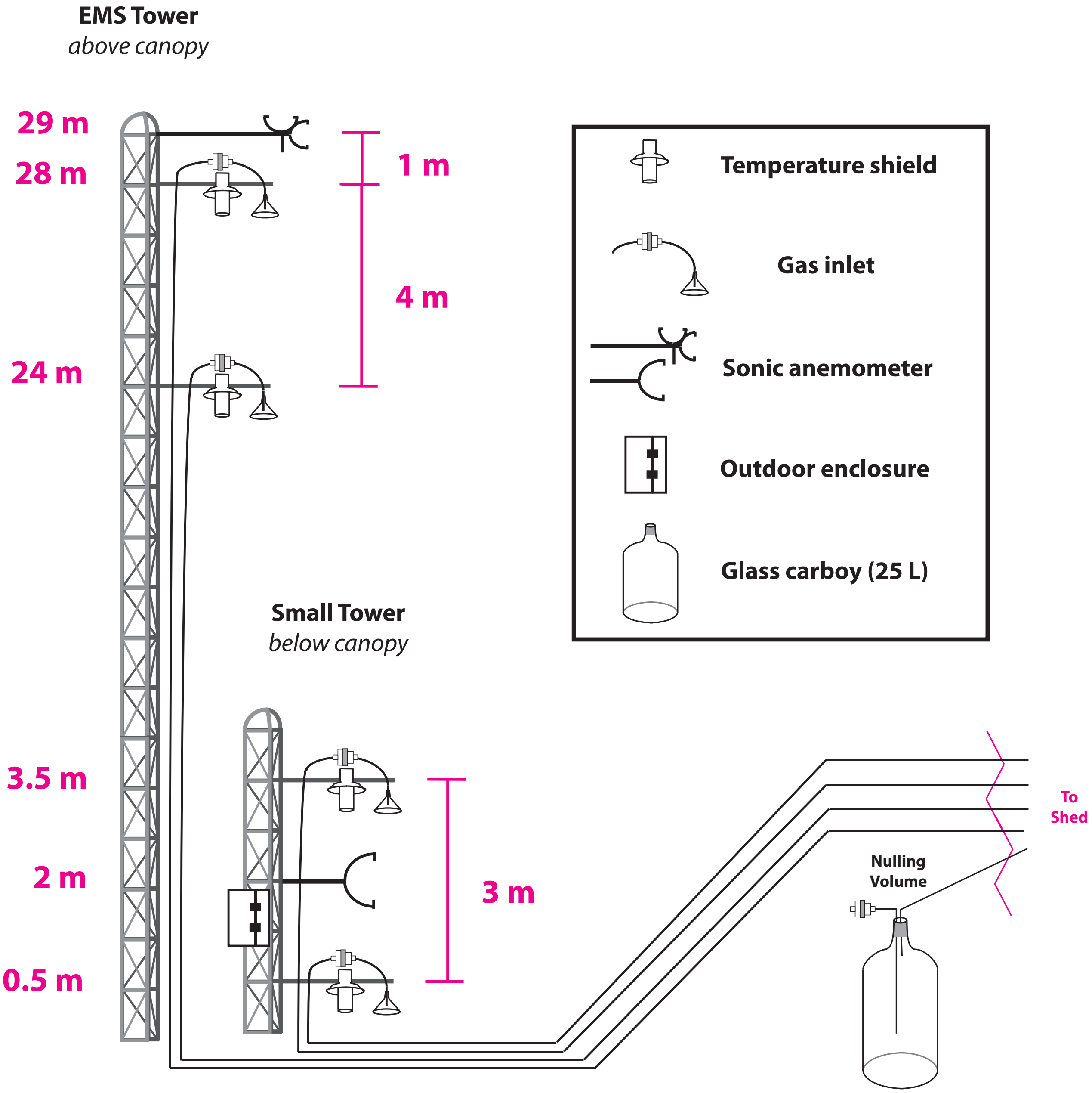

Figure 2-2: Outdoor installation of meteorological equipment and gas inlets on the Environmental Measurement Site (EMS) tower and a small tower installed over undisturbed soil at the same site in Harvard Forest.

the relative positioning of the EMS shed, EMS tower and small tower is depicted in Figure 4-2 (this view is shown later in Chapter 4 because the positioning of the shed and towers relative to snow depth stakes is important).

Temperature shields were mounted on metal rods extending out ~1 m from the tower. Gas inlets were co-located with the temperature shields. The Harvard sonic anemometer on the EMS tower was at approximately 29 m, which is 1 m above the uppermost above-canopy flux inlet. The sonic anemometer on the small tower was located halfway between the 0.5 and 3.5 m gas inlets at 2.0 m and extended out about 60 cm from the tower.

2.1.2 Gas Chromatographic measurement of H_2

Motivations for design

Atmospheric H_2 mole fractions were measured by gas chromatography (GC) using a Helium ionization Pulsed-Discharge helium ionization Detector (HePDD). The GC design was based on the recently described adaptation of a HePDD to atmospheric H_2 measurements by Novelli et al. (2009) at NOAA in Boulder, CO[3]. The detector, developed by Wentworth et al. (1992), ionizes high purity helium with a stable, low power pulsed DC discharge source. The helium discharge region emits photons to ionize the eluents exiting the column, which flow counter to the flow of the helium discharge region. Atmospheric bulk (*e.g.*, O_2, N_2) and trace (*e.g.*, H_2, Ne) gases are either ionized directly by the pulsed voltage or by photoionization. The transition of diatomic helium He_2 to the dissociative 2He ground state is the principal mode of photoionization. Electrons from the ionization of column eluents are focused from a bias to a collector electrode; this results in a positive response to fixed gases (*i.e.*, the standing current increases). The detector is universal, linear (over five orders of magnitude), highly sensitive (down to picogram minimum detectable quantities), and essentially nondestructive to the eluent (0.01 - 0.1% ionization).

---

[3] Global Monitoring Laboratory, Earth System Research Laboratory, National Oceanic and Atmospheric Administration, Boulder, Colorado, USA; and Cooperative Institute for Research in Environmental Sciences, University of Colorado, Boulder, Colorado, USA

Although helium ionization was explored in the early 1970s as an option for atmospheric H_2 measurements (Heidt and Ehhalt, 1972), the method was overshadowed by wide adoption of GCs with mercuric oxide reduced gas detectors (GC-HgORD); therefore, nearly all atmospheric H_2 measurements to date have been made with the GC-HgORD. In that detector, reduced species such as H_2, CO, and CH_4 are oxidized by a bed of hot mercuric oxide ($HgO_{(s)}$) and the subsequent production of Hg gas (Reaction 2.1) is measured photometrically at 254 nm.

$$H_2 + HgO_{(s)} \rightarrow H_2O + Hg_{(g)} \tag{2.1}$$

The GC-HgORD precision (0.5% to 1%) and detection limit are suitable for atmospheric measurements, but the detector response deviates from linearity[4] even over the narrow range of atmospheric mole fractions. Careful calibration of the GC-HgORD is required; standard mole fractions should be close to samples and at least a two point calibration spanning the range of measurements is required. An HgORD will exhibit different response curves over time as it degrades until the HgO bed needs to be replaced. Over the lifetime of the HgORD rigorous calibration is required and ultimately the detector will require refurbishment, which can cause gaps in site measurements.

The GC-HePDD system has superior performance for measuring atmospheric H_2, as has been thoroughly explored (Novelli et al., 2009). They achieved 0.12% (2σ) relative precision for the GC-HePDD over a range of 100-2000 ppb H_2 (*i.e.*, nearly an order of magnitude better precision than the HgO). Importantly, the HePDD exhibited a linear response to within 0.3% over a 2000 ppb range. Additionally, the GC-HePDD exhibited good instrument repeatability; detector response was stable within ±1.6 % (2σ) over nine months. In general, the superior precision, linearity, and stability of the detector will improve long-term measurements of atmospheric H_2 significantly. Because the GC-HePDD is universal, it requires more attention to minimizing contamination from leaks, and to measure H_2 rapidly, a pre-column and

---

[4] Deviations of the assigned versus GC-HgORD measured H_2 mole fractions of gravimetric static dilution standards were -3.5% to +1% over the atmospheric range (Novelli et al., 2009)

valve with more ports must be used to backflush the other atmospheric constituents that move more slowly through the columns.

For this work, the GC-HePDD was chosen over the GC-HgORD for the following reasons: 1) to make very precise measurements to resolve small atmospheric concentration gradients, 2) to absolve the need for more than one field calibration standard because the detector is linear, and 3) to better diagnose drift in the H_2 standard[5] because the detector response is stable over time.

GC design

In this study, a gas chromatograph (model 6890, Agilent Technologies, Santa Clara, CA) was equipped with a pulsed discharge helium ionization detector (model D-3 PDD, Valco Instruments Co. Inc. (VICI), Houston, TX). The plumbing configuration, shown in Figure 2-3, was based on Novelli et al. (2009), which is, in turn, an elaboration upon the configuration detailed in the VICI manual.

The GC-HePDD design was optimized for high precision by limiting the possibility for interferences due to gas leaks and for a short analysis time by using a shorter precolumn than the exemplary system by Novelli et al. (2009). GC design details are given in Appendix A.1.4. Example gas chromatograms are shown in Figure 2-4 for Neon and H_2 peaks from the topmost (air.1, 1T) to lowest (air.4, 2B) tower inlets during a relatively well established nighttime concentration gradient (25 April, 2011, 7:22-7:34am UTC).

GC calibration methods

A GC H_2 secondary calibration standard (No. SX-4249) was graciously prepared by AGAGE collaborators at NOAA[6]. A standard tank (34 L 900 psig operating pressure, 304L stainless steel electropolished, DOT certified, Essex Industries, St.

---

[5] H_2 standards are known to drift ($<$ 1 ppb to several 10s of ppb per year), which has made long-term measurements of H_2 difficult. Indeed, reported annual growth rates from different global monitoring networks disagree on the sign of the trend (Langenfelds et al., 2002; Novelli et al., 1999; Simmonds et al., 2000), which is likely related to the difficulties encountered with the GC-HgORD detector and calibration tank stability.

[6] Thank you to Duane Kitzis, Brad Hall, and Paul Novelli.

A: Load / Backflush

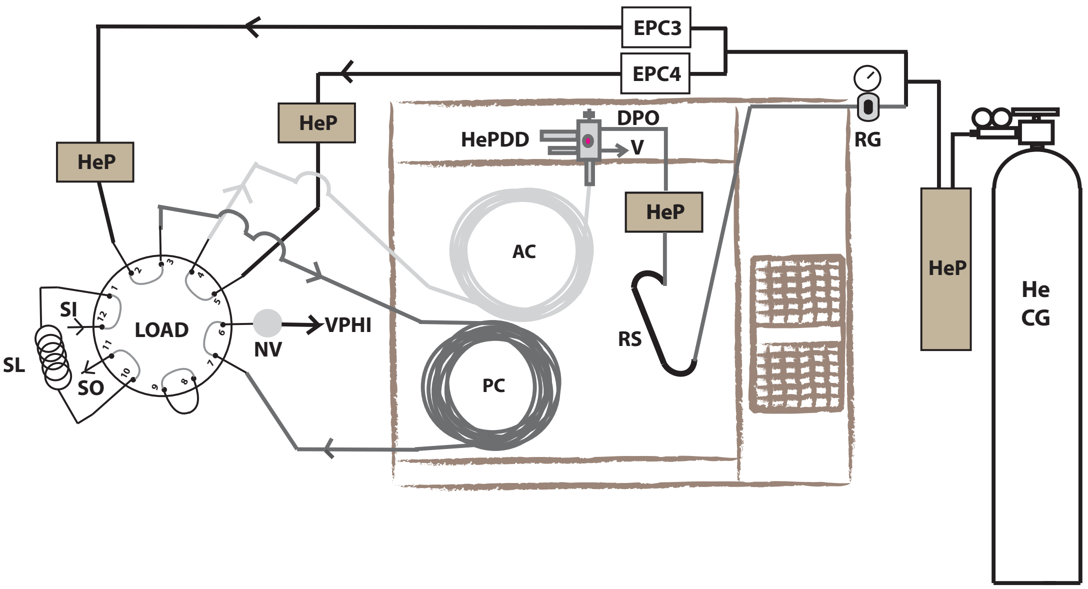

B: Inject

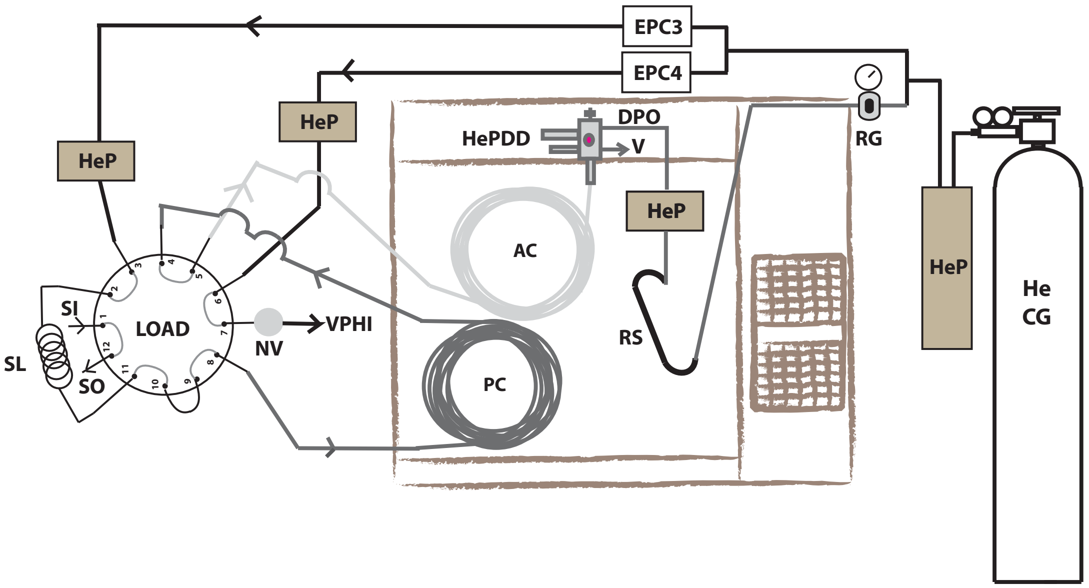

Key:

AC = analytical column
CG = carrier gas
DPO = discharge purge outlet
EPC = electronic pressure controller
HeP = Helium purifier
HePDD = He pulsed discharge detector
NV = needle valve
PC = pre-column

PH = valve purged housing
RG = regulator
RS = restrictor
SI = sample in
SL = sample loop
SO = sample out
V = Vent
VPHI = valve purged housing inlet

Figure 2-3: Schematic of the GC-HePDD system constructed in this study; samples are loaded and the pre-column is backflushed in sample valve position (A) and samples are injected in sample valve position (B).

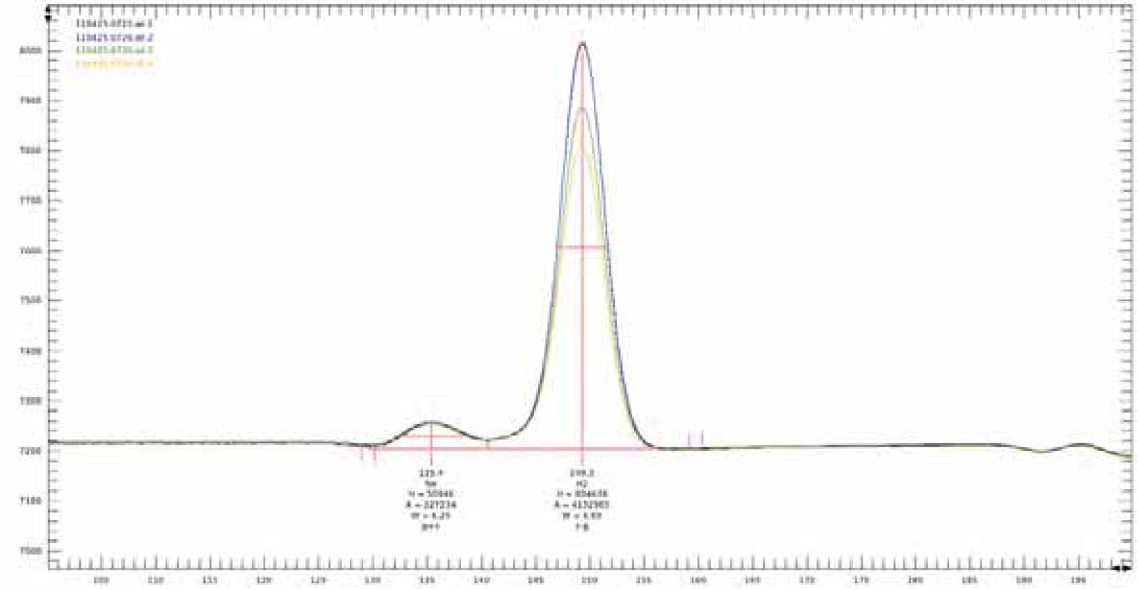

Figure 2-4: Example chromatograms (detector response versus time in seconds) for Neon and H_2 peaks from the topmost (air.1) to lowest (air.4) tower inlets during a relatively well established nighttime concentration gradient on 25 April, 2011 from 7:22-7:34am UTC.

Louis, MO) was filled with compressed air at the Niwot Ridge LTER site outside of Boulder, Colorado on 14 Jan 2009. It was calibrated twice against the NOAA primary standards on both the old and new Earth System Research Laboratory Global Monitoring Division (ESRL/GMD) scales on their in-house instrument. The 2009 and 2012 tank calibrations exhibited no significant drift at mole fractions (1σ) of 501.5 (10) and 499.0 (7.5) ppb, respectively.

A tertiary H_2 standard for the field site was brought into the calibration tank rotation on 5 October 2011 to reduce the sampling load on the secondary standard. This certified standard blend ($\sim$ 500 ppb H_2, balance air, size 150A aluminum tank, Airgas) was sampled every three hours, while the secondary standard was only used two times per day. The secondary standard is used to link the mole fractions to known scales, while the tertiary standard is used to track changes in detector response throughout the day.

The H_2 peak height (H) and area (A) were determined for each chromatographic measurement using GCwerks integration parameters. The pressure (P) and temperature (T) of the sample loop (details in Section 2.1) were used along with the gas constant (R) to calculate the molecular density, $n_D = \frac{P}{T\,R}$ (mol cm^{-3}), of each sample. Peak areas and heights were weighted by molecular density (H/n_D and A/n_D). Weighted calibration peaks were linearly interpolated onto sample timestamps and sample mole fractions, χ, were calculated using Equation 2.2.

$$\chi_{sample} = \frac{(A/n_D)_{sample}}{(A/n_D)_{std,interp}}\chi_{std} \tag{2.2}$$

2.1.3 Spectrophotometric measurement of CO_2 and H_2O

The custom-built CO_2 flux-gradient instrument system (*IRGA rack*) provided for this study by the Wofsy-Munger group at Harvard University. The IRGA rack contains two non-dispersive, infrared gas analyzers (Model 6262, LI-COR Inc., Lincoln, NE) that measure the 4.26 and 2.59 micron absorption bands for CO_2 and H_2O, respectively. The IRGA rack was deployed from 2003-2006 at the Northern Old Black Spruce (NOBS) site in central Manitoba, Canada for the Dunn et al. (2009) comparative study of the link between soil hydrology and carbon exchange at a“dry” and a “wet” site in the highly heterogeneous boreal forest environment. A detailed description of the instrumentation and methods can be found in the Appendix of Dunn, Wofsy, and Bright (2009) (Ecological Archives A019-021-A1). The sampling procedure alternated between measuring the top and bottom inlets of each concentration gradient pair for one minute each. A schematic of the IRGA rack is presented in Figure 2-5 and details regarding the system are given in Appendix A.1.5

IRGA calibration methods

The IRGAs measure the infrared absorption of CO_2 and H_2O in the sample cell, which is zeroed by CO_2- and H_2O-free air in the reference cell. Absorption is a non-linear function of CO_2 and H_2O mole fraction; therefore, calibration curves of mole fraction versus signal voltage had to be constructed. Although calibration curves for CO_2 and H_2O were obtained from a factory calibration in May of 2009, field calibrations were

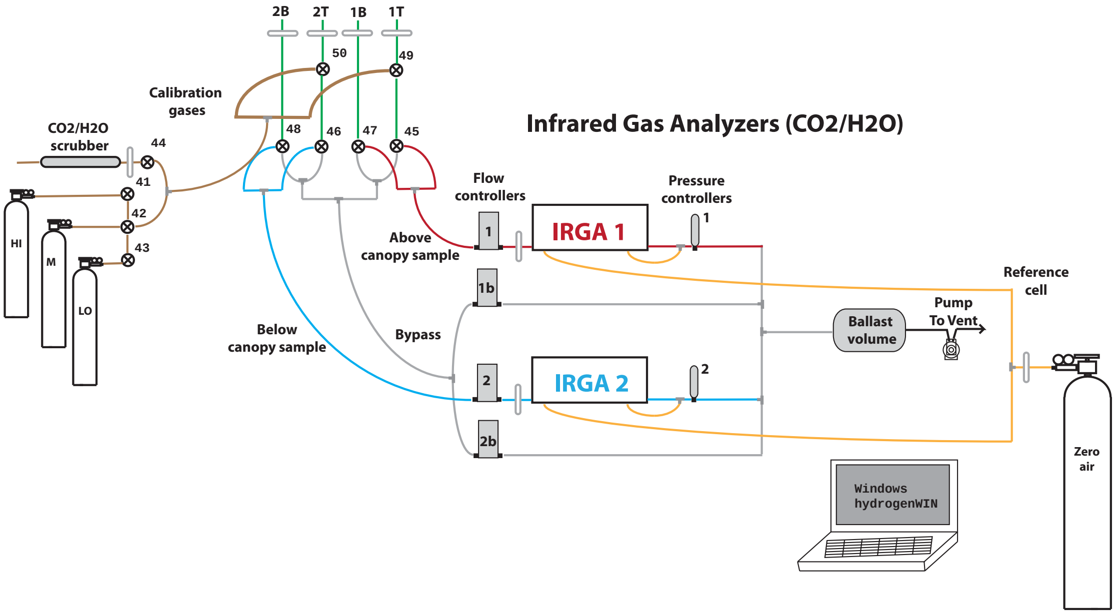

Figure 2-5: Schematic of the custom-designed IRGA rack adopted from Dunn, Wofsy, and Bright, 2009 (Dunn et al., 2009).

performed for the IRGAs installed within the flux-gradient system *in situ*.

A H_2O calibration curve was generated by performing a field calibration using a supply of known water vapor mole fraction provided by a dew point generator (Model 610, LI-COR Inc., Lincoln, NE). Dew points of 5, 10, and 15°C were generated with the unit, which corresponded to approximately 33%, 46%, and 64% relative humidity or 5.4, 7.5, and 11 ppth H_2O mole fractions, respectively. The CO_2 span gas tanks provided a dry sample for comparison as they contain only 2 ppm H_2O. A calibration curve was generated for each IRGA from a second order polynomial fit of H_2O mole fraction versus raw signal voltage as is shown in Figure 2-6.

To verify the calibration method, water vapor mole fractions were calculated from a year of relative humidity data from the nearby Fisher meteorological station and were compared with water vapor measured by the IRGAs at the EMS tower (not shown). A superior fit to the Fisher data (lower average residual over a year-long comparison of H_2O time series) was obtained using the field calibration curve rather than the factory calibration; therefore, the field calibration curve was used throughout

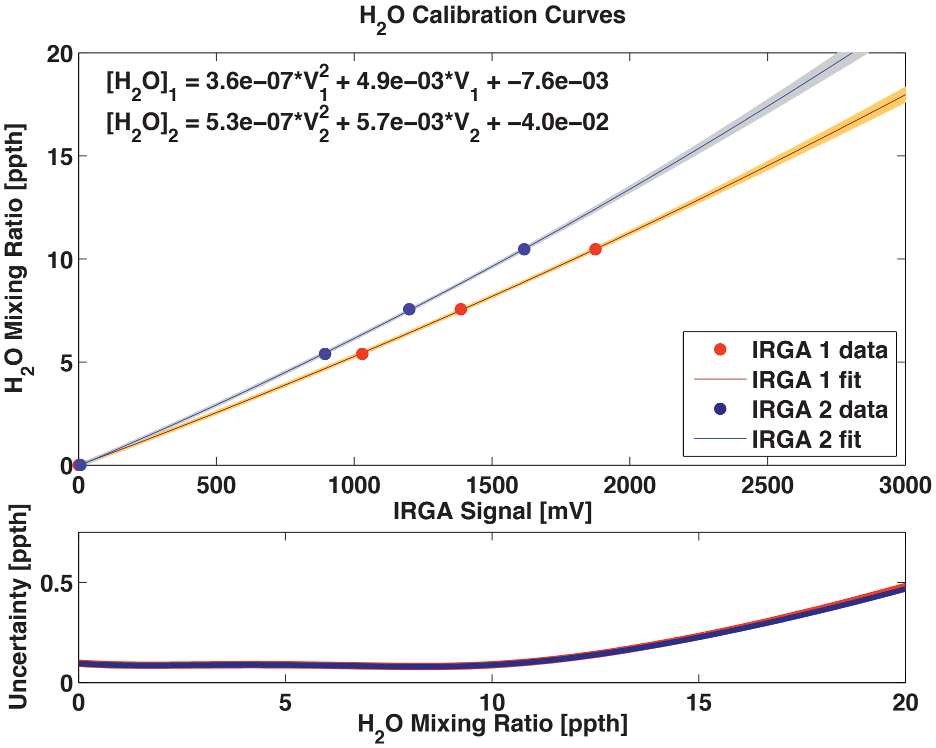

Figure 2-6: H_2O calibration curves (upper plot, lines) and predicted uncertainty (upper plot, shading) generated from dew point generator and gas tank calibrations (points) for IRGAs 1 and 2. The estimated uncertainty (lower plot) in calculated H_2O mole fractions using the polynomial calibration curve.

this study.

Frequent CO_2 calibrations were performed to correct for drift in the nonlinear IRGA response, which was important for quantification of both CO_2 concentration gradients and absolute mole fractions. CO_2 calibration curves were constructed every three hours by sampling three CO_2 calibration gases spanning typical ambient mole fractions (HI ∼350 ppm, MID ∼420 ppm, and LO ∼500 ppm) and one scrubbed zero (Z) air sample to provide a zero CO_2 and H_2O baseline reference. The CO_2 span gases (150A, Airgas, Riverton, NJ, regulators 05-2SS30-590-DAT, Scott-Marrin, Inc., Riverside, CA) were calibrated against primary cylinders calibrated at NOAA and tied to the World Meteorological Organization (WMO) CO_2 scale. For the zero air, filtered instrument room air was drawn through a gas purifier trap (HI-EFF in-line trap, P/N 81350, Alltech Associates, Inc., Deerfield, IL), which contained equal-width layers of a CO_2 scrubber (soda lime, CaO) and a desiccant (magnesium perchlorate, $Mg(ClO_4)_2$,). Calibration gases and zero (CO_2- and H_2O-free) air were controlled to the same pressure and flow rate as the samples.

Corrections were applied for two interfering effects to obtain the mole fraction of CO_2 in dry air: 1) dilution and 2) pressure broadening [*LI-COR 6262 Instruction Manual*]. In theory, variations in the concentrations of any trace gas can cause these effects to some degree. In practice, we can just account for the effects of water vapor because it is quite concentrated and variable in the tropospheric boundary layer, especially so close to the soils and vegetation. The presence of water vapor in the sample dilutes the CO_2 mole fraction from the dry air mole fraction, which is the value of interest. A dilution factor, f_d, was calculated using Equation 2.3 using the water vapor mole fraction, w, calculated as described above for the air samples and using the manufacturer's value of 2 ppm (∼water vapor free) for the calibration tanks.

$$f_d = \frac{1}{1 - w/1000} \tag{2.3}$$

At a given absorber concentration, broadband infrared absorption increases with pressure, which is caused by pressure broadening of spectral lines. The effect is negligible for ambient atmospheric CO_2 mole fractions, but not for the more abundant H_2O. Therefore, a pressure broadening factor, χ, was calculated using Equation 2.4.

$$\chi = 1 + 0.5 \times w/1000 \tag{2.4}$$

Sample cell temperature, T, and pressure, P, were recorded during calibration and sampling periods. Reference temperatures, T_0, of 42.78°C and 41.95°C and reference pressures, P_0, of 496.86 torr and 496.92 torr were used for IRGAs 1 and 2, respectively. Temperature $T_r = T/T_0$ (K) and pressure $P_r = P/P_0$ (kPa) ratios were computed and a calibration curve was prepared for each set of calibration measurements for raw voltages, V, and known calibration standard CO_2 mole fractions. Calibration measurements used to determine polynomial coefficients a, b, and c are shown in Equation 2.5 and are denoted by * to differentiate from sample measurements.

$$\frac{CO_2^*}{\chi^*\, f_d^*\, T_r^*} = F\left(\frac{V^*}{\chi^*\, Pr^*}\right), \quad y = F(x) = ax^2 + bx + c \tag{2.5}$$

The y and x terms were calculated for each calibration period and were then linearly interpolated to the timestamp of each measurement. A second order polynomial was fit to the interpolated terms to yield calibration curve coefficients (a, b, and c) at each sample timestamp. Raw sample measurement voltages were converted to CO_2 mole fractions using the calibration coefficients and sample correction factors (Pr, Tr, f_d, χ) in Equation 2.6.

$$CO_2 = \big(ax^2 + bx + c\big) \times (\chi\, f_d\, T_r), \quad x = \left(\frac{V}{\chi\, Pr}\right) \tag{2.6}$$

Calibration data were filtered based on variability in standard tank measurement voltages. Periods with high variability in the calibration coefficients, which was usually due to variability in the pressure controllers, were marked with a calibration flag.

Calibration curve coefficients (Equation 2.5) could either be calculated for *each calibration* (∼ every 3 hours) or for all the calibration data collected over a longer period (a *whole period*, spanning weeks or months). To determine the best approach,

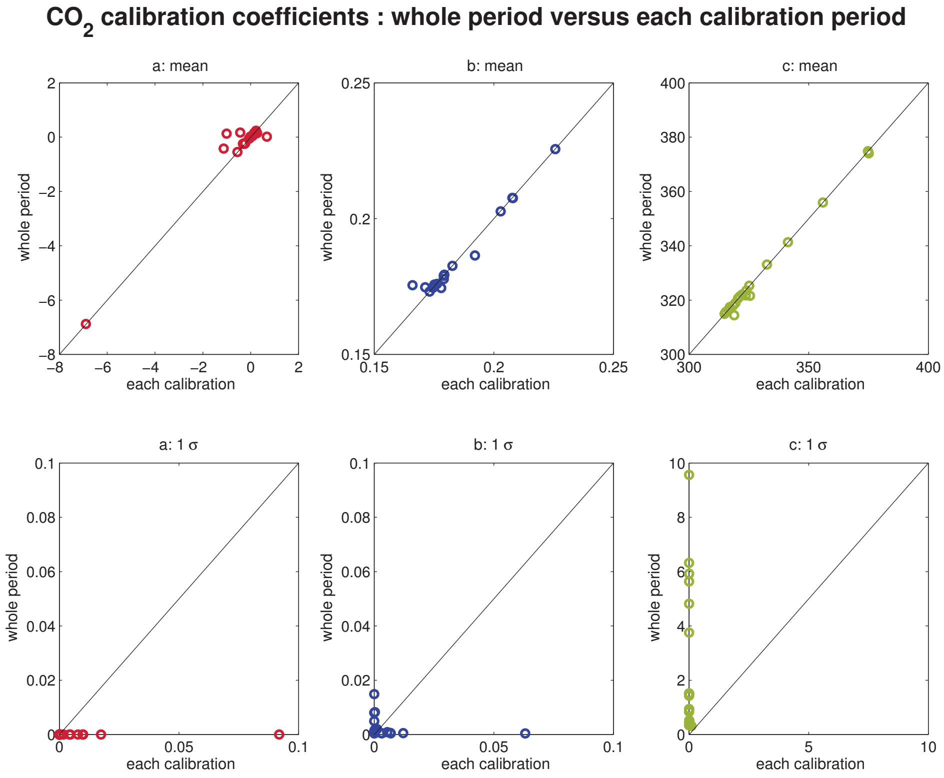

Figure 2-7: Calibration coefficient comparison for IRGA 1 for $y = F(x) = ax^2 + bx + c$ either the mean (top plots) and standard deviation (bottom plots) of coefficients calculated for each calibration period (*each calibration*) or the coefficients and their uncertainty when fitting all data (*whole period*) in a given period. Each data point represents one of the 20 calibration periods. The a, b, and c calibration coefficients represent the nonlinear, the linear, and the offset terms in the calibration equation.

the mean and standard deviation of the a, b, and c calibration coefficients calculated by the two methods were compared for twenty selected time periods (ranging from weeks to months) with similar calibration conditions (*e.g.,* no change in span gas tanks). Figure 2-7 compares the mean (top plots) and standard deviation (bottom plots) for each of the three calibration coefficients determined from either *each calibration* or all data within a *whole period.* The three coefficients, a, b, and c, represent the nonlinear, the linear, and the offset terms in the calibration equation.

Although similar mean calibration coefficients (uniformity about the 1:1 line, upper plots) were calculated using the *each calibration* and *whole period* approaches, there were significant differences in the uncertainty in the of the calculated coefficients (deviation from 1:1 line, lower plots). Reduced uncertainty in the small nonlinear coefficient (a, lower plot) was obtained for the calibration procedure when applied to the whole period, but little difference was observed between the two methods in terms of the linear term (b, lower plot). The most important difference between the two methods arose in the offset term (c, lower plot), which was much more uncertain when fitting a calibration equation to the whole period then for each calibration period. This is because this offset term accounts for changes in the detector cell pressure and temperature that were not constant throughout selected whole calibration periods. It would have been helpful to sample a zero CO_2 gas more often than the calibration gases to correct for this calibration offset; however, the merits of doing so were realized too late to apply this method to this experiment. Therefore, to avoid any uncertainties associated with changes in the voltage offset during a given analysis period, calibration curves were calculated for each calibration performed and were not averaged over longer periods.

2.1.4 Meteorological measurements of sensible heat

The below- and above-canopy sonic anemometers were mounted at 2 m and 29 m, respectively, and measured three-dimensional wind and virtual temperature at 8 Hz and 10 Hz, respectively. Raw data files were acquired from the Wofsy-Munger group for the above-canopy sonic. As shown in Figure 2-2, the sonic measurements above the canopy were taken 1 m above the top gas inlet on the EMS tower and below the canopy the measurements were centered exactly between the top and bottom gas inlets on the small tower. Sonic data were tilt-corrected on half-hour intervals using the procedure described for a sonic rotation by individual data run by Wilczak et al. (2001). The first rotation is about the x-axis to orient the mean velocity, $\overline{u}$ such that the crosswind term is zero ($\overline{v} = 0$). The second rotation swings about the y-axis to set the mean vertical wind to zero ($\overline{w}$=0).

Temperature shields were co-located with gas inlets at each level; the temperature shield and gas tubing were secured such that the inlet funnel was sampling air at the same height as the temperature shield. Air temperatures were read using the thermistors inside the temperature shield by an AC half-bridge. Detailed information on instrument components and measurements is given in Appendix A.1.6.

2.2 Instrument performance

This section discusses the instrument performance in measuring atmospheric concentration gradients in Section 2.2.1 and the method for calculating concentration gradients in Section 2.2.3. Flux calculations are discussed in Chapter 3.2.

2.2.1 GC-HePDD performance: H_2 measurements

Several factors are important when assessing the GC-HePDD performance to determine how well the system is able to rapidly quantify concentration gradients of H_2 at high precision. First, HePDD response stability and standard tank drift determine the accuracy of the absolute H_2 mole fractions. Secondly, the precision achieved by the GC-HePDD determines the minimum detectable concentration gradient, which is key for converting small above-canopy concentration gradients to gas fluxes.

HePDD chromatographic precision

The HePDD H_2 peak was well-resolved with a signal-to-noise ratio of ∼700 for the standard tank and a baseline noise of ∼0.7 ppb (assessed as the maximum peak-to-

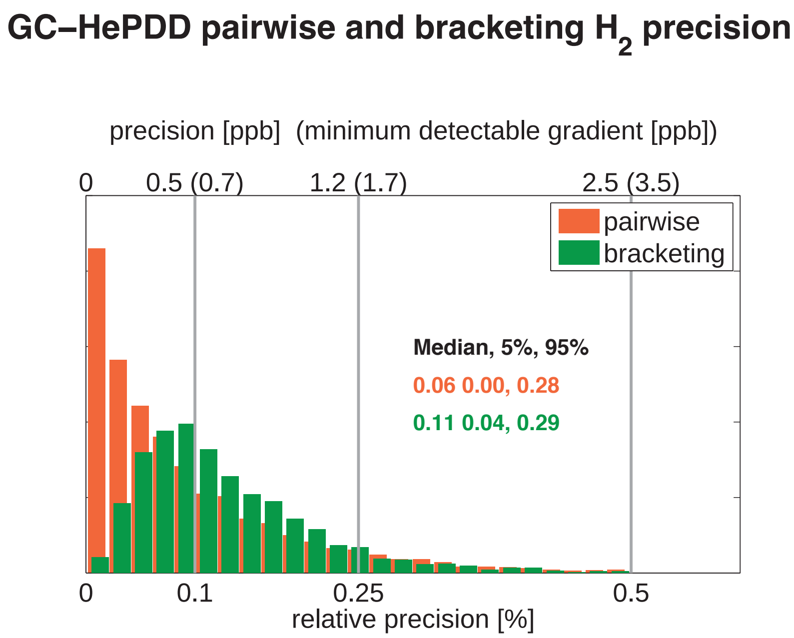

Figure 2-8: Histograms of GC-HePDD H_2 1σ standard precision (minimum detectable concentration gradient in ppb only) as determined from either successive pairs of measurements or four bracketing measurements over 1.6 hours of a calibration standard.

trough height difference in 10-second windows of both routine sample and He blank chromatograms).

GC-HePDD H_2 measurement precision was determined by successive measurements of calibration tanks of known composition. During routine sampling, calibration gas was sampled twice in a row every 1.6 hours. The 1σ standard deviation of the standard measurement can be calculated in a *pairwise* (n=2) fashion by correcting for the small sample bias with a multiplication factor[7]. Similarly, the 1σ standard deviation of the two pairs of standard measurements (n=4) *bracketing* six rounds of tower air measurements over 1.6 hours is a measure of the uncertainty in the H_2 mole fraction over that sampling period. A histogram of the GC-HePDD H_2 precision for one year of measurements is shown in Figure 2-8 for the *pairwise* and the *bracketed* calculations.

The bracketing method yields reduced precisions, likely due to the influence of

---

[7] Small sample bias multiplication factors c_4 of $\sqrt{2/\pi}$ and $2\sqrt{2/(3\pi)}$ for n=2 and n=4, respectively, assuming a normal distribution. The bias-corrected standard error is then $s = \sigma\sqrt{1 - c_4^2}$, where σ is the uncorrected standard deviation.

pressure and temperature changes on instrument components and calibration tanks in the shed over the longer interval between standard measurements. HePDD precisions based on the pairwise and bracketing method have a medians of 0.06% and 0.11%, respectively. Although some loss of precision was anticipated as a result of faster chromatography runtime and operation in field conditions, these precisions are on par with the 0.06% (1σ) precision achieved by Novelli et al. (1999). Notably, GC-HePDD precisions are almost always better than 0.5 to 1%, which is the typical range for the traditionally used GC-HgORD system for atmospheric H_2 quantification.

Standard precisions, especially of bracketed standard pairs, were improved by including sample loop temperature in the molecular density calculation (Section 2.1.2). Pressure corrections clearly improved both bracketed and pairwise standard precisions. The improvement in standard precision verifies that these corrections are useful; therefore, changes in molecular number density due to pressure and temperature fluctuations were accounted for in all air samples.

During the course of the field deployment, the balance between carrier gas stream pressures drifted slightly and chromatographic settings were adjusted accordingly. During some periods, different integration parameters were used, which made either peak area or height a more precise determination of H_2 abundance. The GC-HePDD precision time series using either peak area or peak height were compared to select the best integration methods, which were selected for the best peak resolution and the baseline fit.

Standard precisions were used to determine the minimum detectable difference (mdd) in H_2 by the flux-gradient system, where the minimum detectable concentration gradient (mdg) will then be $mdd/\Delta z$, where Δz is the inlet height difference. The uncertainty, σ_{grad}, in the mole fraction difference between the top and bottom inlet streams, which are assigned the same but uncorrelated instrumental precision, σ_{HePDD}, is just $\sigma_{grad} = \sqrt{\sigma_{HePDD}^2 + \sigma_{HePDD}^2} = \sqrt{2} \times \sigma_{HePDD}$. The distribution of the minimum detectable difference is shown on the upper axis (Figure 2-8). The median minimum detectable H_2 difference for the flux-gradient system is between 0.4 to 0.8 ppb, which is a significant improvement over the capabilities of the traditional

GC-HgORD of 3.7 or 7.5 ppb, respectively. This corresponds to a respective 0.1 and 0.2 ppb/m minimum detectable concentration gradient above the forest canopy. Achieving such a low minimum detectable concentration gradient was key to the contributions of this work. As will be seen in the above canopy observations, the traditional GC-HgORD system for measuring H_2 would not have been able to detect a H_2 concentration gradient most of the time.

HePDD response stability

Detectors exhibiting stable long term response can be used to quantify drift in calibration tanks. The response stability of the GC-HePDD system has been reported to be as low as 3.6 ppb yr^{-1} (Novelli et al., 1999). Detector response stability is important for differentiating measured changes in air samples that are driven by real changes in the atmosphere from those that are driven by instabilities in the detector. For this purpose, the response stability is assessed over the short term. In this section, the long- and short-term HePDD response stability are assessed.

The first exercise is to determine whether the HePDD response was stable over the long term. As discussed in Section 2.1.2, the secondary calibration tank mole fractions were stable over the course of the experiment. Therefore, the HePDD response to the secondary standard, which was calibrated twice at NOAA and was found to have stable H_2 mole fractions over time, should be stable if the HePDD itself is stable. A time series of the response to the secondary standard tanks and their statistics are plotted in Figure 2-9.

Periodic adjustments were made to the chromatographic and integration parameters over the course of this study, which caused step changes in detector response to both standard and air samples. As a relative technique[8], this does not affect the GC measurements, but it does complicate the assessment of detector response drift. Therefore, the normalized detector response to the calibration tank was separated

---

[8] Gas chromatography is a relative technique, meaning that the detector response to an unknown sample is only meaningful when compared to the response to a known calibration standard. Detector response to a given number of moles may change, so unknown measurements must be bracketed by known standards to quantify the detector response to a given number of analyze moles at that time.

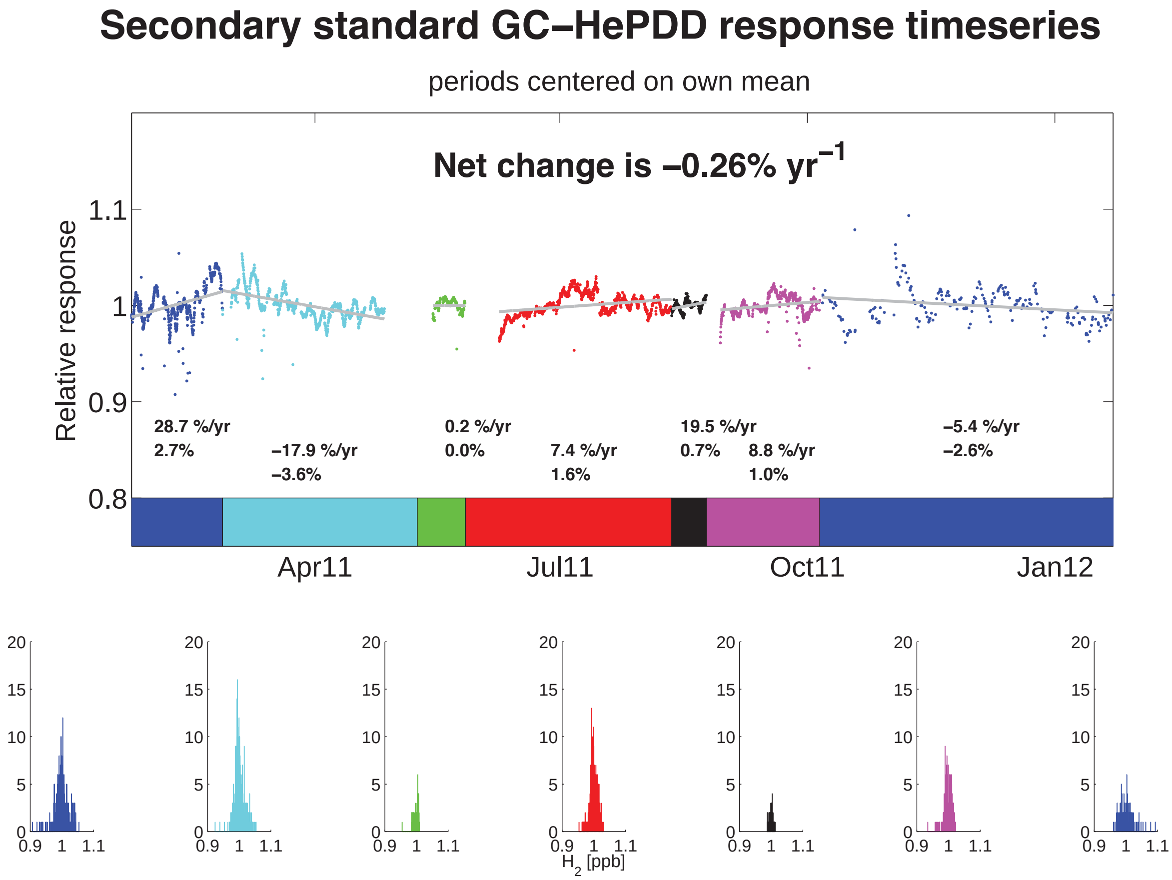

Figure 2-9: Time series of normalized GC-HePDD response stability to secondary calibration standard for successive periods with approximately normal response distributions (also shown) over the course of this experiment.

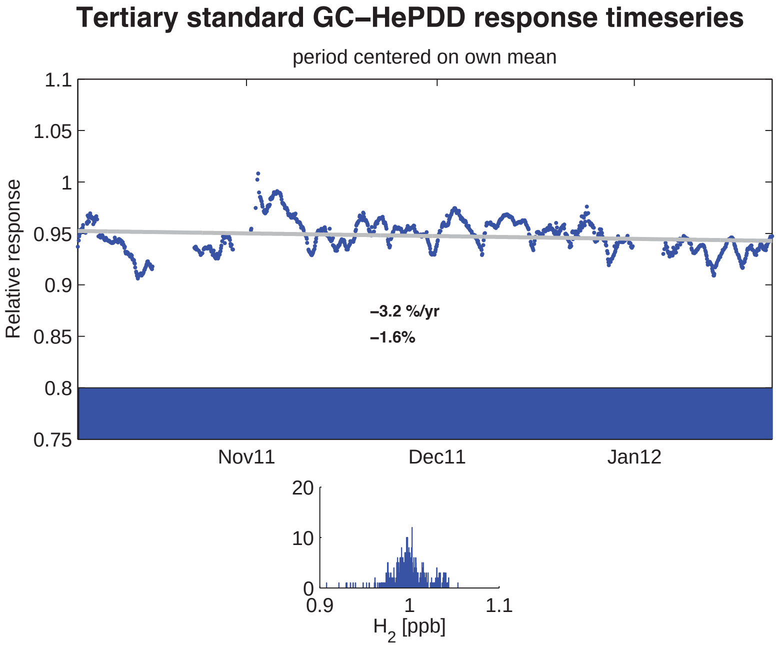

Figure 2-10: Time series of GC-HePDD response stability to the tertiary calibration standard over the course of this experiment. Stability is better for this tertiary standard than for the secondary standard over this period.

into seven time periods with consistent chromatographic parameters. The seven response histograms in Figure 2-9 indicate that detector response was approximately normally distributed in each period.

Linear trend lines were fit to each period and the slope in detector response (% change per year and total % change) over each period were calculated. The net change in detector response over the year to the secondary standard was -0.26% yr^{-1} (1.4 ppb yr^{-1}), indicating that the HePDD response itself was reasonably stable. The reported secondary standard drift at -0.5% was on the same order, which is insignificant with respect to NOAA's reported precisions discussed earlier.

Figure 2-10 shows the HePDD response time series to the tertiary standard, which was installed for over four months. The slope of the detector response change to the tertiary was -3.2 % yr^{-1} (-17 ppb yr^{-1}), which is actually smaller than the drift observed in the secondary tank over the same period (-5.4 % yr^{-1}, -26 ppb yr^{-1}). This indicates that no significant H_2 drift in the aluminum tertiary standard tank occurred over its use.

The short-term HePDD response is assessed to ensure that measured changes are associated with real atmospheric changes. The long term drift discussed above would not affect measurements on the 1.6 calibration measurement hour interval. Even the period with the most rapid detector response drift to the secondary tank (Figure 2-9, Period 2) corresponds to a change over 1.6 hours of 0.005 %, which is at least an order of magnitude smaller than the instrumental precision. Higher frequency changes superimposed on the long term drift are likely driven by changing environmental conditions within the shed (*e.g.*, pressure, temperature) that may affect the instrument response.

Another method for assessing the shorter term HePDD response simply uses the four bracketing standard precision distribution shown in Figure 2-8. This indicates that the median detector response is stable within 0.11% over 1.6 hours. Real variability in H_2 in air samples can be assessed by calculating the standard deviation of measurements from a given inlet over the same time period. Air sample variability has mean and median values of 0.28 - 0.72% and 0.42 - 0.96%, as shown in Figure 2-11, which are comfortably above the typical instrument precision and stability. The results described here provide confidence that the detector is indeed stable enough to measure real variability in the physically averaged air samples.

2.2.2 IRGA performance : CO_2 and H_2O measurements

CO_2 precisions

Precisions for the IRGA CO_2 measurements for both LI-6262 analyzers in the IRGA rack were assessed by sampling a calibration tank for long periods to generate an Allan variance plot. Precisions were determined by sampling a mid-span calibration tank (390.353 ppm) continuously at 1 Hz for 20 minutes. The calibrated CO_2 mole fraction time series are shown in the upper portion of Figures 2-12 for IRGA 1. A plot exhibiting the same general shape was generated for IRGA 2 (not shown).

The precision of the measurements were evaluated by constructing Allan variance

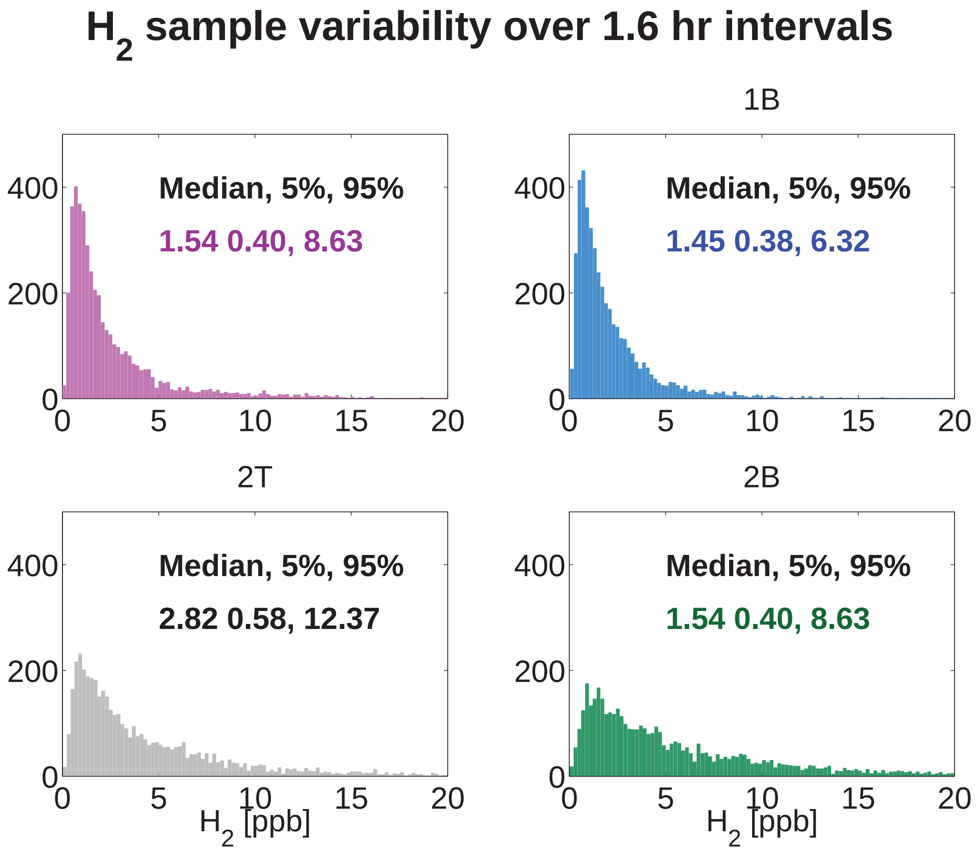

Figure 2-11: H_2 variability in air sample measurements from each inlet for 1.6 hour intervals, which is the frequency of bracketing standard pair measurements. Variability is taken as the standard deviation of H_2 measurements from a given height over the time interval; the median and the 5th and 9th percentile variability in ppb are printed on each plot. GC precisions are 0.6 ppb or less in the median, which is much smaller than the median air sample variability, which provides confidence for measuring the atmospheric variability. Note that these air samples pass through a $\tau =$ 8 min integrating volume.

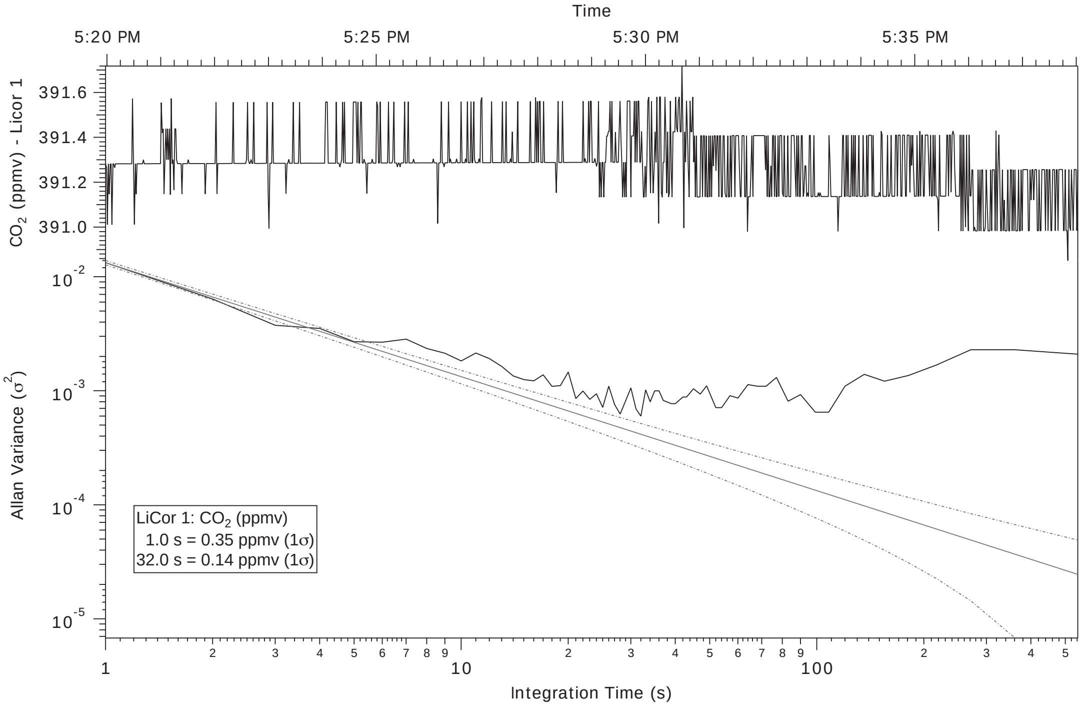

Figure 2-12: IRGA 1 precision as determined by Allan variance plot (bottom) of 20 minutes of mid-span tank CO_2 sampling (top). A similar plot was generated for IRGA 2 (not shown). The straight and dotted lines show the white noise limit and 95% confidence limits, respectively. The 1σ 1 Hz precision of IRGA 1 and 2 are 0.35 and 0.33 ppm, respectively. Precision values were 0.14 and 0.17 ppm for IRGA 1 and 2, respectively, at 32 s averaging times and 0.35 and 0.33 ppm at 1 s averaging times.

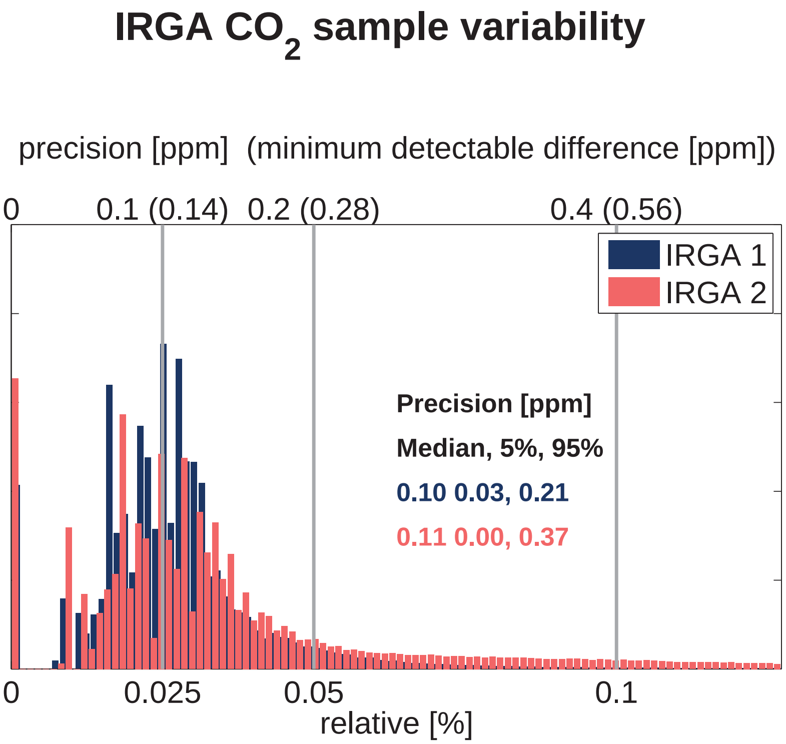

Figure 2-13: Distribution of CO_2 air sample mole fraction variability for IRGA 1 and 2 for each one-minute measurement over entire the sampling period.

plots with IGOR Pro (WaveMetrics) with the help of Roisin Commane. The plot shown in the lower portion of Figure 2-12 is a measure of variance as a function of averaging period or integration time. The straight and dotted lines show the white noise limit and 95% confidence limits, respectively. The 1σ 1 Hz precision of IRGAs 1 and 2 to be 0.35 and 0.33 ppm, respectively. Minimum precision values were 0.14 and 0.17 ppm for IRGA 1 and 2, respectively at 32 s averaging times and 0.35 and 0.33 ppm at 1 s averaging times. IRGA data were averaged in 16 s increments.

The IRGA standard CO_2 precision can be compared with the variability in the one-minute CO_2 air measurements over the course of the year. These air samples are physically averaged and should have relatively low variability over the 15 sec averaging window for each one-minute measurement. As shown in Figure 2-13, the median CO_2 measurement standard deviation was 0.10 and 0.11 ppm for IRGAs 1 and 2, respectively. The Allan variance analysis and this analysis of over a year of sample standard deviation distributions indicate that the IRGA precisions were typically better than 0.2 ppm.

H_2O precisions

Accuracy of the IRGA H_2O measurements for both LI-6262 analyzers were assessed by generating uncertainty estimates from the calibration curve fit. An estimate of the standard deviation of predicted H_2O mole fractions given a signal voltage (50% standard deviation on least squares fit, generated by the *polyval* MATLAB F7.11.0 R2010b function) is shown as the shading around the calibration curve in Figure 2-6. The uncertainty was a function of the water vapor loading; water vapor mole fractions below 10 ppth had an uncertainty of approximately 0.1 ppth for both IRGAs, which increased to 0.5 ppth at mole fractions of 20 ppth.

As was done for CO_2, an estimate of IRGA H_2O precisions can be derived from air sample variability over the entire measurement period. The median variability was 3.5 and 3.9 ppm H_2O for IRGA 1 and 2, respectively. These precisions were corroborated with an assessment of a time series of the calibration standard variability on a dry calibration tank (not shown).

On warm and humid days with dew points above the relatively cool shed temperature (21°C), condensation of water vapor occurred in tubing lines. Sample line tubing was not heated and condensation of water vapor introduced noise to water vapor measurements. In theory, persistent biases due to condensation should occur at or above 15 ppth H_2O for a climate controlled 21°C instrument room. In practice, the air conditioning unit operated on roughly a 10 minute cycle and caused: 1) increased condensation on tubing and fittings during cooling cycles, and thus a spurious decline in measured H_2O, and 2) increased evaporation of the condensed H_2O reservoir during the non-cooling cycle, and thus a spurious increase in measured H_2O. Foam insulation was installed on August 29, 2011 around tubing lines to limit the brunt of the air conditioner temperature oscillations felt by the tubing. The loss in H_2O precision and accuracy due to the above summertime condensation-evaporation cycle is a stronger limitation than the basic H_2O detector precision.

A summary of the typical precisions for the analyzers and gases in this flux-

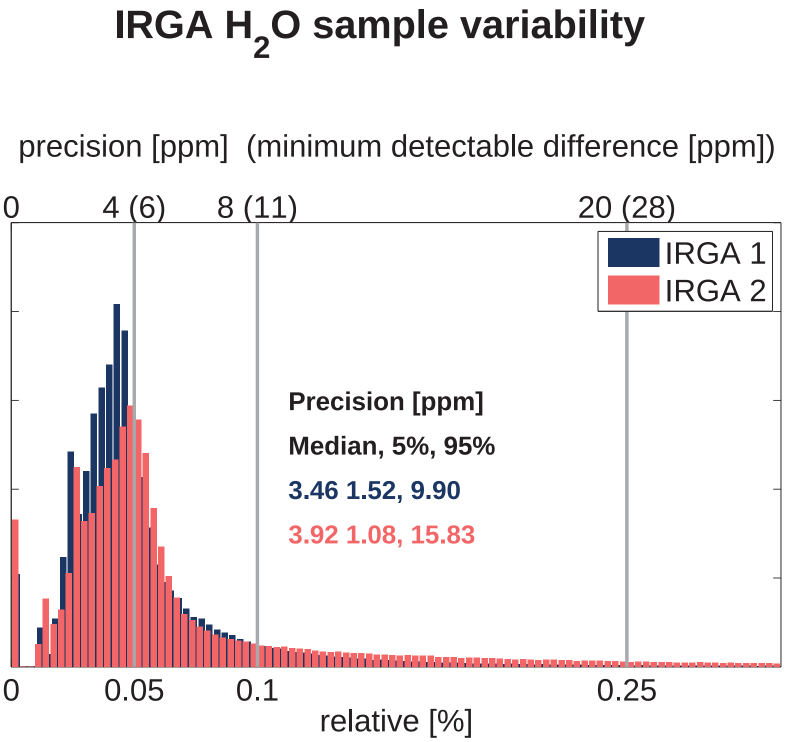

Figure 2-14: Distribution of IRGA 1 and 2 H_2O air sample mole fraction variability for each one-minute measurement over entire the sampling period. Slightly higher sample variability is not surprising for the wetter below-canopy inlet set.

Table 2.1: Summary of median precisions reported for trace gases measured in this study

Instrument	**Species**	**Median precision**	**Abundance**	**Relative precision**
GC	H_2	0.3 - 0.6 ppb	530 ppb	0.06 - 0.11%
IRGA 1	CO_2	0.10 - 0.14 ppm	393 ppm	0.025 - 0.036%
IRGA 1	H_2O	3.5 ppm	8 ppth	0.04%
IRGA 2	CO_2	0.11 - 0.17 ppm	393 ppm	0.028 - 0.043%
IRGA 2	H_2O	3.9 ppm	8 ppth	0.05%

gradient system are listed in Table 2.1. However, precisions were time-dependent, typically being worse in the summertime for the reasons just given, which was taken into account when analyzing the concentration gradient time series.

2.2.3 Calculation of concentration gradients

The calculation of concentration gradients from measurements of H_2, CO_2, H_2O, and temperature at different heights is discussed in this section. The importance of physically averaging the sample streams using integrating volumes (1 to 8 minute residence time) was discussed in Section 2.1, and an example showing why is given below in Section 2.2.3. It is important to test for biases in the mole fractions measured by different inlets that would systematically affect the magnitude, and possibly the sign, of calculated concentration gradients. So-called nulling procedures are presented in Section 2.2.3. Methods for calculating trace gas concentration gradients is discussed in Section 2.2.3.

Importance of physical averaging

The importance of using the integrating volumes to physically average gas streams drawn from the tower is shown by example. Figure 2-15 shows an example time series of mole fraction measurements staggered in time, from which we wish to calculate concentration gradients. This is a special case, where one gas stream (3.5 m) is physically averaged by passing through the well-mixed integrating volume, whereas

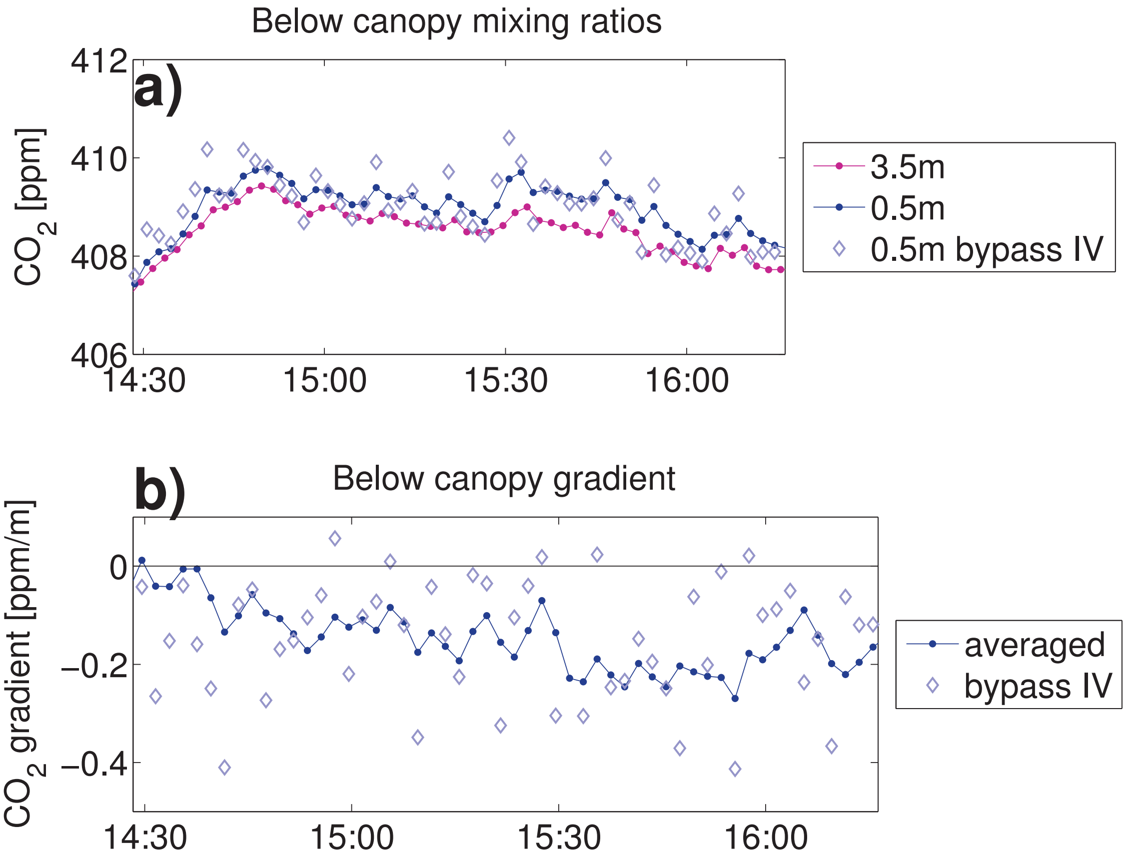

Figure 2-15: Example data series for a two hour period highlighting the importance of physically averaging the sample stream for concentration gradient measurements. During this period, the 0.5 m inlet sample stream bypassed the integrating volume (**a**, blue diamonds) and each one-minute measurement exhibited high variability, while the 3.5 m inlet sample stream passed through the integrating volume and was physically averaged (**a**, pink points). The action that the integrating volume would have had on the 0.5 m inlet measurements is simulated with an exponential moving average with a time constant equal to the integrating volume, which is 4 minutes in this case (**a**, dark blue points). Calculated concentration gradients from the physically averaged 3.5 m inlet data and either the 0.5 m inlet measurements bypassing the integrating volume (**b**, blue diamonds) or the computationally smoothed (exponential filter) 0.5 m inlet data (**b**, dark blue points) is shown. Clearly, the integrating volumes do reduce the natural variability by physically averaging the sample stream, which is especially important for the H_2 concentration gradients that require a total of eight minutes to sample.

the other (0.5 m) is not. About two hours of data are shown when the 0.5 m height inlet sample stream bypassed the integrating volume. The one-minute measurements of the 0.5 m un-averaged samples are clearly more variable than the averaged 3.5 m sample stream passed.

The averaging effect of the 0.5 m integrating volume is simulated by computing the exponential moving average with the time constant of the integrating volume. The variability and time-course of the computationally averaged 0.5 m CO_2 mole fractions is much more akin to the physically averaged 3.5 m data then the raw 0.5 m data were. As a result, much more variability is introduced into the calculated concentration gradient in the case where one sample stream is not physically averaged.

This example provides insight into the high natural variability in trace gas mole fractions at the forest. Clearly, if H_2 mole fractions were measured without any physical averaging every four minutes, calculated concentration gradients would be very noisy and would not represent the average vertical difference in H_2 mole fractions over that time period. CO_2 measurements were used in this example because mole fractions can be measured by this instrument every minute to diagnose the effect of physical averaging. The data is much more sparse from the same time when the H_2 mole fractions are analyzed, but the same conclusions are drawn.

Nulling procedure to test for biases

The nulling procedure described in Section 2.1 temporarily diverted all four sampling lines from their respective inlets to simultaneously sample a 25 L flow-through mixing volume, in which H_2, CO_2, and H_2O mole fractions should change slowly enough to test for biases between the four different sampling lines. The nulling procedure is described in this section with an example, which illustrates the corrections required for the test and how to interpret the results. Within the uncertainties and potential pitfalls of the nulling procedure as it was designed, we will show that the instrument system did not have any biases between the gradient pairs that need to be addressed for the flux calculations.

A nulling procedure example on the morning of August 2, 2011 is shown in Figure

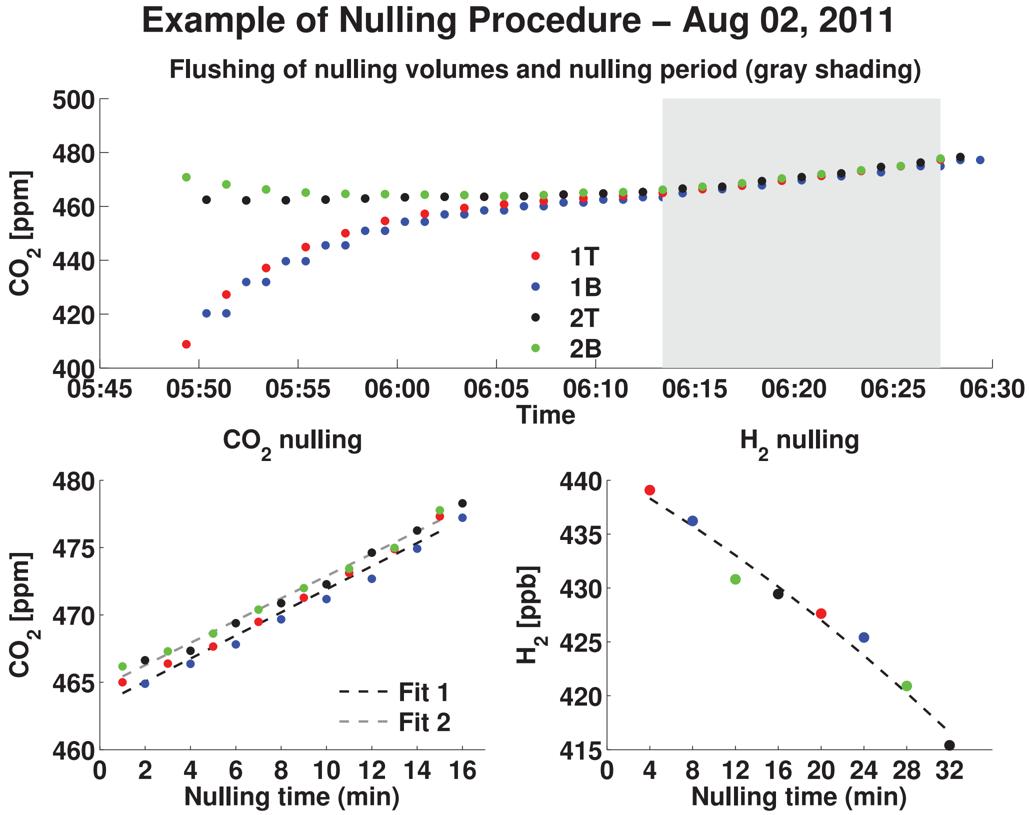

Figure 2-16: Nulling procedure example on August 2, 2011. Around 5:50 a.m. the nulling valves are activated to draw air from the nulling volume, which had been rapidly flushed immediately prior to sampling (∼3 l min^{-1} for 40 min). The four gas inlets for the above- (1) and below- (2) canopy set are labeled as either the top (T) or bottom (B) inlet of a given concentration gradient pair such that 1T, 1B, 2T, and 2B correspond to the 28, 24, 2.5, and 0.5 m inlets, respectively. During the nulling procedure, all gas sample streams sample from the same 25 L volume instead of the normal inlets on the towers. The full CO_2 time series (upper plot) shows that it takes over 20 min to flush the integrating volumes of the memory of the strong nighttime CO_2 concentration gradient. H_2 sampling begins around 6:00 am and continues for 32 minutes (lower right); over this time interval, each inlet is only sampled twice. For CO_2, only the last 16 minutes of sampling (shaded portion in upper plot and lower left plot) is used for the nulling calculation. Over this period, mole fractions from the nulling volume drifted approximately 0.8 ppm and -0.8 ppb for CO_2 and H_2. Second-order polynomial functions are fit and used to detrend the data so that nulling volume drift does not affect the calculated bias between the sample lines.

2-16. Around 5:50 am the nulling valves are activated to draw air from the nulling volume, which had just been rapidly flushed (∼3 LPM for 40 min). As can be seen from the CO_2 measurements, it takes over 20 min to flush the integrating volumes of the memory of the strong nighttime CO_2 concentration gradient that was being sampled beforehand on that day. Ultimately, equilibration within each concentration gradient pair was achieved around 6:10 am. H_2 sampling begins around 6:00 am and continues for 32 minutes. For CO_2, only the last 16 minutes of sampling (shaded) is used for the nulling calculation; with a larger number of observations, less time is needed for a statistical calculation of the CO_2 bias than for H_2.

The following example illustrates an important point about the procedure: the nulling volume is a source of physically averaged air, but mole fractions are certainly not stationary. In fact, concentrations of H_2, CO_2, and H_2 were observed to drift over the course of the nulling procedure, especially in the summertime when soil-atmosphere exchange of trace gases was higher and larger gradients established. This drift, when inlets are sampled in the same order every time, can lead to an artificial null bias. A larger volume with a fan should be used in future studies to help avoid this problem. Additionally, the nulling volume inlet should be installed high on a sampling tower, farther from the large concentration gradients near the surface.

The periods from this example that were used to calculate bias are shown in the left and right lower plots for CO_2 and H_2, respectively. Over this period, mole fractions from the nulling volume drifted approximately 15 ppm min^{-1} and -25 ppb min^{-1} for CO_2 and H_2, respectively. This example had one of the larger null volume drifts observed from the study. In this case the mole fraction drift is approximately linear, but this is not always the case.

The null bias calculations must be corrected for the obvious concentration drift in the nulling volume. This means that the mean biases between two inlets (*e.g.*, 1T and 1B) should not be calculated as the simple *mean* of each mole fraction, χ, difference (*e.g.*, $\chi_{1T} - \chi_{1B}$). Instead, the time series should first be detrended by subtracting a second-order polynomial fit to the data, and then calculating the mean difference. Both methods are performed and are shown in Figures 2-17, 2-19, and 2-20, which

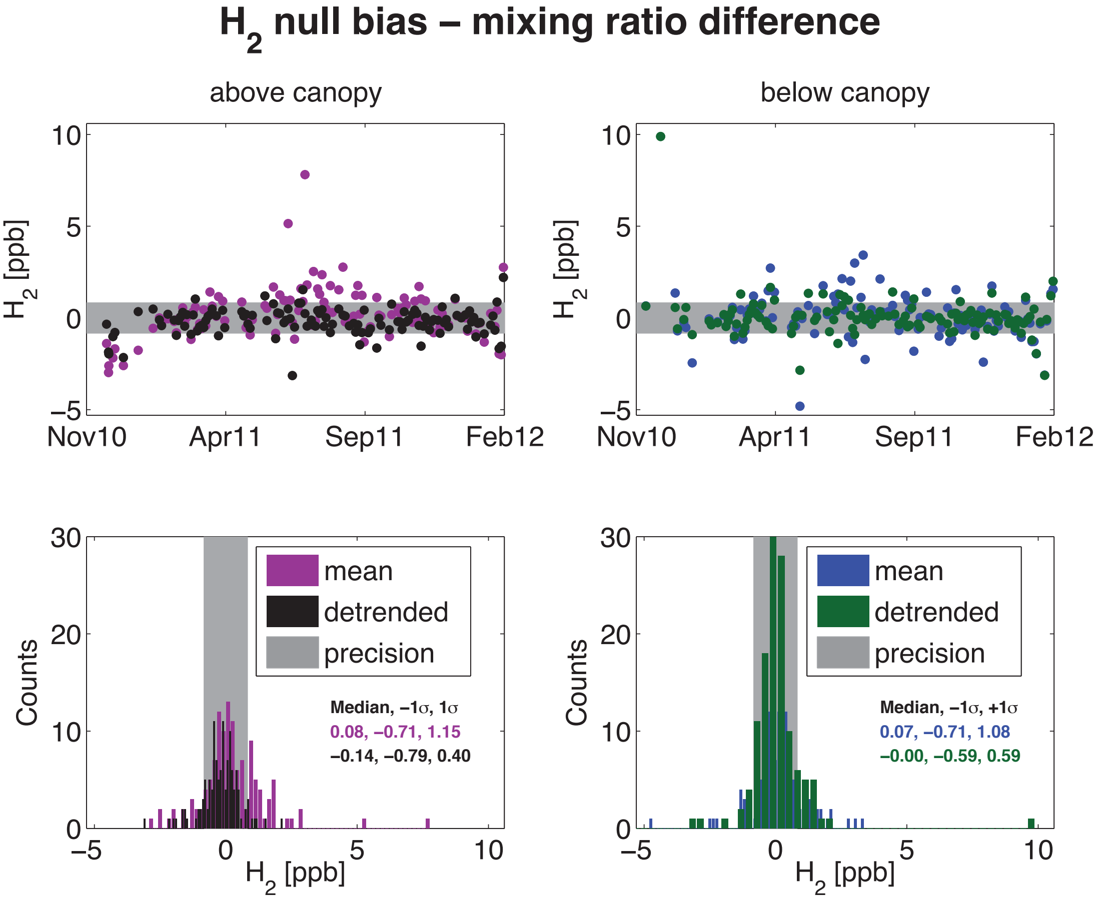

Figure 2-17: Time series (upper plots) and distributions (lower plots) of the bias between sampling lines for above- and below-canopy H_2 measurements as determined with a nulling procedure. Differences in measured mole fractions between inlets of a concentration gradient pair are reported relative to: 1) the mean over the nulling period, or 2) to a detrending second-order polynomial fit of the slowly changing H_2 mole fractions measured in the nulling volume. The median and the 1σ confidence intervals are reported for each distribution; when compared to the GC-HePDD precision (0.3 - 0.6 ppb) it is clear that no persistent significant H_2 bias is observed.

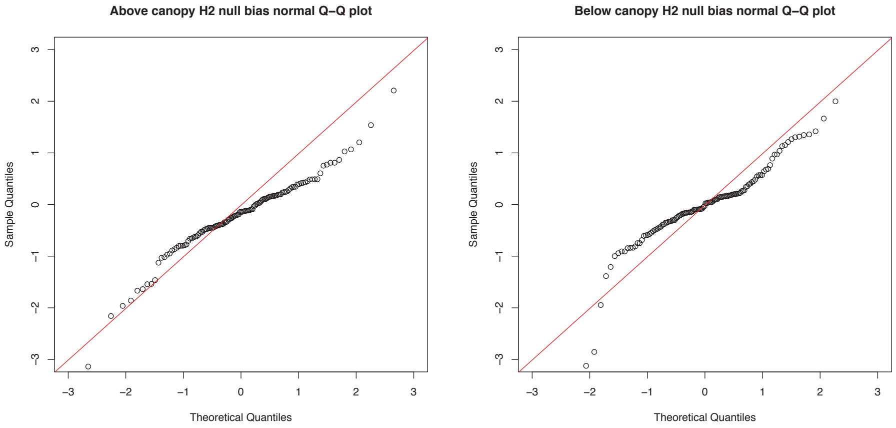

Figure 2-18: Q-Q normal plots of the above (left plot) and below (right plot) canopy H_2 nulling biases, which are not perfectly, but approximately normally distributed.

show time series of apparent biases in the mole fractions within each above- and below-canopy concentration gradient pair (null biases) as a function of time (upper plots) and as distributions (lower plots). Detrending to account for drifting null volume mole fractions is very important for the low-frequency H_2 measurements, but is not important for higher-frequency CO_2 and H_2O bias estimates.

In this example, the above- and below-canopy H_2 mean bias (Figure 2-17) is diagnosed as 2.5 and 3.4 ppm, respectively, which is driven by the mole fraction drift (*e.g.*, one inlet consistently has a higher mole fraction than the other because of the drift in nulling volume mole fraction with time). Detrending the time series to remove the nulling drift yields a calculated null bias of -0.38 and 0.15 ppb for above- and below-canopy, respectively. This is a dramatic reduction in the calculated null bias that brings the bias below the minimum detectable difference of the GC. The reduction was found to be a function of the magnitude of the null drift and the order that inlets were sampled (remained constant) over the sample period.

We conclude that there is no significant H_2 bias between the inlet lines for the data series. Nearly all the detrended H_2 bias estimates lie within 1σ of the minimum detectable differences. As shown in Figure 2-18, the H_2 biases diagnosed from the nulling procedure are approximately normally distributed.

Accounting for drifting mole fractions in the nulling volume was one example of a

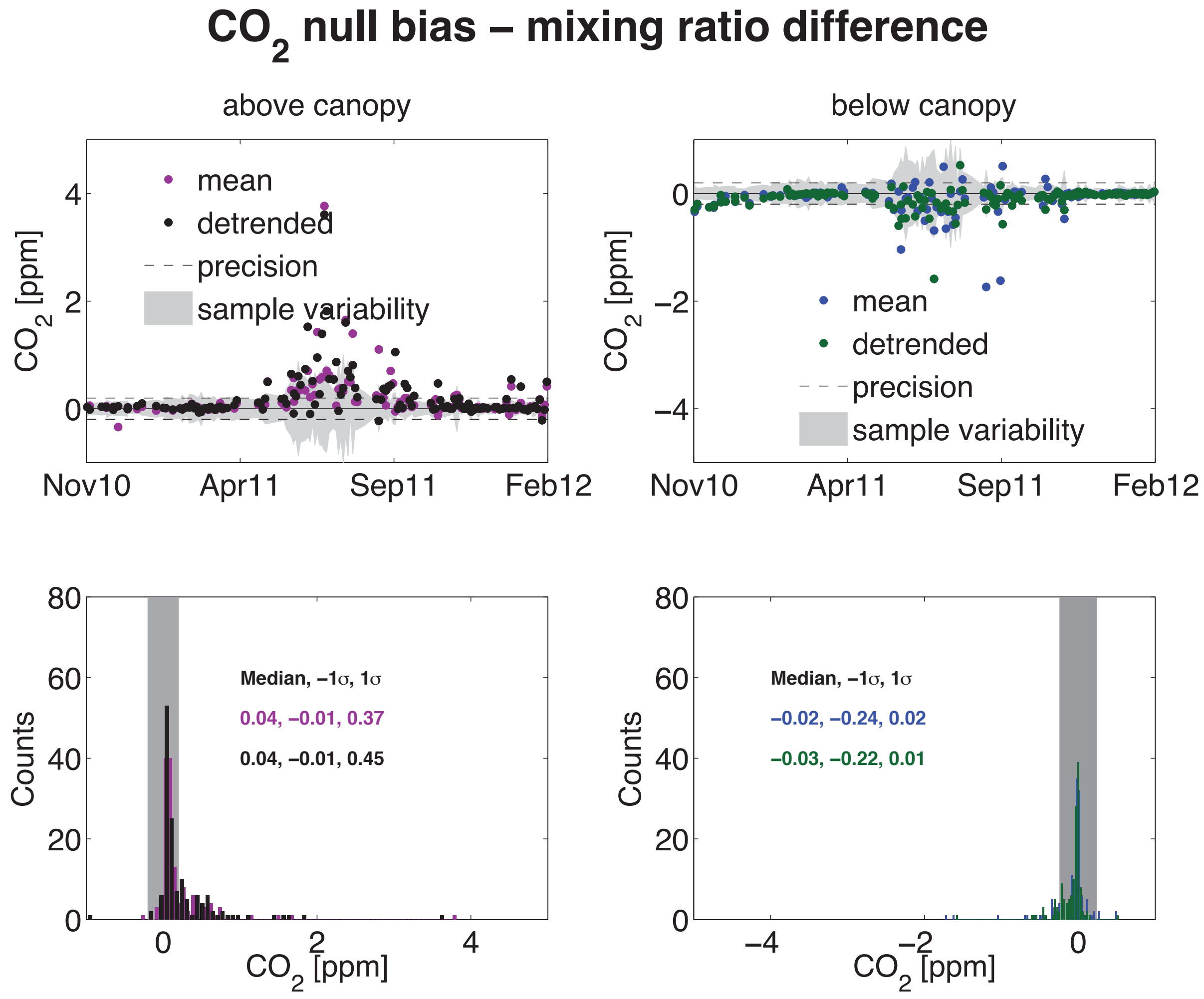

Figure 2-19: Time series (upper plots) and distributions (lower plots) of the bias between sampling lines for above- and below-canopy CO_2 measurements as determined with a nulling procedure. As a guide, the instrument precision (black dashed line) and a smoothed air sample variability time series (grey shading) shown. The median and the 1σ confidence intervals (black dashed) are reported for each distribution; these should be compared to the IRGA precisions of 0.10 to 0.17 ppm.

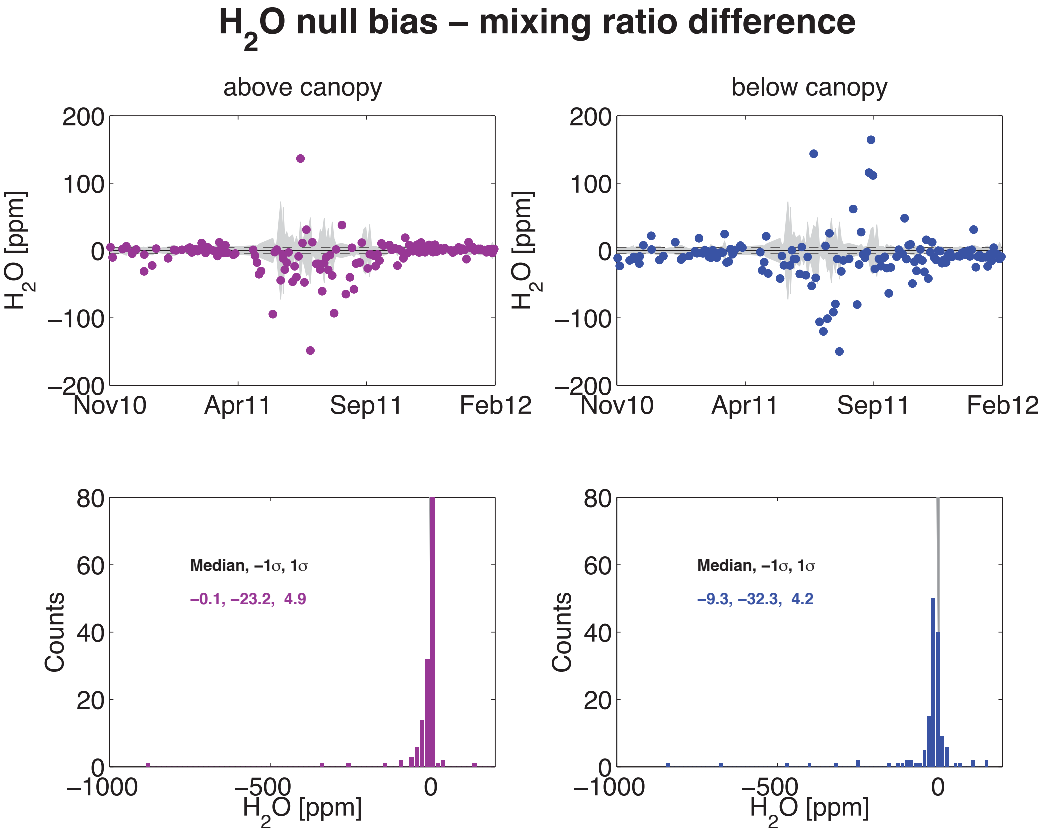

Figure 2-20: Time series (upper plots) and distributions (lower plots) of bias between sampling lines for above and below canopy H_2O measurements as determined with a nulling procedure. Differences in measured mole fractions between inlets of a concentration gradient pair (top - bottom). As a guide, the instrument precision (black dashed line) and a smoothed air sample variability time series (grey shading) is shown. The median and the 1σ confidence intervals are reported for each distribution; these should be compared to the IRGA precision. This figure indicates that the actual IRGA precision is probably much better than 0.1 ppth, and may be as low as 0.01 ppth.

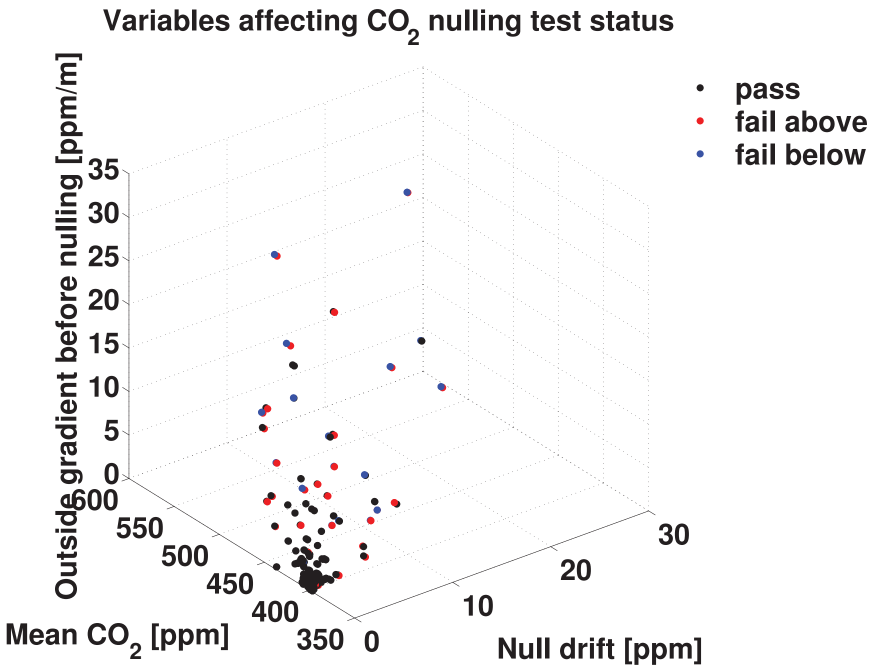

Figure 2-21: Nulling procedures that passed (black) or failed (above canopy in red, below canopy in blue) the bias test and their relationship to three variables: high mean CO_2 mole fractions during the nulling procedure, a large mole fraction drift over the nulling procedure, and large, highly variable concentration gradients directly preceding the nulling procedure. Most failed tests are outliers from the passed tests with respect to these three variables. This indicates that some failing tests may be due to poor averaging by the nulling volume during highly stratified outside conditions and drifting null volume mole fractions.

potential pitfall in the nulling procedure employed in this study, where a confounding process had to be accounted for before being able to determine whether a true bias was present. A second confounding process was identified from the IRGA data. In contrast to H_2, biases in the apparent CO_2 and H_2O mole fractions were diagnosed for both inlet pairs even after detrending the data. In this example, the mean above- and below-canopy CO_2 bias is 0.05 and 0.63 ppm and the detrended bias is 0.91 and -0.20 ppm, respectively. Figures 2-19, and 2-20 shown that during most of the year, there was no significant bias between sampling lines detectable above the instrument precision. However, during the summertime periods when forest fluxes and humidity are high, an apparent null bias is observed.

The apparent null bias in the summertime IRGA data is associated with incomplete mixing of the nulling volume and condensation in tubing lines. As is illustrated in Figure 2-21, failed null bias tests typically had one or more of the following characteristics: high mean CO_2 mole fractions during the nulling procedure, a large mole fraction drift over the nulling procedure, and large, highly variable concentration gradients directly preceding the nulling procedure. During periods with a large vertical trace gas concentration gradients, the air stream may be incompletely mixed when passing through the nulling volume, which had no fan for assuring a well-mixed sample. The failed nulling tests also tend to have high mean CO_2 levels, which may not directly influence the nulling test, but may be associated with large concentration gradients. Finally, tests are more likely to fail with larger rates of concentration drift in the nulling volume. This is likely the result of periods when nulling volume concentrations do not drift linearly and are difficult to correct for. The time of day of sampling did not appear to influence the proportion of failed null tests.

The second association was with condensation in the tubing inside the shed, which was a clear feature in the summertime H_2O data. In fact, the H_2O bias data shown in Figure 2-20 were not detrended because superimposed air conditioner (A/C) cycles on the water vapor mole fraction during warm and humid periods caused oscillatory features that were not simple to remove. These A/C cycles may have induced condensation and evaporation cycles, or simply temperature sensitive adsorption on the tubing walls as was also observed in a CO_2 isotope instrument in the same instrument shed (Rick Wehr, personal communication). We don't expect that the apparent CO_2 null bias shown in Figure 2-19 was caused by a dilution effect brought on by the condensation/evaporation cycles[9] because dilution effects are accounted for in the CO_2 calibration. Instead, dissolution of CO_2 in liquid water condensate in the gas tubing or in water films on the tubing may have been the main cause.

In the summer, humid outside air often condensed in the cool (oscillated about 21°C) shed, and Figure 2-22 shows a significant correlation between of failed null tests and outside dew points near the shed temperature. The fraction of CO_2 that

---

[9] Amplitudes of oscillations and the net change in H_2O mole fractions over the nulling procedure on occasion exceeded 0.3 ppth in the summertime, and sometimes surpassed 2 ppth. It would require an oscillation of $\sim$0.3 ppth H_2O to cause a dilution effect detectable above the CO_2 precision.

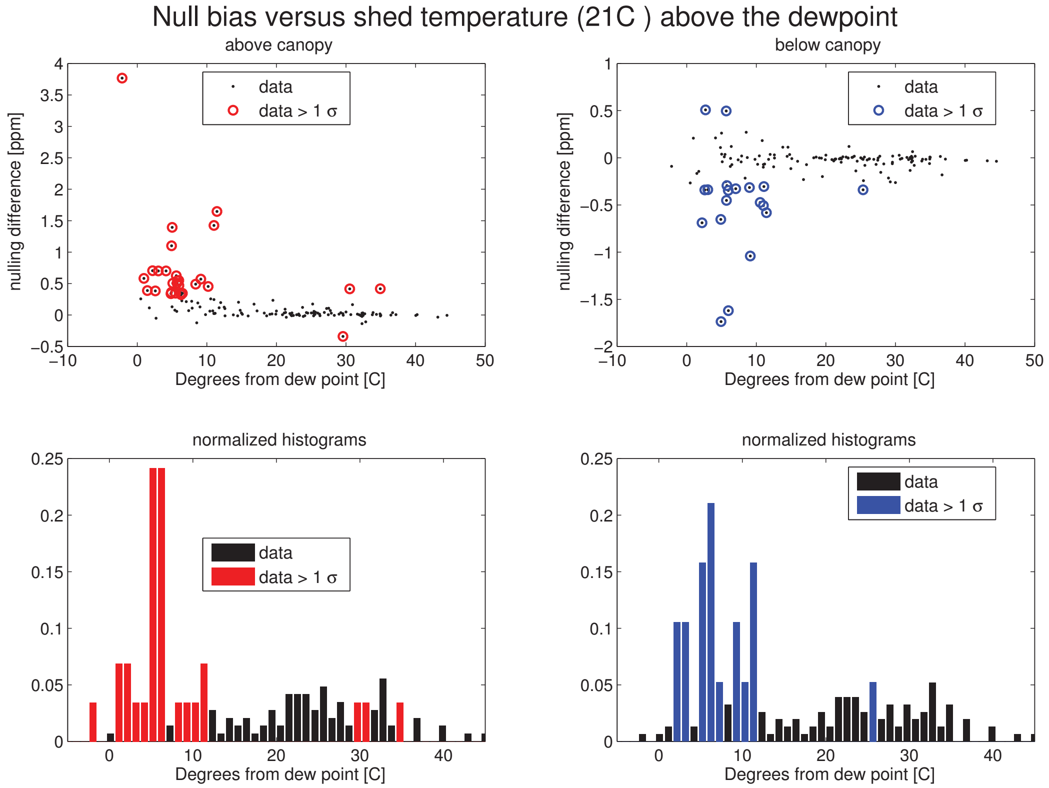

Figure 2-22: Nulling procedures that passed (black) or failed (above canopy in red, below canopy in blue) the bias test as a function of outside air dew point. Specifically, the difference between the mean shed air temperature (approximately 21°C) and the outside air dew point is explored as the independent variable. Most failed tests occur when the dew point exceeds the shed temperature, thus indicating water vapor condensation within tubing lines in the instrument shed contributes to the failure of null tests.

would have dissolved in liquid water condensate in the tubing lines (or volatilized back into the sample stream) would vary according to the temperature- and CO_2 partial pressure-dependence of Henry's Law. This is consistent with the observation that failed null tests occurred during times with both large outside gradients and high humidity. The condensate would have acted as a sort of CO_2 buffer in the sampling lines and should have only caused a "memory" effect during normal sampling. This would have effectively over-averaged the samples in each individual gas inlet sampling line, which is not a problem for the low-frequency flux-gradient calculations performed in this study. The "memory" of the CO_2 mole fractions that were sampled from each gas inlet before nulling may have lasted well into the nulling procedure, causing failed null bias tests. Although the null bias tests failed, no significant detrimental effect is expected on the ambient samples. This indicates that the nulling procedure was a poor test for CO_2 and H_2O bias during the summer. If a real bias due to a leak was the culprit, we would expect a similar bias to be observed for H_2, but it was not. This is likely because the H_2 sample stream was dried and H_2 has a much higher Henry's constant (less soluble) than CO_2.

The nulling procedure is an important test for confirming that concentration gradients can be measured to high precision for flux-gradient measurements. Future procedures could avoid some problems experienced in this study. For instance, the nulling volume size could be increased or multiple volumes could be connected in series to insure a well-mixed sample that did not drift significantly over the procedure or the nulling volume inlet could be moved farther from the soils. A fan inside the volume would help as well. Secondly, the possibility for water vapor condensation inside an instrument shed should be reduced either by heating the inlet lines inside the shed or by dropping the pressure at the gas inlet.

Temperatures were measured simultaneously at all four sampling levels. One-minute averaged data were corrected for temperature shield resistance biases, which were determined during two nulling exercises by bringing temperature shields from a given temperature gradient pair to the same level.

H_2, CO_2 and H_2O concentration gradient calculations

Highest frequency concentration gradients

Two methods for calculation of trace gas concentration gradients at the highest possible frequency given the sampling interval were tested: 1) a simple $(\chi_{top,\,n-1} - \chi_{bot,\,n})/dz$ method and 2) an interpolation method $(\frac{1}{2}\chi_{top,\,n-1} + \frac{1}{2}\chi_{top,\,n+1} - \chi_{bot,\,n})/dz$. The time intervals, between each value n are 1 and 2 minutes for the H_2 and CO_2/H_2O measurements, respectively. The difference between the concentration gradient calculated by the methods (method 2 minus method 1) is illustrated in Figure 2-23 for H_2 and CO_2. Above the canopy, where concentration gradients are small, the difference in the concentration gradient calculated by each method is typically very low (*i.e.*, below the instrumental precision). Below the canopy, concentration gradients are larger and concentration gradient differences are sometimes larger than instrumental precision. Importantly, the medians of the residuals are centered on zero for both the above- and below-canopy concentration gradients, meaning that there is no significant difference between the two concentration gradient calculation methods. The simple method 1, $(\chi_{top,\,n-1} - \chi_{bot,\,n})/dz$, is therefore adopted.

Averaged concentration gradients for flux calculations

High frequency concentration gradients computed in this study provide some insight into how eddies mix the above- and below-canopy environment in the Harvard Forest. To integrate over the spectrum of eddies contributing to fluxes near the surface, the data must be time averaged, and 30 min is a commonly accepted averaging interval in the literature (*e.g.*, Oke (1978); Stull (1988); Bocquet et al. (2011)). An averaging interval of 32 min is used to incorporate at least two H_2 measurements from each sample height in the average.

The schematic in Figure 2-24 depicts the method for calculating concentration gradients from H_2 mole fractions measured every four minutes at a given height. Each sample stream is physically averaged (with an integrating volume with τ=8 min time constant), and a single measurement value is assigned to each of the eight, one-min timestamps. Average concentration gradients are calculated as the difference

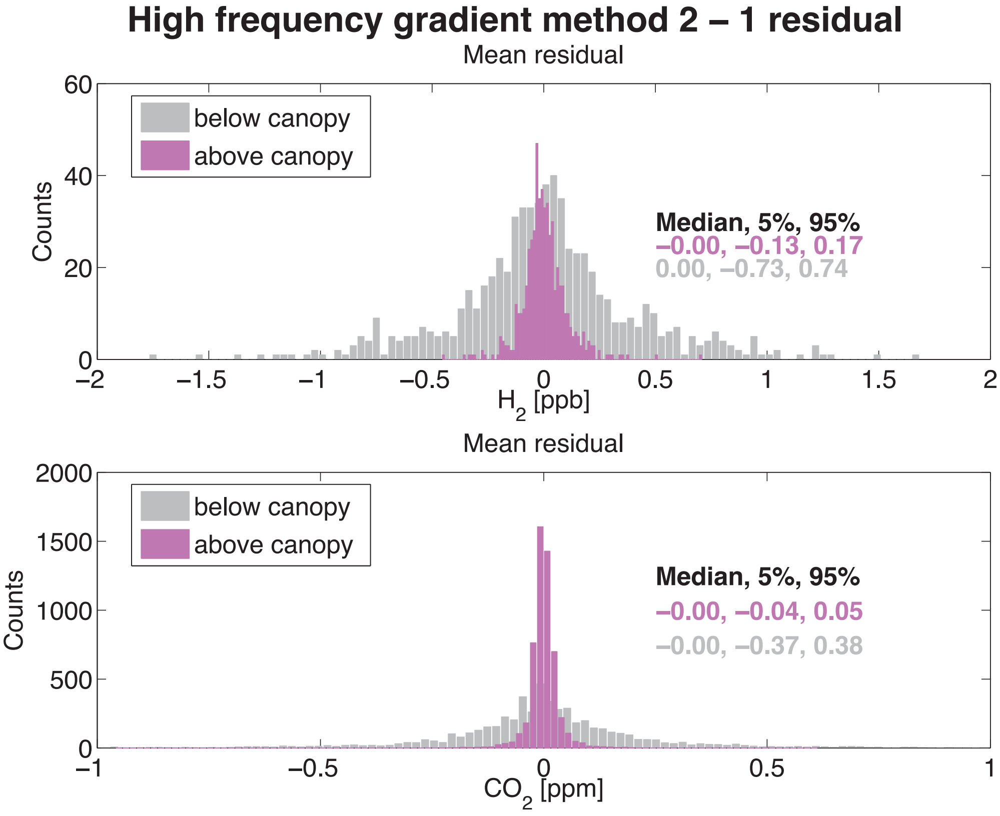

Figure 2-23: The mean difference of the concentration gradients calculated by method 2 minus by method 1 for calculation of the H_2 and CO_2 concentration gradients at the highest possible frequency were tested on data from October 5-11, 2011. The two methods were: 1) a simple $(T_{n-1} - B_n)/dz$ method and 2) an interpolation method $(\frac{1}{2}\chi_{top,\,n-1} + \frac{1}{2}\chi_{top,\,n+1} - \chi_{bot,\,n})/dz$.

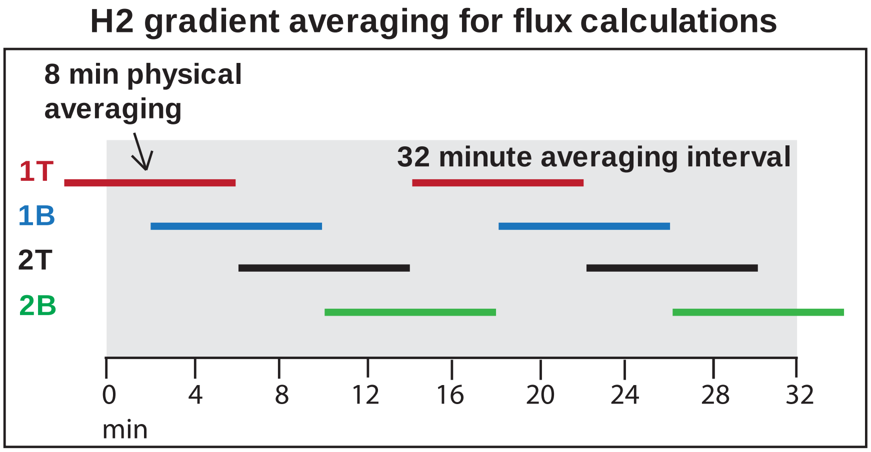

Figure 2-24: Schematic depicting the method for calculating concentration gradients from H_2 mole fractions measured every four minutes at a given height. Each sample stream is physically averaged with an eight-min time constant (horizontal bars), and the single measurement value is assigned to each of the eight one-min timestamps. Average concentration gradients are calculated as the difference of the mean of the one-minute timestamps that fit within the 32 minute averaging interval (grey shading) for the top and bottom of a concentration gradient pair.

of the mean of the one-minute timestamps that fit within the 32 minute averaging interval for the top and bottom of a concentration gradient pair. When compared to other methods tested (involving the averaging of mole fractions or concentration gradients and either an averaging or interpolation technique), this method is chosen because it accounts for the effect of the integrating volume averaging. Also, as the figure shows, gaps exist in the measurements of each concentration gradient set, and the chosen method does not require us to interpolate or fill gaps.

The question arises whether the difference in sampling frequency between the GC (H_2 every 4 min) and the IRGAs (CO_2 every 1 min) causes a flaw in the calculated concentration gradients that would propagate to the flux calculations. The relatively higher frequency CO_2 measurements were used to explore the difference between CO_2 concentration gradients calculated every 2 minutes using the simple $(T_{n-1} - B_n)/dz$ method (high frequency) and those calculated over 8 minutes from CO_2 measurements closest to the H_2 timestamps; an example is shown in Figure 2-25. Concentration gradients calculated at a lower frequency do not capture all of the higher frequency

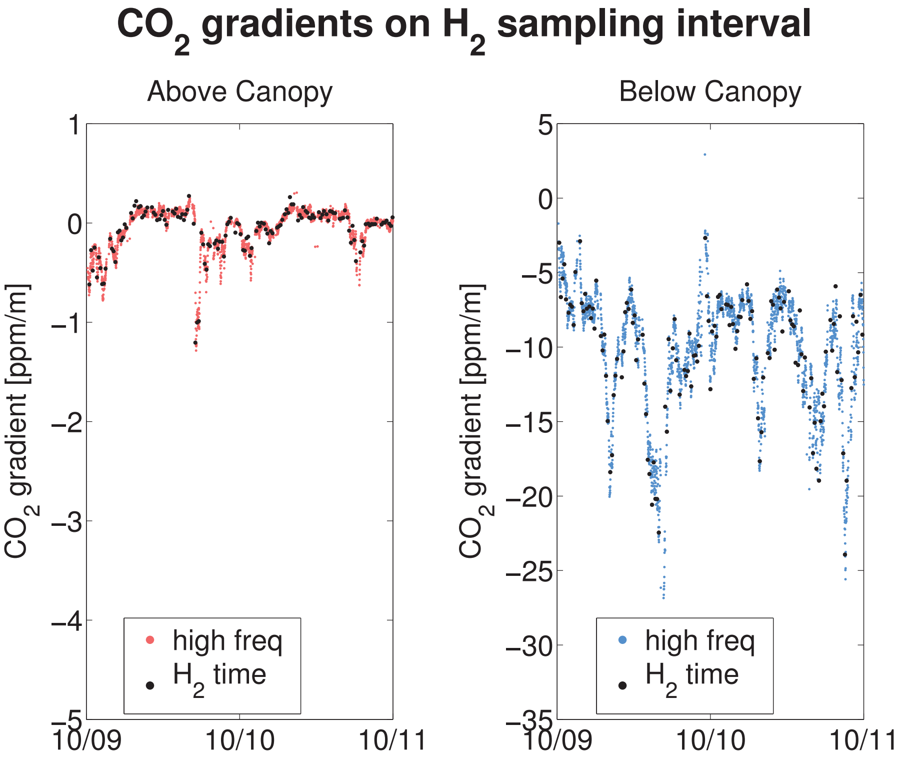

Figure 2-25: Comparison of high frequency (1 per minute) CO_2 concentration gradients above (left) and below (right) the canopy with CO_2 concentration gradients calculated on the lower frequency (1 per 8 minutes) H_2 timestamp.The general trend of the concentration gradient time series is captured even at the lower frequency H_2 timestamp because the 8-minute integrating volume averaging is sufficient to span the longer H_2 measurement interval. The effect on the final flux measurements will be considered as well.

concentration gradient features, but the general concentration gradient time series trend is captured. We expect the same general trend because the integrating volumes should physically average the air stream to span the 8 minute interval required to measure a H_2 concentration gradient. The higher frequency CO_2 measurements are essentially over-sampling the volumes.

2.3 Conclusion

As outlined in the beginning of this chapter, an instrument system to measure H_2 gradients and other correlative variables for the purpose of calculating above- and below-canopy H_2 fluxes at Harvard Forest was designed and built. The performance of the instrument (*i.e.* precision, sample stream averaging, and concentration gradient bias) was critically assessed, and the instrument was found to meet the performance objectives. The material presented in this chapter provides the foundation for understanding the origin of the measurements presented in Chapters 3 and 4. The assessment of instrument performance was critical for substantiating the measurements (and understanding their limitations) in order to support the scientific results presented in the ensuing chapters.

Chapter 3

Seasonality and annual budget of H_2 at Harvard Forest

Objective

In this chapter, H_2 fluxes from measurements are derived and the ecosystem H_2 exchange is characterized. Time series of H_2 mole fractions, concentration gradients, and fluxes at the Harvard Forest over 1.5 years are presented. Three methods for calculating H_2 fluxes above and below the forest canopy are compared. This study describes the seasonality of H_2 ecosystem exchange to improve the process-based understanding of the H_2 soil sink. This work explores the relationship between H_2 fluxes and environmental factors. The possibility of previously unrecognized processes affecting H_2 ecosystem exchange, such as H_2 sources or sinks within the forest canopy, are explored by comparing fluxes of H_2 above and below the forest canopy.

Results

- Continuous, automated measurements of H_2 mole fractions, gradients, and fluxes are made in the Harvard Forest for over one year for the first time in a temperature forest ecosystem.

- The H_2 mole fraction time series is consistent in magnitude with concurrent Northern Hemispheric H_2 measurements and in timing with previous H_2 measurements at Harvard Forest.

- The sensitivity and precision of the custom GC-HePDD instrument system enabled the quantification of above-canopy H_2 gradients that would have been below the detection limit of traditional H_2 detection systems.

- A number of flux-gradient methodologies were tested against direct eddy flux measurements and against each other.

- Significant H_2 fluxes were measured both above and below the Harvard Forest canopy.

- Soil H_2 uptake exhibits a clear seasonal cycle with a distinct summer maximum and broad winter minimum.

- As expected, summertime H_2 uptake correlates with soil and air temperature. No significant correlation with summertime soil moisture is found as of yet.

- Unexpectedly, H_2 *emissions* from the forest are observed. Processes other than microbe-mediated soil uptake must dominate during certain periods.

- H_2 emissions are measured below the canopy in the winter and spring, which may be the result of anaerobic production of H_2 from soils during anoxic conditions.

- We report the first evidence for H_2 emissions from the forest canopy, which occur in the fall and possibly in the summer. Traditional measuring methods would not have been able to diagnose potential canopy H_2 emissions, and have assumed the canopy is inert with respect to H_2. The mechanism is unknown.

- The results described in this section will provide the most comprehensive picture of H_2 ecosystem exchange to date. Further analysis will be performed for publications and eventually the data will be available on the Harvard Forest Data Archive for use by other groups for inter-comparison and modeling projects.

3.1 Seasonality of H_2 mole fractions and gradients

3.1.1 Mole fraction time series

The goal of this project is to understand local processes that govern the fate of H_2 using a flux-gradient methodology. As discussed in Chapter 2, the ability to measure relative mole fractions to high precision is key. Good agreement provides confidence of data quality, which builds a case for its inclusion in future analyses and modeling studies. Mole fraction time series can also be analyzed for seasonal, vertical, and diurnal patterns to diagnose the important local and regional processes.

H_2 time series

The raw and averaged (one-month moving average) H_2 time series from each gas inlet are presented in Figure 3-1. The seasonal cycle is observed at each gas inlet height; amplitudes are smallest above the canopy and increase with proximity to the soil sink. Positive mole fraction anomalies that extend well above the average seasonal cycle (one-month moving averages) are often observed simultaneously at all heights, but depletion events below the seasonal cycle tend to be more prevalent and significant below the canopy. The full range of H_2 mole fractions measured at the forest yield a spread in raw mole fractions during this study between ∼280 ppb and ∼610 ppb over all inlets; this 330 ppb range is quite large relative to the mean mole fraction across all inlets (482 ppb). A narrower range (185 ppb range between ∼425 and 610 ppb) of mole fractions were measured at the uppermost 28 m gas inlet. A larger H_2 mole fraction range was observed below the forest canopy (∼300 ppb at the 0.5 m inlet) than above (∼185 ppb at the 28 m inlet) because of the proximity of the lower inlet to the soil sink.

As was thoroughly explored from 1996 to 1999 by Barnes et al. (2003), air masses containing pollution are transported to Harvard Forest and have positive H_2 anomalies up to 400 ppb above the seasonal baseline. Positive anomalies were correlated with winds from the southwest, implicating the New York City-Washington, D.C. urban/industrial corridor as the origin. Furthermore, using the mean molar ratio of

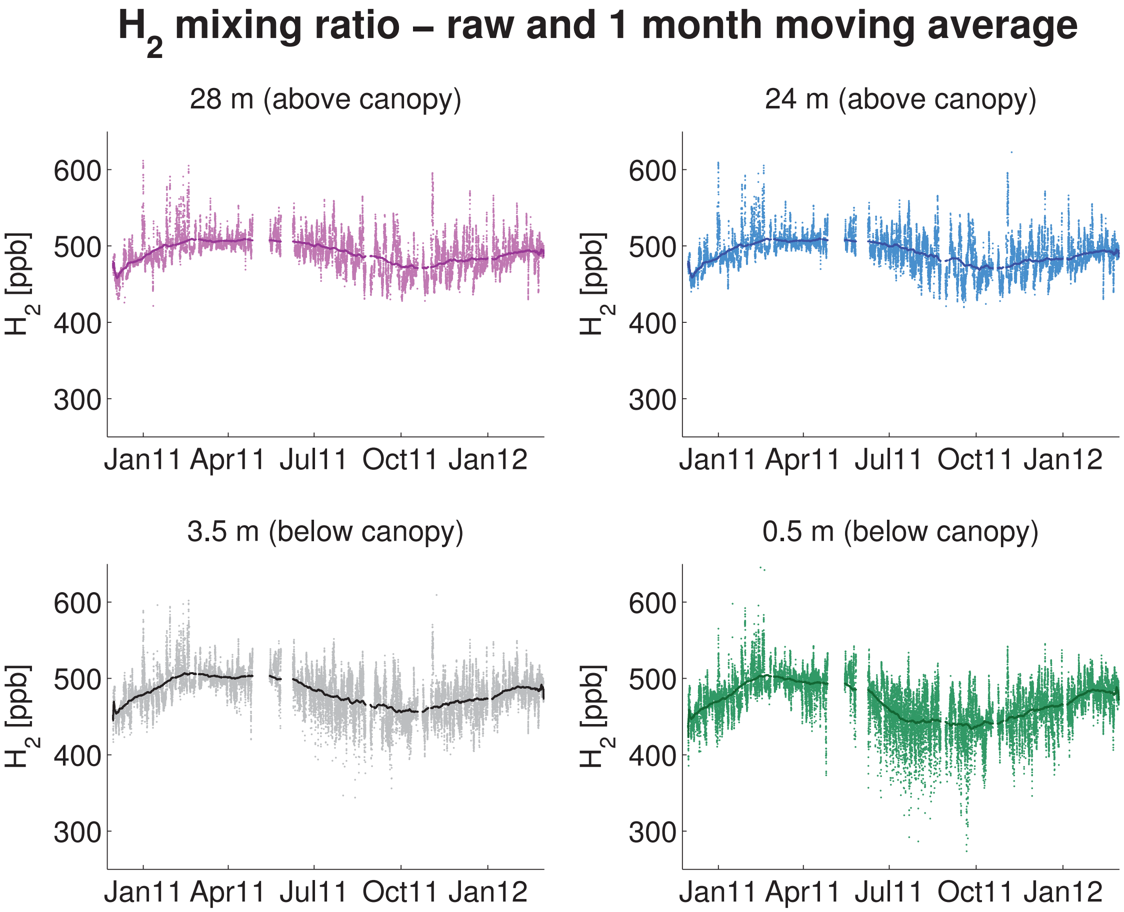

Figure 3-1: H_2 mole fraction time series for each tower gas inlet. Raw data are shown in the light color. Dark lines are the one-month moving average of the data. The seasonal cycle is evident at each vertical height, and has the largest amplitude below the canopy, close to the soils. Anomalously high H_2 mole fraction events tend to occur at all heights. Depletion events occur often below the canopy during all seasons, but especially in the summertime.

H_2 and CO anomalies ($\Delta H_2/\Delta CO$) as a fingerprint of polluted air masses, they identified automobiles as the primary emission source. In this study, similar pollution events were observed. For example, a plume with 580 ppb H_2 was found to have passed over New York City, New Jersey, and Washington D.C. (the regions with the highest deduced emissions of H_2 (Barnes et al., 2003)) before reaching Harvard Forest at 12:00 on February 12, 2011[1], and was therefore likely due to urban anthropogenic emissions.

At all heights, mole fractions were occasionally depleted below the seasonal baseline; this effect was more pronounced at the below canopy inlets, reaching ∼160 ppb below the seasonal baseline during a nocturnal depletion event at 0.5 m. Consistency between all heights for most pollution anomalies, but typically not for depletion anomalies highlights two characteristics of the forest: 1) the establishment of gradients as a result of local trace gas processing, and 2) the coupling of the above and below canopy environments during the turbulent daytime, and their decoupling at night.

To illustrate the seasonal cycle, just the baseline seasonal cycles at each height are plotted in Figure 3-2. The above canopy measurements exhibit the typical extratropical Northern Hemispheric H_2 seasonal pattern (Xiao et al., 2007). Mole fractions reach a broad springtime maximum, and then steeply decline in the early summer, reaching a minimum in late fall. As stated in the introduction, the seasonal minimum in the autumn arises from the superimposed processes of OH oxidation (maximizing in the summer) and the integrated soil loss (throughout the summer into the early fall). Fall H_2 soil uptake may reach the highest annual rates because soils are typically at their driest (Barnes et al., 2003; Conrad and Seiler, 1985; Schuler and Conrad, 1991; Yonemura et al., 2000; Xiao et al., 2007) depending upon whether or not tropical storms and hurricanes have or have not recharged soil moisture. The seasonal maximum is broad and spans the winter-spring months when soil- and OH-derived loss of H_2 is low, allowing the accumulation of emitted H_2, which is mainly released by combustion at those times.

---

[1] Back trajectories calculated using HYSPLIT (Draxler and Rolph, 2012; Rolph, 2012)

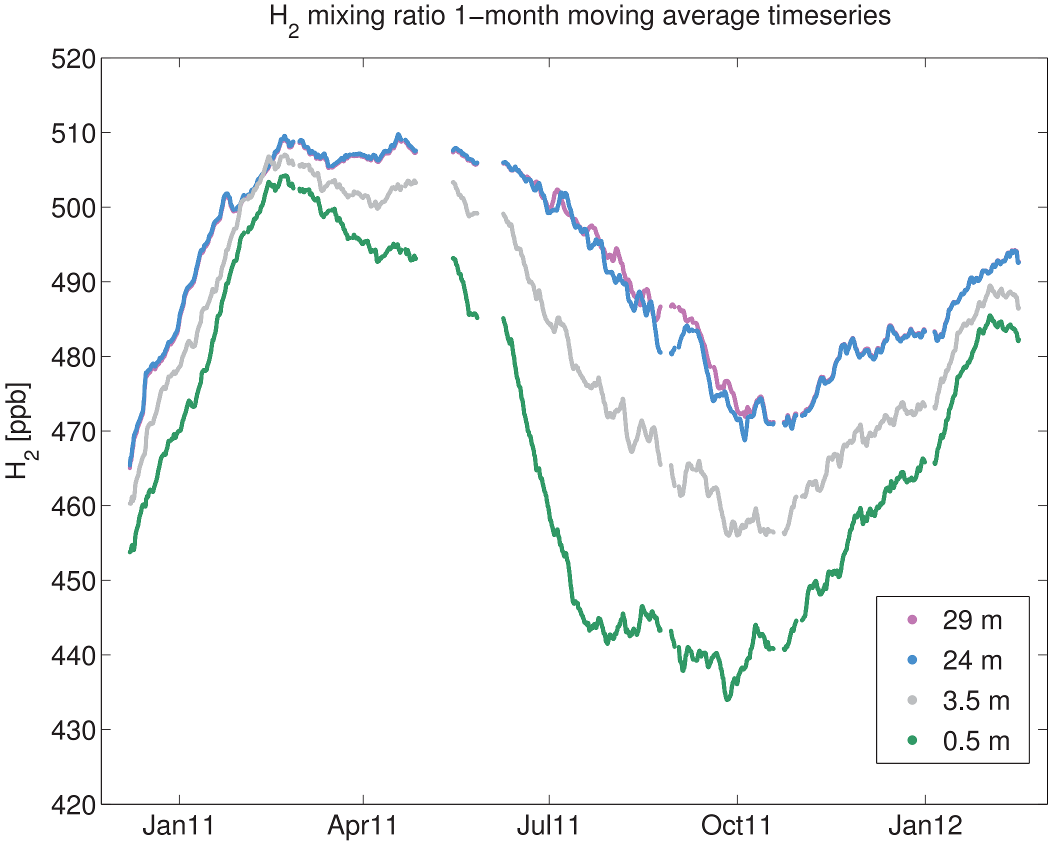

Figure 3-2: Smoothed (1-month moving average) H_2 mole fractions at each inlet height. The seasonal cycle is apparent at all levels. Influence of the soil sink in the spring and summer is felt earlier, and more strongly at the below canopy inlets. Mole fraction gradients, even on this averaged basis, are significant between the above and below canopy environment and within the below canopy environments all year. Above the canopy, gradients are small, but are persistently significant above the canopy in the summer.

The seasonal cycle at Harvard Forest has a strong vertical imprint both in the mean mole fraction differences (gradients) and in the timing of events. Differences in the above and below canopy mean mole fractions vary, but are significant for the entire year. This gradient maximizes in mid-July with a mean difference of ∼55 ppb between the 28 m and 0.5 m inlets. Significant mean differences between the above and below canopy environment are observed throughout the winter, albeit with a reduced magnitude. This signifies that H_2 soil uptake persists over the wintertime, which will be the subject of discussion in Chapter 4.

Differences in the seasonal cycle within gradient pairs (above canopy: 28 and 24m, below canopy: 2.5 and 0.5 m) are strong and year-round below the canopy. Above the canopy, the gradient is small and is only obviously significant on a mean basis in the late summer. Calculated gradients and their relationship to the minimum detectable gradient will be discussed in more detail in Section 3.1.2

Seasonal timing varies at different gas inlet heights at Harvard Forest. At all heights, the air masses are influenced both by local, ecosystem-scale processes and by regional processes that are imprinted upon advected air masses. The above canopy inlets are more influenced by advected regional air and less by the local soil sink than the below canopy inlets. As a result, baseline above canopy mole fractions exhibit a slow depletion of by continental H_2 uptake over the Northern Hemisphere throughout the summer, such that the minimum occurs around November. However, the below canopy baseline minimum is broader and is reached much sooner; specifically, between July and October. This is consistent with the early, local influence of the soil sink being felt at the below canopy inlets and the longer, regional influence being felt above the canopy. The vertical imprint on seasonality at Harvard Forest causes the persistent gradient between the below and above canopy environment to decrease to ∼30 ppb by the regional seasonal minimum in October.

The timing of the seasonal maximum in the H_2 mole fraction occurs around the same time in March for all inlets, but the maximum is broader above the canopy, while the below canopy environment feels soil uptake sooner and does not sustain its maximum mole fractions. Analysis of the H_2 seasonal cycle clearly demonstrates the importance of the soil sink on both the local and the regional environment and its counterbalance of H_2 emissions, which then accumulate when soil uptake slows in the winter and spring.

Comparison to other H_2 time series

H_2 mole fractions observed in this study are compared with data sets that overlap either in time or space. This is important for lending confidence to the measurements made in this study.

H_2 was measured by Barnes et al. (2003) at Harvard Forest between 1996 and 1999 using a gas chromatograph with an electron capture detector (GC-ECD). To induce sensitivity to H_2, N_2O was used as a dopant in the carrier gas stream with precisions of ∼1% for H_2. Only the published (first three years) data set for this Forest and Atmosphere Chromatograph for Trace Species (FACTS) instrument are used for this comparison in space. FACTS measurements were calibrated against the NOAA/CMDL CCG working standards, which are tied to a set of gravimetric standards (Novelli et al., 1999). Assuming no changes to the H_2 scale, these measurements should be on the same calibration scale as the 2011 measurements from this study.

For the comparison in time, data from the Mace Head, Ireland (53N, 10W) station of the Advanced Global Atmospheric Gases Experiment (AGAGE) are used (Prinn et al., 2000). H_2 is measured in this AGAGE data set with a mercuric oxide reduction detector (MRD) on a gas chromatograph multidetector (GC-MD) system, which also achieves ∼1% precision for H_2. Mace Head AGAGE data, devoid of European pollution events are used for the comparison. H_2 standards were prepared with a bootstrap method using gravimetrically prepared methane standards (Francey et al., 1996). Frequent inter-comparison with the NOAA/CMDL CCG H_2 scale has identified a systematic $3 \pm 1\%$ difference, with the AGAGE scale giving higher atmospheric values (Langenfelds et al., 2002; Francey et al., 1996; Xiao et al., 2007).

H_2 measurements in this study have an improved precision, by nearly an order of magnitude, over the FACTS and AGAGE data sets. Those detectors would have significant limitations for flux-gradient calculations, but their increased variability

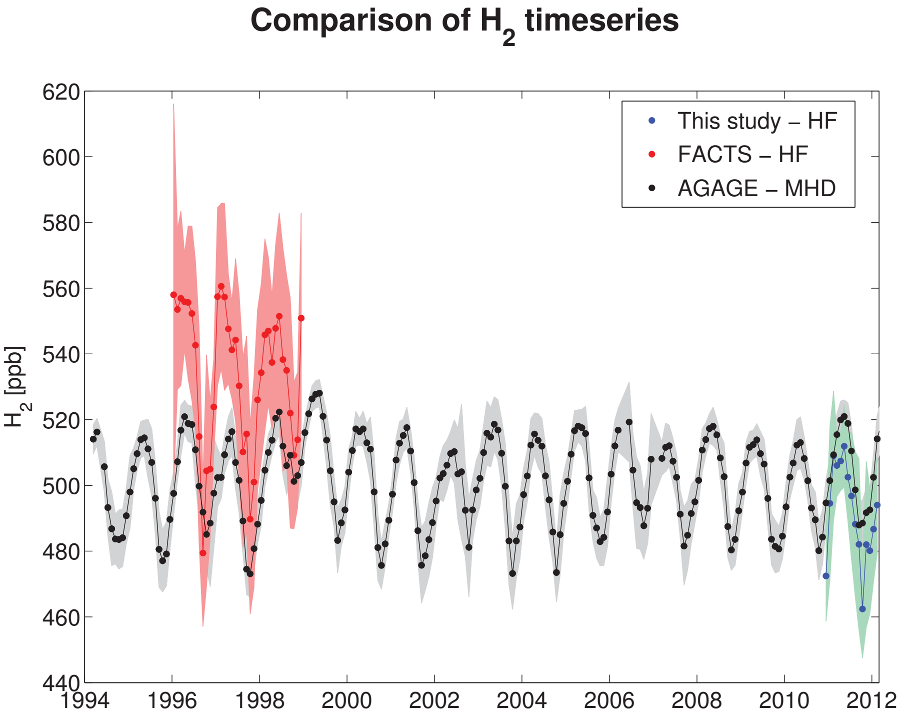

Figure 3-3: Comparison of H_2 mole fraction time series in this study to data collected at Harvard Forest by Barnes et al. (2003) from 1996-2005 using the FACTS instrument and from Mace Head, Ireland by (Prinn et al., 2000) under the AGAGE network. The data in this study agree well with the seasonality observed at Mace Head during the same period. Mole fractions are lower for this study at Harvard Forest, but this is not surprising for a region downwind of large swaths of continental uptake, while Mace Head typically receives its unpolluted air masses from trajectories over the Atlantic. Shading indicates 1σ standard deviation for monthly average.

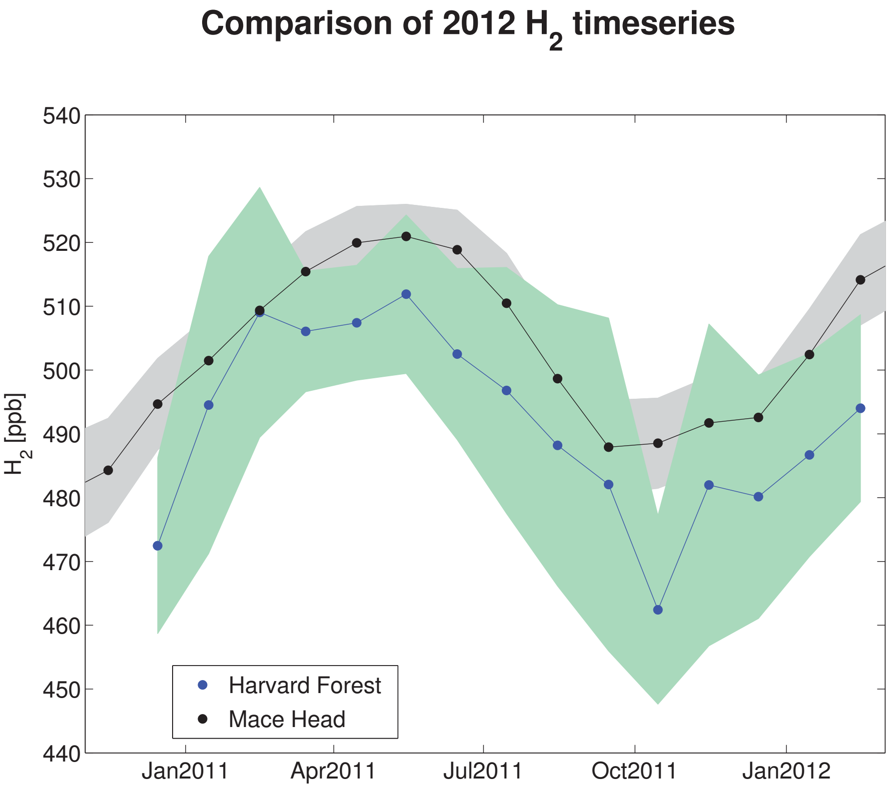

Figure 3-4: Comparison of H_2 mole fraction time series in this study to data from Mace Head, Ireland by (Prinn et al., 2000) under the AGAGE network. The data in this study agree well with the seasonality observed at Mace Head during the same period. mole fractions are lower for this study at Harvard Forest, but this is not surprising for a region downwind of large swaths of continental uptake, while Mace Head typically receives its unpolluted air masses from trajectories over the Atlantic. Shading indicates 1σ standard deviation for monthly average.

should not have a large effect on a comparison of the monthly-averaged mole fractions as is done in Figure 3-3. Inconsistencies in accuracy due to the notorious difficulties in H_2 calibration standard scales are likely a larger problem, as has been recently revisited (Jordan and Steinberg, 2011).

A comparison in time of the H_2 time series from this study in Harvard forest (43N, 72W) to the AGAGE data from Mace Head, Ireland (53N, 10W) is shown in Figure 3-4. The two time series agree very well in the timing of the seasonality. The AGAGE time series is smoother than in this study, which is most likely in the spring because the AGAGE data have been filtered for pollution events, while the Harvard

Forest data have not, resulting in the incorporation of wintertime pollution events in the mean of this study. Secondly, the local influence of the soil sink in late fall is apparent for the Harvard Forest data, but is absent on the breezy coastal background station at Mace Head. There appears to be about a 10-20 ppb offset ($\sim 3\%$) between the two data sets.

A comparison of the absolute H_2 mole fraction time series from this study in 2011 to the previous Harvard Forest measurements in 1996-1998 is shown in Figure 3-3. In that study, Barnes et al. (2003) measured an annual mean H_2 mole fraction of about 533 ppb for 1996-1999. This mean mole fraction is about 50 ppb higher than observed in 2011. The 1996-1999 seasonal cycle amplitude was 24.5 ppb and the 2011 was 19.5 ppb, which is comparable given the inter-annual variability. This indicates an ($\sim$9%) offset in the absolute mole fraction calibration scale between the two data sets.

Atmospheric H_2 mole fractions typically exhibit high inter-annual variability; therefore, it is useful to compare the timing and amplitude of the seasonal cycles for these two Harvard Forest H_2 time series. To account for the apparent inconsistencies in the calibration scales, the annual mean is subtracted from each seasonal cycle to leave just the seasonal cycle amplitude, as shown in Figure 3-5. The comparison shows that the seasonal minimum was reached in November for all years except 1996, which reached the seasonal minimum about 1.5 months earlier in mid-September. The rate of approach to the minimum occurred most rapidly in 1996 as well. A broad maximum was observed in all years, although in 1997 mole fractions approached the minimum earlier, and with a slower and more steady pace. 1998, an El Nino year, had the smallest seasonal amplitude of the sampled years, which is also apparent in the AGAGE and CCG NOAA flask network data (Prinn et al., 2000; ESRL/GMD, 2012). As correlations are drawn between fluxes in this study and other relevant environmental variables, it will be interesting to consider reasons for differences in the highly variable seasonal cycle for H_2 at Harvard Forest.

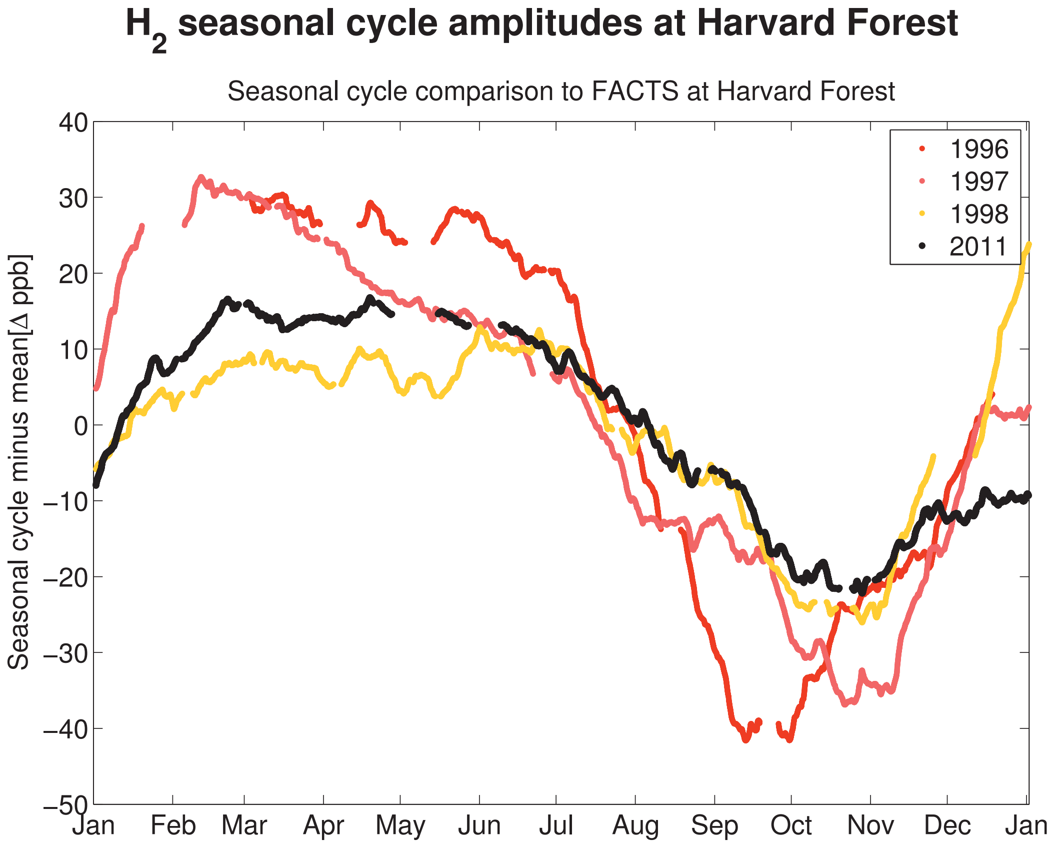

Figure 3-5: Comparison of H_2 mole fraction seasonal cycle time series (mole fraction seasonal cycle minus annual mean for each year) measured in this study to data collected at Harvard Forest by Barnes et al. (2003) from 1996-2005 using the FACTS instrument. The seasonal cycle of H_2 exhibits large interannual variability, especially in the amplitude and in the timing of the seasonal minimum and the breadth of the seasonal maximum.

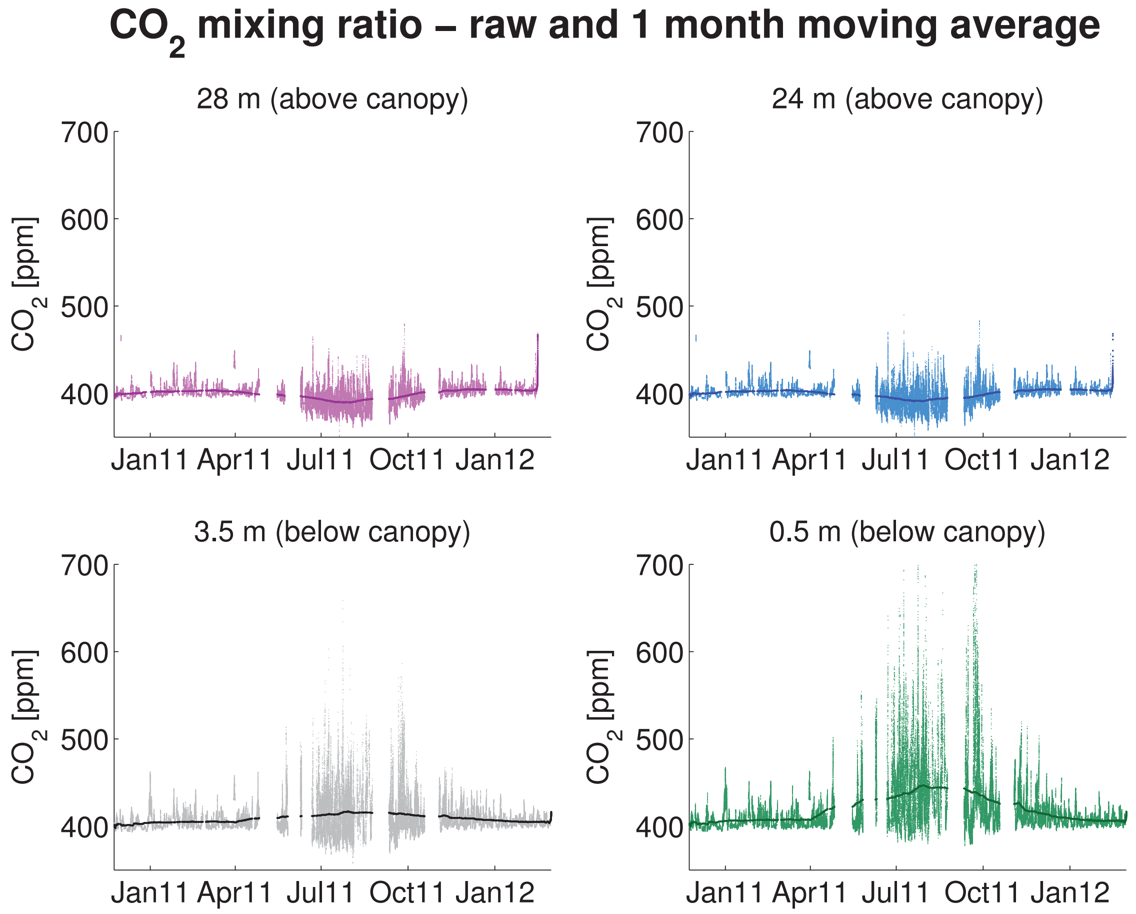

Figure 3-6: CO_2 mole fraction time series for each tower inlet. Raw data are shown with faint shading to indicate instrument precision. Dark lines are one-month moving averages of the data. A seasonal cycle is observed at each vertical height, although the above- and below-canopy cycles oppose each other in the summertime when above canopy mole fractions are depleted by photosynthetic uptake, while below the canopy mole fractions are enhanced due to high soil respiration rates. Soil respiration enhances below canopy CO_2 mole fractions year-round.

CO_2 time series

To use CO_2 as a correlative variable, its mole fractions were measured at each inlet height for the entire analysis period. Those data, which are plotted in Figure 3-6, are discussed in this section to examine the data set quality, in order to lend confidence in its application to better understand the behavior of H_2 in this temperate forest.

CO_2 mole fractions in the wintertime months outside of the growing season are characterized by positive anomalies extending above a background regional value. These anomalies are ascribed to soil respiration or combustion-derived pollution; the former would induce a vertical gradient amongst the sampled inlets and the latter would be an advected source that should affect all vertical heights more equally.

During the growing season, forest concentrations are characterized by a diurnal fluctuation in CO_2 driven by photosynthetic uptake during the day and carbon respiration at night. During the growing season ,carbon respiration is a combination of autotrophic and heterotrophic metabolism originating from the plants and the soil microorganisms, respectively. In contrast, the wintertime respiration is mainly driven by soil microorganisms since photosynthesis in a predominantly deciduous temperate forest does not sustain a strong autotrophic carbon source. Above the canopy, diurnal mole fractions oscillate about the seasonal baseline cycle, whereas nighttime buildup of CO_2 in the stable air below the canopy causes large positive anomalies. The 3.5 m inlet is surrounded by the vegetative understory, and air depleted in CO_2 is measured only during summer days. The 0.5 m inlet does not overlie any significant amount of vegetation, and is thus dominated year-round by soil respiration.

As was observed for H_2, a CO_2 seasonal cycle is observed at each inlet; however, unlike H_2, the directionality of the seasonal cycle (towards higher or lower mole fractions with time) of the above and below inlets oppose each other during the summer months. Furthermore, vertical gradients within the forest reverse diurnally in response to photosynthetic activation. To understand the process governing the seasonal cycle, a one-month moving average was calculated for both the day (12:00-16:00 local time) and night (0:00-4:00 local time) periods as shown in Figure 3-7 at each height.

In the winter and early spring, CO_2 soil respiration is the dominant process, as can be seen by the establishment of a negative gradient throughout the canopy (mole fractions highest closest to the soils). Soil respiration is also a persistent feature in the summer at night, however daytime photosynthetic loss dominates the 28 m, 24 m, and 3.5 m mole fractions in the summer as can be seen by the depleted diel CO_2. The lowermost inlet at 0.5 m continues to be dominated by soil respiration, even during the day. Above the canopy, CO_2 depletion is strongest right above the canopy at 24 m, as can be seen in the small but persistent above-canopy CO_2 gradient in July and August. The above canopy gradients reverse diurnally.

It is important to examine these features and to understand the underlying mechanisms driving them because CO_2 gradients will be used to determine the H_2 flux. From this analysis, we anticipate smaller, but consistent gradients in the winter and spring months, outside of the growing season. During these times, soil CO_2 respiration is the dominant process, which being co-located with H_2 soil loss should make CO_2 an excellent comparative species.

During the growing seasons, the gradients of CO_2 above the canopy change sign following the progression of solar radiation throughout the day. Although the IRGAs are able to detect a minimum gradient in CO_2 of $\sim$ 0.05 ppm/m in the median for the above canopy gradient, during the transition through zero, the gradients will, at some point, be necessarily below the detection limit. Additionally, it is clear from this analysis that there may be some photosynthetic interception of CO_2 between the 3.5 m and 0.5 m inlets given the clear photosynthetic influence in the former inlet, but not necessarily the latter. If this is the case, there may be some periods in which CO_2 is not a conservative tracer for H_2 between the below canopy inlets. During the growing season, CO_2 processes are more complicated, but signals are higher and may only require a little filtering to be used for H_2 flux calculations. This analysis of the CO_2 measurements gives us indications of when and how to safely use CO_2 as a comparative quantity for the flux-gradient calculations of H_2.

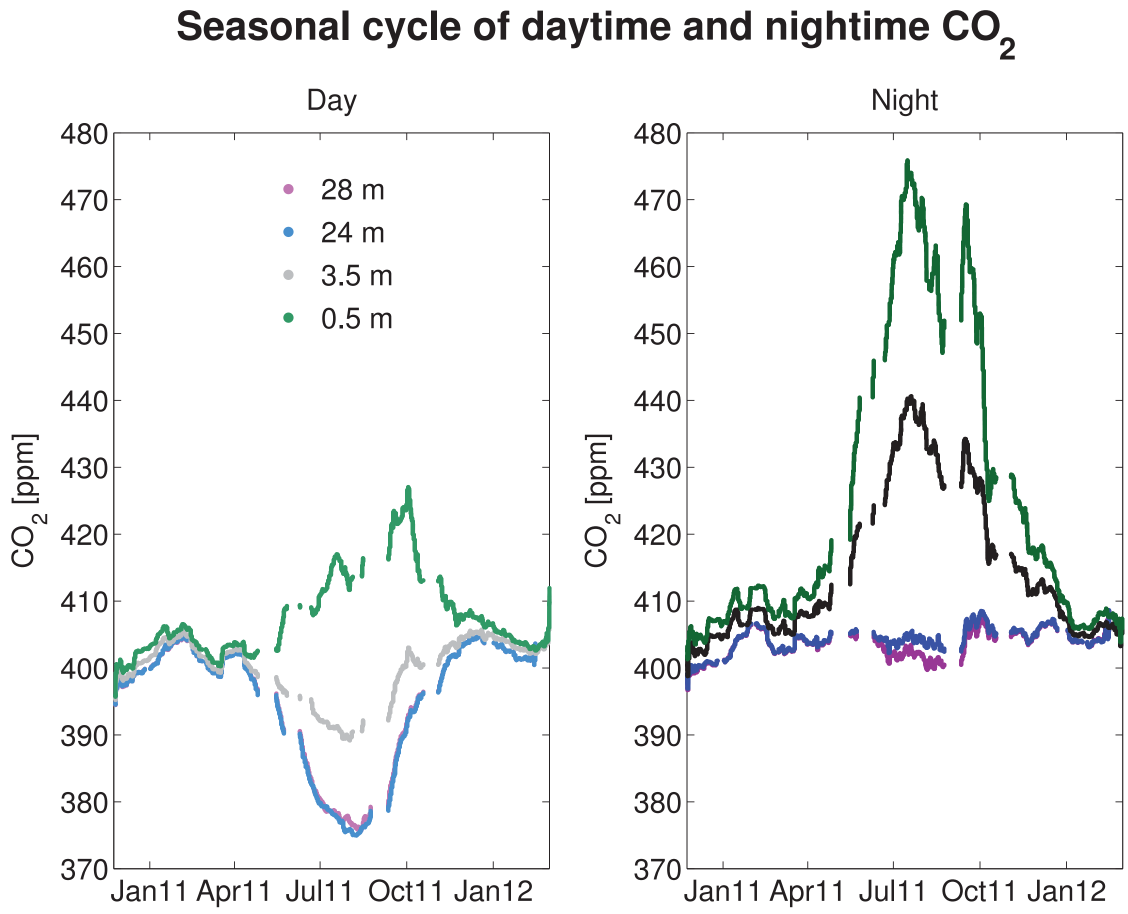

Figure 3-7: Smoothed (1-month moving average) CO_2 mole fractions at each inlet height during the day(12:00-16:00 local time) and night (0:00-4:00 local time). Outside of the growing season, CO_2 soil respiration is the dominant process, as can be seen by the establishment of a negative gradient throughout the canopy (mole fractions highest closest to the soils). Soil respiration is also a persistent feature in the summer at night, however daytime photosynthetic loss dominates the 28 m, 24 m, and 3.5 m mole fractions in the summer as can be seen by the depleted diel CO_2. The lowermost inlet at 0.5 m continues to be dominated by soil respiration, even during the day. Above the canopy, CO_2 depletion is strongest right above the canopy at 24 m, as can be seen in the small but persistent above canopy CO_2 gradient in July and August. The above canopy gradients reverse diurnally.

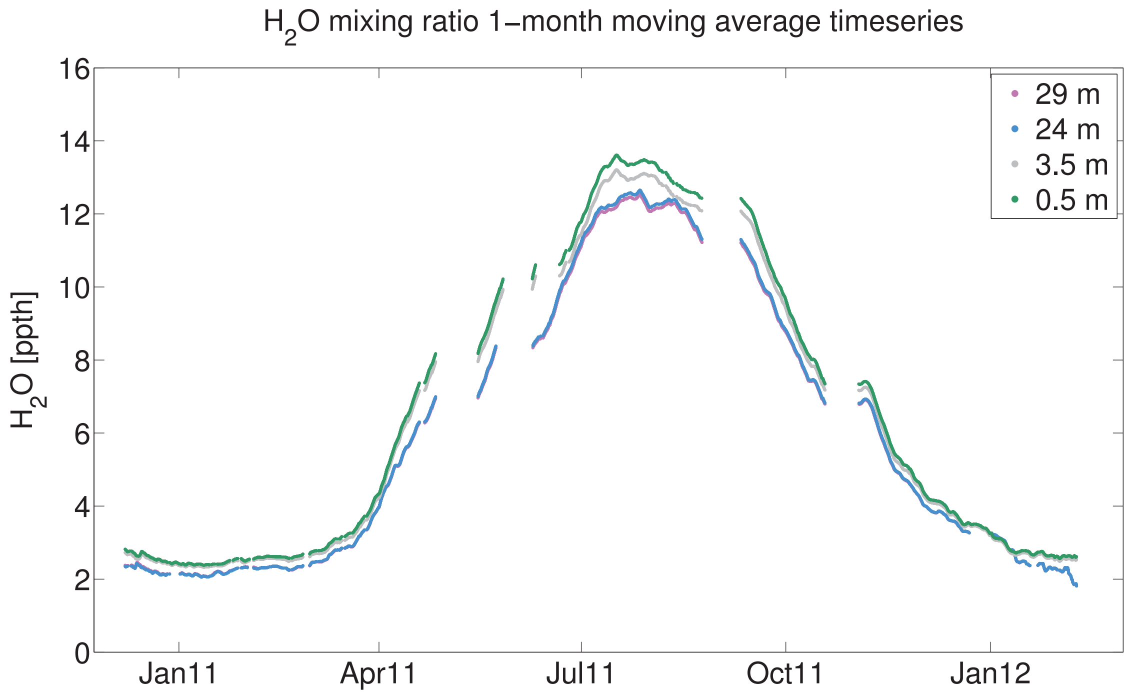

Figure 3-8: Smoothed (1-month moving average) H_2O mole fractions at each inlet height. The atmospheric carrying capacity for water vapor increases in the warmer months driving the observed seasonal cycle. The air is consistently wetter closer to the soils and dryer above the canopy.

H_2O time series

In this study, H_2O was measured at each inlet height for two reasons: 1) to combine with the H_2O eddy flux measurements as an additional correlative variable for deducing K and 2) to apply the Modified Bowen Ratio correction to obtain the sensible heat flux from the sonic anemometer and a temperature gradient. A time series of water vapor mole fractions at each inlet is shown in Figure 3-8. The atmospheric carrying capacity for water vapor tracks seasonal solar heating and heat retention in the troposphere. Liquid H_2O input to soils the ensuing evaporation causes a vertical gradient of H_2O decreasing away from the surface with height. Forest transpiration emits a large flux of water vapor from leaves in the upper canopy during the growing season.

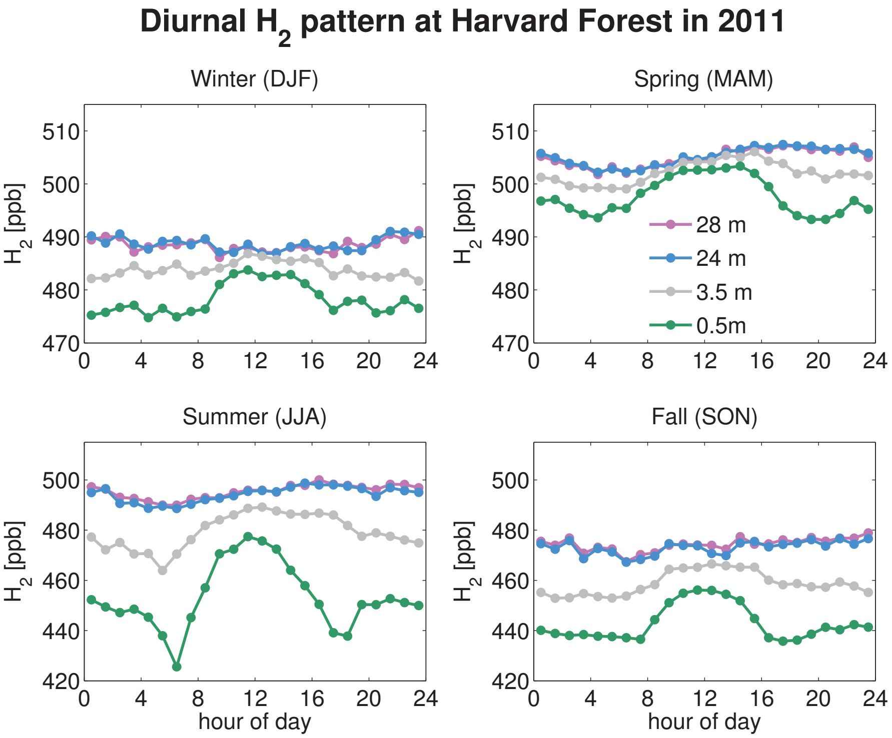

Figure 3-9: Seasonal diurnal pattern in H_2 mole fraction measurements at each gas inlet height. Note the change in scale for the winter/spring versus summer/fall plots.

Diurnal patterns

In addition to seasonal time series, plots of the diurnal mole fractions averaged over some time period can be used to inform our understanding of the processes affecting trace gases at Harvard Forest and how well the flux-gradient method may be applied.

The median diurnal pattern in H_2 mole fractions at each inlet for the four seasons of 2011 are plotted in Figure 3-9. The winter and spring diurnal cycles (on a different scale than summer and fall) exhibit similar, steady patterns. A nocturnal gradient is established, even in these cold and snow-covered months. At night, weak atmospheric mixing enables even small sources or sinks to cause a large concentration change in the nearby air masses with long residence times when mixing is weak. During the daytime hours, enhanced turbulent mixing causes the concentration gradients to be much smaller, although the magnitude of the source or sink may be the same or larger than at night. This is an important reminder not to equate concentration gradients with fluxes; the strength of turbulent mixing must also be accounted for. During the day, H_2 mole fractions increase as air is mixed into the forest from higher in the boundary layer where H_2 mole fractions are larger because they were not locally depleted. In the spring, some early morning H_2 uptake is visible even above the canopy (slight dip with minimum around 7 a.m.). Substantial gradients, in the median values, reestablish after the sun has set.

The gradients are much larger and the patterns more dynamic in the summer and fall (now on larger scale). Mole fractions decrease at night at all levels and the nocturnal gradients steepen until daybreak. Vertical gradients are reduced by daytime mixing, but persist strongly throughout the day. The gradients increase again after noon, which be a result of changes in turbulent mixing or biogeochemical cycling. The atmospheric stability in the canopy may increase in the afternoon if a canopy inversion is formed, where temperature is higher in the upper canopy environment than in the shady below canopy environment, which could suppress mixing and allow larger concentration gradients to establish with no change in source or sink strengths. Alternatively, the increase in gradients could signify an increase in soil H_2 uptake with the diel temperature cycle or perhaps production of H_2 by methane and non-methane hydrocarbon degradation involving formaldehyde (CH_2O) dissociation above the forest canopy. Again, this example serves as a cautionary example of why one cannot diagnose the source or sink strengths of a biogeochemical process from concentration gradients alone, the vertical mixing structure must also be diagnosed. It is not clear what gives the diel cycle an asymmetry in spring and fall.

As a comparison, the median diurnal pattern in CO_2 mole fractions at each inlet for the four seasons of 2011 are plotted in Figure 3-10. In the winter (note the scale is smaller in winter and spring), the diurnal pattern is straightforward, with relatively flat above canopy mole fractions and accumulation of CO_2 below the canopy at night. This indicates that soil CO_2 respiration is the main process in the winter. The story changes slightly in the spring, when CO_2 accumulation is found below the canopy at night, but during the day mole fractions are depleted at all levels. Below canopy depletion is mainly due to mixing with the relatively depleted boundary layer after

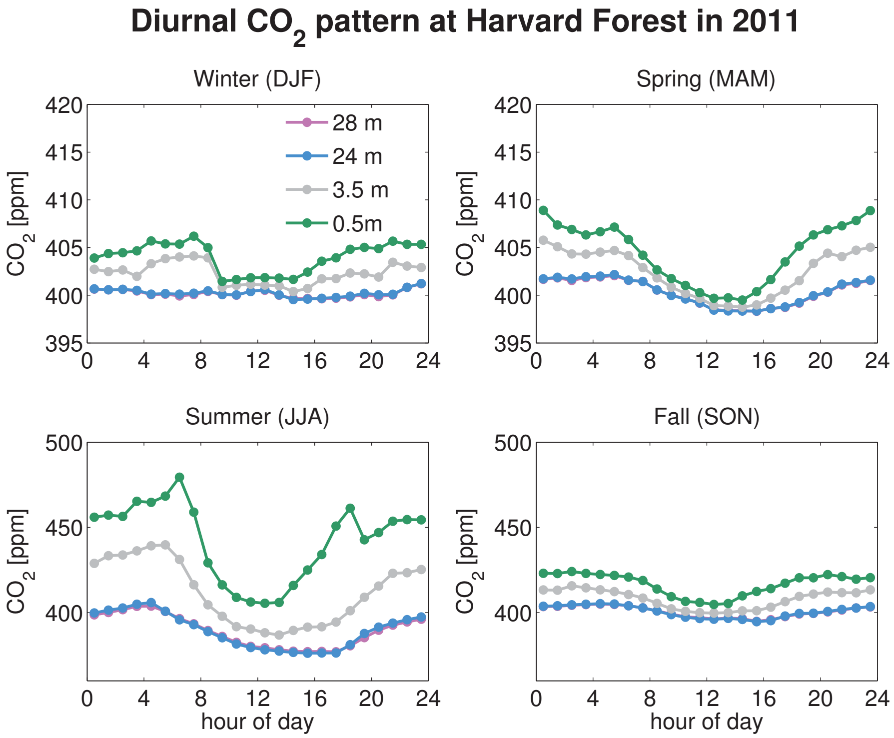

Figure 3-10: Note the change in scale for the winter/spring versus summer/fall plots.

daybreak, but above canopy depletion is likely driven by photosynthetic uptake, which begins in April.

In the summer (now on larger scale), the nocturnal CO_2 accumulation is exaggerated and affects even the above canopy mole fractions an night. Day break mixes lower mole fraction air from the boundary layer down into the forest. The imprint of soil respiration is observed throughout the day below the canopy, and this imprint appears to emerge again strongly after noon, despite the continuation of daytime turbulence. This same pattern, in reverse, was observed for H_2 as well. As an end result of many enzymatic processes, soil respiration is a function of temperature (Raich and Schlesinger, 1992); however, the temperature sensitivity can be masked by concurrent changes in the microbial community, substrate availability, and moisture (Phillips et al., 2010). The temperature response of H_2-consuming organisms may be more straightforward than net soil respiration. It is not clear why a temporary maximum is reached around 18:00, but this may be a transition zone between a halt in the enhanced temperature response and the beginning of the stable and stratified nocturnal condition.

CO_2 respiration and photosynthesis continue in the fall, but the diurnal imprint is greatly reduced. Compared to CO_2 it seems that H_2 uptake is more efficient in the fall. This makes intuitive sense as the largely deciduous forest drops its photosynthetic apparatus to the forest floor and the soil microbial community is left to drive the bulk of CO_2 cycling in the forest. In contrast, there is not a clear reason for the atmospheric H_2-consuming microorganisms to stop utilizing H_2 in the fall, although the enzymatic uptake rates may decrease with decreasing temperatures.

3.1.2 Gradients above and below the forest canopy

Mole fraction time series were used to calculate the time series of gradients for the flux-gradient calculations to determine the H_2 flux. H_2, CO_2, and H_2O gradients, calculated at the highest possible frequency (Section 2.2.3) are shown in Figure 3-11 for the above and below canopy inlet pairs. The above canopy gradients are shown to provide a sense of their small scale; below canopy gradients are much larger, as was expected during the instrument design phase.

The proximity of the below-canopy inlets to soil processing produces very large gradients, sometimes exceeding 40 ppb/m and -60 ppm/m for H_2 and CO_2 ($\sim$45% and 25% mole fraction differences over the 3 meter gradient), respectively. Below the canopy, seasonally larger gradients for both gases in the summer and fall indicate more intensive ecosystem cycling during those periods assuming vertical mixing is equivalent (may actually be stronger in fall in absence of leaves); however, significant gradients persist into the winter and spring for both gases. Below the canopy, H_2 and CO_2 gradients are nearly always positive and negative, respectively indicating soil uptake and respiration dominate ecosystem processing at that height.

The below canopy minimum detectable gradient (*mdg*) is about 0.08 ppb/m and 0.04 ppm/m for H_2 and CO_2, respectively, which is much smaller than the magnitude of most below canopy gradients. In fact, only 15% of the below canopy data are below the minimum detectable gradient achieved by this GC-HePDD system. In

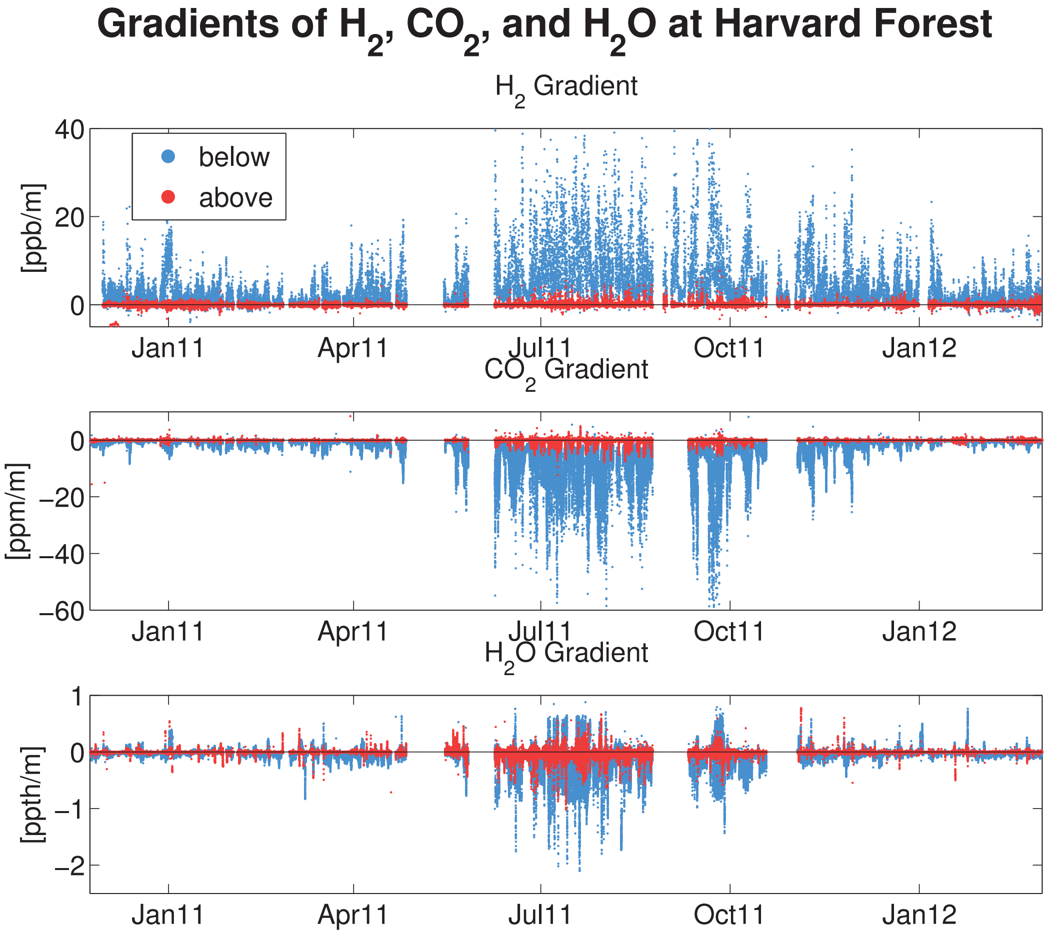

Figure 3-11: Vertical mole fraction gradients of H_2 (ppb/m) and CO_2 (ppm/m) for the above (red, 28 m - 24 m) and below (blue, 3.5 m - 0.5 m) canopy inlet pairs. On this scale, the above canopy gradients are difficult to see, but are plotted for comparison to the below canopy gradients. A plot for the above canopy pair only will follow. Below the canopy, larger gradients for both gases in the summer and fall indicate more intensive ecosystem cycling; however, significant gradients persist into the winter and spring for both gases. Below the canopy, H_2 and CO_2 gradients are nearly always positive and negative, respectively indicating soil uptake and respiration.

contrast, a traditional GC-RGD system with 10x poorer precision would lose over 60% of the measurements compared to the GC-HePDD system to an inability to resolve the below canopy gradient. The quantifiable gradients in both cases may occur during stagnant periods with low turbulence, and reliable fluxes cannot be calculated under those conditions.To study the temperate forest ecosystem as set out by the goals of this study, the entire forest canopy should also be included in the flux-gradient measurements. Therefore, an above canopy gradient was measured, and being much farther from the soil sink, the improved GC-HePDD precisions was critical for resolving gradients at that location.

Figure 3-12 demonstrates the size of the above canopy gradients of H_2 (ppb/m) and CO_2 (ppm/m) relative to the 1σ minimum detectable gradient (*mdg*) time series, which is based on instrument precision. Clearly, the *mdg* is a severe restriction on the measured above-canopy H_2 gradients, especially when ecosystem uptake is reduced in winter and spring. For systems using traditional H_2 detectors, the *mdg* would have been an order of magnitude larger and instead of 73% of H_2 gradients being below the *mdg* with the GC-HePDD, 97% of gradients would be lost with the traditional GC-RGD system. Even above the canopy, turbulence can be too low to confidently calculate a gradient, and this may be be a limitation even for the GC-HePDD system. The CO_2 gradient is above the *mdg* for most of the time series. The above canopy gradients identify H_2 and CO_2 soil respiration as the dominant process for the spring and winter. Positive and negative CO_2 gradients in the summer indicate the additional presence of photosynthetic uptake in the summer and fall

3.2 H_2 flux calculation methodology

Fluxes of H_2 can be calculated from direct H_2 concentration gradient measurements and inferred measures of atmospheric turbulence, which were derived from one of the three methods described conceptually in Section 1.2: 1) the eddy covariance flux and concentration gradient of CO_2 or H_2O, 2) the sensible heat flux and the temperature gradient, or 3) a K-theory parameterization. The first two methods are direct, where

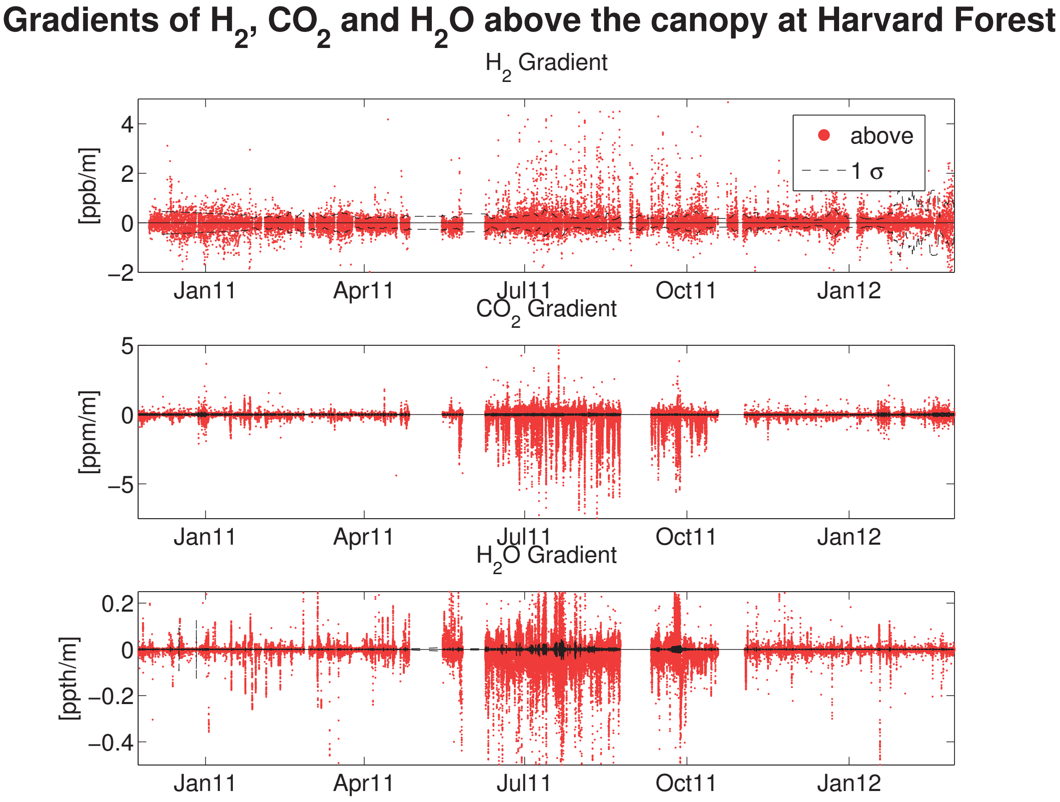

Figure 3-12: Vertical mole fraction gradients of H_2 (ppb/m) and CO_2 (ppm/m) for the above (red, 28 m - 24 m) canopy inlet pairs. The 1σ minimum detectable gradient (*mdg*) (dashed black line) is a severe restriction on the measured above canopy H_2 gradients, especially when ecosystem uptake is reduced in winter and spring. For systems using traditional H_2 detectors, the restriction would have been an order of magnitude worse, and almost no above canopy H_2 gradients would have been detected. The CO_2 gradient is above the *mdg* for most of the time series. The above canopy gradients identify H_2 and CO_2 soil respiration as the dominant process for the spring and winter. Positive and negative CO_2 gradients in the summer indicate the additional presence of photosynthetic uptake in the summer and fall.

the flux density and the vertical gradient of one scalar (trace gas or heat) is used to determine the eddy exchange coefficient for another scalar (H_2). The third method is an indirect energy balance method. Each approach brings its own advantages and limitations, which are discussed here. These methods are used to calculate the atmospheric H_2 fluxes discussed in the remainder of this chapter.

3.2.1 Hydrogen fluxes from CO_2 and H_2O eddy fluxes

In an analogy to Fick's laws for molecular diffusion, flux-gradient theory states that conservative fluxes of gas molecules are proportional to their mole fraction gradient and a coefficient, K, that depends on the intensity of turbulent mixing over time intervals appropriate to the scale of the process (Dunn, 2006; Baldocchi et al., 1995; Goldstein et al., 1996; Goldstein, 1998). In contrast to the molecular diffusion coefficient in Fick's first law that can be derived from first principals, the turbulent mixing coefficient K cannot and must be inferred or parameterized. The diffusion coefficient is denoted K_C for the trace gas fluxes of H_2, CO_2, and H_2O shown in Equations 3.1, 3.2, and 3.3,

$$F_{H_2} = -K_C \times \frac{\Delta\chi_{H_2}}{\Delta z} \times \rho_n \tag{3.1}$$

$$F_{CO_2} = -K_C \times \frac{\Delta\chi_{CO_2}}{\Delta z} \times \rho_n \tag{3.2}$$

$$F_{H_2O} = -K_C \times \frac{\Delta\chi_{H_2O}}{\Delta z} \times \rho_n \tag{3.3}$$

where the vertical concentration gradient of a the mole fraction of chemical χ_S, is defined as $\Delta\chi_S/\Delta z = (\chi_S(z_2) - \chi_S(z_1))/(z_2 - z_1)$, where z is a vertical height and ρ_n is the molar density of dry air. Furthermore, the turbulent transfer coefficient (K) in a given time and space interval is assumed to be the same for all gases, which has been shown to be a reasonable assumption for CO_2 and H_2O at Harvard Forest in the past (Goldstein et al., 1996). For this to be valid, care should be taken to ensure that trace gas species do not have significantly different distributions of sources and sinks in the region of the measurement.

It follows that a trace gas with a directly measurable flux can be used to determine K for the calculation of fluxes of gases that lack direct flux measurement techniques. We will designate the turbulent coefficient determined using CO_2 or H_2O as the comparative gas as K_C, to distinguish it from its derivation using sensible heat or K-theory in the next sections. K_C can be solved for directly (Equations 3.2 and 3.3), but most often it is used implicitly as in Equations 3.4 and 3.5.

$$F_{H_2} = F_{CO_2} \times \frac{\Delta\chi_{H_2}}{\Delta\chi_{CO_2}} \tag{3.4}$$

$$F_{H_2} = F_{H_2O} \times \frac{\Delta\chi_{H_2}}{\Delta\chi_{H_2O}} \tag{3.5}$$

Fluxes of CO_2 and H_2O (F_{CO_2} and F_{H_2O}) are measured in the forest by eddy covariance by Harvard's Wofsy-Munger Group and are reported every 30 minutes. Gradients of H_2 and CO_2 are measured by the flux-gradient system (Chapter 2) every 8 and 2 minutes, respectively, after being physically averaged in the integrating volumes.

3.2.2 Hydrogen fluxes from sensible heat

Sensible heat is another flux-gradient comparative quantity that can be used to determine the H_2 flux (Goldstein et al., 1996; Dunn, 2006; Dunn et al., 2009; Meyers et al., 1996; Liu and Foken, 2001). The sensible heat gradient is determined from high precision measurements of ΔT using the aspirated temperature shields described in Chapter 2 of a custom design as described in Dunn (2006). The flux-gradient equation for the sensible heat flux (H) is given by Equation 3.6,

$$H = -K_H \times \frac{\Delta T}{\Delta z} \times \rho_m \times c_p \tag{3.6}$$

where ρ_m is the mass density of dry air (using the specific gas constant for air:

R_{air} = 287.058 J kg^{-1} K^{-1}) and c_p is the specific heat of air for constant pressure (1.012 J g^{-1} K^{-1}). In this case a modified Bowen ratio technique is used to determine the sensible heat flux from the buoyancy flux (virtual temperature flux) measured by the sonic anemometer by correcting for the effects of water vapor (Liu and Foken, 2001). Following Dunn (2006), the crosswind term in the correction of the buoyancy flux was excluded because it should be small compared to the other terms in the equation for the sensible heat flux, H,

$$H = \rho_m c_p \overline{< w'T' >_C} = \frac{\rho_m c_p \overline{< w'T'_s >}}{1 + (0.51\overline{T}c_p)/(\lambda B_o)} \tag{3.7}$$

where a time series for any given measured quantity x can be described as: $x = \overline{x}$ + x', if $\overline{x}$ is the average value over some interval (in this case ∼30 minutes) and x' is the deviation in time at each data point from that mean value. The covariance of a time series of deviations, say of vertical wind speed (w') and sonic temperature (T'_s), is calculated for all data points and then averaged into the same 30 minute intervals to yield average covariances, such as the sonic heat flux: $\overline{< w'T'_s >}$. The transformed sonic derived heat flux is represented by $\overline{< w'T' >_C}$. Additionally, λ is the latent heat of vaporization of water (2.26 J/kg) and B_o is the Bowen ratio, which is the ratio of the sensible to the latent heat flux, $H/\lambda E$. The Bowen ratio can be computed using finite differences assuming similarity between the eddy diffusivities of heat and water vapor as shown in Equation 3.8,

$$B_o = \frac{H}{\lambda E} = \frac{c_p \Delta T}{\lambda \Delta q} \tag{3.8}$$

where q is specific humidity (g H_2O / kg air). Substituting Equation 3.8 into 3.7 yields Equation 3.9,

$$H = \frac{\overline{< w'T'_s >}}{\Delta T/\Delta z + 0.51\overline{T}\Delta q/\Delta z} \times \frac{\Delta T}{\Delta z} \times \rho_m \times c_p \tag{3.9}$$

which now resembles the flux-gradient relationship for H (Equation 3.6), and can be used to solve for the turbulent transfer coefficient K_H:

$$K_H = -\frac{\overline{< w'T_s' >}}{\Delta T/\Delta z + 0.51\overline{T}\Delta q/\Delta z} \tag{3.10}$$

The flux of H_2 can then be determined using K_H in Equation 3.11. The turbulent transfer coefficient (K) in a given time and space interval is assumed to be the same for all trace gases and sensible heat, which has been shown to be a reasonable assumption (agreeing within 12 ± 10%) at Harvard Forest in the past (Goldstein et al., 1996).

$$F_{H_2} = -K_H \times \frac{\Delta H_2}{\Delta z} \times \rho_n \tag{3.11}$$

3.2.3 Hydrogen fluxes from K-theory

The friction velocity, u_*, is related to the surface shearing stress, τ, that is caused by horizontal wind ($u_*^2 = \tau/\rho$) (Baldocchi, 2012). The friction velocity can be calculated from 3D sonic anemometer measurements of momentum fluxes $\overline{u'w'}$ and $\overline{v'w'}$ by Equation 3.12.

$$u_* = (\overline{u'w'}^2 + \overline{v'w'}^2)^{\frac{1}{4}} \tag{3.12}$$

As given by Equation 3.15, the eddy transfer coefficient can be approximated from the friction velocity and the von Kármán's constant, k, a constant of proportionality with an estimated value of $k \simeq 0.35$ (Pielke Sr., 1984; Businger et al., 1971; Baldocchi, 2012). The method assumes that shear of the mean wind is the source of turbulent eddies, with an approximate length scale of kz, and does not apply when buoyancy production of turbulent kinetic energy is non-negligible.

$$K = k\, u_*\, z \tag{3.13}$$

At this time, the this K-theory method will be used to calculate K for the below canopy H_2 fluxes in this thesis as shown in Equation 3.14.

$$F_{H_2} = -K \times \frac{\Delta H_2}{\Delta z} \times \rho_n \tag{3.14}$$

A potentially superior method (Cheng-I Hsieh, personal communication) for parameterizing K below the canopy is based on an equation for flux covariance of a scalar c (assuming near neutral thermal stratification):

$$\overline{w'c'} = \frac{-\overline{w'^2}}{\tau}\frac{\partial \overline{c}}{\partial z} - \frac{\partial \overline{w'w'c'}}{\tau \partial z} \tag{3.15}$$

given by Baldocchi (2012). The first right-hand-side (RHS) term is equivalent to the RHS of Equations 3.1 through 3.3. If the second RHS turbulent transport term can be neglected, it follows that K can be determined from:

$$K = \frac{\overline{w'^2}}{\tau} = \frac{\overline{w'^2}}{\rho u_*^2} \tag{3.16}$$

Large concentration gradients below the canopy that arise from soil-atmosphere trace gas exchange may dwarf the second RHS term, making Equation 3.16 a valid parameterization method. The $\overline{w'w'c'}$ term is not measured in this study for H_2, but the size of that second RHS term as calculated using the sonic temperature could be compared to the magnitude of the sonic heat flux to diagnose periods when this parameterization is valid. Calculations are currently being made to apply this second K-theory parameterization, but are not ready at this time.

The calculation of gradient-diffusion below canopy fluxes has been shown to fail (Baldocchi et al., 1988; Denmead and Bradley, 1983; Raupach, 1981). Counter- or zero-gradient fluxes are often observed below the canopy, which may be driven by sporadic and large-scale invasion of transporting eddies, which cause the failure of traditional flux-gradient relations. In our study, we use integrating volumes to physically average the measured samples, which may average over some of these eddy transport events. In the future, the validity of the below canopy flux calculations will be investigated by calculating larger averages and by comparing the below canopy, above canopy, and storage terms to determine whether they balance.

3.2.4 Comparison of methods

The performance of the three H_2 flux calculation methods are compared in this section in two example periods to determine which methods are appropriate for part or all of the study period.

Summertime above canopy fluxes

First, fluxes above the forest canopy are compared. At this location, only the trace gas similarity method is applied. The temperature shields required for the sensible heat similarity method were not operational in the summer and fall, and low concentration and temperature gradients make the method difficult to apply in the winter and spring. K-theory requires large concentration gradients in order to neglect the turbulent transfer term (Baldocchi, 2012). As was shown in Figures 3-11 and 3-12, gradients above the canopy tend to be much smaller than below the canopy.

The trace gas similarity method can be tested between CO_2 and H_2O before being applied to calculate H_2 fluxes. The flux of CO_2 can be calculated from the CO_2 gradient by inferring K from the H_2O flux and H_2O gradient (denoted *via* H_2O). Likewise, the flux of H_2O can be calculated from the H_2O gradient by inferring K from the CO_2 flux and gradient (denoted *via* CO_2). The results of these calculations are compared to the directly measured eddy fluxes in Figure 3-13 in four hour of day (hod) intervals (hod: 1-7, 8-13, 13-18, 19-1) averaged over the 2011 summer (June 15 - September 15). Average fluxes are calculated two ways: 1) by calculating 30 min fluxes first, and then aggregating summertime averages (Flux 1st) of 2) by calculating summertime average gradients and eddy fluxes first, and then calculating the similarity flux last (Flux last).

The eddy flux and flux-gradient similarity results for CO_2 and H_2O fluxes for the aggregated intervals shown in Figure 3-13 exhibit the same timing and in most cases the sign of the flux. The magnitudes are quite similar, but do not always lie within the 95% confidence intervals (calculated by student's t-test) shown. This agreement lends confidence to this method; if there is a true flux of H_2 above the canopy and

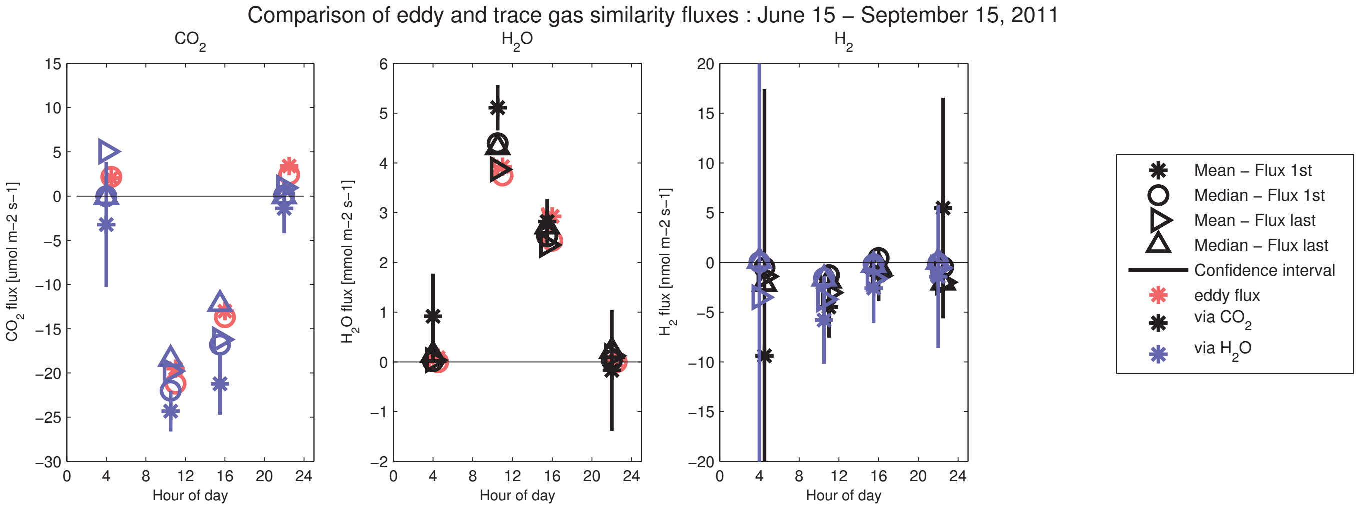

Figure 3-13: Summertime fluxes of H_2, CO_2, and H_2O above the forest canopy calculated by the trace gas similarity method compared to direct eddy fluxes. The flux of CO_2 can be calculated using the H_2O flux and gradient (denoted *via* H_2O). Likewise, the flux of H_2O can be calculated using the CO_2 flux and gradient (denoted *via* CO_2). Average fluxes are calculated two ways: 1) by calculating 30 min fluxes first, and then aggregating summertime averages (Flux 1st) of 2) by calculating summertime average gradients and eddy fluxes first, and then calculating the similarity flux last (Flux last). The results of these calculations are compared to the directly measured eddy fluxes in four hour of day (hod) intervals (hod: 1-7, 8-13, 13-18, 19-1) averaged over the 2011 summer (June 15 - September 15). The eddy flux and similarity results agree remarkably well as shown by the agreement of aggregated averages, which are often in or near the 95% confidence intervals (calculated by student's t-test).

the instrument signal-to-noise is sufficient, we should be able to detect the flux using the trace gas similarity method. Indeed, a statistically significant midday flux was detected for H_2 both *via* CO_2 and *via* H_2O as shown in Figure 3-13. The mean midday summertime flux of H_2 is calculated to be between -2 and -7 nmol m^{-2} s^{-1} by this method.

The time series of the 30-min CO_2 and H_2O fluxes calculated by the trace gas similarity method also agree well with the eddy flux time series (not shown). Calculated H_2 fluxes are much noisier due to the low signal-to-noise ratio of its above-canopy gradients; therefore only aggregated fluxes will be shown like in Figure 3-13. Above canopy concentration H_2 gradients are often close or below the estimated minimum detectable gradient (*mdg*, discussed in Section 2.2.1), while the concentration gradients of CO_2 and H_2O are typically well above the *mdg* (Figure 3-12).

Wintertime below canopy fluxes

The second comparison will focus on below canopy fluxes in the wintertime. No CO_2 or H_2O eddy flux data are available below the canopy, so the trace gas similarity method cannot be directly applied to the below canopy gradient set. This comparison is performed in the winter because during both winters the temperature shields were operational and the sensible heat similarity method can be tested. The K-theory method is the only applicable method below the canopy for the entire study period.

Figure 3-14 is a comparison of the H_2 fluxes calculated by the sensible heat similarity and the K-theory methods for January 1 through March 1 for the 2010-2011 winter. The sensible heat similarity fluxes yield more variable results, which is likely a result of two factors: 1) the uncertainty in the bias between temperature gradient shields (was measured infrequently) is large with respect to the actual gradients and 2) low heat fluxes in the wintertime (unfortunately the only period when the temperature shields were working) are difficult to measure. Both methods exhibit similar diurnal patterns of H_2 uptake over the winter period, and lower H_2 fluxes are calculated using the sensible heat method.

We cannot distinguish which method is superior from this simple analysis; a de-

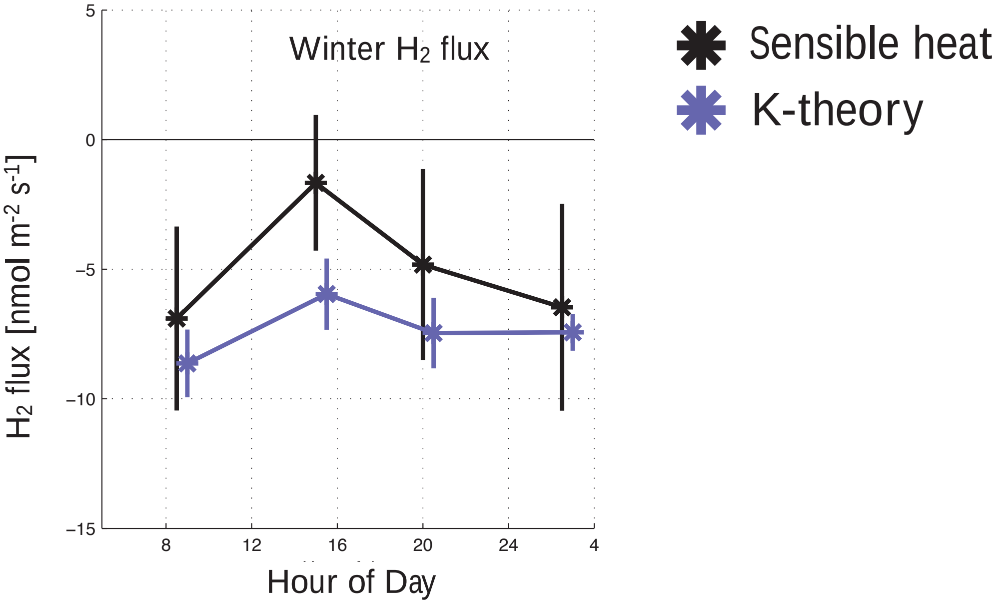

Figure 3-14: H_2 flux by hour of day calculated by two methods: the sensible heat similarity below canopy flux method and the K-theory below canopy flux method. These three calculated fluxes are compared for January 1 through March 1 for the 2010-2011 winter.

tailed analysis of the above canopy eddy flux, storage, and below canopy flux methods should be performed for CO_2 to determine whether the K-theory or sensible heat method is superior. The better method can then be used to calculate H_2 fluxes. Given the available data, however, only the K-theory method can be applied over the entire data set. For the remainder of the analysis, the below canopy fluxes will be calculated using K-theory with the understanding that a more detailed analysis of the method will be performed to ensure the method can be suitably applied before publishing below canopy fluxes.

3.3 Annual H_2 fluxes at Harvard Forest

In this section, annual H_2 fluxes at Harvard Forest are presented using the methods that were tested in Section 4.4.2. Aggregated above canopy fluxes (trace gas similarity method, Section 3.2.1) will be presented for the summer and fall seasons; the low signal-to-noise ratio of concentration gradients above the canopy requires a large amount of averaging for those data. In contrast, a high-frequency (30 min interval) below canopy flux time series can be calculated (K-theory method, Section 3.2.3) and is presented below.

The seasonality of the summer and fall CO_2 and H_2O fluxes measured above the canopy are shown in Figures 3-15 and 3-16, respectively. CO_2 fluxes reflect photosynthetic uptake (negative flux) from the canopy during mid-day and ecosystem respiration at night (positive flux). H_2O fluxes are driven by evapotranspiration, both driven by solar radiation in mid-day. The fluxes reflect that similar processes occur for both gases in the summer and fall, and flux magnitudes decrease from summer to fall.

As was shown in the last section, the eddy flux of CO_2 and H_2O and their fluxes derived from the trace gas similarity method agree quite well in terms of the timing and sign of the diurnal flux. A scaling issue arises in the CO_2 flux comparison, which could be due to slight offsets in the calibration scales between the different CO_2 analyzers or may be due to differences in filtering before aggregation applied to each

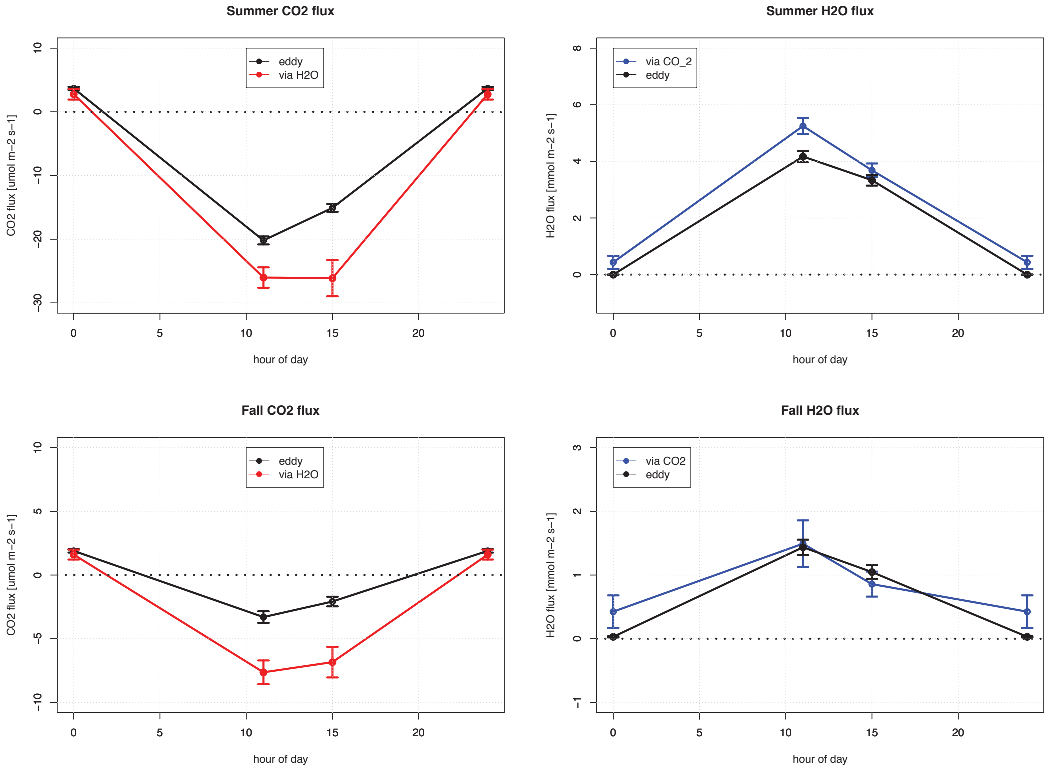

Figure 3-15: Fluxes of CO_2, and H_2O above the forest canopy (26 m) calculated by the trace gas similarity method compared to direct eddy fluxes for Summer and Fall in hour of day intervals (hod: 9-13, 13-15, 20-4). Mean fluxes and the 95% confidence intervals calculated using by Student's t-test are shown. The eddy flux measurements (black) are compared to fluxes derived using the trace gas similarity method with either CO_2 as the correlative variable (blue) or H_2O as the correlative variable (red).

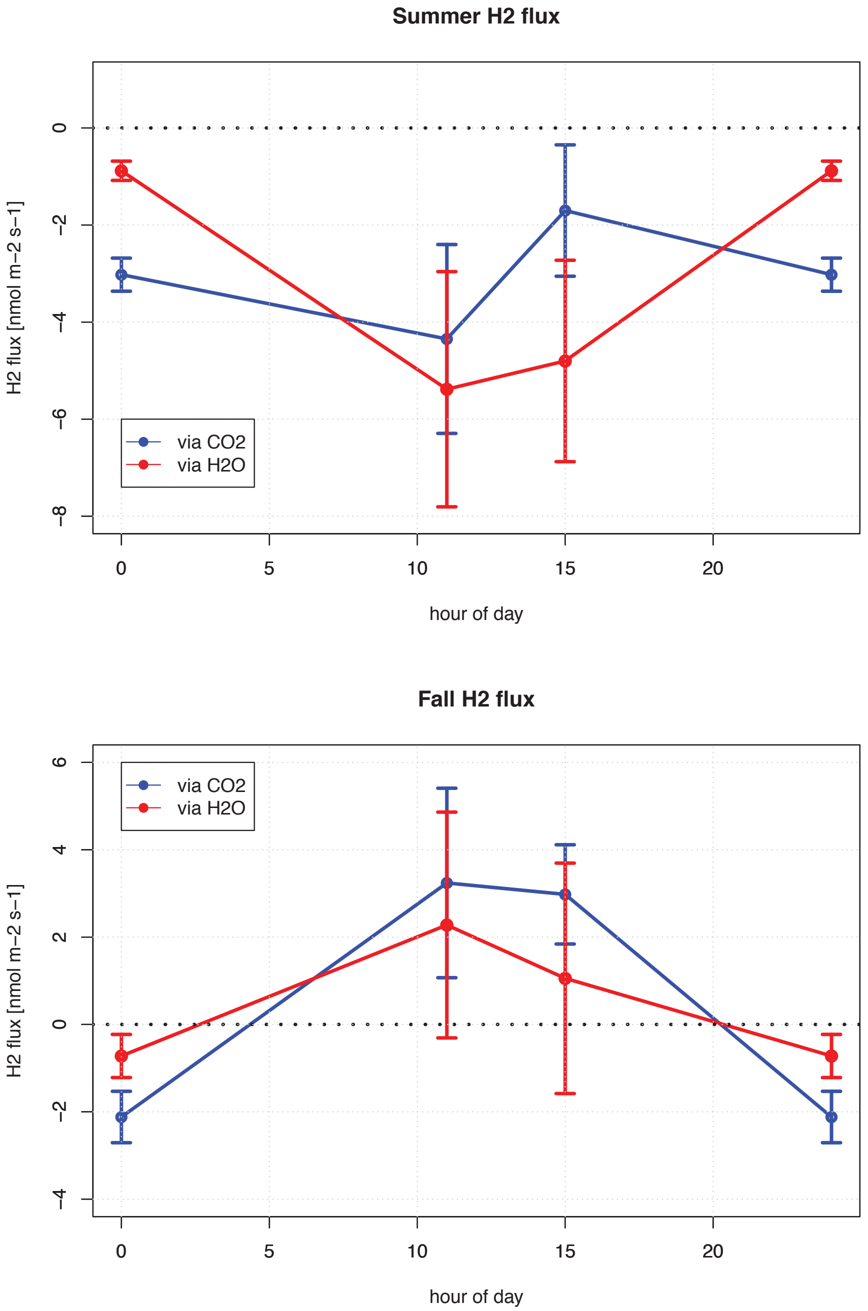

Figure 3-16: Fluxes of H_2 above the forest canopy (26 m) calculated by the trace gas similarity method for Summer and Fall in hour of day intervals (hod: 9-13, 13-15, 20-4). Mean fluxes and the 95% confidence intervals calculated using by Student's t-test are shown. The data show that ecosystem H_2 uptake dominates in the Summer and emissions dominate in the Fall.

data set. This reason is being investigated at this time. However, in general the trace gas similarity method performs very well above the canopy and we can be confident that the timing, sign, and approximate magnitude of H_2 fluxes calculated above the canopy are valid. The ability to compare the H_2 flux calculated using both CO_2 and H_2O also provides confidence in the method.

The summer and fall above-canopy fluxes calculated for H_2 are shown in Figure 3-16. In the case of H_2, the data show that ecosystem H_2 uptake dominates in the summertime. Uptake appears to increase slightly in the daytime and more constant fluxes are observed at night. We anticipate some "storage" of H_2-depleted air beneath the canopy during stable nighttime periods that may suppress the measured above canopy H_2 flux, which will be calculated before publication of the flux results.

Quite unexpectedly, the fall data indicate that H_2 emissions from the forest dominate midday H_2 fluxes from the Harvard Forest ecosystem. This feature is robust in the flux data regardless of the hour of day bins selected for aggregation or the filtering criteria applied to the flux data. The H_2 ecosystem exchange reverses to H_2 uptake again at night, which indicates that the daytime emission process are somehow related to temperature or solar radiation. During this period, below canopy H_2 fluxes are dominated by soil uptake (shown later in this section), so the H_2 emission processes would have to be located somewhere within the forest canopy.

Looking more closely at the Summer H_2 fluxes, apparent uptake in the 13:00 - 17:00 bin appear to decrease relative to the 9:00-13:00 bin, although the trend is not statistically significant within the 95% confidence intervals. This could indicate that H_2 emission processes also occur in the summer, but either at a reduced rate or are offset to a greater degree by H_2 soil uptake in the summer than in the fall when we will find that soil uptake is lower. Correlations with environmental data and potential mechanisms will be discussed in Section 3.4.

A few potential mechanisms may be the cause of H_2 emissions from the forest canopy during the fall. Photo-thermal degradation of organic matter has been shown to be a potential emission source for atmospheric H_2 (Lee et al., 2012; Derendorp et al., 2011). Additionally, these emissions in late September and early October during warm spells (17-30°C) may co-occur with hardwood leaf senescence, which could be a source for many organic compounds, and may be a source of H_2. Leaf senescence is a tightly regulated programmed cell death process where the cellular materials (*e.g.*, chlorophyll, proteins, membrane lipids, and RNA) of leaves are catabolized and nutrients are remobilized to support the formation of seeds or other plant organs (Lim et al., 2007). Senescence is age-dependent and can be additionally triggered by environmental signals, including UV-B, O_3, nutrient limitation, heat or cold, drought, shading, pathogen attack, or wounding. Leaf senescence is correlated with a reduction in emissions of some trace gases, most notably isoprene (Fuentes and Wang, 1999; Monson et al., 1994), and emissions of other gases, such as C5 biogenic volatile organic compounds (Fall et al., 2001). Laboratory and field measurements using chambers on canopy leaves, stems, and trunks should be performed in the future to diagnose the origin of these H_2 emissions. Testing whether H_2 emissions are dependent upon light, temperature, or the timing of senescence could help pinpoint the mechanism.

Work is underway to further to unravel the underlying mechanisms driving the measured H_2 fluxes through correlations with environmental variables. For now, we can say that many of the expected correlations with environmental variables were observed in the above-canopy flux measurements, which is a unique finding of this thesis work that has not been observed by previous chamber-based studies or studies relying on model interpretations of mole fraction time series. The goal of this thesis to target the processes affecting the ecosystem-scale exchange of H_2 is perfectly suited to identify these sometimes subtle, but potentially important processes.

Time series of the below canopy fluxes are shown Figure 3-17. The below-canopy fluxes are representative of a smaller footprint than the above canopy measurements, and the below-canopy footprint is only sparsely covered by vegetation. The fluxes of CO_2, H_2O, and H_2 increase from low levels of exchange in the winter to the highest levels in the summer, as was observed from the above canopy fluxes. From the detail available in the below-canopy fluxes, we observed co-occurring episodic events in the H_2 and CO_2 fluxes, which may reflect a commonality between stimulation and suppression of the whole soil microbial community (reflected in CO_2 flux) and the

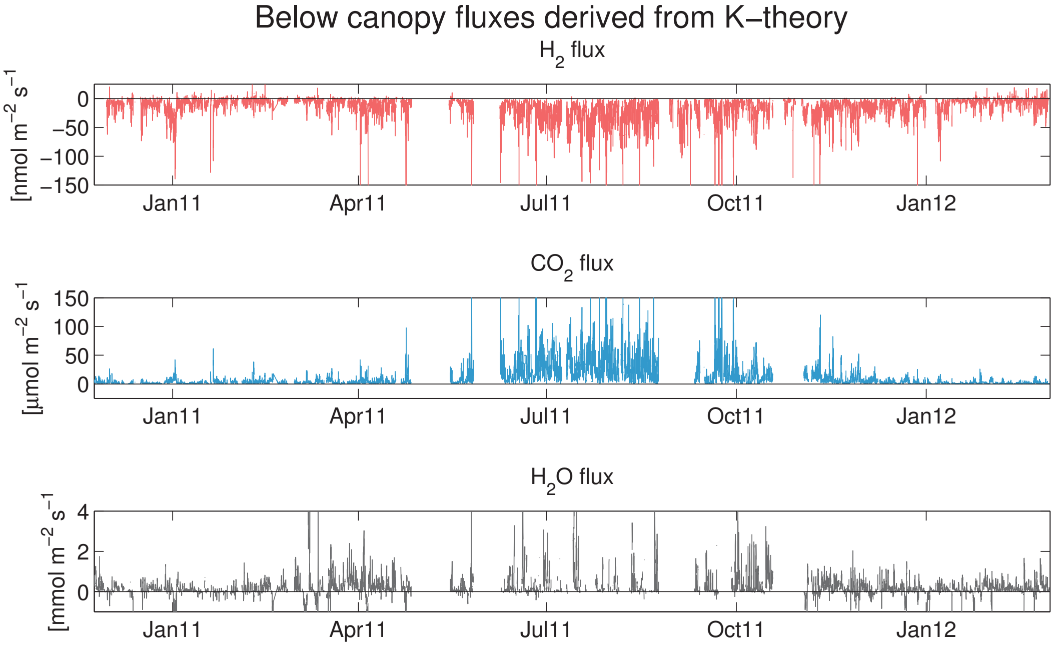

Figure 3-17: Time series of fluxes of H_2, CO_2, and H_2O below the forest canopy (2 m) calculated by the K-theory parameterization method compared to direct eddy fluxes for all seasons over the stay period.

H_2 consuming portion (reflected in H_2 flux). The H_2 soil sink exhibits a more consistent uptake rate throughout the seasons, whereas soil CO_2 respiration is highly concentrated during the growing season. CO_2 efflux combines the contribution from microbial respiration and the autotrophic respiration by plant roots. Furthermore, microbial respiration is influenced by substrate availability that is controlled by plant activity (*e.g.*, root exudates), and the phenology of microbial activity. On the other hand, the substrate for H_2 uptake is nearly constant throughout the year. An additional feature to note in Figure 3-17 is the episodic occurrence of H_2 emissions in the winter and spring, which may be tied to anaerobic processes that may occur during freeze-thaw cycles and snowmelt in those seasons.

Figure 3-18 shows the monthly below canopy fluxes for all three trace gases at Harvard Forest. The fluxes are significantly higher during the growing season for all three gases during the daytime, indicating a sensitivity to temperature and/or radiation. The time course of fluxes shown in Figure 3-18 indicates why it is difficult to measure above-canopy H_2 fluxes in any season except the summer and fall. Namely, H_2 fluxes maximize at an average of -25 nmol m^{-2} s^{-1} during the summer season By the fall season, H_2 fluxes have dropped to rates about 1/3 of the summer values, which makes their detection by the above-canopy method much more difficult to measure during the winter and spring. Given the expected temperature dependence of the enzymatic oxidation of H_2 by microorganisms, it is not surprising that uptake rates are largest in the summer. Indeed this temperature dependence has been shown in the lab (Smith-Downey et al., 2006) and in field observations (Constant et al., 2008a; Conrad and Seiler, 1985; Yonemura et al., 2000).

Soil CO_2 respiration has been quantified by chamber-based studies Savage and Davidson (2003, 2001) at Harvard Forest. The seasonal progression of the chamber-based respiration measurements agree well with qualitative features of the below-canopy fluxes presented in Figure 3-18; however, soil chamber studies report fluxes that are about 5 times lower on average. The authors report soil respiration rates between 100 to more than 400 mg C m^{-2} hr^{-1}, which corresponds to a range of approximately 2 to 13 μmol CO_2 m^{-2} s^{-1}. The mid-June to mid-August seasonal mean

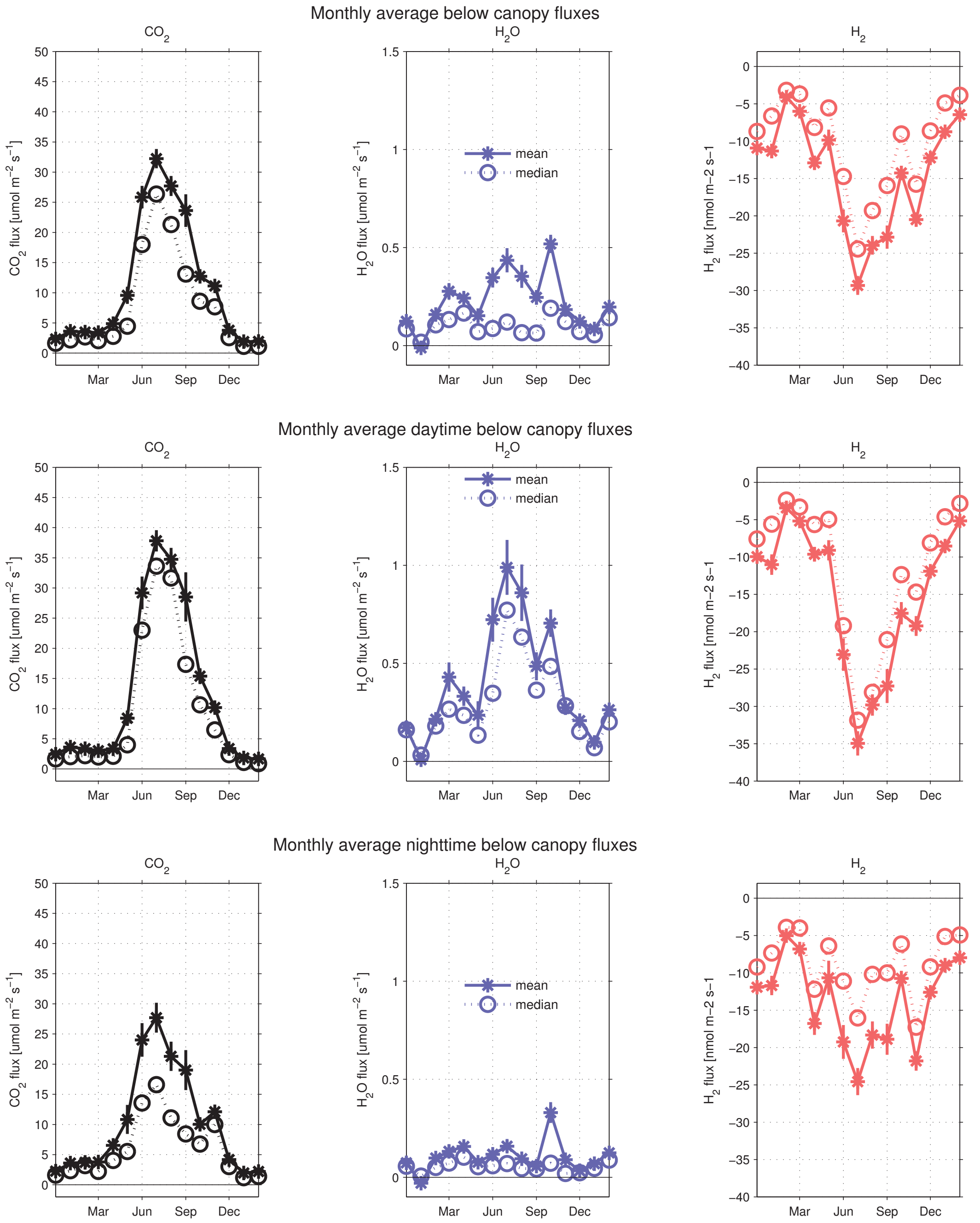

Figure 3-18: Monthly average mean and median fluxes of H_2, CO_2, and H_2O below the forest canopy (2 m) calculated by the K-theory parameterization method. Confidence intervals are indicated with vertical lines. The whole monthly average (upper plot) is split into daytime (6am to 6pm, middle plot) and nighttime (6pm to 6am, lower plot) averages. Growing season fluxes are significantly higher in the daytime indicating a sensitivity to temperature and/or radiation for all three gases.

was approximately 200 mg C m^{-2} hr^{-1} (4.6 μmol CO_2 m^{-2} s^{-1}). Another chamber study from Harvard Forest reports similar respiration rates, and observed a diurnal cycle in respiration peaking at 18:00 local time and reaching a minimum before daybreak with an amplitude of around 4μmol CO_2 m^{-2} s^{-1}. Although there may be biases associated with chamber measurements, the authors providing these estimates have studied these biases and presented methods for minimizing them in detail (Davidson, 2002). An additional source of the disagreement could be an overestimation of K by the K-theory parametrization, which is presently being investigated.

The rates of H_2 soil exchange calculated in this study can be compared to those measured at 2 m over a grassland in Quebec by Constant et al. (2008a). In that study, H_2 uptake was strongest in the summer and early fall. The mean H_2 exchange rate for soil temperatures (2-6 cm) between 10 and 20°C was -9 nmol m^{-2} s^{-1}, and the range of daily H_2 exchange rates was reported to range from approximately -80 to 180 nmol m^{-2} s^{-1}. In comparison, observed flux rates in this study over the same temperature interval (10 cm) were -17 nmol m^{-2} s^{-1}, and the range of 30-min H_2 exchange rates ranged from approximately -150 to 20 nmol m^{-2} s^{-1}. The Constant et al. (2008a) measurements indicate that some H_2 uptake persisted in the winter, at temperatures near the freezing point. Large H_2 episodic emissions are visible in the study data during early winter and in spring, which could be associated with anaerobic H_2 release. In fact, the mean H_2 exchange rate for soil temperatures (2-6 cm) between -10 to 0°C and 0 to 10°C were 2 nmol m^{-2} s^{-1} and 11 nmol m^{-2} s^{-1}, respectively, which indicate that cold-period H_2 exchange was dominated by emissions in the mean. The Harvard Forest soils at 10 depth never fell into the -10 and 0°C range, but the mean exchange rates were -10 nmol m^{-2} s^{-1} the 0 and 10°C range, indicating that soil uptake still dominated those temperature intervals in the mean.

This cursory comparison with the only available H_2 flux-gradient study (Constant et al., 2008a) indicates relatively good agreement. The uptake rates tend to be higher in Harvard Forest. Similar patterns of H_2 emissions in the winter and spring were observed between the two studies, but the emission rates were much more dramatic in Quebec. An increased duration (and likely depth) of frost in Quebec than in Harvard

Forest soils may have implications for the timing and duration of anoxia in the soils. Absolute mole fractions reported by Constant et al. (2008a) were very low: ∼270 ppb in the warm season. Even at 0.5 m at the Fall mole fraction time series minimum, the average Harvard Forest H_2 mole fractions were about 435 ppb. If there were problems with the calibration scale in that study, which used the traditional and nonlinear HgORD system, they may have propagated to the calculated concentration gradients and to the calculated H_2 fluxes. Given this uncertainty, the H_2 flux rates in this study agree well, and importantly we find agreement in the timing of H_2 uptake and emissions.

3.4 Environmental control on H_2 fluxes

In this section, H_2 fluxes are compared to environmental variables (air temperature, soil temperature, soil moisture, and wind speed) to identify potential factors of environmental control. This can be done on the ecosystem scale by considering aggregated above canopy fluxes, or with a focus only on soil-atmosphere exchange by exploring the below canopy flux data.

3.4.1 Environmental control on ecosystem-scale H_2 fluxes

Above canopy fluxes

Above-canopy fluxes have to be aggregated to overcome the level of noise in the measurements, as was done in Figures 3-16 and 3-15 for the seasonal averages. The data can be tested for statistically significant correlations with environmental variables, but the measurement noise can complicate this procedure. In this study, a multivariate analysis (R-project, glm generalized linear model) is performed to look for environmental factors that drive H_2 fluxes, which are detectable in the above-canopy fluxes.

From this analysis, we find that air temperature and soil temperature are statistically significant predictors of above-canopy H_2 fluxes. Specifically, the afternoon

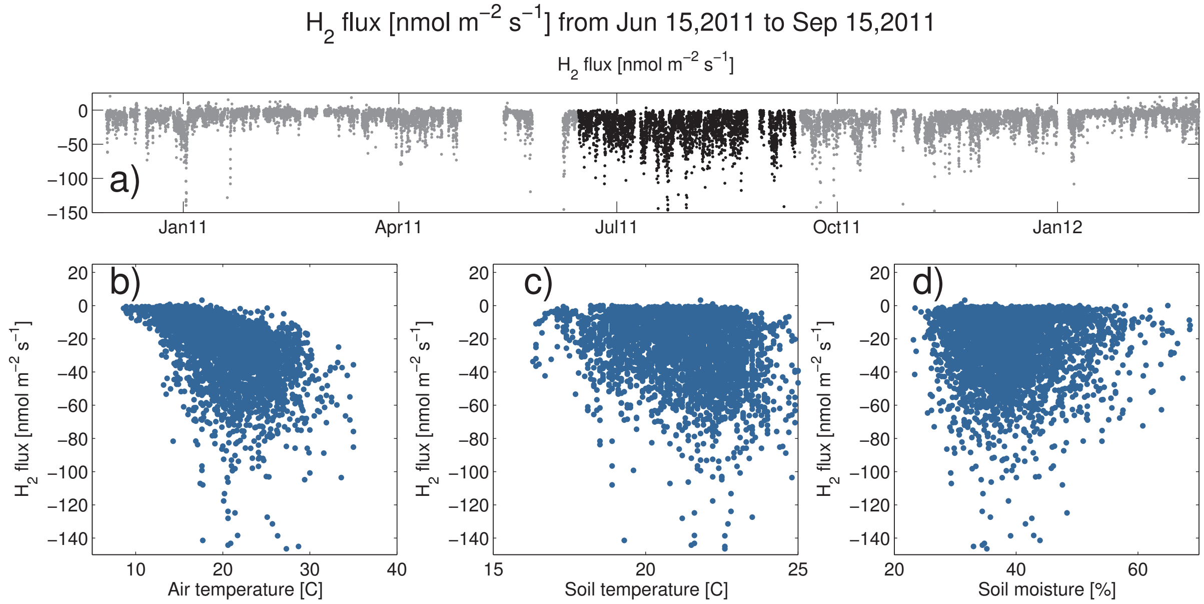

Figure 3-19: Below-canopy H_2 flux time series (a) in the 2011-2012 summertime period (black points) in comparison to the rest of the study period (grey points). Scatterplots of the summertime H_2 flux with air temperature (b), soil temperature (c), and soil moisture (c) in scatterplots. The summertime correlations of the below canopy H_2 flux with air temperature and soil temperature are significant (p=0). H_2 uptake increases with both soil and air temperature, and is more sensitive to air temperature changes (r=-0.53) than soil temperature changes (r=-0.21). No significant relationship to soil moisture was found when considering the entire summer.

(13:00-17:00) H_2 fluxes are correlated with air and soil temperatures (student's t-test, p<0.01) transitions within the 0°C and 17°C interval and the 15°C and 25°C interval. The preliminary analysis indicates a clear relationship with temperature and above-canopy H_2 fluxes. Soil moisture and wind speed were not found to be significantly descriptive of the H_2 fluxes above the canopy.

3.4.2 Environmental control on soil-atmosphere H_2 exchange

The below canopy fluxes can be used to diagnose environmental processes important for soil uptake of H_2. As an example, the influence of air temperature, soil temperature, and soil moisture on the summertime below canopy H_2 fluxes is plotted in Figure 3-19. A significant correlation between the soil H_2 uptake and air and soil temperature was found (p=0). H_2 uptake increases with both soil and air temperature, and is more sensitive to air temperature changes (r=-0.53) than soil temperature (10 cm) changes (r=-0.21). These correlations persisted even when considering only nighttime data. Similarly, the study by Constant et al. (2008a) found temperature to be the most significant factor influencing H_2 soil-atmosphere exchange over a grassland in Quebec. The higher sensitivity to air temperature than soil temperature at 10 cm depth is likely because the atmospheric H_2 consumption is thought to occur within the first upper few cm of the soil, which would be more coupled to air temperatures than soil temperature at 10cm depth, which will have a delayed and dampened temperature response to air temperature.

No significant relationship to soil moisture was found when considering the entire summer (r=0.02, p=0.3). Similar to the observation made for the temperature-dependency, it may be the soil moisture availability just in the upper few cm of soil that is important for atmospheric H_2 consuming organisms, whereas soil moisture sensors are typically buried deeper or are a measure of widespread soil moisture (as in the case of the COSMOS data shown in Figure 3-19).

The relationships between H_2 fluxes and temperature and moisture found in this analysis of below-canopy fluxes in the Summer has drawn very similar conclusions to the multivariate analysis of the above-canopy H_2 fluxes over the same period. Air and soil temperature are important predictors of H_2 fluxes, while a clear relationship with soil moisture has not yet been determined. Shorter time periods are being analyzed at the present time to look for episodic evidence for a soil moisture dependence. The data may need to be considered on shorter intervals. Currently, these below canopy fluxes are being explored using a multivariate statistical approach to quantify the variance in H_2 fluxes explained by different environmental factors.

3.5 Chapter conclusions

In this chapter, a new data set of H_2, CO_2, and H_2O mole fractions, gradients, and fluxes is presented. Three types of methods for calculating atmospheric fluxes from mole fraction gradients are presented and tested with the available data: a trace gas similarity method, a sensible heat similarity method, and a K-theory method. Above the canopy, the trace gas similarity method was shown to perform well for calculating CO_2 and H_2O fluxes when tested against concurrent eddy flux measurements. The above canopy flux of H_2 was calculated using the trace gas similarity method. Below the canopy, the sensible heat similarity and K-theory methods were compared. In general, the methods agreed quite well, although fluxes derived from sensible heat were highly variable as a result of the uncertainty in the temperature gradient measurements. The K-theory method was adopted because it was the only below-canopy method available over the entire study period. The below canopy fluxes provide a high-frequency picture of the seasonality of H_2 fluxes at Harvard Forest.

The calculated H_2 fluxes indicate that the Harvard Forest is a net H_2 sink, as was expected. This indicates that microbe-mediated soil uptake is the dominant process affecting atmospheric H_2 exchange at the forest. Interestingly, H_2 emissions were also periodically observed in the forest. Below the canopy, H_2 emissions occurred in winter and spring, which are likely tied to anaerobic production of H_2 during periodically anoxic soil conditions. Above the canopy, H_2 emissions dominate the fall midday H_2 exchange and may play a more minor role in summertime exchange as well. These emissions must originate from the canopy because concurrent below canopy fluxes are still strongly negative. Canopy emissions of H_2 would be a previously unrecognized source of H_2, which could potentially help explain the discrepancy in H_2 budgets produced from top-down and bottom-up approaches, where the latter have not considered canopy effects in the past (Ehhalt and Rohrer, 2009). The mechanism for canopy emissions is unknown, but may be tied to photo- or thermal-degradation of organic matter (Lee et al., 2012; Derendorp et al., 2011), leaf senescence (Lim et al., 2007; Fall et al., 2001), microbial processes occurring within or on trees (Covey et al., 2012), or some other unknown mechanism.

To contribute to the process-based understanding of H_2 ecosystem-atmosphere exchange, correlations with the calculated H_2 fluxes and environmental variables were tested. In the summer, the above- and below-canopy fluxes are correlated with air and soil temperature; H_2 uptake increases with temperature as should be expected for the a microbe-mediated enzymatic process and as has been shown in the lab and field before (Constant et al., 2008a; Smith-Downey et al., 2006; Conrad and Seiler, 1985; Yonemura et al., 2000). Summertime soil moisture was not found to have a significant influence on H_2 fluxes in the summer, which contrasts with previous work (Smith-Downey et al., 2008; Conrad and Seiler, 1985; Fallon, 1982; Conrad and Seiler, 1981). Currently, the correlation of H_2 fluxes with environmental variables are being tested in more detail, over different time scales and using additional environmental measurements than presented in the thesis so far. This data set is rich with process-based information that will be analyzed for inclusion in future publications and that can be used to test existing models of the H_2 soil sink.

Chapter 4

H_2 exchange through the snowpack

Objective

In this section, the soil-atmosphere exchange of H_2 and CO_2 is compared over two contrasting winters to investigate the sensitivity of microbe-mediated processes to changes in wintertime environmental forcing. Measurements were made over the 2010-2011 winter, which was cold and had a deep and enduring snowpack, and over the 2011-2012 winter, which was warmer and did not have a significant snowpack. As a result, the conditions in the soil, and thus the experience of the microbial community, differed greatly between the two years. In the first winter, soil temperature (>0 °C) and moisture were very stable beneath the snowpack, in the second winter, the soil microbial community community experienced frequent freeze-thaw cycles and liquid moisture inputs. In this chapter, H_2 and CO_2 fluxes are compared between the two winters. The influence of the physical properties of snowpack, such as depth, extent, and porosity, on trace gas exchange is explored. In addition, the influence of environmental factors, such as temperature, moisture, and frost on the activity of the soil microbial community and, in turn, on H_2 and CO_2 fluxes are explored. Wintertime trace gas fluxes are important to understand because they can contribute significantly to the annual ecosystem exchange and because wintertime conditions may be very sensitive to global change. The process-based findings of the mean and episodic nature of wintertime trace gas exchange at Harvard Forest may be extended to other sites and trace gases for studying questions relevant to global change.

Results

- Greater CO_2 and H_2 soil atmosphere fluxes were observed in the colder 2010-2011 winter with a substantial snowpack protecting the soil microbial community than the warmer, low-snow 2011-2012 winter.
- Freeze-thaw disturbance to the soil microbial community may have played a role in the reduced CO_2 and H_2 fluxes during the warmer, low-snow 2011-2012 winter.
- Wintertime H_2 uptake and CO_2 respiration are correlated with soil moisture and temperature.
- Trace gas fluxes through the snowpack increase with snow porosity, with decreasing snow area extent, and with wind-induced ventilation of the snowpack.
- Snowpack discriminates against first-order H_2 uptake more than soil CO_2 emissions because of the increased resistance of substrate (H_2) diffusion to the reaction site (soils).

4.1 Background information

Trace gas exchange between the atmosphere and the terrestrial biosphere is driven by microbial, plant, animal, and geochemical processes throughout the year. Many of these biogeochemical processes undergo a slowdown or complete cessation as cold-season temperatures drop below freezing; however, soil biological communities may be insulated from below-zero temperatures in areas with a wintertime snowpack. An enduring snowpack will often maintain soils at above-freezing temperatures and nearly constant moisture conditions. This low-temperature environment (0°C to a few °C) can host an active microbial community such that wintertime CO_2 respiration can significantly influence the annual carbon budget (Monson et al., 2006). In addition to soil respiration, other biogeochemical processes persist in the below-snow environment and a wide range of trace gases exhibit continued exchange between the soil and atmosphere through the porous snow matrix (Helmig et al., 2009). The uppermost layer of the snowpack may also foster photochemically-driven chemistry. The behavior of low-temperature soil biogeochemical cycling and the mechanisms dictating gas transport through the snowpack are required for interpretation of wintertime gas fluxes measured above the snowpack. Seasonal and annual snowpack affects large areas globally, for instance nearly one half of the Northern Hemisphere is snow covered in January during the maximum extent (Lemke et al., 2007). Widespread reductions in snow cover are expected over the 21st century of between 9 and 17% (for the somewhat modest B2 emission scenario) mainly driven by reductions in spring and late autumn/early winter snow cover (Lemke et al., 2007). Together, this means that trace gas cycling through snowpack is a widespread process anticipated to be highly susceptible to global change.

In this chapter, the influence of the Harvard Forest snowpack on the continued soil-atmosphere exchange of H_2 and CO_2 is investigated over two New England winters with very different meteorological forcings. First, a model of gas transport through the snow is described to aid the conceptual interpretation of the measurements. Second, observations of the snowpack using a novel snowcam method and measurements of the below-snow soil environment are presented. Third, wintertime flux measurements of H_2 and CO_2 are considered in terms of both their winter-long trends and episodic behavior. Finally, the sensitivity of the cycling of these two trace gases to the snow and soil conditions throughout the winter is considered.

4.2 Fluxes through the snowpack - framework and expectations

A conceptual framework for interpreting wintertime flux measurements above the snowpack is presented in this section, first, by presenting a model for trace gas diffusion through snow, and then by discussing the potential importance of the flux directionality (*e.g.*, uptake or emission) of a given trace gas. Finally, the expected influence of environmental factors from the literature are listed.

4.2.1 Diffusion of gases through the snowpack

A simple one-dimensional model based on Fick's first law of diffusion relates the flux, F, of trace gases (H_2 and CO_2) between the soil and atmosphere through the snowpack to their vertical concentration gradients dC/dz within the snowpack as shown in Equation 4.1,

$$F = -\rho_a \eta D \frac{dC}{dz} \tag{4.1}$$

where ρ_a is the molar density of air, η is the air-filled porosity of the snow, and D is the molecular diffusivity of a given trace gas in air, which for H_2 and CO_2 are 4.2×10^{-5} and 1.1×10^{-5} m^{-2} s^{-1}, respectively, at 273 K and 101.3 hPa (Helmig et al., 2009; Bowling and Massman, 2011). The snowpack is assumed to be inert (*i.e.*, no production or loss within the snowpack) with respect to these trace gases. In this simple representation, the rate of steady-state diffusion of trace gases through the snowpack will increase linearly with snow porosity, the molecular diffusivity of a given trace gas, and the concentration gradients.

Diffusion of these gases is enhanced above the the rate set by molecular diffusion (Equation 4.1) by pressure changes due to large-scale atmospheric dynamics (*e.g.*, synoptic scale fronts and gravity waves) and by wind interactions with the forest topography. The wind-driven process, known as pressure- or wind-pumping, has been thoroughly explored and described mathematically by Bowling and Massman

(2011) for the flux of CO_2 through the snowpack. The authors propose including an additional diffusive term, the wind-dependent enhanced diffusivity **K**, in the model equation to represent this small, but persistent enhancement to molecular diffusion as is shown in Equation 4.2.

$$F = -\rho_a \eta (D + K) \frac{dC}{dz} \tag{4.2}$$

The relative role of the wind-dependent enhanced diffusivity **K** to the molecular diffusivity was observed by Bowling and Massman (2011) to increase with windspeed, although a meaningful regression was not determined. Typical enhancements of diffusivity due to wind were around 11% over the winter, but were up to a 40% enhancement in the short term (*i.e.*, K/D ranged from $\sim$0 to 0.4).

In this study, Equations 4.1 and 4.2 serve as conceptual models to interpret the expected forcing of the variables that are measured, such as porosity and windspeed, on the fluxes measured at Harvard Forest. For example, we can expect a linear relationship between porosity and trace gas fluxes. The other variables in Equations 4.1 and 4.2 were not measured in this study, such as the concentration gradient across the snowpack and the tortuousity.

4.2.2 Bidirectional fluxes through the snowpack

The directionality of atmosphere-soil trace gas exchange across the snowpack may unequally affect emissions and uptake processes, Figure 4-1 shows an theoretical example of trace gas mole fraction profiles of H_2 and CO_2 within and above a forest snowpack. The snowpack is assumed to be inert to these trace gases as they exchange bidirectionally through the snowpack.

Soil emissions (*e.g.*, CO_2 respiration) drive positive fluxes out of the snowpack that can be measured in the overlying atmosphere. The rate of CO_2 production is governed by substrate and environmental conditions within the soil, and is independent of the accumulation of CO_2 within the snowpack (Figure 4-1: blue/black circle). The magnitude of the observed fluxes depends upon snowpack properties that influence

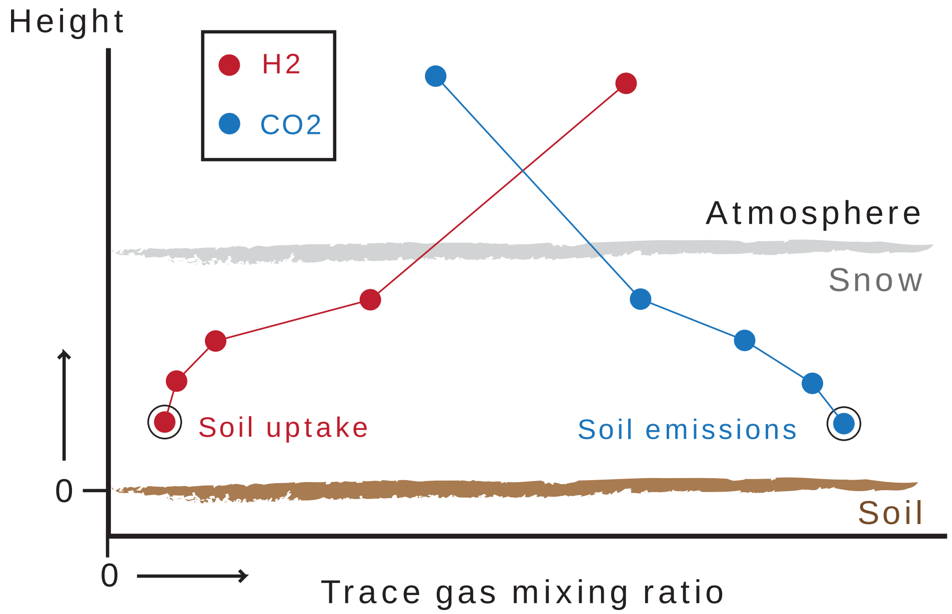

Figure 4-1: Conceptual schematic of trace gas mole fraction profiles of H_2 (red) and CO_2 (blue) within and above a forest snowpack (profiles adapted from general shape of data presented in Helmig et al. (2009)), which is assumed to be an inert environment for these trace gases. Black circles indicate mole fractions at the soil-snow interface.

diffusion (porosity, tortuosity, snow depth), on the molecular diffusivity of the gas, and the concentration gradient (Equation 4.1). Wind can enhance the diffusivity (Equation 4.2).

In contrast, the rate of H_2 uptake is a first-order loss process (Smith-Downey et al., 2006; Conrad, 1996; Conrad and Seiler, 1981) and is thus dependent upon the standing mole fraction of H_2 at the soil-snow interface, which is depleted (Figure 4-1: red/black circle) because of the concentration gradient that establishes across the snowpack diffusional barrier. Therefore, the flux of a gas with a soil sink (negative flux), like H_2, measured above the snowpack depends not only on factors affecting the resistance to diffusion of H_2 through the snowpack (porosity, tortuosity, snow depth, Equation 4.1) but also on standing H_2 mole fractions at the soil-snow interface.

In summary, the snowpack barrier impedes trace gas diffusion across the snowpack, which slows soil uptake processes whereas soil emission processes are largely unaffected. This discrimination against H_2 uptake relative to CO_2 respiration will be explored in the data set over the two winters covered in this study.

4.2.3 Expected environmental correlations

The sensitivity of wintertime H_2 fluxes to changes in temperature around the freezing point are expected to be high based on the lab measurements by Smith-Downey et al. (2006). They found that boreal forest soil H_2 uptake occurs down to -4°C, uptake increases with temperature, and the increase with temperature is steepest across the -4°C to 0°C transition. They did not find H_2 uptake to be a strong function of soil moisture except at very high (>55%) or low soil moisture levels (<10%). A chamber-based study in Finland found that H_2 uptake decreased with increasing snow depth and soil moisture, and increased with increases in soil and air temperature (Lallo et al., 2008).

An exemplary study of winter carbon cycling beneath snowpack by Monson et al. (2006) is used to build the set of expectations for our CO_2 soil respiration measurements. In that study, wintertime CO_2 respiration was highly sensitive to temperature, especially to small changes in soil temperature around the freezing point. The snowpack protected the soil microbial community during the winter. Enhancement of CO_2 fluxes by wind ventilation of the snowpack was observed. During snowmelt, snowpack porosity decreases and ice lenses can form, both of which impede the diffusion of trace gases through the snowpack. However, the authors found that any potential impediment to diffusion due to snowmelt was countered by the moisture input to the soils, which strongly stimulated soil respiration (Monson et al., 2006). Whether the moisture input stimulates respiration directly or indirectly by leaching carbon substrates from litter material is not resolved (Hirano, 2005).

The flux measurements at Harvard Forest over two very different winters will be analyzed with these expectations in mind. This study will be a novel contribution to our understanding of H_2 uptake in the winter and across snow, which is to date only sparsely represented in the literature by limited number of flux chamber measurements (Lallo et al., 2008) and flux-gradient measurements (Constant et al., 2008a).

4.3 Snowpack and soil properties-contrasting two winters of extremes

4.3.1 Methods

Snowcam observations - snow depth and area coverage

Snowpack depth and area coverage were quantified using webcam images of striped snow stakes and the below canopy environment at the EMS tower (data source: *Richardson A. 2008. Harvard Forest PhenoCam Images. Harvard Forest Data Archive: HF158*[1] Specifically HF158-02: EMS subcanopy images). The fraction of soil area covered by snow was determined by the number of white pixels in each webcam image. Snow stakes (PVC pipes, ∼10 cm diameter, painted with alternating 5 cm swaths of red and white) were distributed within the webcam field of vision in the Fall of 2010.

The snow-stake installation around the sub-canopy tower is shown in schematics for both the camera view and a bird's eye view in Figure 4-2. The camera view image is from the afternoon of January 14, 2011. The tower and snow stakes have been overlaid with cartoon renditions for ease of view in this schematic. The red stripes on each of the four snow stakes installed over that season are clearly visible from the webcam. The number of visible snow stake stripes in each webcam image is inversely proportional to the snowpack depth. Stripes are counted and averaged to determine a representative snow depth in the field of view. This *snowcam* approach was used to obtain snowpack information every 30 minutes during daylight hours over the 2010-2011 and 2011-2012 winters. This automated method avoids the person-hour cost and the snow disruption of manually measuring snow depth with a ruler.

To assess the fractional area covered by snow, pixel whiteness is assessed. This is done by combining vertical strips of pixels from each day of the winter season into a kymograph as is shown for the 2010-2011 season in Figure 4-3. Snow coverage is indicated by the degree of greyscale of a given pixel, where white is snow-covered and black is snow-free. A percent area coverage time series is obtained from the average

---

[1] http://harvardforest.fas.harvard.edu/data-archive

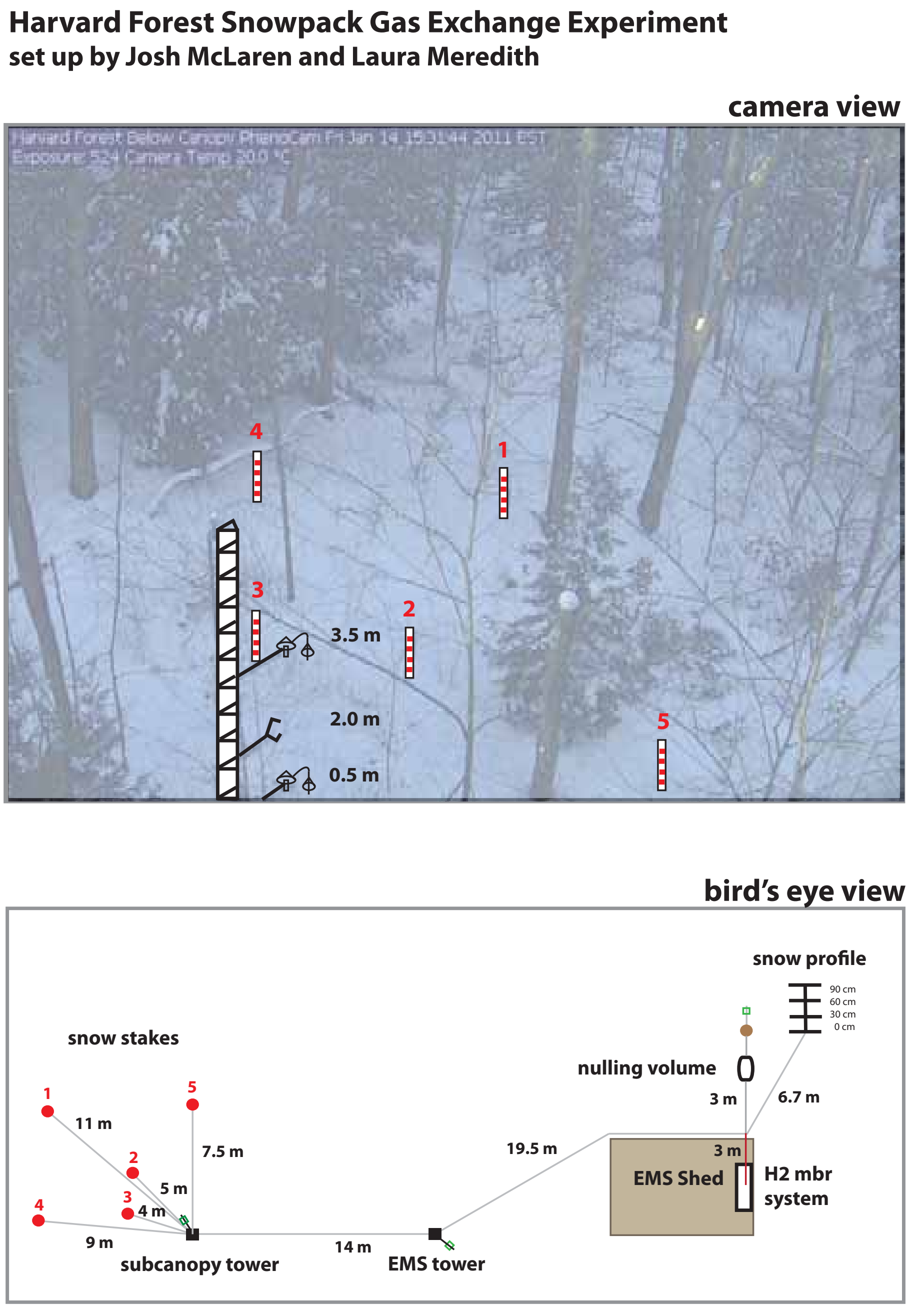

Figure 4-2: Harvard Forest snowpack gas exchange experiment installment. Example of a snowcam image (top) on January 24, 2011 with overlaid schematic of snow stake installation around the subcanopy tower. the snowcam is mounted to the main EMS tower and the small tower with the lower two H_2 and CO_2 inlets is in the field of view. Red and white painted snow stakes are used to determine snow depth, where each red or white stripe is 5 cm tall. A bird's eye view (bottom) of the snow-stake installation around the sub-canopy tower as well as the positioning of the subcanopy and EMS tower relative to the instrument shed.

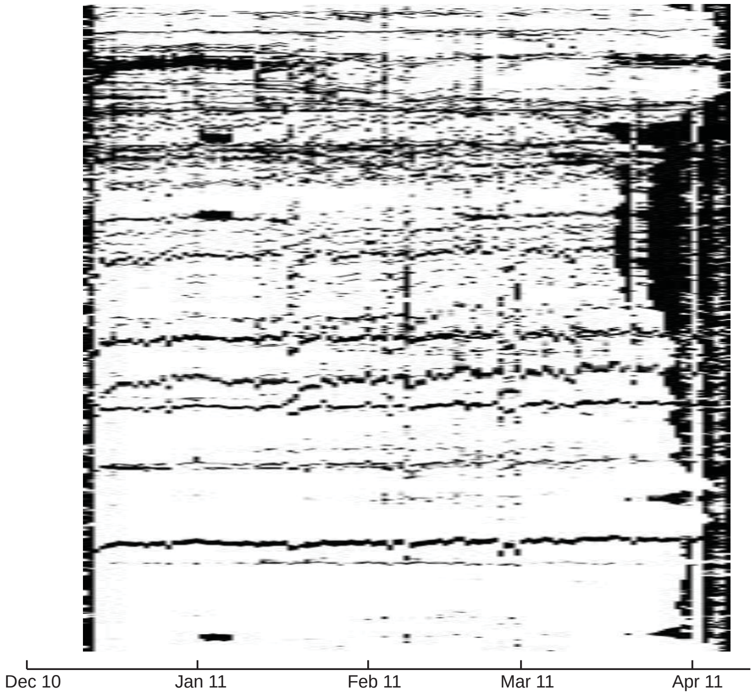

Figure 4-3: Kymograph of snow cover built from a series of vertical pixels from the snowcam image (y-axis) taken around 3pm for each day of the winter season (x-axis). The degree of greyscale indicates snow coverage, where white is snow-covered and black is snow-free. A percent area coverage time series is obtained from the average coverage over each vertical pixel layer.

coverage over each vertical pixel layer. The snow area coverage data are not presented in this thesis, but have been prepared and will be considered for a future publication.

Snow pillow measurements - snow mass

Continuous measurements of the water content (snow water equivalent) of the snowpack were available from Harvard Forest snow pillow data set (data source: *Boose E. 2009. Harvard Forest Snow Pillow. Harvard Forest Data Archive: HF155*[2]). A rubber snow pillow filled with propylene glycol and water is connected to a pressure transducer that measures the mass of the overlying snow every fifteen minutes. The snow pillow is located in the Prospect Hill Tract in a similar forest stand to the EMS tower (lat +42.53, long -72.19, 340 m a.s.l.). The snow pillow is not, however, co-

---

[2] http://harvardforest.fas.harvard.edu/data-archive

located with the snowcam observations, and snow water equivalent data can only be used to track qualitative trends in the snowpack.

Snow water equivalent (*swe*, centimeters) can be converted to a rough measure of snow porosity if the snow depth (*sd*) is known. The percent water-filled space is sd/swe*100%, and the percent air-filled space, or the porosity, is (1- sd/swe)*100%. In order to use these simple tools, we can only assume a single porosity for the entire snowpack. In reality, snow density will vary with depth depending on the freeze-thaw history of the snowpack and will vary in space because of topographic heterogeneity (Albert and Shultz, 2002). Although this measure of porosity is simplified, it can provide useful information about the influence of snowpack aging on trace gas diffusion. Fresh snow is very porous, allowing trace gas exchange. The snow pack becomes less porous (more dense) throughout the winter, especially when above-freezing air temperature anomalies drive snow melt. We expect to see an increased resistance to trace gas diffusion through the snowpack as the snowpack becomes more dense.

Soil and meteorological measurements

Two main data sources were used for soil and meteorological data: 1) the Harvard Forest Fisher Meteorological Station (data source: *Boose E. 2001. Fisher Meteorological Station (since 2001). Harvard Forest Data Archive: HF001*) and 2) unpublished EMS site data collected by the Munger and Wofsy group to be submitted to the Harvard Forest data archive. When available, air temperature and windspeed data were used from measurements made in this study, which are described in detail in Chapter 1. Data from the National Science Foundation supported COSMOS[3] soil moisture instrument deployed to Harvard Forest is used for the 2011-2012 winter because the measurement covers a larger area than can be accomplished with the temperature probes used in the other data sets.

---

[3] COSMOS data source: http://cosmos.hwr.arizona.edu/

Table 4.1: Contrasting properties of two New England winters of extremes

Mean	**Units, measurement depth**	**Months**	**Winter 1 (2010-11)**	**Winter 2 (2011-12)**
Air temperature	°C, 2.2 m (high)	DJFM	-3.6	0.9
Soil temperature	°C, 10 cm	DJFM	1.9	3.4
Soil temperature	°C, 10 cm	JF	1.6	1.5
Soil moisture	% volumetric, 15 cm	DJF	29.5	31.0
Soil moisture	% volumetric, 15 cm	M	33.0	30.5
Max snow depth	cm		70	15

4.3.2 Observations

The winters of 2010-2011 and 2011-2012, referred to henceforth as Winters 1 and 2, differed dramatically at Harvard Forest. This provides an opportunity to infer the meteorological, snowpack, and soil conditions that influence the magnitude, and possibly the sign, of wintertime trace gas fluxes of CO_2 and H_2. Table 4.1 summarizes the main meteorological differences between the two winters (comparison periods are indicated by the months in the table). Winter 1 air temperatures were significantly colder than Winter 2 (-3.6°C versus 0.9°C). Precipitation during Winter 1 fell predominantly as snow, which accumulated to a maximum snowpack depth of about 70 cm. As shown in Figure 4-4, a stable snowpack was present throughout Winter 1 (December 14 - April 7), whereas a shallow snow cover (defined in this analysis as snow < 25 cm) was only present during two short periods during Winter 2. The enduring Winter 1 snowpack aged throughout the winter as snow settling and melt events reduced the porosity and increased snowpack density (Figure 4-4). The snow measurements indicate that snowpack aging occurred slowly over most of the winter, but then rapidly during melt events from February through April, until complete snow melt in early April.

The presence of a substantial wintertime snowpack significantly affects the thermal and moisture properties of the underlying soil. First, snowpack insulates subniveal (below the snow) soils against wintertime air temperatures that can dip far below 0°C.

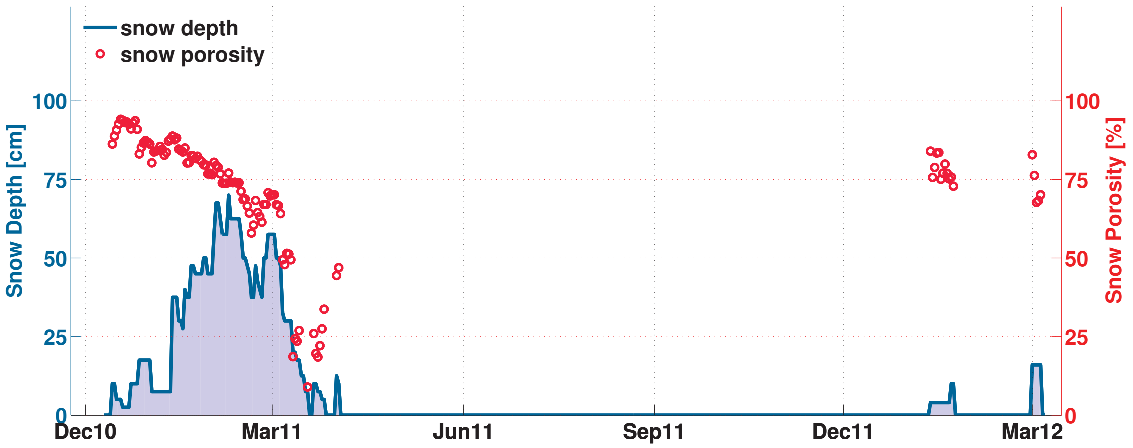

Figure 4-4: Snowpack depth (blue area) and porosity (red circles).

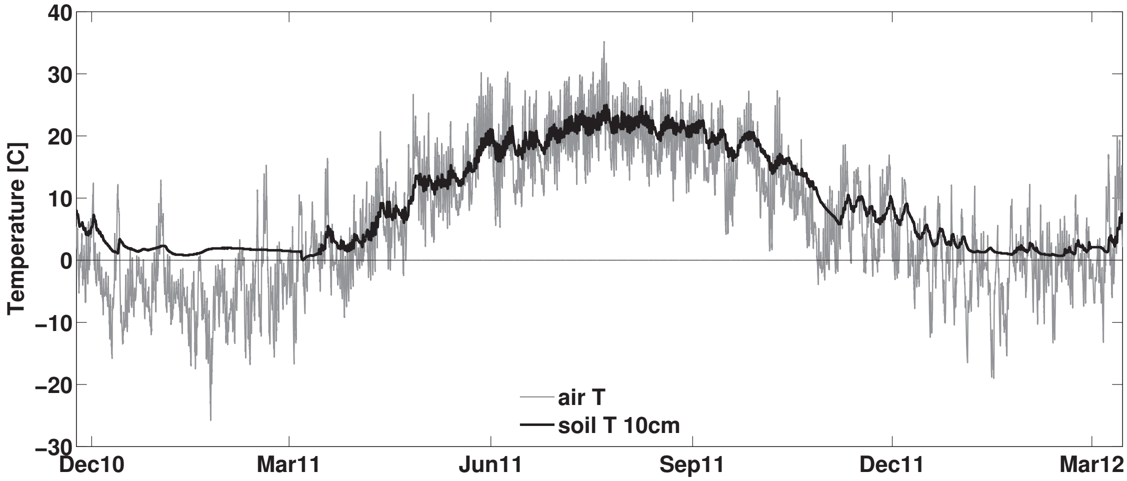

Figure 4-5: Air temperature (gray) and soil temperature at 10 cm depth (black).

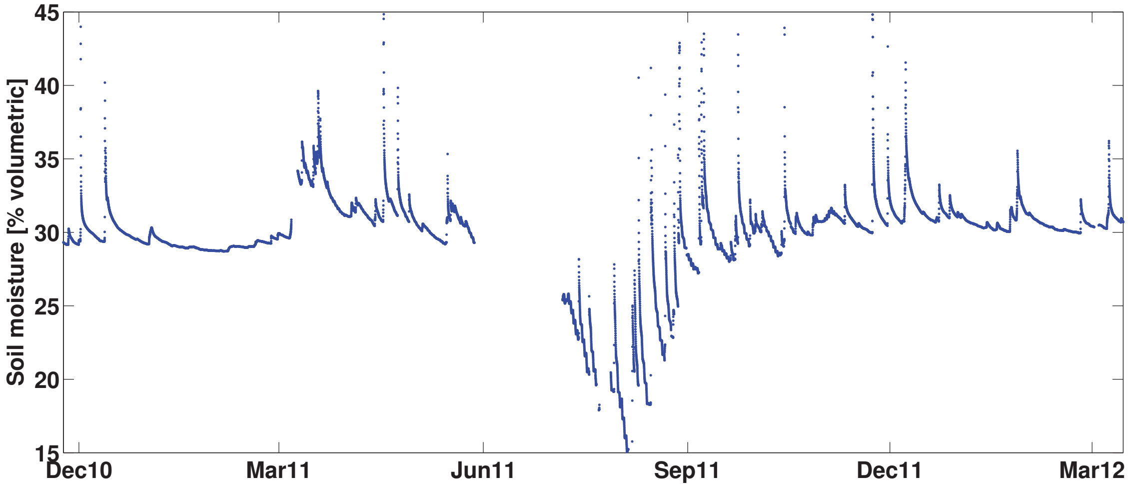

Figure 4-6: Soil moisture as a fraction of the water-filled space.

The insulating effect of snowpack is illustrated in Figure 4-5, which shows Harvard forest air and 10 cm soil temperatures over the study periods. Air and soil temperatures are coupled during snow-free seasons; soil temperatures exhibit a dampened temperature response to air temperature forcing. Air and soil temperatures become decoupled in the presence of even a modest snowpack. In this study, this decoupling is observed during Winter 1 between mid-December and March; air temperatures oscillate in response to synoptic weathers systems, whereas soil temperatures remain steady and above freezing (1.9°C at 10 cm depth) over the entire winter. Despite significantly colder Winter 1 air temperatures, mean soil temperatures were about the same for the two winters (Table 4.1) in January and February, during the period that Winter 1 had a stable and deep snowpack. The average December through March soil temperatures were colder in Winter 1, which were months without a significant snowpack (December) or with a declining, melting snowpack (March).

A second significant effect of the wintertime snowpack is on soil moisture levels. A time series of Harvard Forest soil moisture is shown in Figure 4-6. Precipitation during Winter 1 fell largely as snow. Thus, Winter 1 had limited liquid water input to the soil, and subniveal soil moisture levels remained steady until the onset of melt in March. The deep snowpack in Winter 1 kept soil moisture variability low during the wintertime period, and then led to a large moisture input in early spring as the snow melted as is shown in Figure 4-6. In contrast, Winter 2 experienced high soil moisture variability. Winter 2 precipitation events occurred both as rain, resulting in an instant soil moisture input, and as short-lived snow, resulting in only a short term moisture input delay. As a result, average soil moisture levels were slightly higher in Winter 2 for December through February (Table 4.1); however, March moisture levels were lower in Winter 2 because of the lack of snowpack input.

4.4 Gas fluxes over snowpack

4.4.1 Methods for wintertime H_2 flux calculations

For the wintertime gas flux comparison, fluxes were calculated by the flux-gradient technique using either CO_2 or H_2O as the correlative flux-gradient variable. Wintertime trace gas processing tends to be slower than other seasons, which causes mean concentration gradients to be smaller and thus closer to the instrument precision (see Figure 3-11). Therefore, the vertical concentration gradient is calculated over a larger distance than during the rest of the year (spanning the 2.5 and 24 m inlets). The barren wintertime canopy does not significantly interfere with turbulent transfer between the 2.5 and 24 m inlets, whereas the presence of leaves in the growing season would be expected to. Whole canopy calculations would also be invalidated during the growing season because of photosynthetic perturbation on the gradient across the forest canopy, but this is not a problem in the winter in the dominantly hardwood forest. Calculated fluxes were filtered based on the inferred turbulent transfer coefficient ($0 < k < 0.5 \times dz$, dz=21.5 m) and the minimum detectable gradient given instrument precision.

The flux of H_2 can be calculated using a flux gradient technique utilizing the flux of CO_2 or H_2O. For the purposes of studying the flux of H_2 through the snowpack, we find CO_2 to be the superior comparative variable (instead of H_2O) for a number of reasons. First, mole fractions and water vapor fluxes are often low during the cold winter time, which causes the relative measurement uncertainty due to instrument error to increase. In fact, the H_2 fluxes calculated via the H_2O flux and gradient have approximately eight times the variance of those calculated via the CO_2 flux and gradient (F=8.3, 95% confidence interval 7.5 to 9.2, p-value $< 2.2 \times 10^{-16}$).

Theoretically, the same turbulent transfer coefficient, k, should be calculated from either tracer. Indeed, there is no significant difference between the mean wintertime H_2 fluxes calculated either via CO_2 or H_2O (Student's t-test, t=0.54, df = 1490, p-value=0.59). In the following analysis we use CO_2 as the correlative variable because there is not a systematic difference, because the less variability is introduced from the flux-gradient calculation, and because we anticipate that the processes controlling the wintertime flux of CO_2 are more closely tied to soil uptake of H_2 than the processes controlling H_2O fluxes.

4.4.2 Inter-winter flux comparisons

Soil-atmosphere exchange of H_2 and CO_2 was observed to persist during both Winter 1 and 2 as shown in Figure 4-7. In the mean, H_2 fluxes were negative (into the soil) during both winters but exhibited greater variability during Winter 1. Positive soil CO_2 fluxes (out of the soil) were predominantly observed during the two winters. Photosynthetic uptake was observed in the middle of Winter 2 (likely coniferous photosynthesis on above-freezing days) and upon leaf-out in April 2011 (April 2012 not shown here). In this section, the measured fluxes are compared between the two winters and within each winter. In the following section, the relationship between microbe-mediated H_2 and CO_2 fluxes is examined.

The 2010-2011 and 2011-2012 winters were forced by quite different meteorological conditions, which resulted in dramatically different snow and soil conditions as was shown in Section 4.3. In this section, we determine whether the inter-winter trace gas fluxes of interest were significantly different.

First, the H_2 and CO_2 flux distributions are compared over the"whole winter" period (dates with data from both winters: November 24 to March 1) as shown by the density plots in Figure 4-8. For both H_2 and CO_2, the flux distribution in Winter 1 was characterized by higher variance and a longer tail, indicating that more episodes of high flux rates occurred during that first winter. In contrast, the flux distribution in Winter 2 was much tighter. These differences in variance are corroborated by the results of F-tests listed in Table 4.2, which show that the fluxes were more variable for both gases in Winter 1. The variance ratios (Winter 1 variance : Winter 2 variance) over the whole winter were 4.0 and 10.1 for H_2 and CO_2, respectively (p-values ~ 0). In addition, inter-winter mean H_2 and CO_2 fluxes were significantly different. Flux rates were found to be significantly higher in Winter 1 than in Winter 2 (H_2: -4.9 versus -2.4 nmol m^{-2} s^{-1}, CO_2: 3.1 versus 1.0 μmol m^{-2} s^{-1}) as listed in Table 4.2.

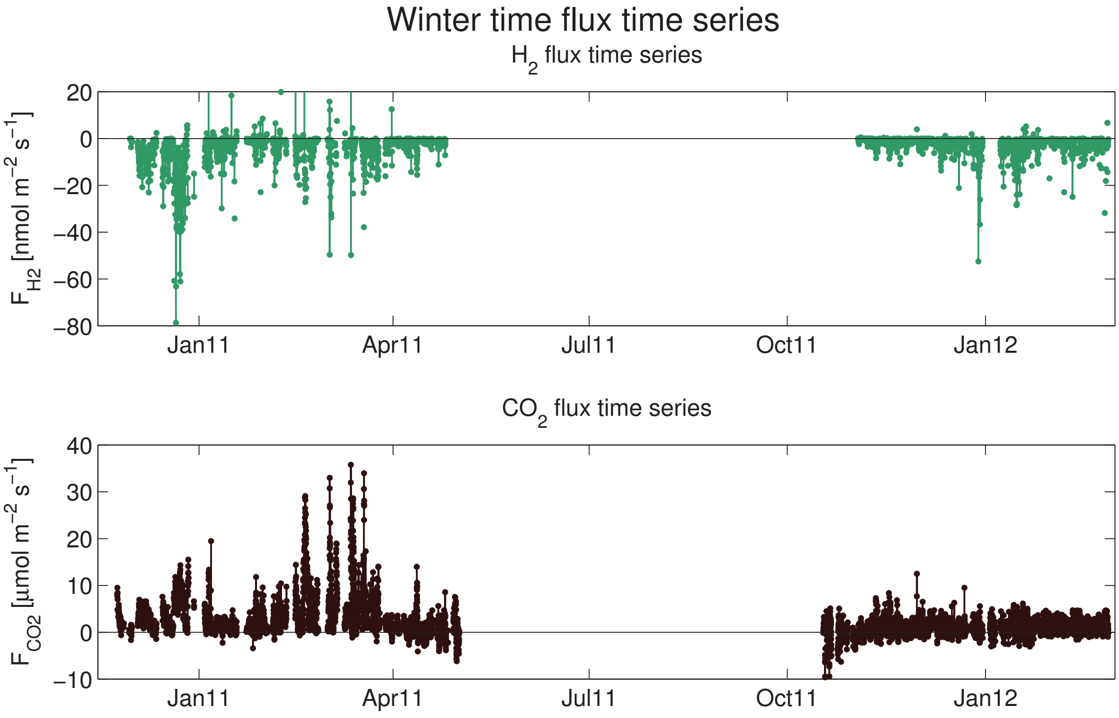

Figure 4-7: Time series of CO_2 eddy flux data (lower) and the H_2 flux (upper) calculated using the flux gradient approach across the 2.5 m and 24 m inlets.

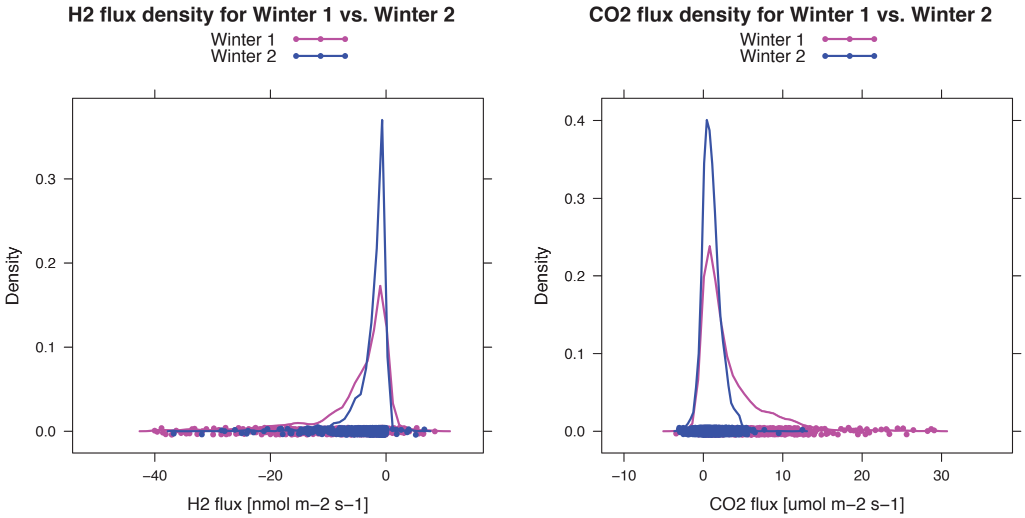

Figure 4-8: Flux density for H_2 (left) and CO_2 (right) for Winter 1 (magenta) and Winter 2 (blue) from November 24 to March 1 of each winter.

Table 4.2: Results of Students' t-test for difference in the inter-winter mean fluxes of H_2 and CO_2 over the whole winter period (November 24 - March 1), the periods in each winter without snow, and the periods with low snowpack (0-25 cm). F-test results are listed to compare the variance of the flux distribution (shown as variance ratios) for each period. Asterisks denote a statistically significant difference at the 95% level. Much of Winter 1 was covered by deep (>25 cm) snow, but not in Winter 2, so an inter-winter deep snow comparison is not possible.

		whole winter	**no snow**	**low snow**
H_2 flux mean	Winter 1, Winter 2	*-4.9, -2.4	*-6.1, -2.2	*-7.6, -3.7
(nmol m^{-2} s^{-1})	p-value	$p<2.2\times10^{-16}$	$p<2.2\times10^{-16}$	$p<5.8\times10^{-14}$
H_2 variance	Winter 1/Winter 2	*4.0	*2.3	*3.7
	p-value	$p<2.2\times10^{-16}$	$p<5.5\times10^{-14}$	$p<2.2\times10^{-16}$
CO_2 flux mean	Winter 1, Winter 2	*3.1,1.0	*2.5,1.0	*3.2,1.0
(μmol m^{-2} s^{-1})	p-value	$p<2.2\times10^{-16}$	$p<2.2\times10^{-16}$	$p<2.2\times10^{-16}$
CO_2 variance	Winter 1/Winter 2	*10.1	*2.9	*5.0
	p-value	$p<2.2\times10^{-16}$	$p<2.2\times10^{-16}$	$p<2.2\times10^{-16}$

On a whole-winter basis, Winter 1 fluxes were significantly larger and more variable.

To compare the winters on a more equal basis, the data were separated into periods with no snow, low snow (0-25 cm), and deep snow (>25 cm). Deep snow did not occur during the warmer Winter 2. The fluxes in these periods were compared for the two winters as is shown in Figure 4-10 and is listed in Table 4.2. The inter-winter mean differences were significant for H_2 for both the no snow and low snow periods. Similarly, CO_2 flux distributions were significantly different in both periods. A larger inter-winter difference was observed for low snow CO_2 fluxes than for the no snow period. In all cases, fluxes of both CO_2 and H_2 were larger during the colder Winter 1, which had a significant snowpack.

For both gases and periods, fluxes were more variable during Winter 1 than Winter 2. As was seen for the whole winter period, the increased flux variance is more pronounced for CO_2 than for H_2. Fluxes of H_2 and CO_2 were more variable during

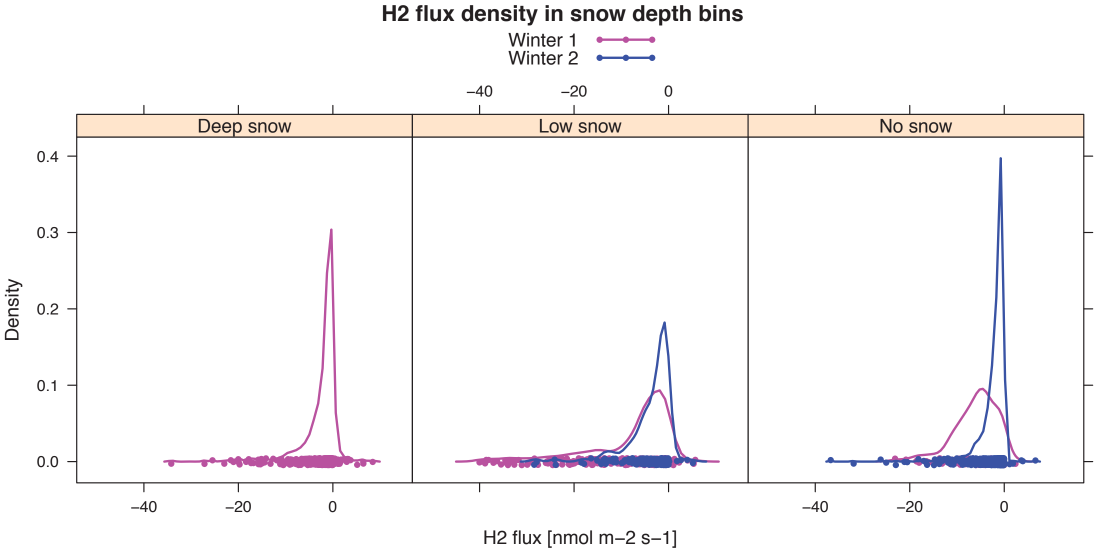

Figure 4-9: H_2 flux density for Winter 1 (magenta) and Winter 2 (blue) binned by snowpack depth from November 24 to March 1 of each winter. Low snow is defined as 0-25 cm depth and deep snow as >25 cm.

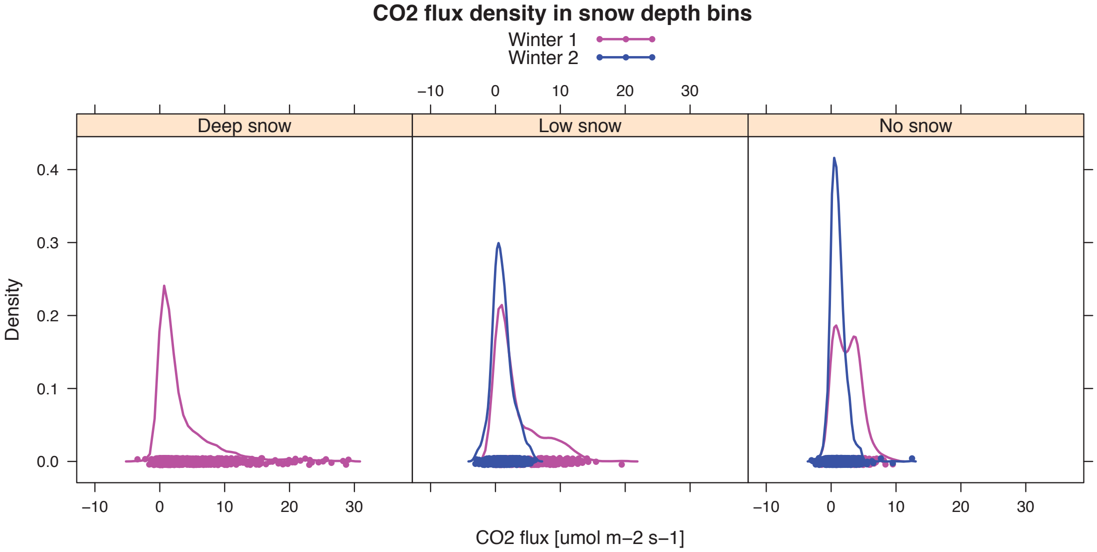

Figure 4-10: H_2 flux density for Winter 1 (magenta) and Winter 2 (blue) binned by snowpack depth from November 24 to March 1 of each winter. Low snow is defined as 0-25 cm depth and deep snow as >25 cm.

low snow periods than periods without snow, and the effect was especially exaggerated for CO_2. This analysis shows that the mean and variance of both fluxes were higher in Winter 1, even when they were considered only during periods with similar snowpack loadings. Potential environmental drivers for these differences will be explored in the rest of this chapter.

4.4.3 Relative change in the H_2 and CO_2 fluxes

Another informative method for comparing the flux of H_2 and CO_2 at Harvard Forest over the two different winters is to compare the flux ratio of the two, or F_{H_2}/F_{CO_2}. This also begins to highlight some environmental factors influencing one or both of the trace gas fluxes. During the winter, in the predominantly hardwood forest around the EMS tower at Harvard Forest, little photosynthesis occurs. Therefore, the net CO_2 flux is considered to originate predominantly from soil microbial respiration. Microbial respiration is in turn considered to be a proxy for soil microbial activity. The flux of H_2 is driven by the activity of the fraction of the soil microbial community that expresses the necessary genetic machinery to utilize atmospheric H_2. Therefore, the ratio of H_2 to CO_2 fluxes represents the relative activity of the H_2 consuming organisms to the activity of the whole community (reflected in CO_2 respiration). In this discussion, the wintertime flux ratio of H_2 to CO_2 will be considered to be a proxy for the ratio of these two activities.

A time series of the H_2 to CO_2 flux ratio is shown in Figure 4-11. Above- and below-canopy data demonstrate the same trends, but the below-canopy gradients are much larger and easier to measure given the instrument precision, especially in the winter. The relative activity of the H_2-consuming portion of the soil microbial community is largest in the winter and spring months and is smallest in the summer and fall. This seasonal divide aligns with the growing season, and does not necessarily reflect a decrease in the relative activity of H_2 bacteria. Instead, the assumption that the soil microbial community is the only source of soil CO_2 exchange breaks down in the growing season. During that period, CO_2 is respired both heterotrophically (microbes, soil fauna) and autotrophically (root) (Hanson et al., 2000). Rates of

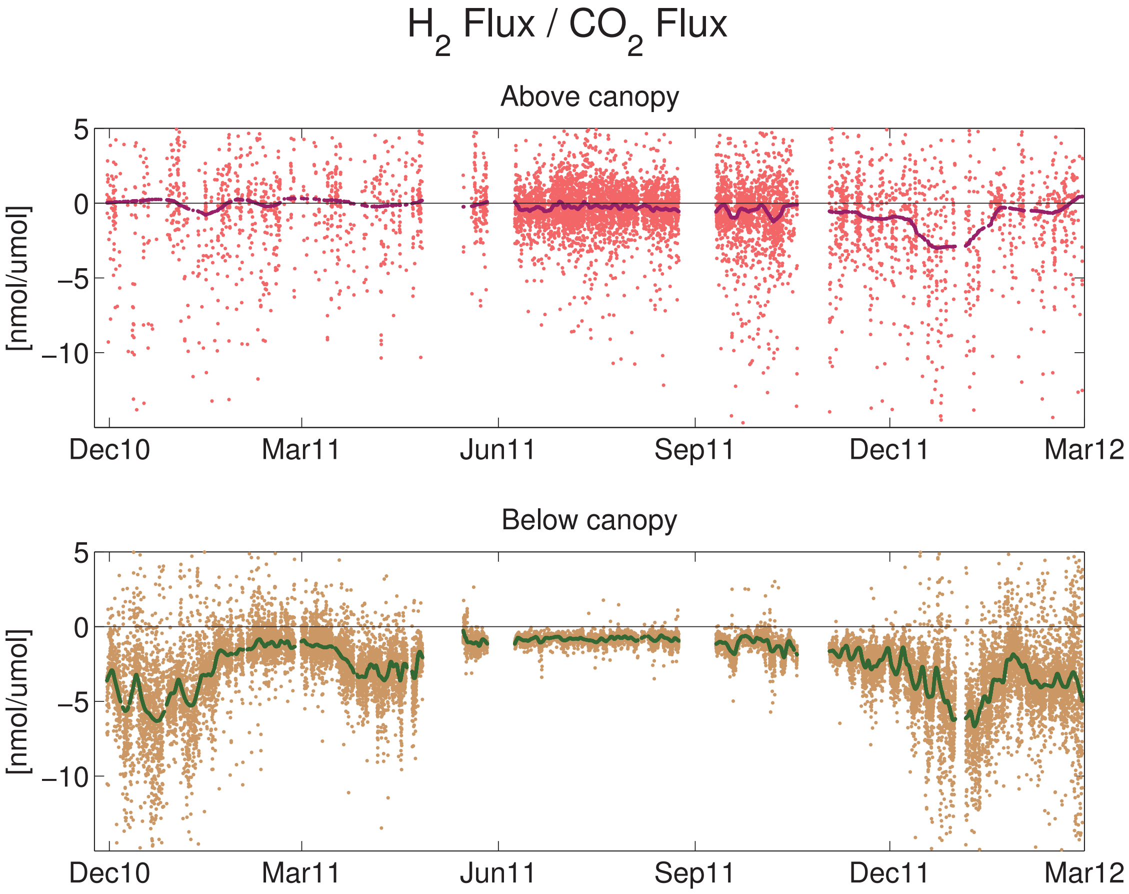

Figure 4-11: Time series of the ratio of the H_2 to the CO_2 flux over the study period for the above-canopy concentration gradient (upper plot) and below canopy concentration gradient (lower plot). The 30-minute fluxes (light points) and a 2-day moving average (rlowess filter, R project) on the 30-minute fluxes are plotted (dark points). The flux ratio is typically negative, reflecting the opposite signs of H_2 soil uptake and CO_2 soil respiration fluxes. The greater the magnitude (in this case negative) of the flux ratio, the relatively larger the rate of the H_2 consumption activity to the whole soil community activity (reflected by CO_2 respiration).

CO_2 respiration are increased by the recycling of photosynthetic carbon captured from plants during the growing season through the roots and plant structures. In addition, plants excrete metabolites that stimulate respiration of the soil microbial pool. Above the canopy, photosynthetic uptake in the canopy reverses the above-canopy CO_2 gradients diurnally and the sign of the flux ratio changes correspondingly. For the rest of the analysis, the focus will be on the winter and spring flux ratios when it is a more valid assumption that the soil CO_2 respiration predominantly reflects the activity of just the soil microbial pool.

Within the winter and spring seasons, flux ratios exhibit fine scale oscillations that correlate with environmental variables, which can help identify important processes affecting either the H_2 consuming community or the total soil microbial community. To this end, the flux ratios from Winter 1 and 2 are overlaid in Figure 4-12 and are compared to the time series of air temperature, soil temperature, and soil moisture.

Periodic temperature anomalies are observed during both winters (Figure 4-12), resulting from soil moisture input either from liquid precipitation or snow melt. Positive anomalies in soil temperature (warming) and moisture (wetting) correlate in time with decreases in the absolute value of the flux ratio (the negative ratio of the H_2 to CO_2 fluxes becomes smaller in magnitude). This may indicate that during warming and wetting events, the relative activity of H_2 consuming microbes lessens relative to the total soil microbial community. Alternatively, the uptake of H_2 may be limited in water-logged soils. Flux ratios do not indicate whether H_2 or CO_2 fluxes drive the anomaly, but they highlight a potential environmental driver.

A second potential mechanism is highlighted by a clear difference in the flux ratio between the two winters in January and February where the H_2 consuming community was less active relative to the total community in Winter 1 than Winter 2. During this period, soil temperature and moisture are quite similar for the two winters. The patterns observed in the early part of the winter would suggest that the flux ratios should be similar in this situation. This period correlates with the presence of a deep snowpack in Winter 1, as shown in Figure 4-13. In fact, even the short-lived snow cover in mid-January of Winter 1 was correlated with a reduction in the flux ratio.

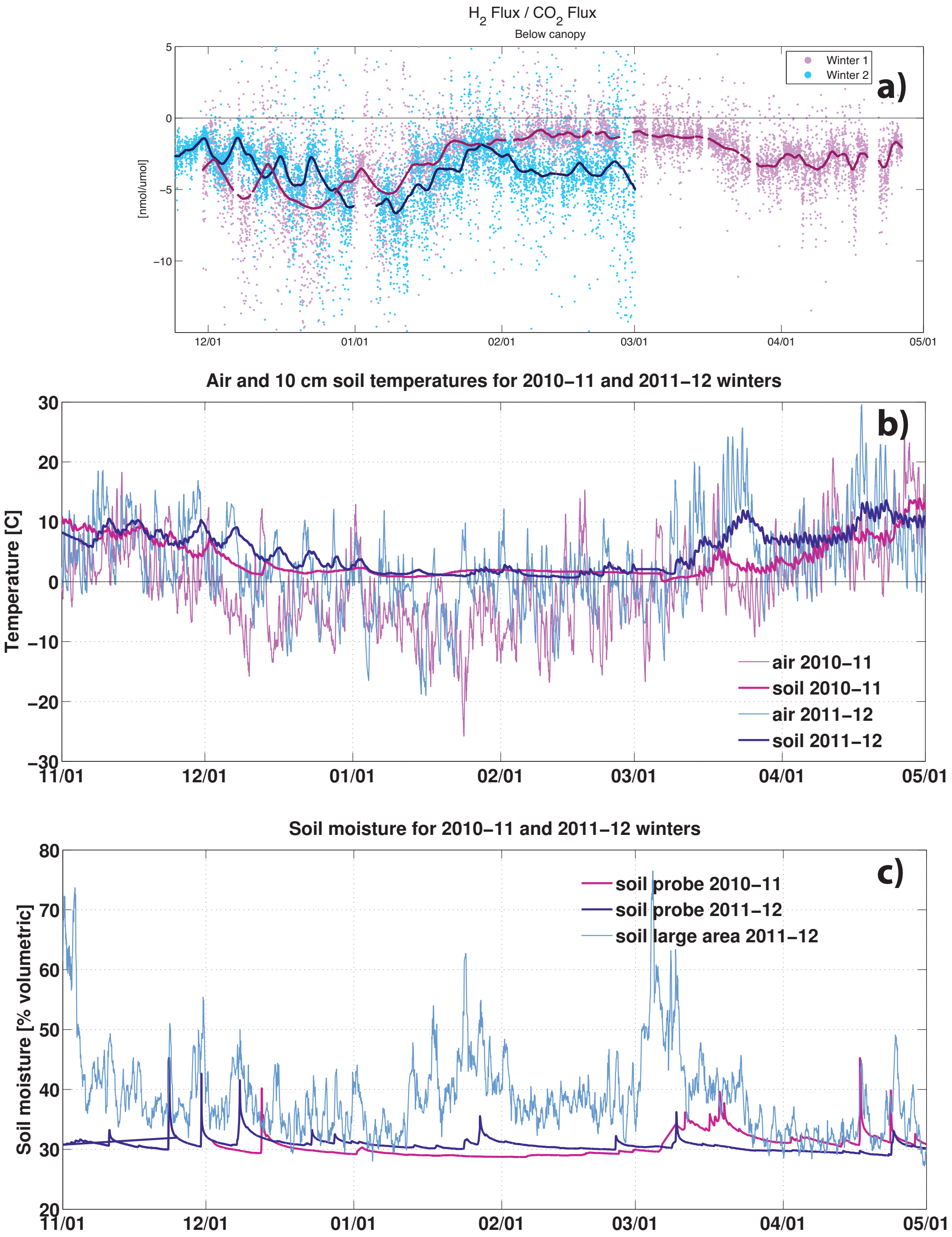

Figure 4-12: H_2 to CO_2 flux ratio time series (a) for Winter 1 (magenta) and Winter 2 (blue). The air (light line) and soil (dark line) temperatures are plotted for each winter (b) for comparison to the flux ratios. Similarly, soil moisture is shown for both winters (c) from a temperature probe, and from the COSMOS soil moisture data set in 2011-2012, which covers fluctuations in soil moisture over a larger area.

As will now be discussed, the snowpack might reduce rates of H_2 uptake relative to soil CO_2 respiration by virtue of the directionality of the flux.

Microbial soil respiration of CO_2 is dependent upon the concentrations of carbon substrates within the soil and is independent of overlying concentrations of CO_2. Regardless of snowpack depth, soil respiration can continue throughout the winter (although oxygen limitation might become a factor at some point). CO_2 can accumulate in the snowpack without affecting the respiration rate, and previous studies have quantified the concentration buildup and used it to understand the snowpack fluxes (Monson et al., 2006).

In contrast, H_2 consumption is a first-order process that is directly dependent upon the concentrations of H_2 at the site of reaction. For a given uptake rate, concentration gradients of H_2 establish within the snowpack, the size of which depends upon the snowpack depth, porosity, and molecular diffusion (see Section 4.2). The presence of snowpack therefore leads to reduced concentrations of H_2 at the soil snow interface, where the uptake reactions occur. This causes the rate of H_2 uptake to be reduced while the rate of CO_2 respiration has experienced no such snowpack inhibition. As a result, the flux ratio of H_2 to CO_2 would be reduced because of the snowpack, as was observed during Winter 1, simply because of the flux directionality.

In this study, the significant inter-winter differences in H_2 and CO_2 fluxes are presented. In addition, changes in the ratio of the fluxes were observed to correlate in time with inter- and intra-winter changes in environmental variables like soil moisture, soil temperature, and snow depth and porosity.

4.5 Environmental control on wintertime trace gas fluxes

In this section, potential environmental drivers of H_2 and CO_2 fluxes are investigated to build a process-based understanding of the wintertime fluxes of these two gases.

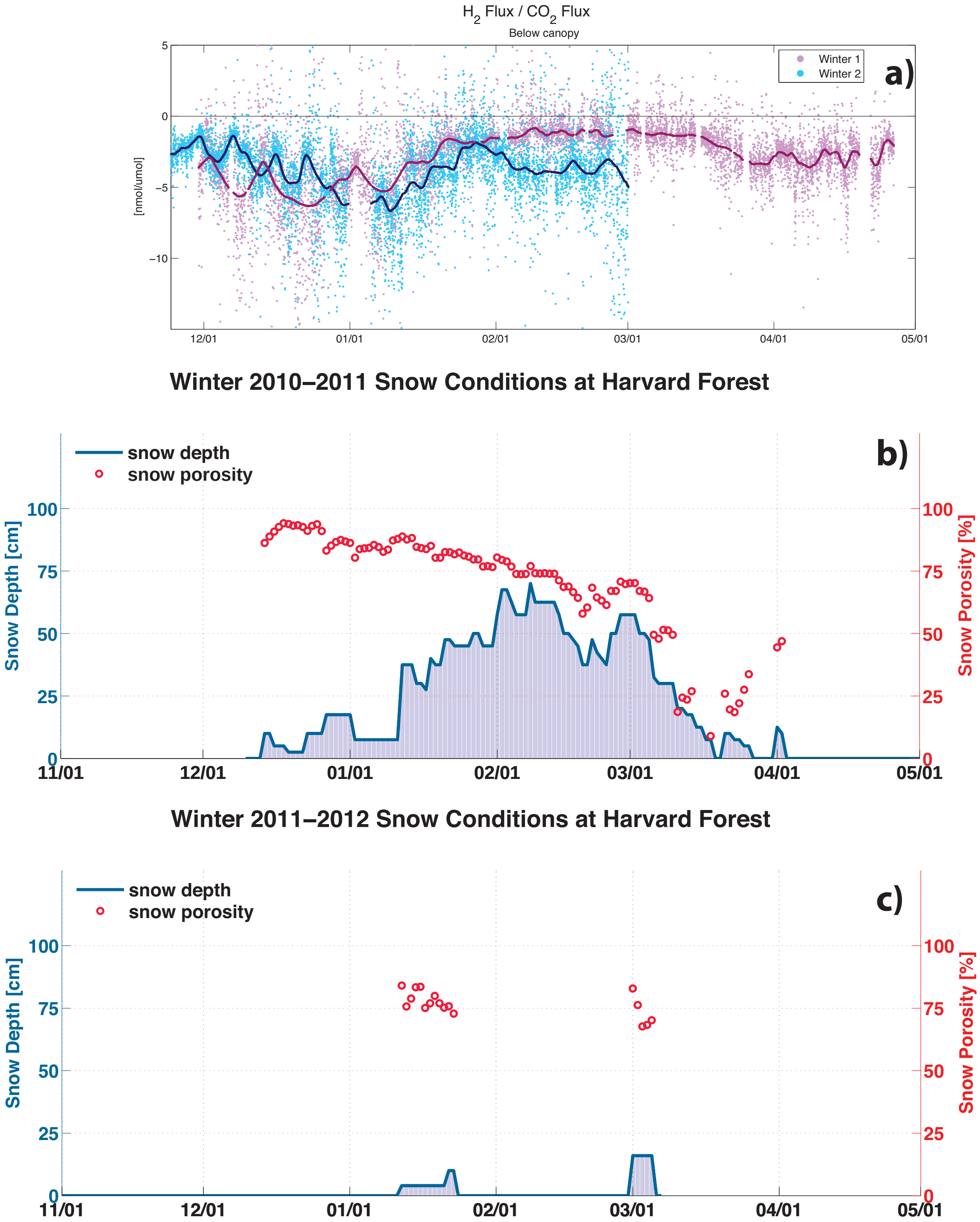

Figure 4-13: H_2 to CO_2 flux ratio time series (a) for Winter 1 (magenta) and Winter 2 (blue) shown again for comparison to snow properties. Snow depth and porosity are shown for Winter 1 (b) and Winter 2 (c).

4.5.1 How do snow properties affect fluxes?

As was inferred from the flux ratios, Figure 4-14 shows that H_2 uptake through the snowpack is anti-correlated with snow depth. As the snowpack deepens, resistance to the diffusion of H_2 molecules from the atmosphere to the soils for microbe-mediated uptake increases. In contrast, CO_2 fluxes are relatively insensitive to snow depth (see Figure 4-14). Winter 1 H_2 fluxes versus snow depth have a correlation coefficient of 0.32 ($p \sim 0$) while the correlation coefficient between CO_2 fluxes and snow depth is only 0.02 ($p=0.5$, not a significant correlation). Although the Winter 1 snowpack protected the soil microbial community, its also applies increased resistance to first-order uptake of gases like H_2.

As was discussed in Section 4.2, trace gas fluxes through the snowpack depend not only on snow depth, but also on snow porosity. These soil-mediated fluxes increase from porosities of 0.7 to 0.9 (data not shown). This could be explained by greater soil-atmosphere exchange of trace gases through the snowpack for a more porous snowpack. Interestingly, flux rates increase again at low snow porosities of around 0.7 to 0.5. This unexpected trend may be an indirect mechanism, such as stimulation of soil activity during melt events that happen to coincide with low porosity. Another explanation could be that an aged, low-porosity and melting snowpack may have snow-free areas surrounding dark materials in the snow, especially tree trunks. These snow-free areas may act like chimneys and facilitate soil-atmosphere gas exchange despite the low snowpack porosity. More analysis will be performed to further refine our understanding of the relationship between trace gas fluxes and snow porosity.

The relationship between the fluxes of H_2 and CO_2 and windspeed was explored to look for an enhancement of fluxes through the snowpack via “wind pumping”. For this analysis, a set of box-and-whisker plots is presented in Figure 4-15. These plots indicate that the flux of both H_2 and CO_2 is enhanced with wind, even when there is no snow present. All correlations between fluxes and windspeed are statistically significant (Pearson’s correlation test, data not shown). The correlation might arise from the increase in trace gas fluxes above the canopy measured by eddy covariance

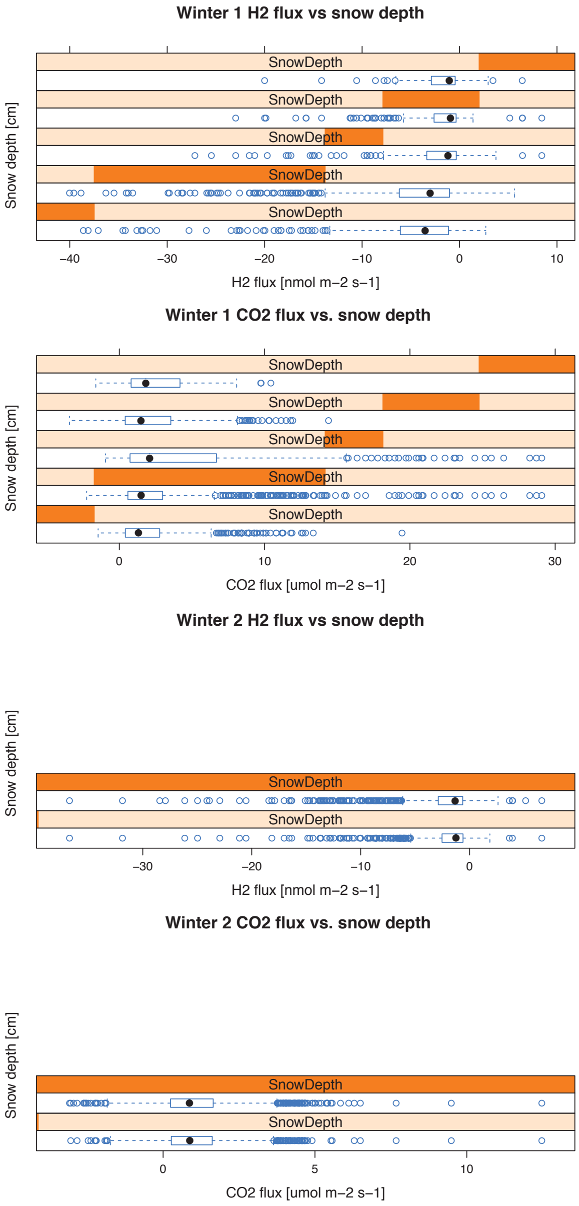

Figure 4-14: Box-and-whisker plots of H_2 (top) and CO_2 (bottom) fluxes in 20 cm snow depth intervals. H_2 fluxes decrease in magnitude and variability as the snowpack increases in depth; however, CO_2 fluxes appear relatively insensitive to snowpack depth. Data are separated into equal-size snow depth bins, as indicated by the orange bars. The median (black dot), upper (75%) and lower (25%) quartiles (box), minimum and maximum values (whisker), and outliers, which extend more than 3/2 times beyond the quartiles (open blue circles) are shown for the distribution of H_2 and CO_2 fluxes in each bin.

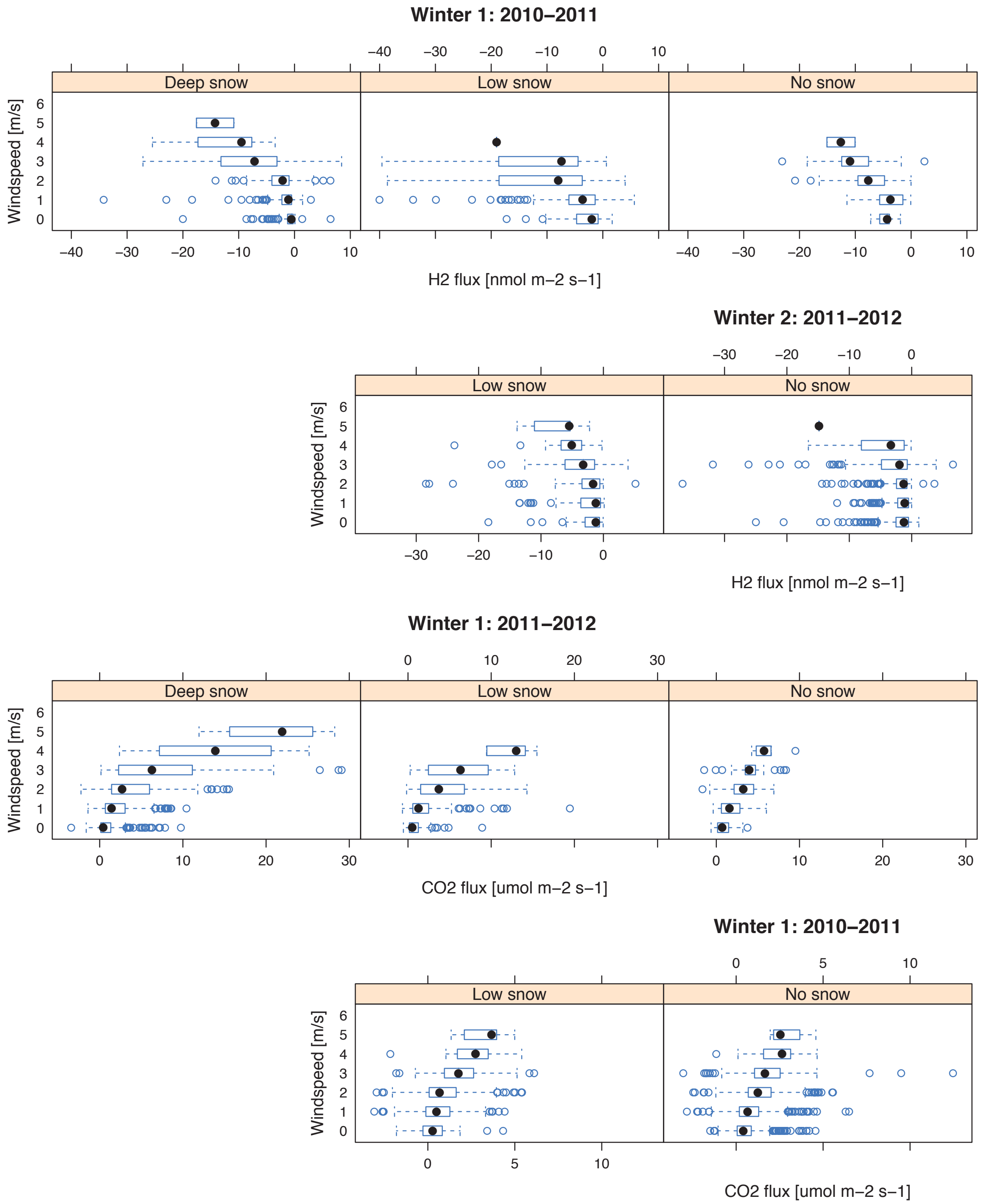

Figure 4-15: Plot showing the increase in trace gas fluxes of CO_2 and H_2 with increasing windspeed for both winters; the relationship is strongest during periods of deep snow. Box-and-whisker plots of H_2 (top) and CO_2 (bottom) fluxes for wind speed intervals. Data are separated into wind speed bins and are further separated into three snow depth bins: no snow, low snow (<25 cm), and deep snow (>= 25 cm). The median (black dot), upper (75%) and lower (25%) quartiles (box), minimum and maximum values (whisker), and outliers, which extend more than 3/2 times beyond the quartiles (open blue circles) are shown for the distribution of H_2 and CO_2 fluxes in each bin.

Table 4.3: Correlation tests for H_2 and CO_2 fluxes with soil temperature and soil moisture. Periods are divided by winter and by snow depth (deep snow is >25 cm and low snow is 0-25 cm). Correlations are determined using a Pearson's test, for which p-values are calculated to test for significance.

Period	**H_2 vs. T**	**CO_2 vs. T**	**H_2 vs. H_2O**	**CO_2 vs. H_2O**
Winter 1 : deep snow	-0.11 p=0.007	*0.40 p∼0	*-0.26 p∼0	*0.59 p∼0
Winter 1 : low snow	*-0.33 p∼0	*0.35 p∼0	*-0.23 p∼0	*0.22 p∼0
Winter 1 : no snow	-0.19 p=0.03	*0.62 p∼0	*-0.25 p=0.002	*0.47 p∼0
Winter 2 : low snow	-0.12 p=0.04	0.12 p=0.01	*-0.31 p∼0	*0.32 p∼0
Winter 2 : no snow	*0.21 p∼0	∼0 p=0.72	-0.02 p=0.44	*0.13 p∼0

with wind-induced turbulence (*i.e.*, fluxes are low in stagnant air). In the case of H_2, uptake rates may be stimulated by wind-induced turbulence because air with higher mole fractions of H_2 can be mixed down from above the canopy to the soil interface for consumption. The apparent correlation between trace gas fluxes and wind speed is larger with a snowpack and increases with snowpack depths. This suggests that wind-pumping is indeed a mechanism that enhances trace gas exchange through the snowpack, as has been explored by Bowling and Massman (2011). The effect appears stronger for CO_2 than for H_2 fluxes, which may again reflect the inhibition of first-order H_2 uptake rates through a deep snowpack. In contrast, CO_2 respiration is more or less unabated and high concentrations of CO_2 may build up in the snowpack. Its release by molecular diffusion may be greatly enhanced by wind-pumping.

4.5.2 How do soil properties affect fluxes?

Soil properties, most notably soil temperature and moisture, are known to influence rates of soil-atmosphere exchange of trace gases (Smith-Downey et al., 2006; Monson et al., 2006). The relationship of soil temperature with H_2 and CO_2 fluxes was explored by separating the wintertime data into the three snow depth bins: no snow, low snow (0-25 cm), and deep snow (>25 cm). Figure 4-16 shows box-and-whisker plots for the flux of both gases, for each winter and snow depth. Table 4.3 lists the correlation coefficient between trace gas flux and soil temperature pair (Pearson's test, for which p-values are calculated to test for significance).

In summary, the results indicate an increase in H_2 uptake and CO_2 respiration with increasing soil temperatures during Winter 1. The correlation is significant for CO_2 at all snowpack depths, but only for "low" snowpack in the case of H_2. During Winter 1 the biologically controlled fluxes of CO_2 and H_2 increase with soil temperature. During Winter 2, the correlations between CO_2 fluxes and soil temperature are very low and are not statistically significant. Similarly, the correlation between H_2 fluxes with these environmental variables during "low" snowpack periods are weak. Interestingly, the correlation of H_2 fluxes with soil temperature reverses during Winter 2 when there is no snow; H_2 uptake appears to decrease as soil temperature increases. During Winter 2, soil temperature appears not to be as important of an environmental factor as was observed in Winter 1.

The relationship between soil moisture and CO_2 and H_2 fluxes is presented in Figure 4-17 and Table 4.3 in the same fashion as was done for soil temperature. In all cases, flux rates are correlated with soil moisture. The correlations are significant for all periods, except for during for H_2 fluxes in Winter 2 with no snowpack. In that case, it appears from Figure 4-17 that H_2 fluxes were stimulated up to a saturation level of around 0.18, but were reduced by additional soil moisture thereafter. This could reflect a limitation to H_2 diffusion into the soils or a biological reaction to moist soils. Like soil temperature, soil moisture appears to be an important environmental factor exerting a control on wintertime fluxes of H_2 and CO_2.

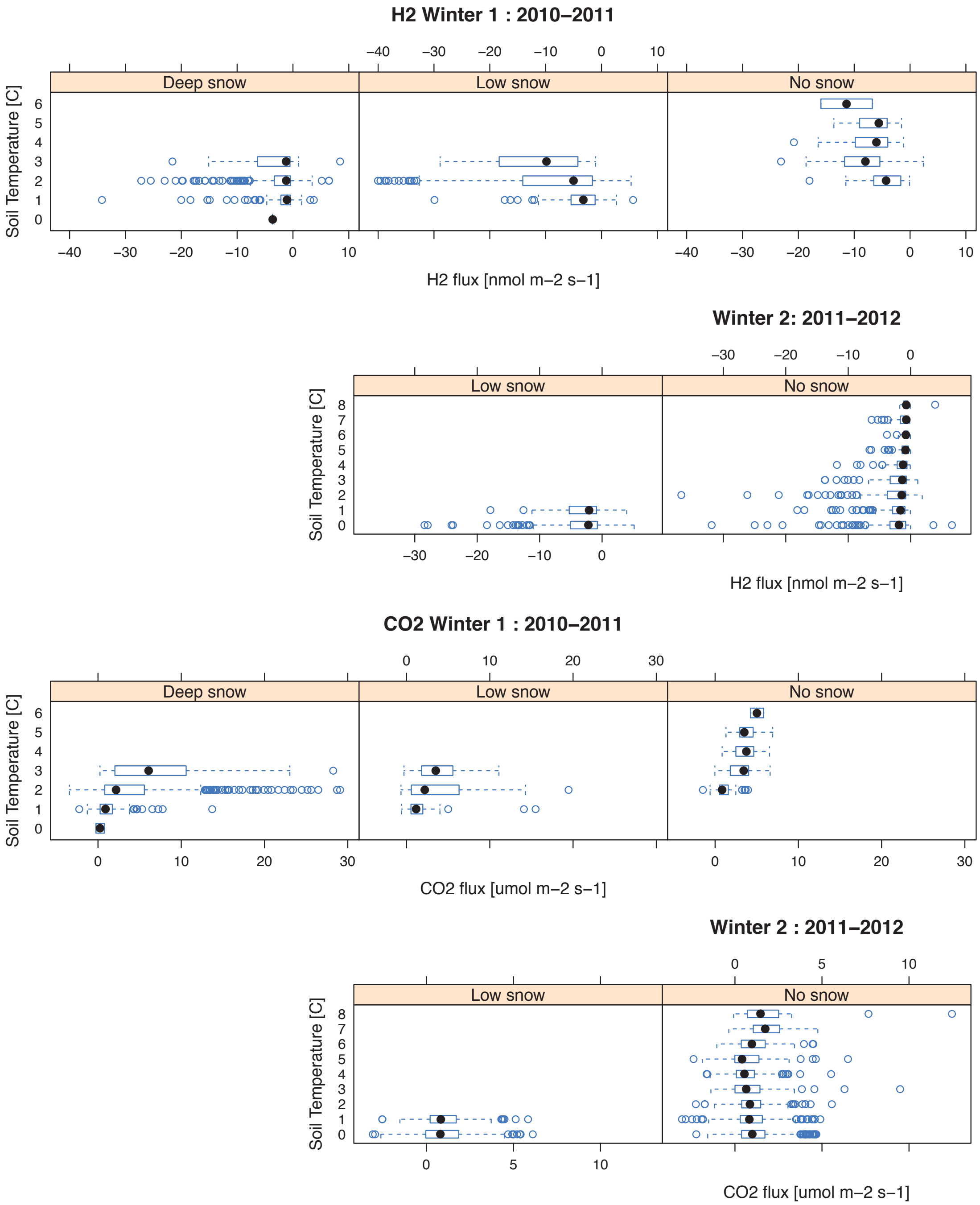

Figure 4-16: Relationship of soil uptake of H_2 and emissions of CO_2 with soil temperature. Significant correlations for each period are shown in Table 4.3, which tend to indicate increases in trace gas fluxes with increasing temperature, but not in all cases. Box-and-whisker plots of H_2 (top) and CO_2 (bottom) fluxes for soil temperature intervals. Data are separated into soil temperature bins and are further separated into three snow depth bins: no snow, low snow (<25 cm), and deep snow (>= 25 cm). The median (black dot), upper (75%) and lower (25%) quartiles (box), minimum and maximum values (whisker), and outliers, which extend more than 3/2 times beyond the quartiles (open blue circles) are shown for the distribution of H_2 and CO_2 fluxes in each bin.

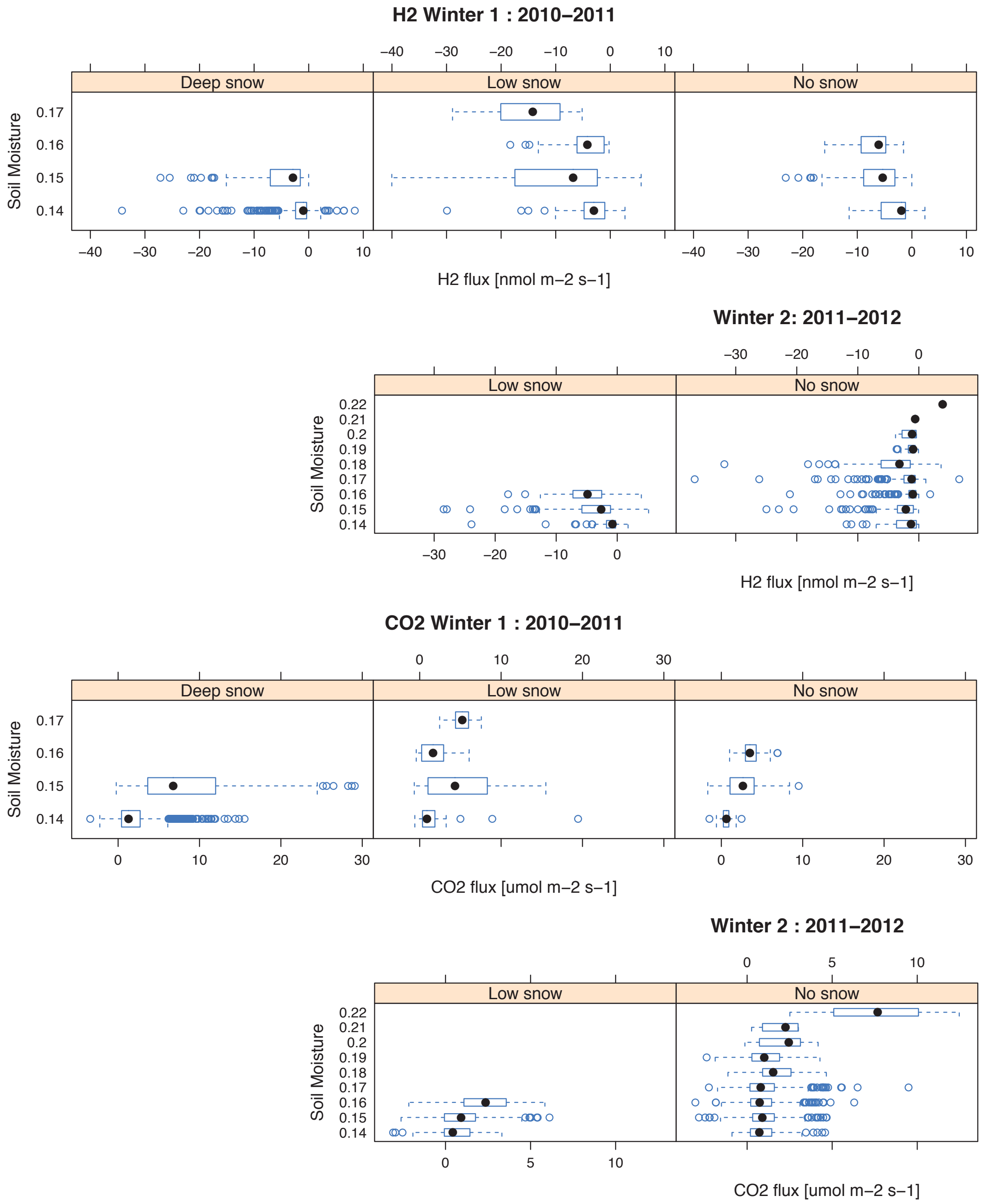

Figure 4-17: Relationship of soil uptake of H_2 and emissions of CO_2 with soil moisture. Significant correlations for each period are shown in Table 4.3, which tend to indicate increases in trace gas fluxes with increasing soil moisture in nearly all cases. Box-and-whisker plots of H_2 (top) and CO_2 (bottom) fluxes for soil moisture intervals. Data are separated into soil moisture bins and are further separated into three snow depth bins: no snow, low snow (<25 cm), and deep snow (>= 25 cm). The median (black dot), upper (75%) and lower (25%) quartiles (box), minimum and maximum values (whisker), and outliers, which extend more than 3/2 times beyond the quartiles (open blue circles) are shown for the distribution of H_2 and CO_2 fluxes in each bin.

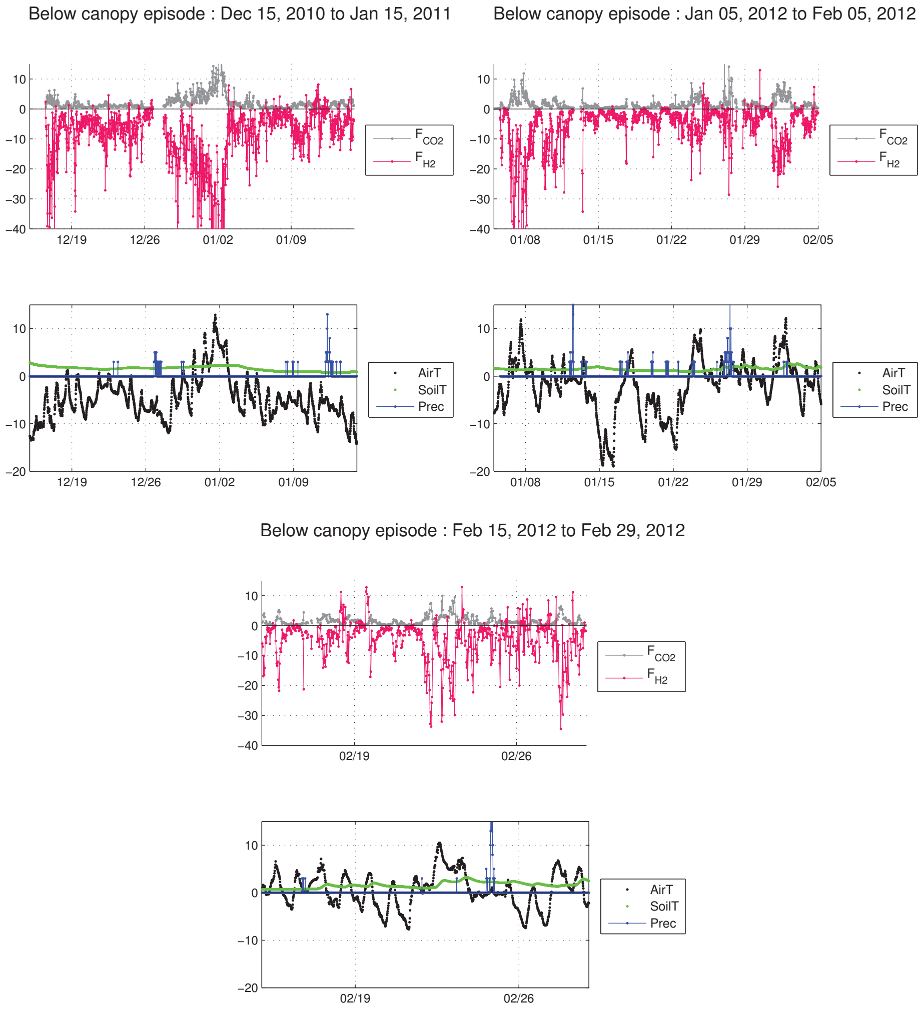

Figure 4-18: A first look at the episodic nature of H_2 and CO_2 soil fluxes at Harvard Forest during the winter in response to dynamic environmental drivers such as air temperature and moisture inputs. Production of CO_2 and uptake of H_2 by the soils increases with air temperature and likely precipitation. On occasion, apparent emissions of H_2 (positive fluxes) are observed, possibly due to anaerobic processes.

4.5.3 Episodic events

In addition to season-wide averages and correlations, it is interesting to consider the episodic nature of trace gas fluxes in the winter during dynamic events such as freeze-thaw cycles, liquid water input via rain or snowmelt, and snowfall. The below canopy fluxes (K-theory method, Section 3.2.3) can be used to look at relatively high-frequency time series to assess the time-response of H_2 fluxes to dynamic environmental drivers. Little time will be dedicated to this analysis within the scope of the thesis, but Figure 4-18 compares the trace gas fluxes of H_2 and CO_2 with changes in air temperature, soil temperature, and precipitation for three example periods.

From these figures, we find that H_2 uptake and CO_2 respiration increase with air and soil temperature. Fluxes of both gases are very low when air temperatures are far below freezing, and increase rapidly as temperatures increase above freezing. We should note that the 10 cm soil temperature shown here is almost always above freezing, but the uppermost layers of soil will have a frost layer in proportion to the extent and duration of freezing air temperature events.

Interestingly, some of the freeze-thaw events are associated with apparent H_2 emissions (positive fluxes) from the soil. These periods appear to be associated with specific warming and precipitation events. The soil moisture data will be analyzed later to determine whether these periods could foster the anaerobic production of H_2 and allow its unimpeded release to the overlying atmosphere. These H_2 emission periods could be associated with the release of CH_4 from the forest soils to the atmosphere.

4.6 Conclusions

In this chapter, the wintertime subset of H_2 and CO_2 fluxes are considered in detail. The relationship between the snowpack and persistence of soil microbiogeochemical cycling of these trace gases is explored. Measurements spanning the 2010-2011 and 2011-2012 winters show that fluxes of H_2 and CO_2 persist in the winter. Stark differences in the meteorological forcing between the two years provided an opportunity to understand the natural variability of wintertime trace gas exchange. Furthermore, investigating the relationship between environmental variables and wintertime trace gas fluxes over these two different years contributes to their process-based understanding.

We find that the soil-atmosphere exchange of CO_2 and H_2 is larger and more variable in a very cold 2010-2011 winter with a significant snowpack than the warmer low-snow 2011-2012 winter. Precipitation fell as snow, producing a long and enduring snowpack reaching 70 cm at its maximum. The beneath snow (subniveal) soil conditions were steady and remained above freezing for months until snowmelt. The snowpack protected the soil microbial community from freezing air temperatures, and in this stable environment, microbial respiration and H_2 consumption persisted, and the rates of both were found to increase with temperature and moisture. The snowpack was an added resistance to the diffusion of H_2 to soil organisms, and uptake rates decreased with snow depth, while the rates of CO_2 respiration were unaffected. Wind-induced ventilation of the snowpack enhanced the measured atmospheric fluxes, and led to the more episodic behavior of the 2010-2011 winter than the 2011-2012 winter. The largest CO_2 respiration rates observed over the winter period were associated with high wind speeds over a deep snow pack, which indicates that stored CO_2 was ventilated by wind-pumping in those situations

In contrast, the second, warmer 2011-2012 winter without an enduring snowpack had reduced rates CO_2 and H_2 exchange. The soil environment in the second winter was highly dynamic; in the absence of a snowpack, soil temperatures are coupled to atmospheric temperatures, which routinely dipped and rose above the freezing point. Additionally, precipitation largely fell as rain instead of snow. These precipitation events brought heat and moisture into the soils. These features caused the soils to undergo many freeze-thaw cycles throughout the winter, and in contrast to the first winter, soil frost penetrated up to 10 cm into the snow (Pamela Templer, personal communication). We propose that the freeze-thaw cycles and frost in the second winter were a challenge to survival in the soil microbial community and may have reduced the vigor of the microbial community. In these demanding conditions, the microbial community may not have been primed to respond to favorable changes in soil temperature and moisture. Indeed, the correlations between the CO_2 and H_2 fluxes and environmental variables are less consistent (or statistically significant) in the second winter as compared to the first. Soil temperatures used in this study were measured at 10 cm depth or deeper, and will not necessarily reflect freezing of the upper 1-2 cm of soil where much of the atmospheric H_2 consumption is expected to occur.

Trace gas exchange during wintertime can contribute significant amounts to the annual ecosystem exchange (Monson et al., 2006). Building a process-based understanding of the environmental control on trace gas exchange during winter is important for trace gas budgets today and for projecting the effect of climate change on large land swaths (up to 50%) of the northern hemisphere that are typically covered by snow in the wintertime (Lemke et al., 2007). As seen for CO_2 and H_2 in Harvard Forest, a warmer winter does not necessarily lead to an increase in trace gas exchange, as might typically be anticipated. The role of snowpack in facilitating microbiogeochemical cycles during the winter can be unintuitive. Our findings regarding the exchange of H_2 and CO_2 between the soil and atmosphere, which represent both soil emission and uptake processes, may be translatable to other trace gases important for climate and ecosystem function even in the winter.

Chapter 5

Microbiology of the H_2 soil sink

Objective

In addition to the field work described in this thesis, a laboratory-based approach was taken to contribute to the process-based understanding of the H_2 soil sink. We isolated microbial strains from Harvard Forest that consume atmospheric H_2 to study their H_2 uptake characteristics. First, we wanted to know whether environmental isolates and reference strains with the genetic potential for atmospheric H_2 consumption actually exhibited atmospheric H_2 uptake (*i.e.*, did the gene predict function?). Secondly, because the lifecycle of soil microorganisms can be quite complex as an adaptation to variable conditions in the soil environment, we sought to determine whether H_2 consumption occurred in a specific life cycle stage for a given soil microorganism. Furthermore, understanding how environmental conditions, organismal life cycle, and H_2 uptake are connected can help reduce the uncertainty in atmospheric models.

Results

- Microorganisms isolated from Harvard Forest demonstrated high-affinity low-threshold atmospheric H_2 consumption.

- 16S rRNA and high affinity hydrogenase (*hhyL*) genes of Harvard Forest Isolate

(HFI) strains were sequenced, contributing to the relatively small library of known atmospheric H_2-consuming microbes.

- The *hhyL* gene was found to be predictive of H_2 consumption for *Streptomyces* HFI spp. and reference strains, including *Streptomyces cattleya* and *Rhodococcus equi*.

- In *Streptomyces* HFI spp., H_2 consumption commenced only after the aerial growth and sporulation phases of the lifecycle had begun. H_2 consumption was not detected during the vegetative growth phase that follows spore germination.

- Only one strain with the *hhyL* gene, reference strain *Streptomyces griseoflavus* Tu4000, did not exhibit atmospheric H_2 consumption. This strain is a so-called bald (*bld*) mutant that bypasses the aerial hyphae phase of its lifecycle.

- In *Rhodococcus equi*, H_2 consumption did not commence until the late exponential phase, and consumption persisted well into the stationary phase. The activation of H_2 consumption in these late growth phases indicates that H_2 is consumed when culture density is high and nutrients become limiting.

- This study demonstrates that lifecycle stage correlates with the timing of H_2 consumption in both *Streptomyces* spp. and *Rhodococcus equi*. In particular, H_2 consumption occurs at stages in the life cycle often correlated with nutrient limitation. This suggests that H_2 may be an important supplement for nutrient-starved soil microorganisms.

- Our results suggest that, contrary to what might be expected, environmental H_2 uptake may not occur when soil conditions are optimal for most organisms because H_2-consuming microorganisms may only rely on H_2 during nutrient-limiting conditions.

The work accomplished in this chapter has been in large part due to the contributions of Ms. Deepa Rao, (B.S., MIT, 2012). Her senior thesis, entitled "Exploring the microbe-mediated soil H_2 sink: A lab-based study of the physiology and related

H_2 consumption of isolates from the Harvard Forest LTER", from the Department of Earth, Atmospheric and Planetary Sciences at MIT, presents a more detailed methods and analysis section than given here (Rao, 2012). Her contributions will continue in the form of authorship on a scientific publication.

5.1 Introduction

Atmospheric H_2 exerts a significant influence on tropospheric atmospheric chemistry and on the protective stratospheric ozone layer. Many trace gas cycles, such as that of atmospheric H_2, include significant biospheric components, largely driven by microorganisms (Conrad, 1996). H_2 is an indirect greenhouse gas (GHG) present at approximately 530 parts per billion (ppb) in the troposphere (Novelli et al., 1999). An abundant oxidizable trace gas, H_2 is scavenged by the atmosphere's "cleansing" hydroxyl radical ($\cdot$OH), thereby attenuating the ability of $\cdot$OH to scavenge potent GHGs, like methane (CH_4) from the atmosphere. The atmospheric H_2 budget is dominated by the microbe-mediated soil sink, which has been estimated to comprise between 62% and 92% of total loss, and is a relatively stronger component of the H_2 budget in the Northern Hemisphere (Conrad and Seiler, 1985; Novelli et al., 1999; Gerst, 2001; Hauglustaine, 2002; Ehhalt and Rohrer, 2009). Although it is estimated to be the largest term in the H_2 budget, the microbe-mediated soil sink remains the most poorly constrained term largely because of the paucity of field and lab measurements. Atmospheric H_2 has no discernible growth rate, and it is possible that the soil sink has buffered anthropogenic combustion H_2 emissions since pre-industrial times to keep mole fractions relatively stable. Additional research is needed, especially to understand the processes behind the H_2 soil sink, to understand the true dynamics of the H_2 cycle.

Until recently, an understanding of the fundamental processes driving the H_2 soil sink was lacking. Traditionally, free soil hydrogenases were presumed to be the primary drivers of the H_2 soil sink because sterilization of soils had no apparent effect on H_2 uptake rates (Conrad et al., 1983; Conrad, 1996). Furthermore, only low affinity (K_m ~1000 ppmv), high-threshold hydrogenases had been characterized, but these enzymes are not functional at the low atmospheric H_2 mole fractions. Indirect evidence existed to support the notion that atmospheric H_2 utilization was an active microbial process (King, 2003; Conrad and Seiler, 1981; Conrad et al., 1983). Direct evidence was obtained only recently upon the isolation of *Streptomyces* sp. PCB7, the first microorganism with a demonstrated high-affinity, low-threshold consumption of atmospheric H_2 (Constant et al., 2008b). *Streptomyces* sp. PCB7 belongs to the ubiquitous genus of soil microbes, *Streptomyces*. This microbe contains a novel group-5 [NiFe]-hydrogenase composed of small and large protein subunits, *hhyS* and *hhyL*, respectively (Constant et al., 2008b, 2010, 2011a,b). The *hhyL* occurs in many, but not all of *Streptomyces* spp. isolated from temperate forest and agricultural soils (Constant et al., 2010). In *Streptomyces* sp. PCB7, H_2 utilization occurs in the spore stage of the life cycle typical of that genus (Constant et al., 2008b). Furthermore, *hhyL* transcription is more strongly correlated with the spores than the substrate mycelia of that organism (Constant et al., 2011a). *In situ* soil H_2 consumption rates can theoretically sustain the maintenance energy requirements for the number (10^6-10^7) of *Streptomyces* spp. typically found in soils (Constant et al., 2010; Conrad, 1999). A soil survey and genome data-mining investigation revealed the ubiquity of high-affinity H_2 uptake activity and *hhyL* gene in soils from diverse ecosystems around the world (Constant et al., 2011b). The *hhyL* gene is distributed unevenly amongst the *Actinobacteria*, *Proteobacteria*, *Chloroflexi*, and *Acidobacteria* phyla, and *hhyL* DNA copy number was not found to predict soil H_2 uptake activity (Constant et al., 2011b).

As a result of these recent exciting advances, many new questions have arisen regarding the fundamental biology of these H_2-utilizing microorganisms. In this study, we focus on understanding the role of *Streptomyces* spp. and other microorganisms containing the putative group 5 [NiFe]-hydrogenase in the global atmospheric H_2 metabolism. Specifically, we focus on two objectives. First, we seek to determine whether environmental isolates and reference strains with the genetic potential for atmospheric H_2 uptake actually exhibit H_2 uptake (*i.e.*, does the gene predict function?). Because the lifecycle of soil microorganisms can be quite complex as an adaptation to variable conditions in the soil environment, the second objective of this study is to determine whether H_2 consumption occurs during a specific life cycle stage of a given soil microorganism. The timing of H_2 uptake with respect to the stage in the life cycle may point to the advantage of atmospheric H_2 consumption for that organism. Furthermore, understanding how environmental conditions, organismal life cycle, and H_2 uptake are connected can help reduce the uncertainty in atmospheric models.

For this study, we isolate *Streptomyces* spp. from the Harvard Forest Long Term Ecological Research Site (LTER), where atmospheric H_2 fluxes are concurrently measured (Meredith et al., *in prep*). We retain Harvard Forest Isolates (HFI) that contain the *hhyL* gene and characterize their H_2 uptake behavior. Uptake behavior of reference strains from a different genus within the *Actinobacteria* (*Rhodococcus equi*) or from the same genus but from in a highly similar (*Streptomyces griseoflavus* Tu4000) or divergent (*Streptomyces cattleya*) group-5 [NiFe]-hydrogenase clade, respectively, is also characterized. *S. griseoflavus* Tu4000 is found to be a *bld* mutant unable to produce aerial hyphae under the culture conditions.

The relationship between the organismal life cycle and H_2 uptake is explored in detail for a *Streptomyces* sp. HFI strain and for *R. equi*. We expect a relationship between the timing of H_2 utilization in the sporulating and non-sporulating *Actinobacteria*. *Streptomyces* spp. are common soil bacteria whose spores germinate in response to environmental triggers and enter the vegetative growth stage. During vegetative growth, a network of hyphae (mycelia) extend and embed into a nearby substrate and start solubilizing organic debris (Flärdh and Buttner, 2009). Over time, the substrate mycelia are lysed and the biomass is recycled to create aerial hyphae coated with hydrophobic proteins, which allow the hyphae to break the surface tension of the medium and extend above the colony surface (Schrempf, 2008). The aerial hyphae grow into the air and resemble a millimeter-scale tree canopy in immediate contact with the atmospheric trace gas constituents. As the colony matures, the aerial hyphae differentiate into chains of spores. Spores of *Streptomyces* spp. are largely dormant cells containing genomic DNA that are resistant to many kinds of environmental stress (*e.g.*, heat, desiccation, uv light) because of their thick spore walls (Flärdh and Buttner, 2009). However, *Streptomyces* spores are less resistant to adverse conditions than the endospores produced by *Bacillus* and other genre of the Firmicutes (McCormick and Flärdh, 2012). When the encasing sheath of the aerial hyphae breaks, individual spores are released into their surroundings. During the more vulnerable stage of aerial hyphae production and spore differentiation, metabolites, pigments, and signature *Streptomyces* antibiotics are produced as chemical protection against other potentially threatening cells.

Rhodococci, like *Streptomyces*, are also actinomycetes. *Rhodococcus* spp. are nocardioform, meaning that they reproduce by fragmentation of parts of their hyphae into bacilli and coccoid elements (Bergey et al., 1957). They exhibit rod-to-coccus morphologic variation during the growth cycle (Prescott, 1991). Their growth stages can be described by a typical bacterial growth curve. *Rhodococcus* spp. are prevalent in nature, especially in dry soil and herbivore manure. *Rhodococcus equi* is an obligate aerobe that has pathogenic potential for animals, including immunocompromised humans, to cause pneumonia or enteritis (Takai et al., 1991). *R. equi* prefers warm temperatures, such as found in warm soils or the host organism, and does not multiply at 10°C or below.

Correlations between H_2 utilization and organismal life cycle stage have been observed previously (Constant et al., 2008b; Rao, 2012). Environmental factors trigger the biological progression through the life cycle stages, and efforts to understand these links may contribute to an explanation of the sensitivity of the H_2 soil sink to environmental forcing. This research aims to increase the understanding of role that soil microbes play in global H_2 biogeochemical cycling.

5.2 Methods

Microbial Strains:

Streptomyces spp. were isolated from soils within the footprint of the Environmental Measurement Site (EMS) atmospheric trace gas flux tower at the Harvard Forest Long Term Ecological Research site in Peterhsam, MA (42°32'N, 72°11'W). Harvard Forest is a mixed deciduous forest with acidic soils originating from sandy loam glacial till (Allen, 1995). Samples were collected from the uppermost six inches of soil after removal of the leaf litter.

An isolation approach was adopted to exploit the susceptibility of non-sporulating organisms to desiccation and chemical destruction (*e.g.*, by low concentrations of calcium carbonate), thereby enriching sporulating soil organisms such as *Streptomyces* spp. (El-Nakeeb and Lechevalier, 1963; Schrempf, 2008). Soils were dried for 3-4 hours at 55°C. Dry 1 g soil samples were ground with a mortar and pestle and were combined with 1 g of $CaCO_3$. The mixtures were incubated in a humid environment in Petri dishes (sterile, polystyrene, 100x15 mm, VWR, Radnor, PA) with moistened filter papers (11.0 cm diameter, Grade 1, Whatman®, Kent, ME) fitted in the lids for 2 days at 28°C. After this period, incubated soil mixtures were suspended in 100 ml sterile water and thoroughly vortexed. After allowing to settle for 30 min, soil suspensions were serially diluted, and the 10^0, 10^{-2}, and 10^{-4} dilutions were spread onto R2A plates (Difco™R2A, BD, Franklin Lakes, NJ) treated with 1.75 mg/plate cycloheximide, an antifungal agent (Porter et al., 1960). After incubation at 30°C for 3-5 days, microbial colonies demonstrating any of the following four distinctive *Streptomyces* traits were transferred onto fresh R2A plates until pure isolates were obtained: 1) antibiotic inhibition of neighboring growth (*i.e.*, zone of clearing), 2) a fuzzy appearance indicating the production of aerial hyphae, 3) pigmentation, or 4) the distinctive earthy scent of geosmin. The resulting set of isolates, henceforth referred to as Harvard Forest Isolates (HFI), were maintained in culture on R2A agar at room temperature. Stock cultures were also prepared from spore suspensions in 20% sterile glycerol and stored at -80°C.

Reference strains used in this study have published genomes accessible in the National Center for Biotechnology Information (NCBI) databases[1]. *Streptomyces griseoflavus* Tu4000 (accession NZ GG657758) was kindly provided by the genome authors and collaborators (Michael Fischbach, John Clardy, Joshua Blodgett). The following strains were obtained from culture collections: *Streptomyces sviceus* ATCC 29083™(accession CM000951), *Rhodococcus equi* ATCC 33707™(accession CM001149), and *Streptomyces cattleya* NRRL 8057 (accession NC 016111).

DNA extraction and PCR amplification

Two primer pairs were used in this study for PCR amplification reactions (Integrated DNA Technologies, Coralville, Iowa): 1) a ready-made primer pair to amplify the 16S rRNA gene, (5' - AGA GTT TGA TCC TGG CTC AG-3') and (5'-ACG GCT ACC TTG TTA CGA CTT-3'), and 2) a custom primer pair to amplify *hhyL* gene sequences, NiFe-244f (5' - GGG ATC TGC GGG GAC AAC CA -3') and NiFe-1640r (5' - TGC ACG GCG TCC TCG TAC GG -3'), which were previously designed to encode for the putative group 5 [NiFe]-hydrogenase large subunit of *S. avermitilis* 46492 (Constant et al., 2010).

DNA was extracted using the PowerSoil® DNA Extraction Kit (MoBio Laboratories, Carlsbad, CA) from colonies picked from plates. PCR amplification of 16S rRNA and *hhyL* genes, respectively, were performed in 25 μl reaction volumes with the following reaction mixture: 12.5 μl PCR Master Mix 2x (Promega, Madison, WI), 2μl of each primer suspended at 10 μM, 6.5 μl nuclease free H_2O, and 2 μl of DNA template (typically between 250-800 ng/μl). The reactions were performed using a Biorad MyCycler™thermal cycler (Biorad, Hercules, CA) with the following program: 5 min initial denaturation at 95°C, followed by 30 cycles consisting of 30 s template denaturation at 95°C, 30 s hold at the primer annealing temperature, and 1.5 min extension at 72°C, and with a final extension at 72°C for 5 min. Annealing temperatures of 50°C and 60.7°C were used for the amplification of the 16S rRNA and *hhyL* genes, respectively. The *hhyL* annealing temperature was optimized over

---

[1] http://www.ncbi.nlm.nih.gov/

a temperature gradient spanning eight temperatures between 50°C and 62.2°C on *S. griseoflavus* Tu4000 DNA template.

Each HFI strain was evaluated for the presence of a putative group 5 [NiFe]-hydrogenase by gel electrophoresis of the *hhyL* gene PCR reaction product. Gels were cast (1% agarose, 5μl GelRed nucleic acid stain (Biotum, Hayward, CA)), loaded (5μl PCR product and 2μl DNA loading dye (Fermentas, Glen Burnie, MD)), run (100 V for 1 hr), and visualized (UVP MultiDoc-It$^{\text{TM}}$Digital Imaging System (UVP, Upland, CA)) to verify successful PCR amplification. Migration of HFI strain PCR product was compared to the *S. griseoflavus* Tu4000 *hhyL* gene as a positive control and to DNA Molecular Weight Marker X (Roche, Indianapolis, IN) for reference.

Gene sequencing and analysis

PCR products were prepared for sequencing using the Wizard® SV Gel and PCR Clean-Up System (Promega, Madison, WI). DNA concentrations were measured using a Nanodrop ND-1000 (NanoDrop, Wilmington, DE). PCR products were sequenced at the MIT Biopolymers Laboratory (Applied Biosystems Model 3730 capillary DNA sequencer) following their sample preparation guidelines. 16S rRNA gene sequences were compared with the in the National Center for Biotechnology Information (NCBI) gene databases (BLASTN, http://blast.ncbi.nlm.nih.gov) for phylogenetic identification. Hydrogenase *hhyL* sequences were aligned and a 100 bootstrap parsimony tree was constructed using SeaView v4 (Gouy et al., 2010) and rendered using FigTree v1.3.1[2].

H_2 uptake assays

H_2 uptake rates were quantified by measuring the decrease in H_2 mole fractions in the microbial culture headspace as a function of time. Microbial strains were cultivated aerobically on solid or liquid media inside 160 ml glass serum vials. H_2 uptake rate measurements were initiated by isolating the serum vial headspace from the atmosphere with a crimped stopper. Vials were slightly pressurized by adding 15 ml sterile

---

[2] http://tree.bio.ed.ac.uk/software/figtree/

lab air after closure. Liquid cultures were continuously agitated at 200 rpm during the H_2 uptake assay to facilitate gas exchange across the air-liquid interface.

The change in the headspace H_2 mole fraction was measured three times approximately every 40 minutes using a Gas Chromatograph (GC, Model 2014, Shimadzu Co., Kyoto, Japan) that had been retrofit with a Helium ionization Pulsed Discharge Detector (HePDD, D-4-I-SH17-R Model, Valco Instruments Co. Inc., Houston, Texas). The instrument is similar to a system recently described for measuring H_2 at atmospheric levels (approximately 530 ppb) with improved precision, linearity and stability as compared to traditional methods (*e.g.*, GC with a mercuric oxide detector) (Novelli et al., 2009). Details can be found in Appendix B. Stainless steel flasks containing compressed air were used as working standards with ambient H_2 mole fractions. These were calibrated using the GC-HePDD system against a tertiary standard (514.3 ppb H_2 in air, aluminum 150A tank, Airgas, Radnor, PA) tied to the NOAA CMD/ESRL H_2 scale. Precisions, assessed by repeated standard measurements, were typically <1% (1 sigma) on the Shimadzu GC-HePDD.

H_2 uptake followed apparent first-order kinetics over the small range (0.1 to 4 ppm) of laboratory atmospheric H_2 mole fractions: $H_2(t) = H_2(0)e^{-bt}$. First-order rate constants were determined from the slope (-b) of the logarithmic decrease in the headspace H_2 mole fraction. H_2 oxidation rates are reported at a H_2 mole fraction of 530 ppb, the estimated global mean (Novelli et al., 1999). Michaelis-Menten kinetics parameters describe the nature of H_2 uptake over the broad range of H_2 concentrations that occur in soils (H_2 mole fractions ranging from 0.01 to 1000 ppm) (Schink, 1997). K_m and v_{max} were determined for each strain by measuring the linear rate of H_2 for various initial headspace H_2 mole fractions (0.5 to 20 ppm H_2), which were achieved injecting a 1% H_2 in N_2 mix into the sealed headspace. K_m and v_{max} were determined from Lineweaver-Burke plots (x-intercept = $-1/K_m$, y-intercept = $1/v_{max}$, slope = K_m/v_{max}) (Schuler and Conrad, 1990). H_2 uptake thresholds were determined after allowing the cultures to utilize H_2 mole fractions for at least 90 minutes until headspace H_2 mole fractions reached stable values.

Lifecycle analysis of *Streptomyces* spp.

The life cycle stage of cells in *Streptomyces* spp. cultures was tracked in parallel with the H_2 uptake to study the influence of developmental stage of atmospheric H_2 utilization. Serum vials (160 mL) containing 10 ml of R2A medium were inoculated with 100 μl of the spore suspension onto the agar surface. Control vials were supplemented with 100 μl sterile H_2O. The lifecycle state was assessed by microscopy using a Zeiss Axio Imager.M1 microscope and Axio Cam MRm camera using Axio Vision (4.8) software (Zeiss, Peabody, MA).

Growth rates of filamentous organisms grown on solid media are difficult to measure; instead, photographs of the fractional area covered by *Streptomyces* colonies in the serum vial were used as an indication of growth rate (Appendix B). Final aerial biomass was quantified by a protein assay. Aerial biomass was aseptically harvested using a metal spatula and transferred to 1.5 ml tubes containing 0.3 g of glass beads (0.2 mm diameter) and 0.7 ml water. Cells were disrupted by vortexing for 5 min at 2000 rpm followed by cooling on ice, and then by sonication with three 30 s bursts and 1 min intermittent cooling on ice. Residues of membranes and nucleic acids were removed by transferring 0.5 ml of the protein extract to Costar® Spin-X® microcentrifuge filter tubes (Corning, Inc., Corning, NY) and centrifuging at 10,000 rpm for 15 minutes. Protein concentrations were determined using the Pierce BCA protein assay kit (Thermo Scientific, Rockford, IL) and a Synergy 2 Microplate Reader (BioTek, Winooski, VT) controlled by Gen5 (1.04.5) software.

To determine whether the uptake in the aerial fraction (containing hyphae and spores) would persist when separated from the rest of the colony and the medium, glass beads were used to transfer aerial biomass to a sterile glass serum vial containing no medium. At three time points after sporulation (on days 2, 8, and 15), 10 g of 4 mm glass beads were used to transfer aerial biomass to a each fresh vial. H_2 uptake rates were measured in the original serum vial before and after the biomass transfer, and uptake was measured in the sterile vial containing only glass beads and the transferred biomass. The amount of biomass that was transferred was quantified using the described protein extraction procedure.

Life cycle analysis of *R. equi*

The relationship between life cycle, or growth phase, of *R. equi* and atmospheric H_2 utilization by this organism was assessed in a similar fashion as for the *Streptomyces* spp. *R. equi* were inoculated by adding 100 μl of a cell suspension into 20 ml sterile TSB (Bacto^{TM}Triptic soy broth, BD) liquid medium in 160 ml glass serum vials and were incubated shaking at 200 rpm at 30°C. Growth curves were monitored by measuring the optical density (OD) (*i.e.*, the absorbance of *R. equi* cultures at 600 nm at 25°C in the Synergy 2 Microplate Reader). The relationship between OD and protein concentration was established by constructing a calibration curve between OD measurements of serial dilutions with known protein concentrations. *R. equi* protein concentrations were determined using the same general procedure as described for the *Streptomyces* spp.

H_2 uptake by *R. equi* was generally low. A concentration/dilution experiment was performed to test whether the negligible H_2 oxidation rates at low cell densities in early exponential growth phase were the result of a lack of H_2 oxidation activity or the low signal-to-noise ratio due to the small number of active cells. *R. equi* cultures were inoculated at the beginning of the experiment, concentrated in exponential phase on day 1.9 by centrifugation at 8000 rpm for 10 min, and re-suspended in either fresh TSB or in sterile H_2O to a final cellular density similar to those observed in stationary phase. Additionally, a sample was taken on day 7.8 in stationary phase when cultures were quite dense and was diluted in TSB or sterile H_2O to cellular densities resembling the early exponential phase. In both cases, H_2 uptake rates in the concentration/dilution samples were measured and protein concentrations were measured as described above.

5.3 Results

Enrichments of sporulating soil organisms and subsequent morphological screening produced a set of candidate *Streptomyces* spp. isolates referred to as Harvard Forest Isolate (HFI) strains. HFI strains were tested for the possession of the high-affinity [NiFe]-hydrogenase by PCR amplification and gel electrophoresis of the *hhyL* gene. Out of nine HFI strains, six contained the *hhyL* gene, and four strains (*Streptomyces* sp. HFI6-9) were retained to verify H_2 uptake activity. These HFI strains exhibited distinctive *Streptomyces* traits: a fuzzy appearance due to the formation of aerial hyphae, pigmentation of cellular material and/or the agar, and the unmistakable earthy scent of geosmin (strains shown in Appendix B, Figure B-3). Indeed, the 16S rRNA sequences of *Streptomyces* sp. HFI5-8 exhibited high sequence similarity (BLASTn search against the 16S rRNA database resulted in at least 73% maximum identity and E-values $< 10^{-22}$ similarity to known *Streptomyces* spp.) to the 16S rRNA of organisms from the genus *Streptomyces* (Rao, 2012). To date, the sequencing of the 16S rRNA of strain HFI9 has not been successful, but it exhibits the morphological characteristics of a *Streptomyces* sp.

The *hhyL* sequences of HFI strains and other published representatives are compared in the amino acid tree shown in Figure 5-1. The gene is not phylogenetically conserved, implying acquisition by horizontal gene transfer, and its genetic mobility has been discussed (Constant et al., 2011b). The available sequences group into three clusters (Cluster 1, Cluster 2, and Distant) based on a deeply rooted split (98% of bootstrap replicates) that divides the *hhyL*-containing *Streptomyces* spp. Clusters are not strictly phylogenetic (*e.g.*, *Streptomyces* spp. reside in both Cluster 1 and 2). Clusters 1 and 2 contain many common soil bacteria, with representation from the phyla *Actinobacteria*, *Chloroflexi*, *Planctomycetes*, *Verrucomicrobia*, and *Proteobacteria*. Members of the Distant cluster include both archaea (*Chrenarchaeota*, *Euryarchaeota*) and bacteria (*Firmicutes*, *Proteobacteria*, *Bacteroidetes*). The Distant group is largely made up of extremophiles, and their hydrogenase is likely involved in sulfur metabolism. The Distant group hydrogenase most likely does not belong to

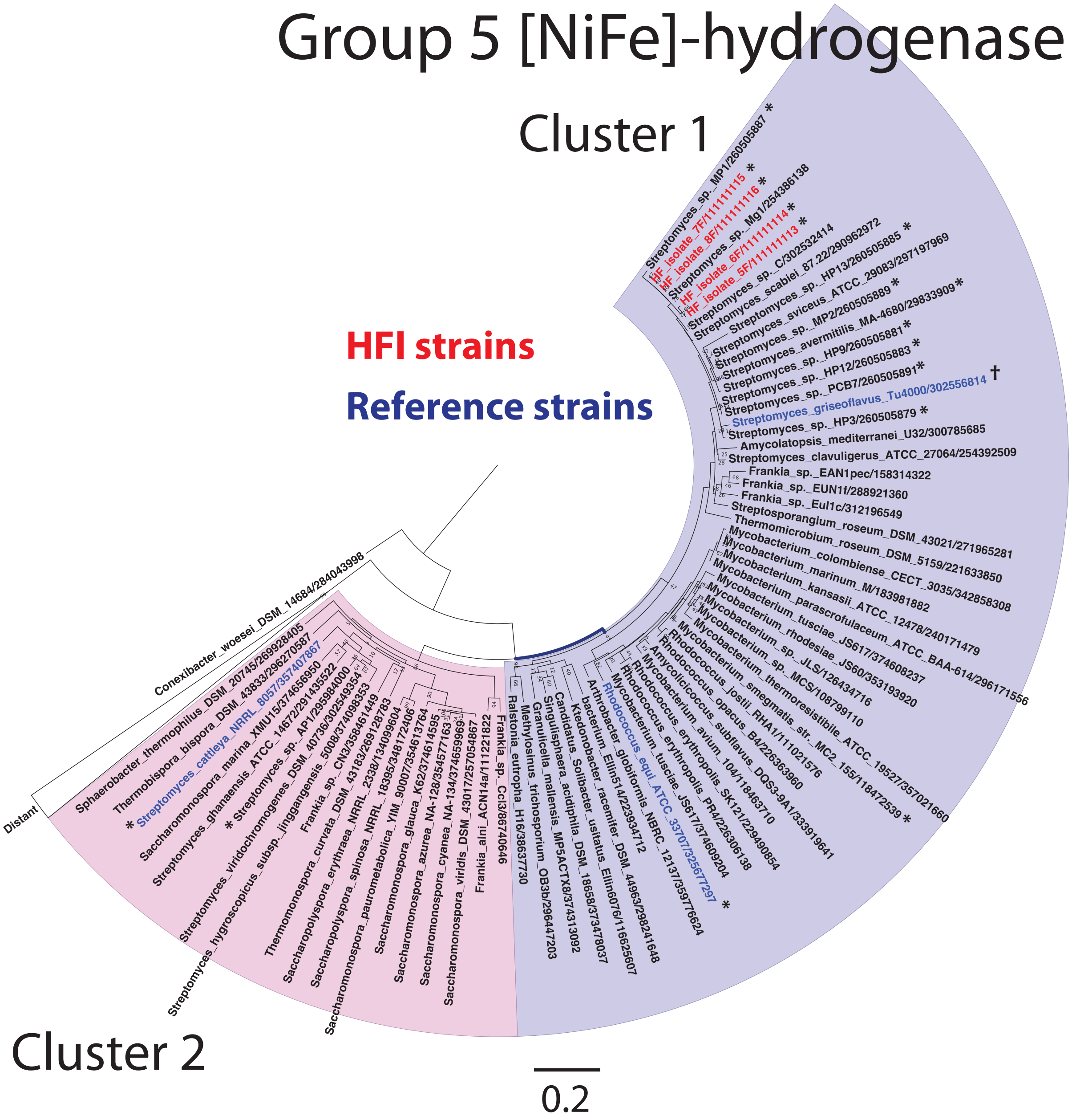

Figure 5-1: Group 5 [NiFe]-hydrogenase amino acid parsimony tree of published strains from the NCBI database cluster into two distinct clusters: Cluster 1 and Cluster 2. A more Distantly related group contains extremeophile bacteria and archaea with a different hydrogenase likely involved in sulfur cycling. Reference strains used in this study (blue) are *Streptomyces griseoflavus* Tu4000 (Cluster 1), *Rhodococcus equi* (Cluster 1), and *Streptomyces cattleya* (Cluster 2). *Streptomyces* spp. HFI hydrogenase sequences (red) group with other *Streptomyces* spp. soil isolates with demonstrated H_2 uptake. Strains that have demonstrated (asterisk) or not demonstrated (dagger) high-affinity H_2 oxidation when tested are marked. The distant cluster contains both bacteria and archaea that typically inhabit extreme environments. The tree was rooted using *Conexibacter woesi*, an *Actinobacteria*.

Table 5.1: H_2 uptake kinetic parameters for reference and Harvard Forest Isolate (HFI) strains. *No uptake was observed for *S. griseoflavus* Tu4000 so no kinetic parameters or threshold are reported.

Strain	**H_2 oxidation rate** [nmol min^{-1} g^{-1}]	**Km** [ppm]	**vmax** [ppm min^{-1}]	**threshold** [ppb]
Streptomyces sp. HFI 6	780	80	1	150
Streptomyces sp. HFI 7	420	80	2	70
Streptomyces sp. HFI 8	240	40	0.7	150
Streptomyces sp. HFI 9	100	40	0.7	120
S. griseoflavus Tu4000	0*	-	-	-
Streptomyces cattleya	130	460	3	TBD
Rhodococcus equi	10	160	1	TBD

the novel group 5 hydrogenase (Constant et al., 2011b). The tree was rooted using *Conexibacter woesi*, an *Actinobacteria*.

Streptomyces sp. HFI6-9 *hhyL* sequences group in Cluster 1 and exhibit high sequence similarity to other *Streptomyces* spp. soil isolates with demonstrated H_2 uptake functionality. The *hhyL* sequence of reference strain *S. griseoflavus* Tu4000 is closely related to HFI strains and to other *Streptomyces* spp. in Cluster 1. In contrast, the *hhyL* of *S. cattleya* groups with Cluster 2, thereby exhibiting genetic divergence of the *hhyL* sequences of HFI strains. To date, whether or not the *hhyL* divergence between Cluster 1 and 2 has any consequence for functionality is unknown. Finally, although *R. equi* represents a different genus within the *Actinobacteria*, its *hhyL* clusters with the sequences of known H_2-oxidizing *Streptomyces* spp. soil isolates (Cluster 1).

To address the first hypothesis in this study, namely that the presence of a group 5 [NiFe]-hydrogenase predicts atmospheric H_2 uptake, *hhyL* containing HFI strains 6-9 and the reference strains were tested for H_2 oxidation activity. H_2 oxidation rates presented in Table 5.1 are weighted by biomass (final protein mass). We found that the presence of the high-affinity hydrogenase predicted atmospheric H_2 uptake activity in the HFI strains. Interestingly, reference strain *S. griseoflavus* Tu4000 did not utilize atmospheric H_2 under experimental conditions, despite possessing a *hhyL* sequence from Cluster 1 (Figure 5-1). In contrast, *S. cattleya*, whose *hhyL* clusters with sequences from Cluster 2 (Figure 5-1), did demonstrate high-affinity H_2 uptake at rates comparable to strain HFI9. Likewise, reference strain *R. equi* utilized atmospheric H_2, both on solid (R2A) and liquid (TSB) media, albeit at rates at least tenfold lower than the *Streptomyces* spp. In summary, presence of the *hhyL* gene did predict atmospheric H_2 uptake functionality in the HFI strains and reference strains tested, with the exception of *S. griseoflavus* Tu4000.

Michaelis-Menten enzyme kinetic parameters were determined from the relationship between first-order H_2 uptake rates and initial headspace H_2 concentrations (0.5 to 20 ppm H_2). The maximum uptake rate (vmax) and substrate concentration at half maximum rate (Km) for each strain are listed in Table 5.1. Km values were typically low (40-80 ppm for HFI strains), indicating that enzymatic processing of H_2 is tuned to operate efficiently at atmospheric levels of H_2 (high-affinity uptake). Interestingly, both *S. cattleya* and *R. equi* had intermediate Km values (between 100 and 1000 ppm); this supports recent observations that H_2 consuming microorganisms exhibit a continuum of affinities rather than a discrete grouping of high and low affinities (Philippe Constant, personal communication). The minimum H_2 concentration, or threshold, that can be utilized by each strain (70 to 150 ppb) was found to be well below atmospheric mole fractions (530 ppb).

Next, we asked whether high-affinity H_2 utilization depended on the developmental stage of *Streptomyces* spp., using strain HFI8. Three replicates were used for H_2 oxidation measurements over a 44-day period, and a fourth replicate was used to determine the developmental lifecycle stage by microscopy as shown in Figure 5-2.

Following germination, the colony produced substrate mycelia (filaments growing on top of and into agar) throughout day 1 (A, B). By day 1.8 (C) the colony had undergone two transformations: 1) differentiation to form aerial hyphae, the specialized hydrophobic branches supported physically and nutritionally by the substrate mycelia, and 2) sporulation, whereby spores are formed in septated compartments of aerial hyphae. Figure 5-2-C shows both partially septated aerial hyphae (punctuated tubular branches) and fully formed spores (round cells). The remaining images from

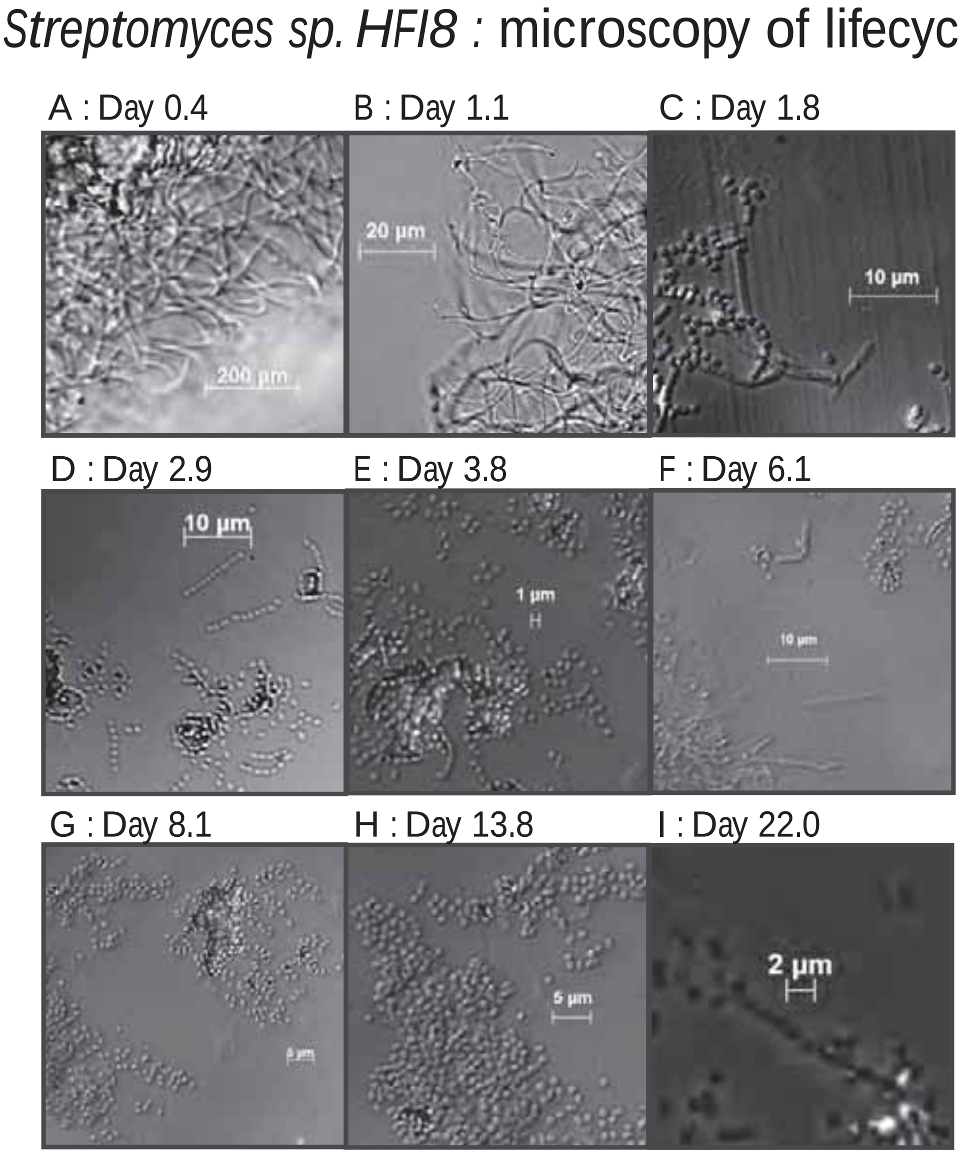

Figure 5-2: Microscopic observations of the developmental lifecycle stage of *Streptomyces* sp. HFI8 as a function of days since culture inoculation. Images A and B show substrate mycelia growing in the first day following germination of the spore inoculum. By day 1.8 (C), septating aerial hyphae and fully formed spores are observed. Colony cells are predominantly observed to exist as dormant spores from day 2.9 to 22 (D-I). Some branch-like cells were also observed over this period (*e.g.*, day 6.1, F), which are likely old aerial hyphae (did not septate) or old substrate mycelia.

day 2.9 to 22 (D-I) show colony cells predominantly remaining as dormant spores thereafter. Some branch-like cells were also observed over this period (*e.g.*, day 6.1, F), which are likely old aerial hyphae (hyphae that did not septate) or old substrate mycelia. These structures are likely tubular remnants of substrate and aerial branches, which resemble the fresh structures in phase-contrast microscopy (Miguélez et al., 1999). These microscopic observations indicate that strain HFI8 undergoes the full lifecycle from spore to spore in less than 1.8 days, after which nearly all viable cells exist as spores for the remaining 40 days of study.

The time series of H_2 oxidation rates for strain HFI8 is shown in Figure 5-3. H_2 uptake was measured approximately twice daily for the first four days (inset, Figure 5-3) as the colony progressed through its developmental cycle. Measurements were made less frequently during the remaining 40 days because the colony remained in the spore state. H_2 uptake began around day 2 and increased dramatically up to the maximum uptake rates (25 ± 6 ppb min^{-1}) around day 4, and then slowly decreased over the next 40 days to negligible levels (below detection limit of 0.9 ppb min^{-1}). All replicates displayed similar timing, but replicate 3 demonstrated systematically lower uptake rates by about 50% although the area coverage of the colony and biomass were not demonstrably different than the other replicates.

Together, the H_2 uptake and microscopy time series show that strain HFI8 did not utilize H_2 during the formation of substrate mycelium, although the maximal area extent of colony biomass had already been achieved (Appendix B, Figure B-5). Only after the formation of aerial hyphae and the onset of sporulation was H_2 utilization observed. Interestingly, strain HFI8 exhibited the highest H_2 oxidation rates on day 3.8, two days after sporulation had begun. H_2 oxidation rates declined slowly to zero after this peak. The cells were in a dormant spore state over this entire time. These results show a clear correlation between H_2 uptake and a *Streptomyces* sp. life cycle state.

To test whether H_2 uptake differed for the aerial fraction of the colony (spores and aerial hyphae) with and without contact with the medium, glass beads were used to transfer aerial biomass to empty vials. Table 5.2 lists H_2 oxidation rates of intact

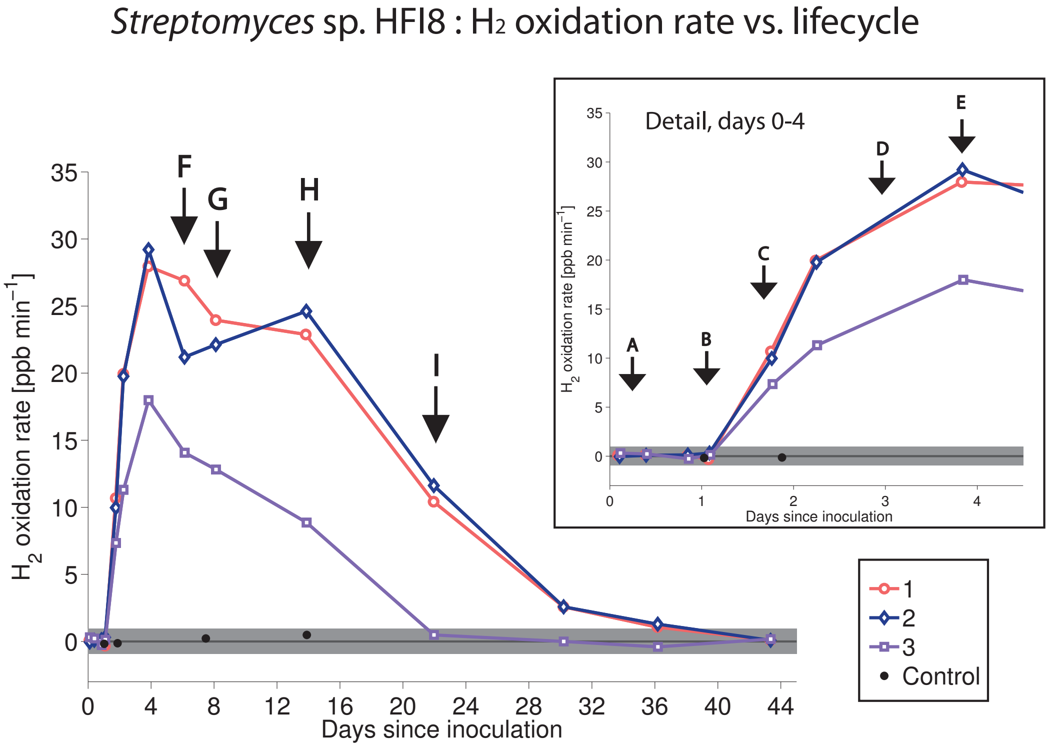

Figure 5-3: H_2 oxidation rate plotted as a function of days since inoculation for *Streptomyces* sp. HFI8. Corresponding microscopy images depicting the lifecycle state (Figure 5-2) are denoted by lettered arrows. Inset shows the first four days in detail. Following the spore germination, no significant H_2 uptake occurred during the formation of the substrate mycelium (A, B), although the maximum area extent of culture on the agar surface had been achieved by timepoint B. Instead, significant H_2 uptake in all three replicates was only observed after the formation of aerial hyphae and onset of sporulation (C). The mature colony remained as dormant spores for the remainder of the experiment (D-L). Uptake reached maximum rates on day 4 and gradually diminished to zero after approximately one month. H_2 uptake rates calculated for the medium-only vial were on the order of 1 ppb min^{-1}, this was adopted as the detection limit for uptake rate tests (grey shading).

Table 5.2: *Streptomyces* sp. HFI8 H_2 uptake [ppb min^{-1}] before (in original vial on R2A medium) and immediately after the transfer of aerial biomass using glass beads. The H_2 uptake activity is reported for the fraction transferred to glass beads, that remaining on the media in the original vial, and the difference in uptake due to transfer (final total minus original). H_2 uptake by aerial biomass on glass beads was measured each week for up to three weeks and these measurements are reported in parentheses.

Replicate	**Before transfer**	**After transfer** (after 1/2/3 weeks)	**Remainder on medium**	**Diffference** [ppb min^{-1}, % original]
1	11.0	1.2 (0.1/0.0/0.1)	2.9	-7.0,-64%
2	18.3	0.9 (0.9/0.4/na)	7.8	-9.6, -52%
3	18.5	0.8 (-0.1/na/na)	3.1	-14.6, -79%

colonies (before transfer) for each of three replicates of *Streptomyces* sp. HFI8. Each replicate (1, 2, 3) was analyzed on separate days after the inoculation (day 2, 8, and 15). Directly after measurement, aerial biomass was transferred to an empty vial using glass beads. H_2 oxidation rates of the aerial biomass on the glass beads (after transfer) and of biomass remaining on the medium (remainder on medium) were measured. Unexpectedly, net H_2 uptake activity was lost in all cases (between 52% and 79% of the original rates) upon transfer of aerial biomass to fresh vials. Very low levels of H_2 uptake activity were transferred to the glass beads (around the detection limit of 0.9 ppb min^{-1}), and uptake did not persist significantly during subsequent weeks.

Next, we probed the relationship between the H_2 oxidation rate and growth stage of a second *Actinobacterium*, *R. equi.* Unlike *Streptomyces* spp., this microbe does not form spores or have such a complex developmental cycle. Figure 5-4 shows the time series of H_2 oxidation rates (a) and of the growth curve (b) of *R. equi*. *R. equi* did not consume measurable quantities of H_2 during the early exponential growth phase (from inoculation to day 3). In late exponential phase (after the inflection point around day 3.5, Figure 5-4) significant atmospheric H_2 utilization (0.91±0.03 ppb min^{-1}) was first observed. H_2 uptake increased to the maximum rates (2.5±0.4

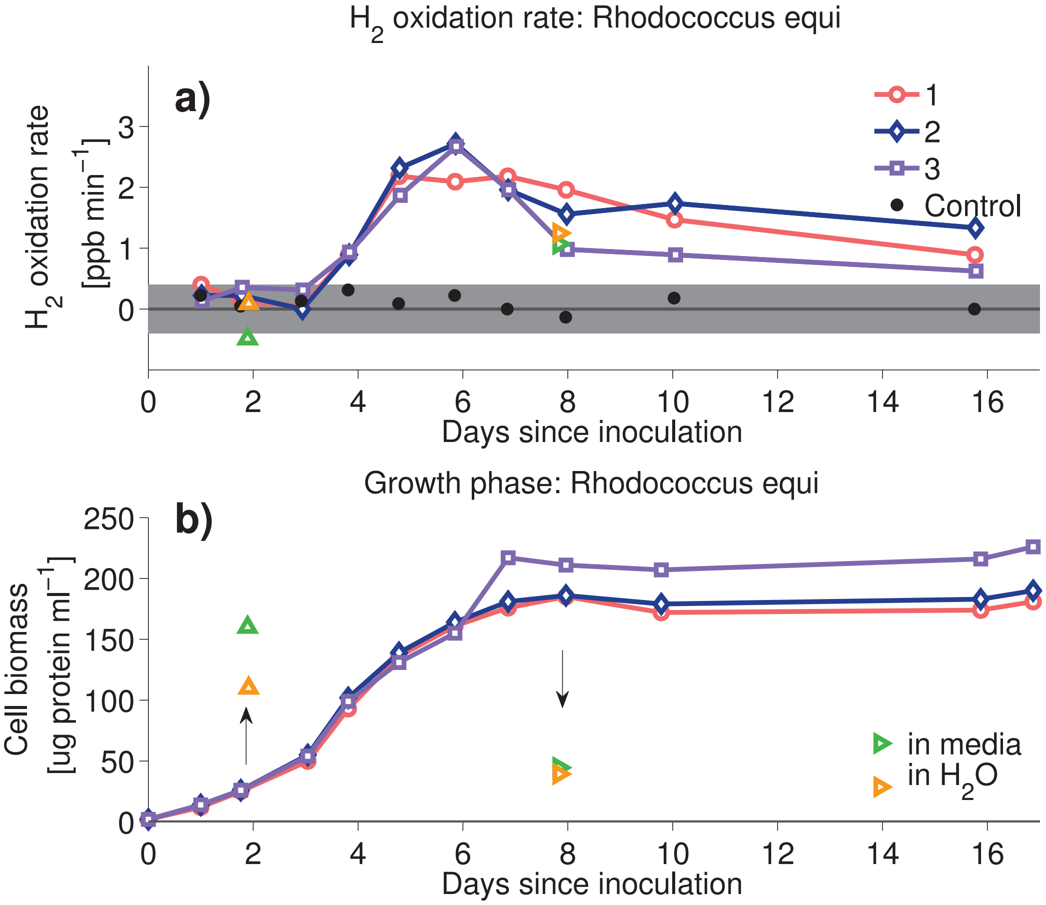

Figure 5-4: H_2 oxidation rate (a) plotted as a function of days since *Rhodococcus equi* inoculation and a corresponding plot of cell biomass (protein concentration) over time (b) to indicate the growth phase. Significant H_2 oxidation rates did not occur until day 4, about mid-way through the exponential growth phase as generation times had begun to decrease. H_2 oxidation rates were highest during late exponential and early stationary phase, and persisted for at least nine days in stationary phase. Triangles represent concentration and dilution experiments where cells from early exponential phase (day 2) were concentrated and from stationary phase (day 8) were diluted in either fresh TSB media (green) or water (black) to determine whether H_2 oxidation rates would be detectable by the GC-based method.

ppb min^{-1}) on day 5.8 just before *R. equi* entered stationary phase. H_2 oxidation rates declined slightly in stationary phase, but persisted for the last nine days of measurements during stationary phase.

The growth characteristics of *R. equi* were correlated with H_2 utilization rates; however, because *R. equi* H_2 oxidation rates were approximately ten-fold lower than those of *Streptomyces* spp. HFI, they were much closer to the detection limit (0.3 ppb min^{-1}) of the measurement. This imparts ambiguity to the H_2 uptake measurements on the first three days of observations. Namely, H_2 oxidation rates could be below the limit of detection because 1) low cell densities masked H_2 oxidation activity or 2) cells did not actively utilize atmospheric H_2 at low cell densities in early exponential phase. To differentiate between these two alternatives, two experiments were conducted. First, cells in early exponential phase (day 1.9) were concentrated into either fresh media or sterile water to cell densities (Figure 5-4b) representative of the late exponential phase (days 4-6) when H_2 oxidation rates were significant (0.9-2.5 ppb min^{-1}). These concentrated cultures did not consume H_2 (Figure 5-4a -0.2±0.4 ppm min^{-1}). In the second test, cells in stationary phase (day 7.8) were diluted (into media or water) to cell densities representative of early exponential phase (days 2-3) when H_2 oxidation rates were below the limit of detection (0.3 ppb min^{-1}). These diluted stationary phase cultures took up H_2 at detectable levels (1.1±0.1 ppb min^{-1}). Both tests indicate that the cells in early exponential phase did not consume H_2. Therefore, H_2 oxidation by *R. equi* was also found to be tied to growth phase, and occurred only in the late stages of exponential growth and during stationary phase.

5.4 Discussion

The first part of this study tested the ability to predict H_2 uptake by probing for the *hhyL* gene. We found that the presence of the hydrogenase in six out of seven tested isolates and reference strains predicted high-affinity low-threshold atmospheric H_2 oxidation activity (Table 1). The isolation procedure yielded a high percentage of H_2 oxidizing isolates (approximately 50% of candidates). These HFI strains exhibited high hydrogenase sequence similarity with other published high-affinity H_2 oxidizing *Streptomyces* spp. from Cluster 1 (Figure 1). Reference strains *S. cattleya* and *R. equi* that represent a different cluster (Cluster 2) and a different genus within the *Actinobacteria*, respectively, also exhibited high-affinity H_2 oxidation. Similarly, previous work has demonstrated atmospheric H_2 utilization in both a Cluster 2 (*Streptomyces* sp. AP1) and a Cluster 1 (*Mycobacterium smegmatis*) representative (Constant et al., 2011b; Berney and Cook, 2010). Collectively, the environmental isolates and reference strains tested in this study lend additional support to the hypothesis that the presence of the *hhyL* gene predicts high-affinity H_2 oxidation activity. Future studies should test whether H_2 uptake occurs in the other phyla containing the *hhyL* gene, such as *Chloroflexi*, *Planctomycetes*, *Verrucomicrobia*, and *Proteobacteria*.

The relationship between life cycle and high-affinity H_2 utilization was supported by high-resolution activity measurements of H_2 uptake by an environmental isolate, *Streptomyces* sp. HFI8. In previous work, higher H_2 uptake rates were reported for colonies of *Streptomyces* sp. PCB7 that had produced spores when grown on solid medium than for substrate mycelia grown in broth, which generally does not support sporulation (Constant et al., 2011a). Our high resolution measurements showed no atmospheric H_2 oxidation in *Streptomyces* sp. HFI8 during its substrate mycelium stage. Only after colony differentiation into aerial hyphae and spores, was H_2 uptake observed. The two differentiation processes occur nearly simultaneously in this strain, making it difficult to resolve whether uptake is initiated in the aerial hyphae formation or sporulation phase. A *whi* mutant strain, which produces aerial hyphae, but does not sporulate, could be isolated and used to explore this further. Our results add to the growing body of evidence for a life cycle dependency of H_2 oxidation in *Streptomyces* spp. This study presents the most detailed and lengthy analysis of H_2 consumption of a *Streptomyces* strain as it progresses through its life cycle.

Utilization of atmospheric H_2 by dormant spores may have interesting consequences for both the organism and the cycling of H_2 in the environment. We observed that H_2 oxidation rates continued to increase for two days after sporulation has already commenced. This could reflect heterogeneity in the sample (not all cells sporulate simultaneously) or could reflect an active energy metabolism in spores. Afterwards, significant H_2 oxidation persisted for over a month, such that the time-integrated H_2 oxidation of cells was much larger in the spore state than any other stage in the life cycle. Even with the conservative assumption that sporulation was not complete until the maximum consumption rate was observed on day four, the net H_2 consumption was at least tenfold larger in the spore state than the germination, substrate mycelium, and unsporulated aerial hyphae states combined. It is not clear whether this time-integrated consumption of H_2 is an energetic benefit to the dormant spores or other parts of the colony (substrate mycelium, aerial hyphae), although the latter should have largely been cannibalized at this point (Miguélez et al., 1999). Both the long duration of H_2 uptake by sporulated cultures and its eventual termination are surprising, and are a novel contribution made by this life cycle analysis extended roughly one and a half months. These results have unintuitive implications for environmental H_2 cycling if H_2 oxidation by *Streptomyces* spp. is highest during sporulation and persists for over one month as long as the spores do not germinate. Soil moisture and nutrient conditions that are favorable for microbial growth may actually limit the amount of H_2 oxidized by *Streptomyces* spp.. Future laboratory and environmental studies could contribute greatly to this unresolved question.

In this study, *S. griseoflavus* Tu4000 was the only strain that did not demonstrate high-affinity H_2 oxidation, although this organism also contains a *hhyL* similar to those of atmospheric H_2 oxidizing *Streptomyces* spp. This departure from the hypothesis may actually refine insight into the H_2 uptake behavior of *Streptomyces.* In culture, *S. griseoflavus* Tu4000 is smooth and waxy, instead of having the diffuse fuzzy appearance of other cultures imbibed by their aerial hyphae. *S. griseoflavus* Tu4000 appears to belong to a class of bald (*bld*) mutants that are deficient in aerial hyphae production. Although there can be many factors within the regulatory cascade at play, the mutants are often γ-butyrolactone factor deficient (Chater and Horinouchi, 2003), and do not exhibit a number of secondary phenotypes including the production of pigments, antibiotics, or geosmin (Schrempf, 2008). Indeed, we did not observe the production of aerial hyphae, pigments, or geosmin in *S. griseoflavus* Tu4000. We propose that the bypass of the aerial hyphae stage, and the resulting poor sporulation efficiency, may also impair the production or activity of the high-affinity hydrogenase in *S. griseoflavus* Tu4000.

To our knowledge, *S. griseoflavus* Tu4000 is the first *hhyL*-containing *Streptomyces* sp. not found to perform high-affinity H_2 oxidation. Similarly, *Ralstonia eutropha* H16 (Cluster 1, *Proteobacteria*) did not oxidize atmospheric H_2, which could occur if the hydrogenase is not produced or active under the experimental growth conditions (Conrad et al., 1983; Constant et al., 2011b). Furthermore, an *in silico* study has identified reference genomes containing the *hhyL* gene, but lacking potentially crucial auxiliary hydrogenase maturation proteins, although the lack of H_2 uptake has not been demonstrated (Constant et al., 2011b). Production of aerial hyphae has been stimulated in bald (*bld*) *Streptomyces* spp. mutants, including *S. griseoflavus* Tu4000, by application of exogenous gamma-butyrolactone factor (Straight and Kolter, 2009; Ueda, 2000). In future work, we plan to stimulate aerial hyphae production in *S. griseoflavus* Tu4000 to determine whether high-affinity H_2 oxidation activity is then released from latency.

We find evidence that the *Streptomyces* colony structure may be important for H_2 uptake, which has not been reported before. Very little H_2 oxidation activity was transferred with the aerial biomass (spores and remnant aerial hyphae) of a *Streptomyces* colony when separated from the substrate biomass. Higher rates of H_2 oxidation remained in the original vial containing the substrate mycelia and any remnant aerial biomass. It is possible that the high-affinity hydrogenase is located in the substrate mycelia (but is only active during and after aerial hyphae formation). The group 5 [NiFe]-hydrogenase is expected to either be soluble or anchored to an internal membrane-bound electron acceptor (Constant et al., 2011b). However, the process of transferring aerial biomass to a fresh vial using glass beads resulted in at least a 50% net loss in H_2 oxidation rates. No biomass was lost in the transfer, so the net loss in uptake must have arisen via other mechanisms, such as from the loss of structural support, colony signaling and nutrient transport, or surface area after being crushed by glass beads. We did not find a correlation of this to the surface area of beads used for the transfer. This may suggest that it was the destruction of the *Streptomyces* colony structure that reduced uptake rates. The aerial hyphae and spores are supported both physically and nutritionally by the substrate mycelia (Miguélez et al., 1999). Nutrients and moisture are transported to aerial biomass via the tubular structures that encased substrate mycelia, which were cannibalized during aerial hyphae formation. Additionally, signaling within the colony is important for coordinating many processes including metabolic functions. Future studies should more carefully dissect the various components of the complex *Streptomyces* colony to determine where H_2 consumption activities occurs and whether preservation of the colony structure is required to maintain function.

In the case of *R. equi*, a non-sporulating *Actinobacteria*, high-affinity H_2 oxidation only occurred during late exponential and stationary phase. The net growth rate slows and eventually ceases during this period because of nutrient limitation or the accumulation of inhibitory products. This is analogous to our observations that H_2 consumption in *Streptomyces* sp. HFI8 occurs during the stages associated with environmental stress and nutrient limitation. Interestingly, previous work on *M. smegmatis*, a closely related non-sporulating *Actinobacteria* containing a Cluster 1 high-affinity [NiFe]-hydrogenase, found that the microbe expresses the hydrogenase gene under starvation conditions (Berney and Cook, 2010). In fact, its growth yield is significantly reduced by inactivation of the hydrogenase. *M. smegmatis* is notable for its ability to persist for many years in host tissue in a nutrient-deprived stationary phase (Smeulders et al., 1999). The ability to scavenge low concentrations of H_2 may be an important adaptation for *M. smegmatis*, *R. equi*, and *Streptomyces* spp., which share common lifestyle characteristics in eukaryotic tissues and in the soil environment where nutrients may be low for extended periods (Smeulders et al., 1999; Prescott, 1991; Scherr and Nguyen, 2009). Thus, despite differences in growth cycles, we propose that the utilization of low concentrations of H_2 by these organisms may be a common mechanism for survival under stress in these *Actinobacteria* over a broad range of environments.

We must gain an understanding of the behavior of the other representatives (within the *Actinobacteria*, different phyla, different clusters) containing the high-affinity hydrogenase to determine whether they are key players in global H_2 cycling. Furthermore, little is known regarding the response of the diverse atmospheric H_2 utilizing strains under various factors of environmental control. Lab studies should focus also on isolates and communities in the mesocosm environment to determine whether the life cycle state still imparts a strong influence in soil where environmental and nutrient conditions are highly heterogeneous. Studies contributing in these areas are needed to build a mechanistic understanding of the microbial driving force behind the significant soil sink of atmospheric H_2.

5.5 Conclusion

In this study, laboratory experiments using environmental isolates and reference strains were designed to address two overarching questions: 1) is the *hhyL* novel group 5 [NiFe]-hydrogenase gene predictive of atmospheric H_2 uptake and 2) is H_2 oxidation activated at specific stages in the organismal life cycle or growth phase? We find that the *hhyL* gene predicts high-affinity H_2 oxidation in all *Streptomyces* spp. environmental isolates tested, in reference strain *S. cattleya* from a different *hhyL* cluster, and reference strain *R. equi*, an *Actinobacterium* with a genus and life cycle distinct from *Streptomyces*. However, we find a *hhyL*-containing reference strain *S. griseoflavus* Tu4000 strain, which is bald-type and thus bypasses differentiation into the aerial hyphae life cycle state, did not oxidize atmospheric H_2. This unexpected result is congruent with our observation that H_2 oxidation in *Streptomyces* sp. HFI8 is tightly regulated by the organism's complex developmental lifecycle and only occurs with the formation of aerial hyphae and sporulation. H_2 oxidation by dormant spores persists for about one month, and our observations suggest that the physical structure of the sporulated colony may be important for H_2 utilization. The growth phase of a second *Actinobacterium*, *R. equi*, was also linked to H_2 uptake; cultures only utilized H_2 in nutrient-limiting conditions during late exponential and stationary phase.

These observations suggest that various *Actinobacteria* utilize atmospheric levels of H_2 during growth stages associated with low energy or nutrient limiting conditions.

Our findings contribute to the basic understanding of the microbiology driving the H_2 soil sink; however, many outstanding questions remain. Future studies that test the predictive power for H_2 consumption of the *hhyL* gene or other molecular markers for the high-affinity group 5 hydrogenase will not only add to our understanding of which organisms play an important role in global H_2 cycle, but also will provide tools for their study. Additionally, future work to characterize the interplay between the life cycle stage, environmental influence, and H_2 consumption for a variety of bacteria will add to a process-based understanding of the significant H_2 soil sink. Microbe-mediated H_2 exchange between the soil and atmosphere is a complex, but important, process that can be studied on many scales. This problem embodies the scientific challenge of understanding the key processes driving exchange of many important trace gases between the biosphere and atmosphere. The impact of these processes on the Earth's climate cannot be understated, and future efforts on the microbial, ecosystem, and global scales are needed.

5.6 Future work

We hope to show that *S. griseoflavus* Tu4000 does not utilize atmospheric H_2 because of it does not differentiate to form aerial hyphae (AH). We have observed this correlation, but have certainly not shown cause and effect. If we can stimulate AH production in *S. griseoflavus* Tu4000 by supplying exogenous bioactive molecules to signal for differentiation into AH, we can test either whether H_2 oxidation occurs or whether the hydrogenase is expressed, or both. Conducting this test will make our results much more conclusive.

Already, we have stimulated some production of AH in *S. griseoflavus* Tu4000 by transplanting agar plugs from strain HFI7, strain HFI8, and *Streptomyces* sviceus to *S. griseoflavus* Tu4000 cultures at different time intervals after inoculation. The results show that the bioactive molecules from other *Streptomyces* spp. can diffuse through agar plugs and stimulate limited AH formation in *S. griseoflavus* Tu4000. photo

In our future work, we will attempt to enhance the amount of AH formation and then determine whether the revival of AH in *S. griseoflavus* Tu4000 also initiates atmospheric H_2 oxidation. If AH production is too minimal for H_2 oxidation to be detected, we could also test whether the *hhyL* is expressed, which may be a more sensitive test. In that case, we would test for *hhyL* expression in *S. griseoflavus* Tu4000 control cultures and cultures with at least some AH production stimulated by bioactive molecules from another *Streptomyces* sp. A second control would be to test a medium plate with a plug from another *Streptomyces* to make sure that the *hhyL* mRNA does not appreciably diffuse to where *S. griseoflavus* Tu4000 is grown and create a false positive.

Chapter 6

Conclusions

The scientific objective is outlined and a list of the major results are listed at the beginning of each science chapter (Chapter 2-5) in this dissertation, and chapter conclusions are drawn at the end of each of those chapters. A summary of conclusions and suggestions for future work are given here.

6.1 Summary of results

The overarching goal of the outlined thesis project was to contribute to the process-based understanding of the H_2 soil sink with targeted field and laboratory measurements.

The field measurements were achieved by designing and building a custom automated instrument to measure gradients of H_2 to high precision for the calculation of H_2 fluxes above and below the forest canopy (Chapter 2). Concurrent measurements were made to infer the turbulent eddy coefficient by similarity or parameterization methods, which was then used in the calculation of H_2 fluxes. The instrument was critically evaluated and performance met and exceeded expectations (*e.g.*, H_2 mole fraction precisions were a ten-fold improvement over traditional methods). Three methods for calculating H_2 fluxes were tested to determine the optimal procedures.

The seasonality and magnitude of time series of H_2 mole fractions and fluxes agree well with existing data sets (Chapter 3). As is expected from the literature, soil uptake dominates annual H_2 ecosystem exchange and temperature is an important controlling variable for H_2 uptake. The role of soil moisture was less straightforward, and will require future efforts to characterize. The timing and magnitude of H_2 fluxes agree relatively well with literature values, and discrepancies could be due to calibration scale differences between the data sets. Emissions of H_2 from the soils were observed in the winter and spring, which is likely the result of anoxic export of H_2 produced by fermentation. Unexpectedly, H_2 emissions originating in the forest canopy dominated the net H_2 ecosystem exchange in the fall, and were a possible contribution to Summer fluxes. Possible mechanisms for canopy H_2 emissions could include photo-thermal degradation of organic matter, leaf senescence, microbiological processes in the canopy or trees, or a completely unforeseen mechanism.

The persistence of H_2 soil uptake over two winters of extremes was studied in detail (Chapter 4). Wintertime soil H_2 uptake was higher in a colder winter with an enduring snowpack (up to 70 cm depth) than a warmer relatively snow-free winter in which soils frequently cycled through the freeze-thaw transition. This unintuitive result is explained by the insulating properties of snowpack, which by protecting the soil microbial community from freezing air temperatures, promotes microbiogeochemical trace gas cycling.

In the lab, atmospheric H_2-oxidizing microorganisms were isolated and their H_2 uptake characteristics were measured (Chapter 5). We found that the genetic potential for atmospheric H_2 uptake predicted H_2 consumption activity in environmental isolates and reference strains. Furthermore, two soil *Actinobacteria* with diverse life styles and life cycles were found to utilize H_2 only at specific life cycle junctures, which were correlated with starvation conditions. Therefore, we find that atmospheric H_2 may be an important energetic supplement to soil microorganisms in nutrient-limited conditions. In addition to a novel set of field measurements, this thesis makes contributions to the understanding of the microbiology driving the significant H_2 soil sink.

6.2 Contributions

The know-how for constructing the instrument system that the measurements are described in detail in this thesis, and data will be made available in the Harvard Forest Data Archive. This study is a proof-of-concept for the GC-HePDD; the detector was found to be stable over the study period and was found to perform well in the field for ecosystem-scale investigations, which is a first-in-kind application for a GC-HePDD optimized for H_2 measurements.

The H_2 mole fraction data could be incorporated into regional or global models if desired. The ability to cross-check the flux-gradient method for CO_2 and H_2O with eddy flux measurements contributes an example to the literature of how this method can work well. These are the first H_2 gradient measurements above a forest canopy that are only separated by 4 m vertically. The quantification of gradients in this situation with the GC-HePDD provides a literature example of the magnitude of gradients to expect in such an ecosystem. This may be useful for future instrument construction.

This thesis contributes the most comprehensive data set of ecosystem-scale H_2 exchange to date because of the automated, high-frequency nature of the data, the measurement of fluxes both above and below the forest canopy, and the abundance of other measurements at Harvard Forest for correlation tests. These data can be used to build process-based models of the H_2 soil sink, or to test existing models.

The quantification of H_2 emissions in the winter and spring, perhaps due to anaerobic production, contributes a new estimate of the process to the literature, which can be combined with observations by Constant et al. (2008a); Mastepanov et al. (2008), to estimate the potential contribution to the H_2 budget.

A truly novel contribution of this study is the observation of net ecosystem H_2 emissions originating from the forest canopy in the fall. Previous studies were not designed to diagnose the forest canopy environment, but the choice to measure H_2 fluxes both above and below the canopy enabled the emission source to be pinpointed. The mechanism for canopy emissions is unknown, but may be tied to photo- or thermal-degradation of organic matter (Lee et al., 2012; Derendorp et al., 2011), leaf senescence (Lim et al., 2007; Fall et al., 2001), microbial processes occurring within or on trees (Covey et al., 2012), or some other unknown mechanism. Canopy emissions of H_2 would be a previously unrecognized source of H_2, which could potentially help explain the discrepancy in H_2 budgets produced from top-down and bottom-up approaches, where the latter have not considered canopy effects in the past (Ehhalt and Rohrer, 2009).

Wintertime fluxes of H_2 have only been described by one chamber-based study (Lallo et al., 2008). Comparison of the H_2 fluxes over two New England winters of extremes is a novel contribution to the field. In combination with environmental measurements, an interesting picture can be painted of the sensitivity of wintertime H_2 fluxes more than ever before.

The nuances of bidirectional trace gas flux through snowpack are discussed for H_2 and CO_2. Uptake processes through snow are slowed in proportion to snow depth because of the resistance to substrate diffusion, whereas emission processes originating in the soils are unaffected. This study serves as an example to modelers of annual trace gas fluxes between the soil and atmosphere in areas with a snowpack.

Environmental isolates from Harvard Forest demonstrating H_2 uptake ability represent contributions to the basic understanding of atmospheric H_2 metabolism. These strains could be made available to other labs and their 16S rRNA and *hhyL* genes have been sequenced for submission to public databases.

Demonstration of the lifecycle dependence of H_2 consumption in *R. equi* is a unique contribution, which links to observations of *Streptomyces* spp., to draw a broad conclusion that soil microorganisms use H_2 at specific periods linked to nutrient limitation.

6.3 Limitations

Field measurements in this thesis are limited to the time periods and geographical locations in which measurements were made. H_2 uptake have been measured in a range of soils, as has been reviewed recently by Ehhalt and Rohrer (2009), and may exhibit large ranges in uptake (Constant et al., 2011b). Given the consistency observed with a flux study over a grassland in Quebec (Constant et al., 2008a), we might assume that similar H_2 soil sink processes occur broadly across the Northern Hemisphere. However, forest canopy emissions at Harvard Forest may not have a counterpart in the Quebec grassland H_2 exchange, so whole ecosystem exchange at Harvard Forest may occur with quite different rates and seasonality than in other ecosystems. More studies are required to answer this question.

6.4 Further development and research

To complete some work in this thesis for publication, several projects are in progress or will be finished in the short term. The second K-theory method will be tested and compared to the first, which was primarily used in this thesis. More environmental correlations than were presented in this thesis will be tested against trace gas fluxes. Whether aerial hyphae stimulation in *bld Streptomyces griseoflavus* Tu4000 induces the expression and/or activity of the high-affinity [NiFe]-hydrogenase will be tested in the lab.

Future work could use the data from this study to develop an ecosystem process-based model to test the understanding of mechanisms behind H_2 uptake. Such a model could then be used to assess the effect of changes in controlling variables due to climate change on H_2 uptake ability. These models should not assume that wintertime trace gas fluxes are necessarily negligible.

Future endeavors to build a flux instrument system for H_2 can use results from this study. The thorough characterization of the instrument precision and the comparison of the signal-to-noise ratio of H_2 uptake at two heights in this temperate forest will help inform the construction and deployment of future systems to measure H_2 fluxes by this flux-gradient approach. Lessons should be learned from the design of the nulling procedure in this study, such as increasing mixing in the nulling volume, increasing the time constant of the nulling volume, and randomizing sample line sampling order.

As a methodology, the use of flux ratios (and in this approach gradient ratios) of H_2 and CO_2 was found to be an informative tool for diagnosing environmental variables that are affecting the rate of one specific soil microbial process (H_2 uptake) relative to the activity of the total soil microbial community (CO_2 respiration). The seasonal and episodic influence of soil temperature, soil moisture and snowpack depth/porosity was easily identified using this analysis approach.

An additional methodology point is that the snowcam method provided a simple method requiring low maintenance and people-hours for providing snow depth and area data. Having snow weight information in addition (snow pillow data), yielded information on the snowpack porosity, which were found to have interesting relationships with the trace gas fluxes. These two methods could be added to many field studies to provide high-frequency and low-upkeep data to correlate with wintertime gas fluxes.

I would recommend investigations into forest canopy H_2 emissions because this source may be important globally and may resolve the controversy in the discrepancy of the H_2 budgets diagnosed using top-down versus bottom-up methods.

Atmospheric H_2 is an interesting and unique constituent of Earth's atmosphere. The field is ripe for more measurements, especially ecosystem scale fluxes, to test our process-based understanding of H_2 ecosystem exchange. Future studies focusing in tropical, wetland, peatland, or desert ecosystems would be welcome contributions to the field because they are terribly underrepresented. Wetland or peatland H_2 exchange may be highly dynamic because anaerobic H_2 emissions may periodically dominate, or they may be intercepted by vigorous H_2 oxidation rates in those soils (Constant et al., 2011b). The recognition of photo-thermal H_2 emissions could make desert ecosystems interesting sites to study; it is open question whether uptake or emissions of H_2 would dominate. Tropical soils are very much underrepresented in H_2 studies, but may be more efficient at H_2 consumption than extra-tropical soils according to an optimal estimation of soil uptake (Xiao et al., 2007).

In addition to field measurements, many open questions exist with regards the underlying microbial mechanisms driving the H_2 soil sink. For instance, only recently have microorganisms with the ability to consume atmospheric H_2 been characterized, but it has not been shown which organisms are primarily responsible for the H_2 uptake in the environment and whether that community is static or dynamic. Additionally, it is an open question whether atmospheric H_2 is an important energetic supplement to soil microorganisms, or somewhat inconsequential. Are these hydrogenases primarily used for atmospheric H_2 extraction, or is the primary goal to harvest H_2 from N_2-fixing sources, such as around root nodules, or from anaerobic micro-environments? Many questions remain, which makes this area an exciting one for future research.

The ultimate goal for future work would be the connection of H_2 uptake processes from the microbial scale to the ecosystem scale. Of course, this is a major challenge for many atmospheric trace gas cycles with a significant microbial imprint. Future studies should be carefully designed to address this question. H_2, with its incredibly strong microbe-mediated soil sink and relatively simple suite of sources and sinks, could be a model trace gas for linking the microbial to the ecosystem scale.

Appendix A

Supplemental information for H_2 flux-gradient measurements

A.1 Instrument design details

A.1.1 Gas stream selection design

During the normal sampling routine, the system was designed such that continuous gas streams from the top or bottom tower inlets of concentration gradient pairs 1 and 2 (labeled 1T, 1B, 2T, 2B) were each sent through an integrating volume after bypassing the nulling valves (N01-N04). Integrating volumes were built from glass reaction vessels (1 & 2 L[1], 6511-53 & 56, Ace Glass Inc., Vineland, NJ) and custom aluminum lids with welded fittings (0.4 in. aluminum, welded 1/4 in. Swagelock bulkhead unions, MIT Machine Shop) that were clamped on (6508-06, Ace Glass) and sealed with a vacuum greased CAPFE O-ring. Two fittings serve as the inlet and outlet gas streams, while a third serves as a silicone-sealed port for the power supply to a small computer fan (12V, Fine-Ace, Sanyo-Denki, Japan) that is mounted to the 1/4 in. stainless steel inlet to produce a well-mixed sample. The integrating volumes, shown in Figure A-1, provide a well-mixed sample with a time constant[2] between τ

---

[1] Integrating volumes were changed from 1 L to 2 L on 24 April 2011.

[2] As discussed in Appendix A.2, the time constant was set to 2 min on 25-Nov-2010, to 4 min on 15-Mar-2011, and to 8 min on 24-Apr-2011.

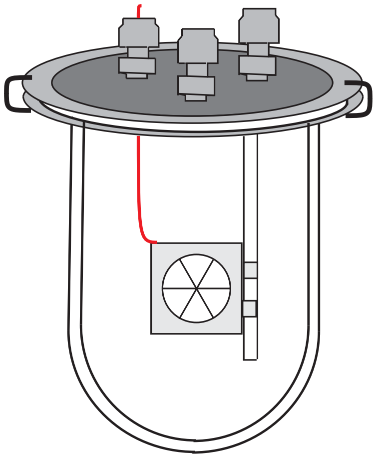

Figure A-1: Custom integrating volume design of a 1 to 2 L glass reaction flask to which a custom aluminum lid is clamped. A small computer fan ensures a well mixed volume to physically average air from tower inlets before analysis by the flux-gradient system.

$= V/Q = 1$ L / 0.5 L min^{-1} = 2 min and $\tau = V/Q = 2$ L / 0.25 L min^{-1} = 8 min.

The gas stream exiting the integrating volume is then split; a micro-diaphragm pump (UNMP830 KTDC-B, KNF Neuberger, Inc., Trenton NJ) draws a side stream of the sample to the GC, and a vacuum diaphragm pump (MPU1221-N838-9.00, KNF) draws the rest of the air through the the IRGA rack, making the diaphragm pump the primary driver of gas flow through the inlet lines. All sampling tubing is continuously flushed by bypass flows for both the GC and the IRGA rack sample streams during routine sampling. The three-way solenoid valve of the selected sample stream (SS05-SS08, 1/4 in., stainless steel, 7133TVN2GV00, Skinner Valve, Parker Hannifin, Cleveland, OH) in concert with a 10-port multi-position stream selection valve (dead-end (SD), MW type, 1/16 in. ports, with M-type rotor and purged housing, VICI, Houston, TX) were used to select a given sample stream. Valves SS05-SS08 were controlled via the GC internal valve drivers (valve 1-4, 24V 13W).

While the IRGAs measure H_2O in the IRGA rack sample stream, H_2O was removed from the GC sample stream so it would not dilute measurements of the H_2 mole fraction in dry air. The GC sample was drawn through a Nafion drying tube (12" x 1/8", stainless steel, MD-070-12S-2, Perma Pure, Toms River, NJ). The Nafion

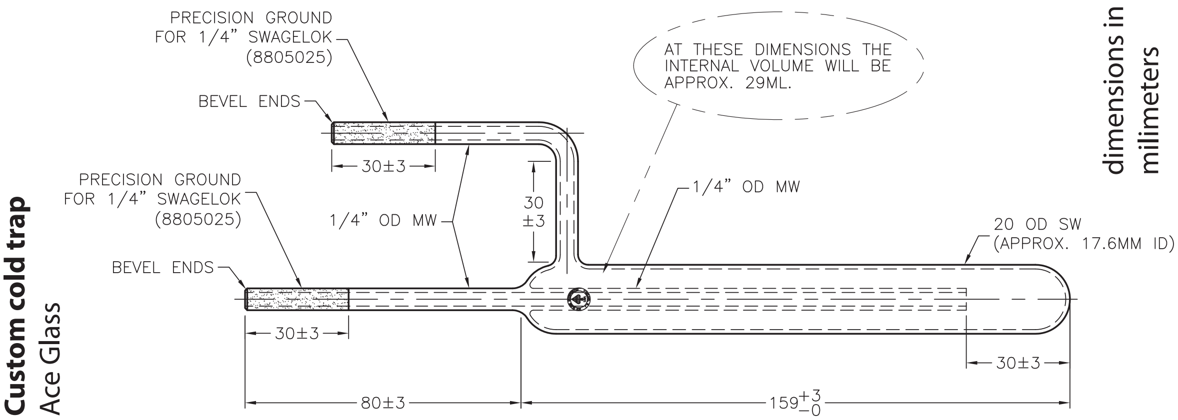

Figure A-2: Custom cold trap as a secondary GC sample stream drying measure. The 29 mL glass volume is submersed in a cold bath to freeze out water vapor concentrations to a dew point equal to the cold bath temperature. Diagram credit: ACE Glass.

requires a counter-flow purge gas, which was initially provided by the sample loop return flow (satisfies Nafion requirements because of pressure drop for return flow) until 16 June, 2011; afterwards, dry ultra zero air (previously flowed the IRGA reference cells) was used at a flow rate of approximately three times the sample stream flow. According to the manufacturer's specifications, the Nafion should dry the sample to a dew point of 0°C to −5°C, which corresponds to approximately 2.5 - 4 parts per thousand (ppth) H_2O. The samples then underwent a second drying step by passing through a custom cold trap shown in Figure A-2 (8750, 35 mL, 1/4" diameter arms, ACE Glass, Vineland, NJ) held in a cold bath (-20°C to 150°C, 6L capacity, Model 1140S, VWR International, Radnor, PA) filled with a 50:50 ethylene glycol and water mixture. The bath was held at its coolest, -20°C, which should have caused condensation to about 0.8 ppth H_2O. After running for a few months, the cold bath was turned off on 12 Dec, 2010 and emptied of coolant because there had been no accumulation of water in the cold trap after four months of sampling. The glass trap was kept in line in case there was reason to use the bath again.

After the sample stream was dried, it was drawn through a pair of 3-way solenoid valves (SL09, SL10, see Skinner valves above) that sent the sample stream either 1) through the GC injection valve sample loop past a pressure transducer (722B13TFF3FA, 0-1000 Torr, MKS Instruments, Andover, MA) when loading the sample loop or 2) through a bypass flow while measuring the isolated sample loop environment pressure. A temperature probe was inserted between coils of the sample loop to record sample temperature. The sample stream flow rate was controlled just upstream of the GC pump with a flow controller (1179A-29371, 0-100 sccm, MKS)[3]. The pressure transducer, flow controller, and temperature probe were controlled and/or read through spare channels on the IRGA rack multiplexer board. The sample loop solenoid valves were controlled by relays driven by the GC external valve drivers (valves 5 & 6, 24VDC 100 mA current source). A restrictor and a 2-way valve were placed on the H_2 standard line; the restrictor was used to match the calibration pressure to sample pressures and the 2-way valve prevented the loss of calibration gas during power failures.

Exterior gas tubing lines made of Synflex® tubing (OD 1/4 in., ID 0.21 in., 1300-04403, Goodrich Sales, Geneva, IL), an aluminum tubing coated by outer high-density polyethylene and an inner teflon layer, were installed with inline PFA filter holders (47mm PFA, EW-06621-40, Cole Palmer, Vernon Hills, IL) containing 2 μm pore size filters (Zefluor^{TM}, P5PJ047, Pall Corporation, Port Washington, NY) approximately 20 cm from the tubing inlet. Inverted teflon funnels were installed to protect the tubing inlet from precipitation. Tubing lengths from the gas inlets to the instrument integrating volumes were between 45-55 meters for both the below-canopy and above-canopy inlets.

A.1.2 Nulling design and procedure

Forty minutes before starting the nulling procedure, 2-way valve N00 was opened and a nulling-micro diaphragm pump (UNMP830 KTDC-B, KNF) was used to flush a gas stream from an outside gas inlet through a 25 L glass carboy protected in a storage container outside the shed (see Figure 2-2). To flush the integrating volumes for 20 minutes the pump and valve N00 were closed after the nulling volume had been

---

[3] GC sample flow was 25 cc/min until 20 June, 2011 and at 40 cc/min afterwards

flushed, and valves N01-N04 were activated. The nulling routine was run by repeating the normal sampling routine sequence twice. Mole fractions in the nulling volume were not static, but were highly averaged; for instance, for a total flow rate of 3 L min^{-1} (LPM), the nulling volume time constant would be 8.3 minutes. All nulling valves and the pump were controlled via channels on the IRGA rack multiplexer board.

A.1.3 Instrument control and data collection

The flux-gradient system was controlled using two computers (Wind Nettop, Micro-Star Int'l Co., City of Industry, CA): "hydrogenWIN" was equipped with WindowsXP and "hydrogenLIN" with Fedora 11. The gas chromatograph was controlled by GCwerks (Version 3.02-2, Peter Salameh, Scripps Institute of Oceanography, http://gcwerks.com) on hydrogenLIN and the instruments controlled by the Campbell Scientific CR10X data loggers were controlled by LoggerNet (CSI) on hydrogenWIN. Communication was enabled between the two computers via two relay-based voltage signals (GC contact closure valve drivers 7 & 8) that either passed a 2.6V signal to a differential voltage channel on the CR10X or diverted the voltage to ground as illustrated in Figure A-3. This allowed the programming of four signals (normal sampling, calibrate, null, shutdown) to be sent from the GC to the IRGA rack CR10X.

System timing was controlled by GCwerks on hydrogenLIN, especially for prompting IRGA rack routines. The meteorological equipment ran continuously, without a need for synchronized timing. Computers were synchronized to a NIST internet time server, though problems did occur with that correction and data were corrected for drift between the computer clocks when necessary. Data were stored locally on each computer, and once a day a crontab schedule initiated two events: 1) data transfer from hydrogenWIN to hydrogenLIN and 2) an rsync transfer of data from both computers to a server at MIT.

To make the instrument field-ready a number of precautions were taken. System power was backed up by a 2000 VA uninterruptible power supply (Model SG2K-1T, Falcon Electric Inc., Irwindale, CA). Power was supplied to the IRGA rack and the

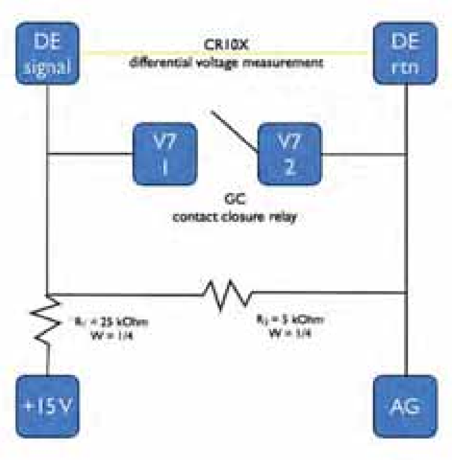

Figure A-3: Method for synchronization between GC and CR10X instrumental systems. Two synchronization signals were sent to CR10X Differential Voltage channels (DE) by operating GC external valves V7 and V8 by the GCwerks software. Potential was applied across 15V and analog ground (AG) channels. A "0" signal was assigned to nonzero voltage potentials and was measured by the CR10X while the GC valve was open, and a "1" signal was assigned when the potential dropped below a designated threshold upon closure of the GC valve.

meteorological equipment by a 24V DC power supply (TDK-Lambda Americas Inc., San Diego, CA).

In the event of a power failure, the helium carrier gas would be less pure with non-functioning purifiers. I wanted to ensure that the sensitive Helium ionization Pulsed-Discharge helium ionization Detector (HePDD) GC detector would stay off in such an event. An electrical box was constructed, which the detector's AC power cord was plugged into, that would carry out this function. The components included a mini contactor (Model XTMC6A10, EATON, Cleveland, OH) and momentary buttons, as shown in Figure A-4.

A.1.4 Gas chromatograph design details

Research grade helium carrier gas (99.9999% purity, HER300, Airgas, Riverton, NJ) was purified first with a large helium purifier and then again downstream with three miniature helium purifiers as close to the detector as possible without interfering with analytes (models HP2 and HPM, VICI). A stream of carrier gas was diverted through

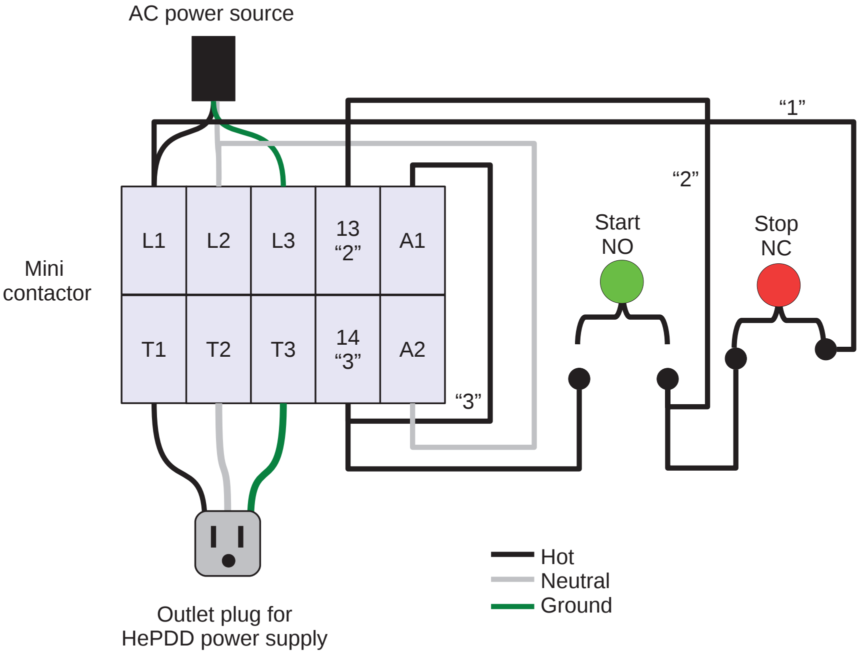

Figure A-4: Contactor switch and momentary button for HePDD shutoff after power failure. The normally-open (NO) momentary start button is held in the closed position if pressed while AC power is on, but relaxes back to the open state upon power failure and must be manually reset. Power can be cut manually using the normally-closed (NC) stop button.

a pressure regulator (model 8310, Parker Hannifin Corporation, Hatfield, PA), which supplied a steady purge stream to the HePDD via a restrictor (30 cc/min @ 60 psig He, TGA-R-30F60P, VICI). Two of the GC electronic pressure controllers (EPC) were used to supply carrier gas to a 2-position, 12-port injection valve (UW type, 1/16 in. ports, with M-type rotor and purged housing, VICI), to which a 2 mL sample loop was affixed. As depicted in Figure 2-3, the valve positions corresponded either to a load/backflush (A) or inject (B) configuration.

For a typical analysis, air samples were loaded onto the sample loop in load/backflush position (A). After samples were loaded, the valve was switched to the inject position (B) and the sample was loaded onto a packed pre-column (HayeSep DB 80/100, 2 m x 1/8 in. OD stainless steel, Chromatographic Specialities, Inc. (CSI), Brockville, Ontario, Canada). Neon and H_2 quickly separate from bulk gases O_2 and N_2 and clear the pre-column in under one minute to move on to the slightly finer-mesh analytical column (HayeSep DB 100/120, 4.5 m x 1/8 in. OD stainless steel, CSI). At this time, the valve is switched back to the load/backflush position (A) to flush bulk and trace gases lingering in the pre-column out of the system, while Neon and H_2 continue on to the HePDD for detection at retention times of around 136 sec and 151 sec, respectively. The backflush stream, which is composed mostly of helium, passes through a needle valve and then through the purged housing encasing the valve; this would cause any diffusion into the valve during valve switching to be composed mainly of helium instead of room air, limiting baseline contamination.

As was discussed in section 2.1, a primary goal for this system was a short analysis time; therefore, a shorter pre-column was used here than used by Novelli et al. (2009) (2 m vs. 4.5 m) to speed up analysis time at the expense of full resolution of the H_2 and Ne peaks. In this configuration, H_2 eluted more quickly from the pre-column, which reduced both the backflush time (60 sec vs. 137 sec) and the total chromatogram runtime (240 sec vs 325 sec). The oven was run isothermally at 40°C and the HePDD detector temperature was set to 100°C. Column flow was 20 $\mathrm{cm}^3\ \mathrm{min}^{-1}$ in accordance to VICI instructions. The detector is sensitive to changes in carrier gas flow rates during valve switching, so the EPC pressures and needle valve restriction were set to

Table A.1: Chromatography parameters for GC-HePDD

GC parameter	Value	Units
oven temperature	40	°C
HePDD temperature	100	°C
epc 3 pressure	40.0	psig
epc 4 pressure	32.0	psig
purge flow regulator	60	psig
He carrier gas tank pressure	80	psig
column flow rate	20	cc min^{-1}
chromatogram runtime	240	s
backflush time	60	s
H_2 retention time	~ 150	s

minimize disturbance to the baseline. These EPC pressures are summarized alongside the other chromatography parameters in Table A.1.

A.1.5 IRGA design details

Air from four inlets was drawn by a vacuum diaphragm pump (MPU1221-N838-9.00, KNF Neuberger, Inc., Trenton NJ) through three-way valves (valves 45-48, Entegris, Inc., Chaska, MN) that sent one stream of each concentration gradient pair to its assigned CO_2/H_2O infrared gas analyzer (IRGA; Model 6262, LI-COR Inc., Lincoln, NE), while bypassing the other two streams. The IRGAs were operated in absolute mode and hydrocarbon free air was used as a purge gas (AI UZ300, Airgas, Riverton, NJ). Samples flows were controlled to 500 or 250 sccm depending on the sampling date (see Section **??**) (MKS 1179A, MKS Instruments, Wilmington, MA) and pressure was controlled to 500 torr (MKS 640A13, MKS Instruments, Wilmington, MA). Detector boxes were lined with insulation (Nomex felt, DuPont, Wilmington, DE). Temperature controllers (CT16A2, Minco Products Inc., Minneapolis, MN) maintained the enclosure at 38°C using thinstrip heaters (HK5344 R40.3L12B, Minco Products Inc., Minneapolis, MN).

Data were collected at 1 Hz using a datalogger (CR10X, Campbell Scientific, Logan, UT), which was connected to a computer in the instrument shed by a multi-drop interface (MD9, Campbell Scientific, Logan, UT). Diagnostic information, such as sample pressure and flow, and the temperate of the IRGA cell and detector box, were recorded. A 16-bit status word was generated at each data point to indicate the status of solenoid valves to differentiate between calibration periods, sampling periods at the different levels, and bias-testing periods. Calibration of the IRGAs was choreographed using valves 41-44 and 49-50, as discussed below.

A.1.6 Meteorological measurement details

Measurement of the meteorological variables required for the modified Bowen ratio approach was accomplished with the following equipment generously provided by the Wofsy-Munger group at Harvard: 1) 3D sonic anemometer (CSAT3, Campbell Scientific Inc. (CSI), Logan, Utah), 2) datalogger (CR10X, CSI), 3) multi-drop interface (MD9, CSI), 4) DC-DC power converter (VI-LCW1-IW, Vicor Power, Andover, Massachusetts), 5) custom-designed-small footprint aspirated temperature shields from the Wofsy-Munger group at Harvard University (Dunn, 2006) containing thermistors (30.1 kOhm at 0°C, type 44032,YSI, Inc., Dayton, OH), and 6) a meteorological enclosure box (CSI). The meteorological enclosure was mounted on the small, below-canopy tower to control the below-canopy sonic and the temperature shields both above and below the canopy. The below-canopy sonic was controlled via the SDM channels of the CR10X inside the meteorological enclosure as described in the CSAT3 manual. Collected data were sent by the MD9 multi-drop interface via a coaxial cable to the windows computer running LoggerNet in the shed. The Wofsy-Munger group operates an above canopy 3D sonic anemometer (Applied Technologies, Inc., Longmont, Colorado) at 10 Hz.

Air temperatures were read using the thermistors inside the temperature shield by an AC half-bridge wired, as shown for temperature shields 1 and 2 in Figure A-5. A 2.5 V excitation voltage, V_x, pulsed through the temperature shield thermistors is then measured as the single-ended voltage, V_s, across the CR10X H and AG channels, which are separated by a reference resistor (30 kOhm Precision Metal Film Resistor, P/N PTF6530K000AYEK, Vishay Intertechnology, Inc., Malvern, PA). The thermis-

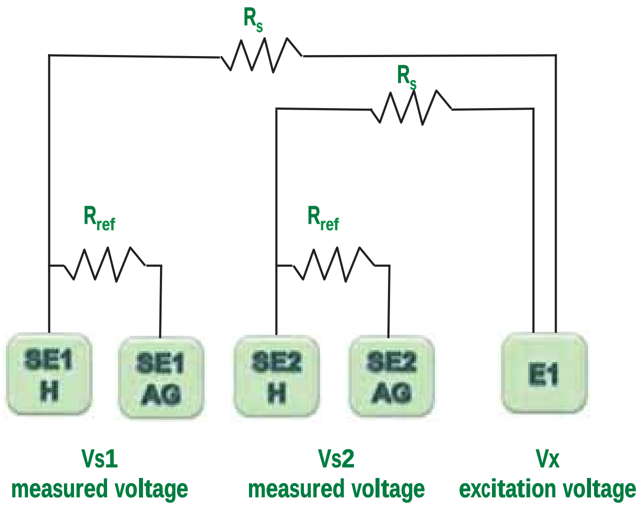

Figure A-5: Temperature shield thermistor wiring diagram for an AC half-bridge wired for temperature shields 1 and 2 and measured by a CR10X data logger. Single ended (SE), high (H), and analog ground (AG) channels received the signal sent by the excitation voltage (E).

tor resistance, R_s, can then be calculated with respect to a reference resistor, R_{ref} from the ratio of the excitation voltage to the single-ended voltage using Equation A.1 (see also Figure A-5).

$$R_s = (V_x/V_s - 1) \times R_{ref} \tag{A.1}$$

The temperature as a function of resistance, R_s, for a 30 kOhm probe is given by Equation A.2, where $A = 2.487281e{-}03$, $B = 2.512072e{-}04$, and $C = 3.151603e{-}07$.

$$T = A + B \times ln(R_s) + C \times ln(R_s)^3 \tag{A.2}$$

A.2 Data issues & limitations

Data collection was intermittently interrupted over the course of the experiment for a number of reasons, including power line testing, power surges or outages, software errors, hardware errors, and gas supply. The most significant of these events are presented in Table A.2 with a brief explanation of the issue and the dates and data affected. Not all streams of data were affected by these events; remaining data will be analyzed when possible.

The quality of the data collected was also affected by a number of issues throughout the experiment, including chromatography instabilities, memory effects, flow, temperature and pressure (FTP) problems, leaks, and unexplained issues. These data quality issues are presented in Table A.3 with a brief explanation of the issue and the dates and data affected. Data affected by these issues will be analyzed with care. Unusable data will be filtered from the final analysis, but usable data will be treated with documented corrections and included with care.

Table A.2: Data collection interruptions (November 25, 2010 to February 29, 2012)

Category	**Dates affected**	**Reason**	**Data affected**
Controlled shutdown	24- to 28-Aug-2011	Power line repair and hurricane Irene	all
	31-Aug to 2-Sep-2011	Power line repair	all
	6-Oct-2011	Power line repair	all
	17-Oct-2011	Power line repair	all
	30-Oct-2011 to 1-Nov-2011	Power line repair and Nor'Easter	gc
Power surge or outage	27-May- 8-Jun-2011	Power surge damage	gc, irga
	27-May-2011 20-Dec-2011	Power surge damage to shield fans	T (below)
	27-May-2011 10-Jan-2012	Power surge damage to shield fans	T (above)
Software error	27- to 29-Jan-2011	Runfile stuck in null routine	gc, irga
	2- to 3-Feb-2011	Sampling N04 because of snow	gc, irga
	25- to 26-Mar-2011	LoggerNet communication error	irga, met
	19- to 21-Apr-2011	Runfile stuck in null routine	gc, irga
	28-Apr- to 11-May-2011	LoggerNet communication error	irga, met
	17- to 18-May-2011	Repeated 1T sampling	gc, irga
	1- to 5-Jan-2012	Y2K12 GCWerks error	gc
Hardware problems	11-Dec-2010 to 6-Jan-2011	Temperature shield grounding	T
	30-Aug- to 10-Sep-2011	Hole in pump line	irga
Gas supply	4-Mar-2011	Carrier gas nearly out	gc
	12- to 15-May-2011	Zero air tank regulator got closed	irga

Table A.3: Data quality issues (November 25, 2010 to February 29, 2012)

Category	**Dates affected**	**Reason**	**Data affected**
Chromatography	25-Nov-2010 to 15-May-2011	Delay post-cal drops baseline - low first 1T	gc
	15-May to 15-Sep-2011	Stagnant tubing during cal - low first 1T	gc
Memory effect	25-Nov-2010 to 20-Jun-2011	GC flow rate too low, % volume remaining	gc
FTP	25-Nov-2010 to 24-Feb-2011	Sample valve box uninsulated	gc
	11-Dec-2010 to 20-Jan-2011	Variability in sample loop pressures	gc
	25-Nov-2010 to 25-Mar-2011	Two min integrating volume averaging	gc
	25-Mar to 24-Apr-2011	Four min integrating volume averaging	gc
	summer & fall intermittent	water vapor condensation in shed tubing	irga
	12-Jun to 29-Aug-2011	Variability in irga 1 pressure	irga
	30-Aug to 10-Sept-2011	Variability in irga pressures pump hole	irga
Leaks	25-Nov-2010 to 17-Feb-2011	Leak in 1B line	gc, irga
	25-Nov-2010 to 24-Feb-2011	Leak in 2B line	gc, irga

Appendix B

Supplemental information for microbiological studies

B.1 Quantification of H_2 uptake in microbial cultures

Molecular hydrogen (H_2) mole fractions were measured for these laboratory-based studies using gas chromatography with a Helium Pulsed Discharge Detector (HePDD). A gas chromatograph (GC) (Model 2014, Shimadzu Co., Kyoto, Japan) configured with a thermal conductivity detector (TCD) and dual flame ionization detectors (FID) was retrofit with a HePDD (D-4-I-SH17-R Model, Valco Instruments Co. Inc. (VICI), Houston, Texas) for measuring H_2 at atmospheric levels (∼530 ppb) to high precision.The instrument is shown in Figure B-1. More details on the HePDD and its application to atmospheric measurements can be found in Chapter 1.

The retrofit HePDD was mounted above the GC oven. The HePDD signal was collected through the left FID electrometer and detector temperature was controlled by an auxiliary GC heater. Carrier gas flow was controlled by pressure regulators external to the GC to satisfy the manufacturer's specifications for permissible fitting types and materials to contact the gas stream.

For timely and targeted measurements, a backflush-to-vent configuration was cre-

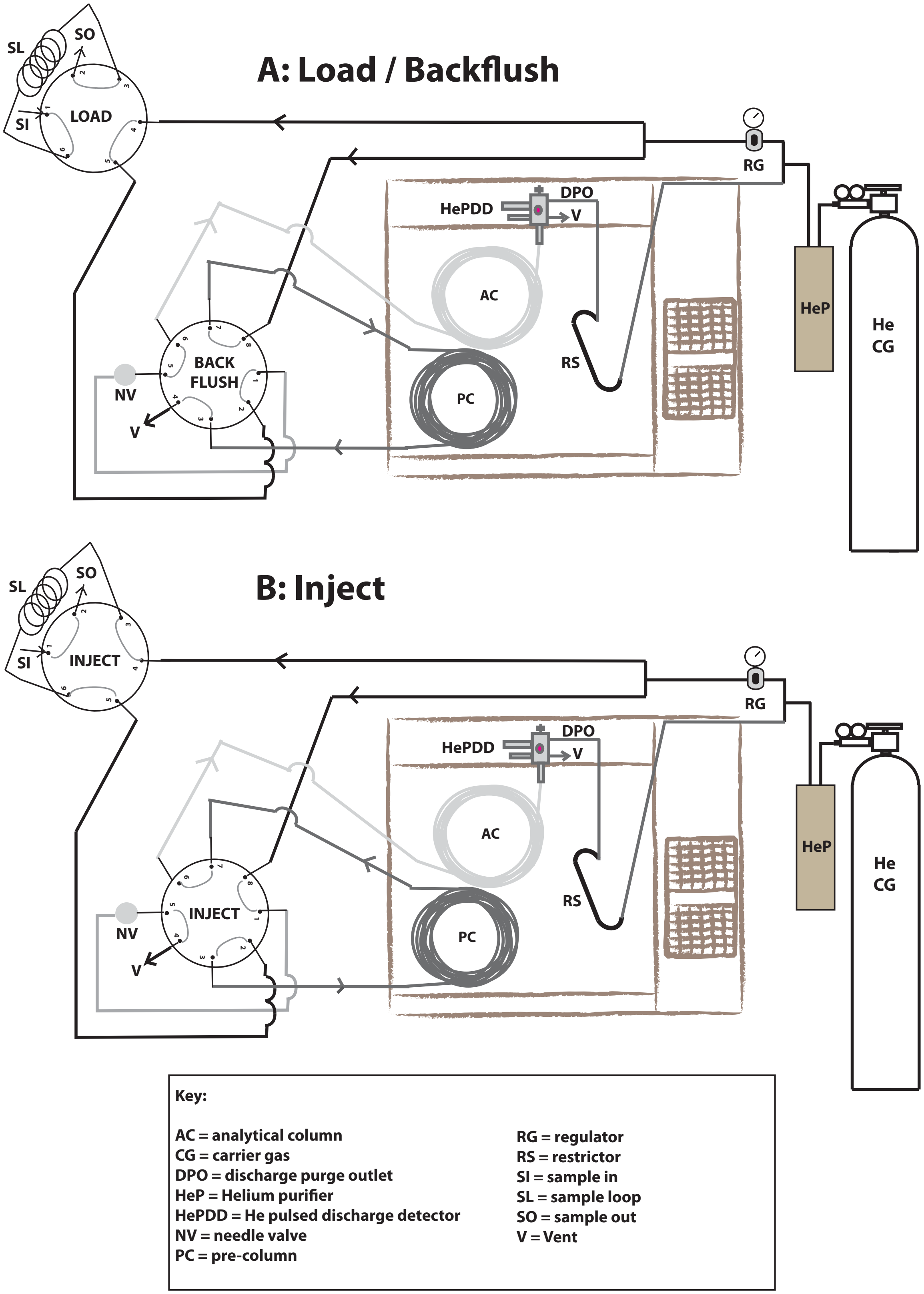

Figure B-1: Schematic of the GC-HePDD system constructed for the laboratory measurements of H_2.

ated using 6- and 8-port 2-position VICI sampling valves as shown in Figure B-1. Research grade helium was sent at 60 psig through a VICI helium purifier and the stream was split at a 'T' to 1) a crimped tube delivering a 30 mL/min purge flow to the detector and 2) to pressure regulator to control the carrier gas pressure. Needle valves were used to mimic the resistance of the pre-column, and pressures were adjusted (∼38 psig) to achieve approximately 15 mL/min of column flow regardless of valve position.

Air samples were loaded via 1/16 in. tubing or luer lock syringe port into a 1 mL sample loop mounted on the 6-port sampling valve before being injected via the 8-port backflush valve onto the somewhat coarse mesh packed pre-column (4 m × 1/8 in. OD stainless steel Hayesep DB, 80/100 mesh, Chromatographic Specialties Inc. (CSI), Brockville, Ontario Canada). Neon and H_2 were the first constituents of atmospheric samples to exit the pre-column, after which time the backflush valve was switched (at 2.2 min) to reverse the carrier gas flow direction to purge the remaining bulk and trace gases from the detection stream. Neon and H_2 were then further resolved in a finer mesh packed main column (4 m × 1/8 in. OD stainless steel, Hayesep DB, 100/120 mesh, CSI) until reaching the HePDD for analysis. The total run duration was 12 minutes to allow adequate time for the pre-column to be cleansed. The oven was run isothermally at 40°C and the detector at 100°C.

Chromatograms were recorded and peaks were integrated using the Shimadzu GCSolutions 2.30.00 SU6 software. A typical chromatogram is shown in Figure B-2. Neon and H_2 eluted at approximately 3.3 and 3.7 min, respectively. These trace gas peaks are centered upon a raised stair-step patterned baseline. The pattern likely results from small differences in pressures and leakiness of the two carrier gas streams (the detector is extremely sensitive to small leaks). Likewise, the peaks bracketing the stairstep pattern are either due to pressure fluctuations or leaks that occur during valve switching and should not be attributed to any specific trace gas species. No purged housing was available for the valves in this system. The GC-HePDD achieves a 2 ppb one-sigma precision on repeat calibration standard runs for H_2.

Hydrogen uptake rates were obtained from H_2 mole fraction measurements made

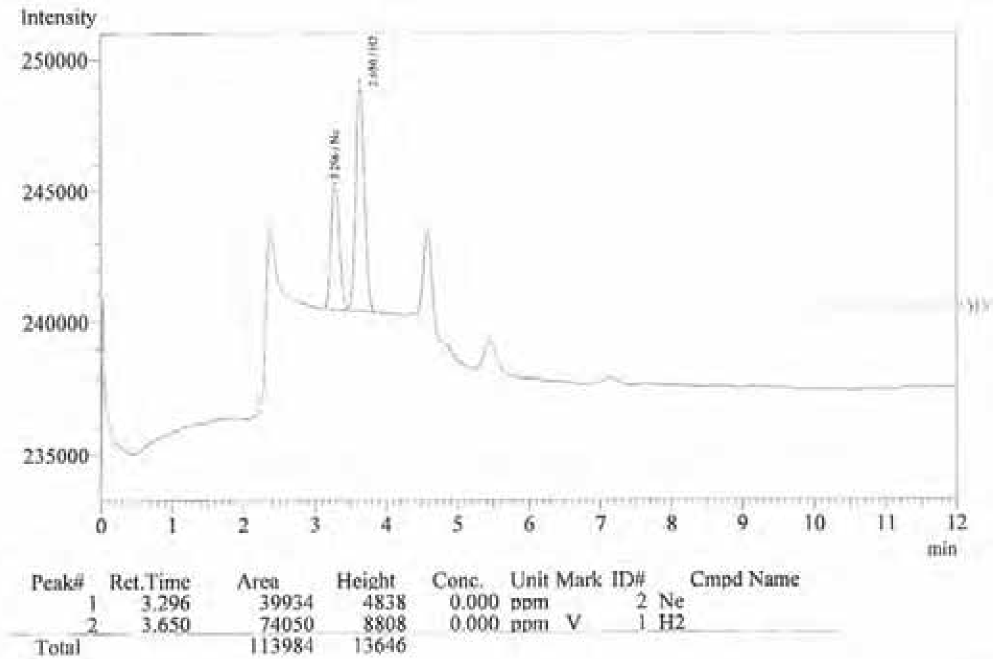

```
Peak#  Ret.Time     Area    Height    Conc.  Unit Mark ID#   Cmpd Name
    1     3.296    39934      4838    0.000  ppm          2  Ne
    2     3.650    74050      8808    0.000  ppm   V      1  H2
Total             113984     13646
```

Figure B-2: Typical chromatogram from laboratory GC-HePDD.

by one of two methods: 1) measuring the change in the H_2 mole fraction over time in a static headspace or 2) measuring the difference of the H_2 mole fraction in the inlet and outlet gas streams in a flow-through headspace.

Static headspace H_2 uptake tests: To measure the H_2 uptake rate of cultures growing within serum vials a sterile rubber stopper was crimped onto the vial. A sterile syringe, syringe filter, and needle were used to pressurize the vial with 20 mL of lab air. Gas-tight syringes were used to remove 4-5 mL samples of headspace gas from the sealed serum vials immediately after pressurizing the vials, and then twice more approximately every 35-40 minutes. Samples were loaded via a luer lock onto the sampling valve and were injected into the GC after waiting 10 sec for the injected sample to relax to atmospheric pressure via the sample loop vent. Crimps and stoppers were removed after the measurement and sterile cotton was used to keep the cultures aerobic and aseptic when not measuring H_2 uptake rates.

Calibration standards were prepared by filling electropolished stainless steel tanks with compressed air, which were then calibrated against the primary field instrument standard. Approximately L electropolished stainless steel flasks were evacuated to

250 mTorr and then flushed with compressed nitrogen at 30 psig three times before a final evacuation to 250 mTorr. a custom-built evacuation line (Hodson, 2008). The evacuated flasks were filled on the roof of the MIT green building with a diaphragm pump and stainless steel sampling line that could be pressurized and flushed before filling the flask itself. Flasks were filled to approximately 30 psig.

B.2 Supplemental Experimental Images

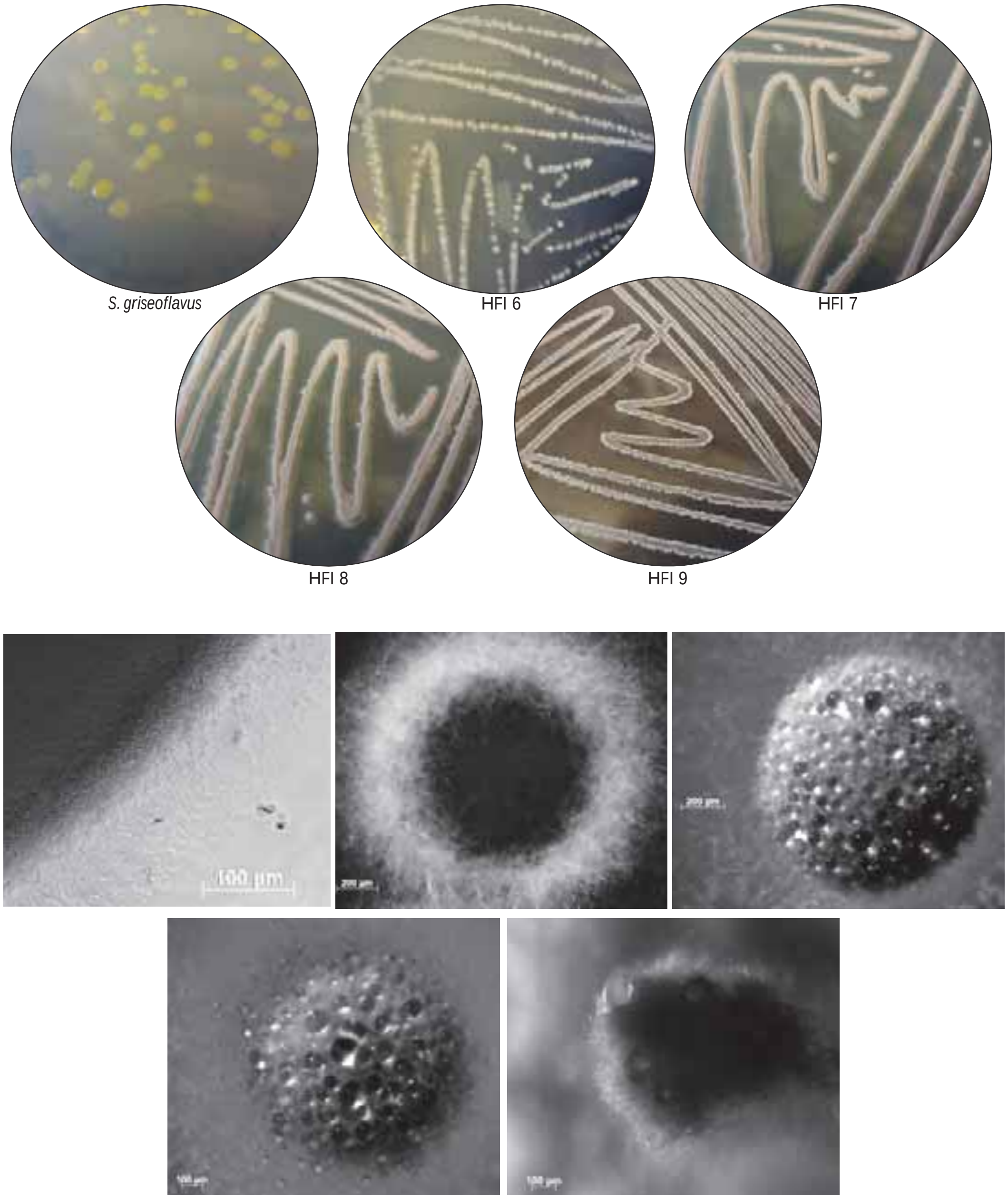
S. griseoflavus HFI 6 HFI 7

HFI 8 HFI 9

Figure B-3: Photographic (upper) and low res microscope (lower) images of *Streptomyces griseoflavus* Tu4000 and the *Streptomyces* sp. HFI strains 6-9. HFI strains produce aerial hyphae, as is visible by the fuzzy appearance in the images, while *S. griseoflavus* Tu4000 does not an has a waxy appearance from the substrate mycelia.

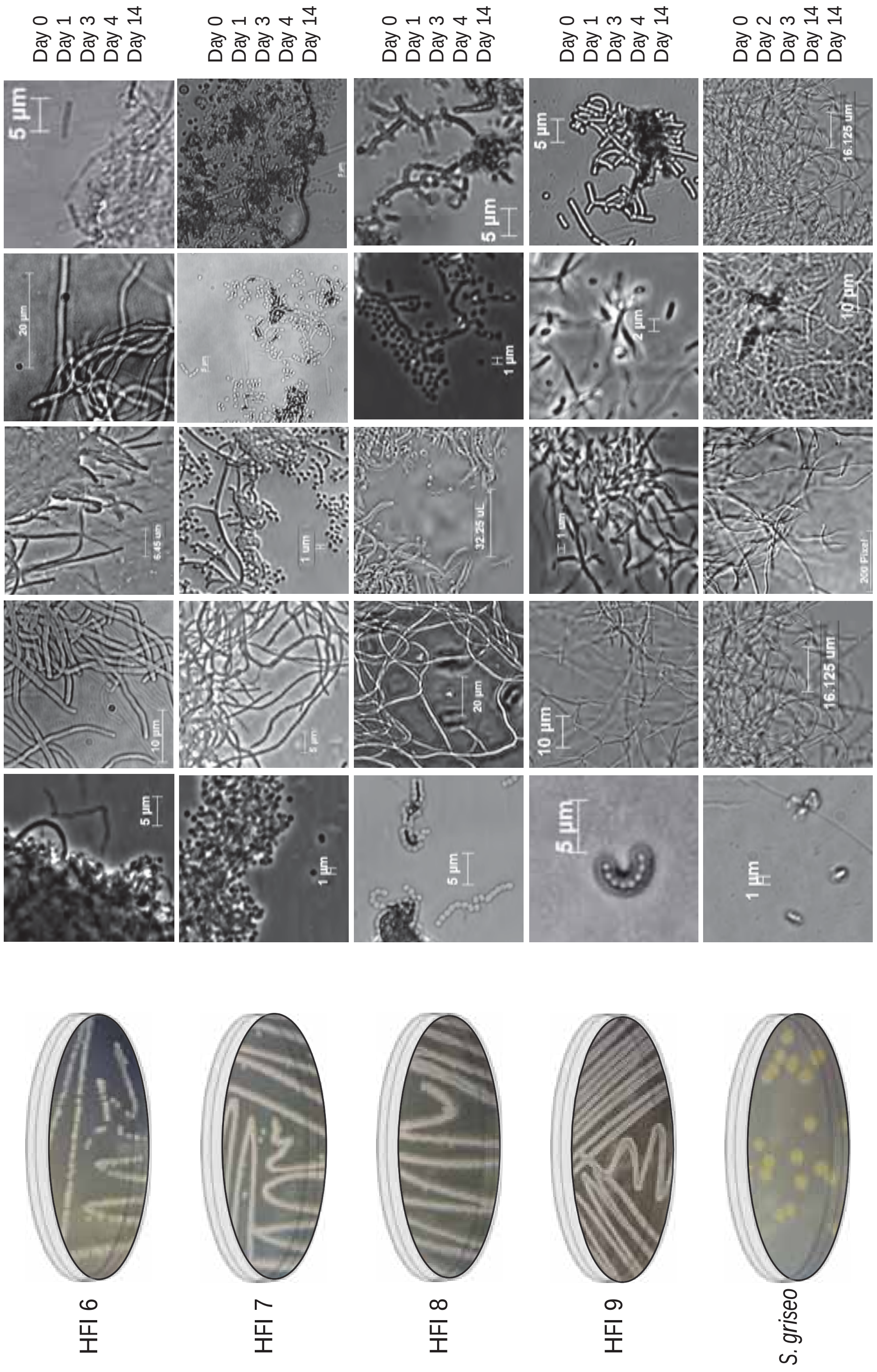

Figure B-4: A two-week time series of high-resolution microscopy photos capturing the transitions between life stage cycles of the HFIs and *S. griseoflavus* Tu4000 strains. HFIs 6-9 visibly went through the cycle of aerial hyphae formation and spore differentiation. HFI 6 and *S. griseoflavus* Tu4000. The formation of spores was not observed using microscopy for *S. griseoflavus* over the two-week timeframe.

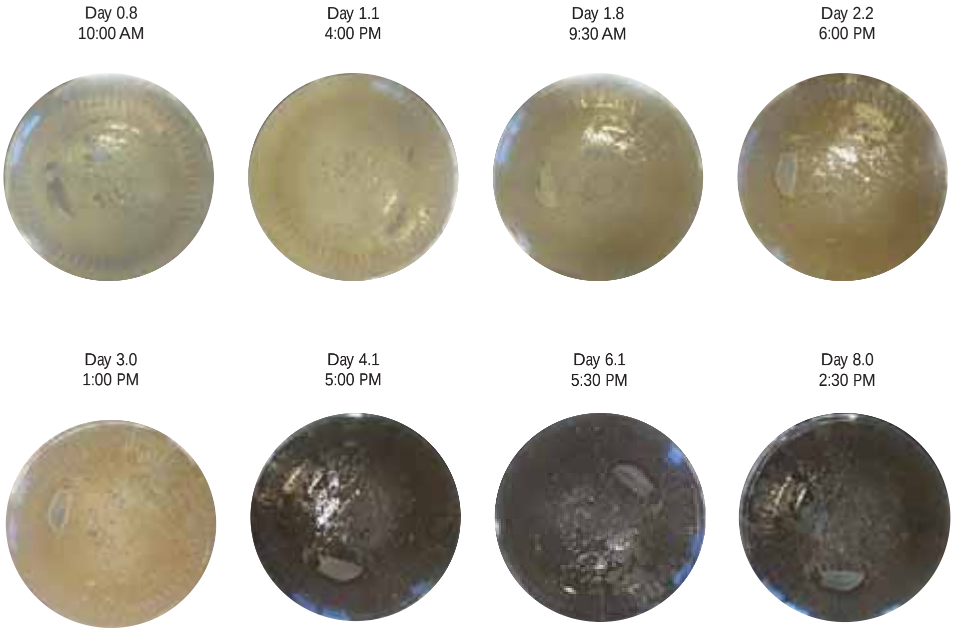

Figure B-5: A time series of HFI 8 serum vials over a week-long period. The percentage of area cover of the R2A agar did not change much over time. Note: The darkness of the last three images is primarily due to photography, not due to colony growth.

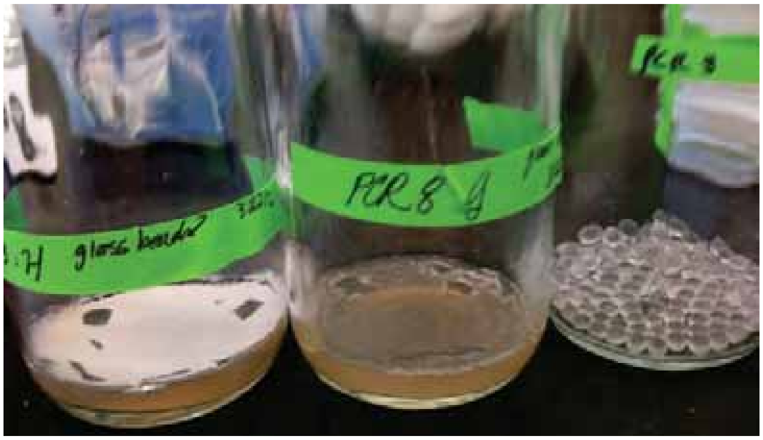

Figure B-6: Example photograph of the glass beads procedure where an example of the cultures before transfer, remainder on the medium, and after transfer are shown from left to right for *Streptomyces* sp. HFI8. Most of the aerial biomass is removed from the medium during the transfer. The slight opacity and pink coloring on the glass beads indicates that at least a portion of the original aerial biomass was transferred.

Bibliography

Albert, M. R. and E. F. Shultz, 2002: Snow and firn properties and air snow transport processes at. *Atmospheric Environment*, **36**, 2789–2797.

Allen, A., 1995: Soil Science and Survey at Harvard Forest. *Soil survey horizons*, **36 (4)**.

Baldocchi, D., 2012: ESPM 228, Advanced Topics in Biometeorology and Micrometeorology. *Lecture notes*.

Baldocchi, D., a. Guenther, P. Harley, L. Klinger, P. Zimmerman, B. Lamb, and H. Westberg, 1995: The Fluxes and Air Chemistry of Isoprene above a Deciduous Hardwood Forest. *Philosophical Transactions of the Royal Society A: Mathematical, Physical and Engineering Sciences*, **351 (1696)**, 279–296, doi: 10.1098/rsta.1995.0034.

Baldocchi, D., B. B. Hincks, and T. P. Meyers, 1988: Measuring Biosphere-Atmosphere Exchanges of Biologically Related Gases with Micrometerological Methods. *Ecology*, **69 (5)**, 1331–1340.

Barnes, D. H., S. C. Wofsy, B. P. Fehlau, E. W. Gottlieb, J. W. Elkins, G. S. Dutton, and P. C. Novelli, 2003: Hydrogen in the atmosphere : Observations above a forest canopy in a polluted environment. *Journal of Geophysical Research*, **108 (D6)**, 1–10, doi:10.1029/2001JD001199.

Bergey, D. H., R. S. Breed, and A. society for Microbiology, 1957: *Bergey's manual of determinative bacteriology*. 7th ed., Baltimore, Williams & Wilkins Co.

Berney, M. and G. M. Cook, 2010: Unique flexibility in energy metabolism allows mycobacteria to combat starvation and hypoxia. *PloS one*, **5 (1)**, 8614, doi: 10.1371/journal.pone.0008614.

Bocquet, F., D. Helmig, B. a. Van Dam, and C. W. Fairall, 2011: Evaluation of the flux gradient technique for measurement of ozone surface fluxes over snowpack at Summit, Greenland. *Atmospheric Measurement Techniques*, **4 (10)**, 2305–2321, doi:10.5194/amt-4-2305-2011.

Bond, S., S. Reimann, M. Steinbacher, M. Vollmer, and B. Buchmann, 2008: Loss reates of hydrogen to the atmopshere from variaous production, distribution, storage, and end-use systems. *EMPA Materials Science & Technology report*.

Bowling, D. R. and W. J. Massman, 2011: Persistent wind-induced enhancement of diffusive CO_2 transport in a mountain forest snowpack. *Journal of Geophysical Research*, **116 (G4)**, 1–15, doi:10.1029/2011JG001722.

Businger, J. A., J. C. Wyngaard, Y. Izumi, and E. F. Bradley, 1971: Flux-Profile Relationships in the Atmospheric Surface Layer. *Journal of the Atmospheric Sciences*, **28**, 181–189.

Chater, K. F. and S. Horinouchi, 2003: Signaling early developmental events in two highly diverged *Streptomyces* species. *Molecular microbiology*, **48 (1)**, 9–15.

Conrad, R., 1996: Soil microorganisms as controllers of atmospheric trace gases (H_2, CO, CH_4, OCS, N_2O, and NO). *Microbiological reviews*, **60 (4)**, 609–640.

Conrad, R., 1999: Soil microorganisms oxidizing atmospheric trace gases (CH_4, CO, H_2, NO). *Indian Journal of MIcrobiology*, **39**, 193–203.

Conrad, R., M. Aragno, and W. Seiler, 1983: The inability of hydrogen bacteria to utilize atmospheric hydrogen is due to threshold and affinity for hydrogen. *FEMS microbiology letters*, **18**, 207–210.

Conrad, R. and W. Seiler, 1980: Contribution of Hydrogen Production by Biological Nitrogen Fixation to the Global Hydrogen Budget. *Journal of Geophysical Research*, **85**, 5493–5498.

Conrad, R. and W. Seiler, 1981: Decomposition of atmospheric hydrogen by soil microorganisms and soil enzymes. *Soil Biology and Biochemistry*, **13 (1)**, 43–49, doi:10.1016/0038-0717(81)90101-2.

Conrad, R. and W. Seiler, 1985: Influence of Temperature, Moisture, and Organic Carbon on the flux of H_2 and CO Between Soil and Atmosphere: Field Studies in Subtropical Regions. *Journal of Geophysical Research*, **90 (D3)**, 5699–5709.

Constant, P., S. P. Chowdhury, L. Hesse, and R. Conrad, 2011a: Co-localization of atmospheric H_2 oxidation activity and high affinity H_2-oxidizing bacteria in non-axenic soil and sterile soil amended with *Streptomyces* sp. PCB7. *Soil Biology and Biochemistry*, **43 (9)**, 1888–1893, doi:10.1016/j.soilbio.2011.05.009.

Constant, P., S. P. Chowdhury, L. Hesse, J. Pratscher, and R. Conrad, 2011b: Genome Data Mining and Soil Survey for the Novel Group 5 [NiFe]-Hydrogenase to Explore the Diversity and Ecological Importance of Presumptive High Affinity H_2-Oxidizing Bacteria. *Applied and environmental microbiology*, doi:10.1128/AEM.00673-11.

Constant, P., S. P. Chowdhury, J. Pratscher, and R. Conrad, 2010: Streptomycetes contributing to atmospheric molecular hydrogen soil uptake are widespread and encode a putative high-affinity [NiFe]-hydrogenase. *Environmental Microbiology*, **12 (3)**, 821–829, doi:10.1111/j.1462-2920.2009.02130.x.

Constant, P., L. Poissant, and R. Villemur, 2008a: Annual hydrogen, carbon monoxide and carbon dioxide concentrations and surface to air exchanges in a rural area (Québec, Canada). *Atmospheric Environment*, **42 (20)**, 5090–5100, doi: 10.1016/j.atmosenv.2008.02.021.

Constant, P., L. Poissant, and R. Villemur, 2008b: Isolation of *Streptomyces* sp. PCB7, the first microorganism demonstrating high-affinity uptake of tropospheric H_2. *The ISME journal*, **2 (10)**, 1066–1076, doi:10.1038/ismej.2008.59.

Constant, P., L. Poissant, and R. Villemur, 2009: Tropospheric H_2 budget and the response of its soil uptake under the changing environment. *The Science of the total environment*, **407 (6)**, 1809–23, doi:10.1016/j.scitotenv.2008.10.064.

Covey, K. R., S. a. Wood, R. J. Warren, X. Lee, and M. a. Bradford, 2012: Elevated methane concentrations in trees of an upland forest. *Geophysical Research Letters*, **39 (15)**, 1–6, doi:10.1029/2012GL052361.

Davidson, E., 2002: Minimizing artifacts and biases in chamber-based measurements of soil respiration. *Agricultural and Forest Meteorology*, **113 (1-4)**, 21–37, doi: 10.1016/S0168-1923(02)00100-4.

Denmead, O. T. and E. F. Bradley, 1983: Flux-gradient relationships in a forest canopy. *The forest-atmosphere interaction. Proceedings of the forest environmental measurements conference held at Oak Ridge, Tennessee, October 23-28, 1983*, B. A. Hutchison and B. B. Hicks, Eds., 421–442.

Derendorp, L., J. Quist, R. Holzinger, and T. Röckmann, 2011: Emissions of H_2 and CO from leaf litter of Sequoiadendron giganteum, and their dependence on UV radiation and temperature. *Atmospheric Environment*, **45 (39)**, 7520–7524, doi:10.1016/j.atmosenv.2011.09.044.

Derwent, R., P. Simmonds, S. O'Doherty, M. Manning, W. J. Collins, and D. Stevenson, 2006: Global environmental impacts of the hydrogen economy. *Int. J. Nuclear Hydrogen Production and Application*, **1 (1)**, 57.

Draxler, R. R. and G. D. Rolph, 2012: HYSPLIT (HYbrid Single-Particle Lagrangian Integrated Trajectory) Model access via NOAA ARL READY Website, http://ready.arl.noaa.gov/HYSPLIT.php.

Dunn, A. L., 2006: Carbon Fluxes and the Boreal Forest Mosaic. Phd thesis, Harvard University, 1–149 pp.

Dunn, A. L., S. C. Wofsy, and A. v H Bright, 2009: Landscape heterogeneity, soil climate, and carbon exchange in a boreal black spruce forest. *Ecological applications : a publication of the Ecological Society of America*, **19 (2)**, 495–504.

Ehhalt, D. H. and F. Rohrer, 2009: The tropospheric cycle of H_2 : a critical review. *Tellus B*, **61 (3)**, 500–535, doi:10.1111/j.1600-0889.2009.00416.x.

El-Nakeeb, M. A. and H. A. Lechevalier, 1963: Selective isolation of aerobic *Actinomycetes*. *Applied microbiology*, **11 (July)**, 75–7.

ESRL/GMD, 2012: Interactive data viewer, http://www.esrl.noaa.gov/gmd/dv/iadv/.

Fall, R., T. Karl, A. Jordan, and W. Lindinger, 2001: Biogenic C5 VOCs: release from leaves after freezethaw wounding and occurrence in air at a high mountain observatory. *Atmospheric Environment*, **35 (22)**, 3905–3916, doi:10.1016/S1352-2310(01)00141-8.

Fallon, R. D., 1982: Influences of pH , Temperature , and Moisture Tritium Uptake in Surface Soils Gaseous. *Applied and environmental microbiology*, **44 (1)**, 171–178.

Farrell, A. E. and D. Sperling, 2007: A low-carbon fuel standard for California, Part 1 : Technical analysis. *Technical report, Regents of the University of California*.

Flärdh, K. and M. J. Buttner, 2009: *Streptomyces* morphogenetics: dissecting differentiation in a filamentous bacterium. *Nature reviews. Microbiology*, **7 (1)**, 36–49, doi:10.1038/nrmicro1968.

Francey, R. J., et al., 1996: Global Atmospheric Sampling Laboratory (GASLAB): supporting and extending the Cape Grim trace gas program. *Baseline Atmospheric Program Australia 1993, Bureau of Meteorology and CSIRO Division of Atmsopheric Research*, 23–25.

Fuentes, J. D. and D. Wang, 1999: On the seasonality of isoprene emissions from a mixed temperate forest. *Ecological Applications*, **9 (4)**, 1118–1131.

Gerst, S., 2001: Deuterium component of the global molecular hydrogen cycle. *Journal of Geophysical Research*, **106 (D5)**, 5021–5031, doi:10.1029/2000JD900593.

Goedde, M., K. Meuser, and R. Conrad, 2000: Hydrogen consumption and carbon monoxide production in soils with different properties. *Biol fertil soils*, **32**, 129–134.

Goldstein, A. H., 1998: Seasonal course of isoprene emissions from a midlatitude deciduous forest. *Journal of Geophysical Research*, **103 (D23)**, 31 045–31 056, doi: 10.1029/98JD02708.

Goldstein, A. H., S. Fan, M. L. Goulden, and S. Munger, J .W.Wofsy, 1996: Emissions of ethene, propene, and 1-butene by a midlatitude forest. *Journal of Geophysical Research*, **101 (D4)**, 9149–9157.

Gouy, M., S. Guindon, and O. Gascuel, 2010: SeaView version 4 : a multiplatform graphical user interface for sequence alignment and phylogenetic tree building. *Molecular biology and evolution*, **27 (2)**, 221–224.

Gu, L., et al., 2005: Objective threshold determination for nighttime eddy flux filtering. *Papers in Natural Resources*, **128 (3-4)**, 179–197, doi: 10.1016/j.agrformet.2004.11.006.

Guo, R. and R. Conrad, 2008: Extraction and characterization of soil hydrogenases oxidizing atmospheric hydrogen. *Soil Biology and Biochemistry*, **40 (5)**, 1149–1154, doi:10.1016/j.soilbio.2007.12.007.

Hanson, P. J., N. T. Edwards, C. T. Garten, and J. A. Andrews, 2000: Separating root and soil microbial contributions to soil respiration : A review of methods and observations. *Biogeochemistry*, **48**, 115–146.

Hauglustaine, D., 2002: A three-dimensional model of molecular hydrogen in the troposphere. *Journal of Geophysical Research*, **107 (D17)**, 1–16, doi: 10.1029/2001JD001156.

Heidt, L. E. and D. H. Ehhalt, 1972: Gas chromatographic measurement of hydrogen, methane, and neon in air. *Chromatography, journal of*, **69**, 103–113.

Helmig, D., E. Apel, D. Blake, L. Ganzeveld, B. L. Lefer, S. Meinardi, and A. L. Swanson, 2009: Release and uptake of volatile inorganic and organic gases through the snowpack at Niwot Ridge, Colorado. *Biogeochemistry*, **95 (1)**, 167–183, doi: 10.1007/s10533-009-9326-8.

Hirano, T., 2005: Seasonal and diurnal variations in topsoil and subsoil respiration under snowpack in a temperate deciduous forest. *Global Biogeochemical Cycles*, **19 (2)**, 1–11, doi:10.1029/2004GB002259.

Hodson, E. L., 2008: The Municipal Solid Waste Landfill as a Source of Montreal Protocol-restricted Halocarbons in the United States and United Kingdom. Phd thesis, Massachusetts Institute of Technology.

Hunten, D. M. and D. F. Strobel, 1974: Production and Escape of Terrestrial Hydrogen. *Journal of Atmospheric Sciences*, **31**, 305–317.

Jordan, a. and B. Steinberg, 2011: Calibration of atmospheric hydrogen measurements. *Atmospheric Measurement Techniques*, **4 (3)**, 509–521, doi:10.5194/amt-4-509-2011.

Kanan, M. W. and D. G. Nocera, 2008: In Situ Formation of an Oxygen-Evolving Catalyst in Neutral Water Containing Phosphate and Co^{2+}. *Science*, **321 (5892)**, 1072–1075.

Khalil, M. A. and R. A. Rasmussen, 1990: Global increase of atmospheric molecular hydrogen. *Letters to Nature*, **347**, 743–745.

King, G. M., 2003: Contributions of Atmospheric CO and Hydrogen Uptake to Microbial Dynamics on Recent Hawaiian Volcanic Deposits. *Applied and environmental microbiology*, **69 (7)**, 4067–4075, doi:10.1128/AEM.69.7.4067.

King, G. M. and C. F. Weber, 2008: Interactions between bacterial carbon monoxide and hydrogen consumption and plant development on recent volcanic deposits. *The ISME journal*, **(2)**, 195–203, doi:10.1038/ismej.2007.101.

Lallo, M., T. Aalto, T. Laurila, and J. Hatakka, 2008: Seasonal variations in hydrogen deposition to boreal forest soil in southern Finland. *Geophysical Research Letters*, **35 (4)**, 1–4, doi:10.1029/2007GL032357.

Langenfelds, R. L., R. J. Francey, B. C. Pak, L. P. Steele, J. Lloyd, C. M. Trudinger, and C. E. Allison, 2002: Interannual growth rate variations of atmospheric CO_2 and its δ^{13}, H_2, CH_4, and CO between 1992 and 1999 linked to biomass burning. *Global Biogeochemical Cycles*, **16 (3)**, 1048, doi:10.1029/2001GB001466.

Lee, H., T. Rahn, and H. L. Throop, 2012: A novel source of atmospheric H2: abiotic degradation of organic material. *Biogeosciences Discussions*, **9 (7)**, 8641–8662, doi:10.5194/bgd-9-8641-2012.

Lemke, P., et al., 2007: Observations: Changes in snow, ice and frozen ground. *Climate Change 2007: The Physical Science Basis*, S. Solomon, D. Qin, M. Manning, Z. Chen, M. Marquis, K. Averyt, M. Tignor, and H. Miller, Eds., Cambridge University Press, Cambridge, United Kingdom and New York, NY, USA, 337–383.

Levene, J., B. Kroposki, and G. Sverdrup, 2006: Wind Energy and Production of Hydrogen and Electricity Opportunities for Renewable Hydrogen Preprint. Tech. Rep. March, Technical Report CP-560-39534, NREL - National Renewable Energy Laboratory, Golden, CO.

Lim, P. O., H. J. Kim, and H. G. Nam, 2007: Leaf senescence. *Annual review of plant biology*, **58**, 115–36, doi:10.1146/annurev.arplant.57.032905.105316.

Liu, H. and T. Foken, 2001: A modifed Bowen ratio method to determine sensible and latent heat fluxes. *Meteorologische Zetschrift*, **10 (1)**, 71–80, doi:10.1127/0941-2948/2001/0010-0071.

Liu, Y., R. G. Prinn, C. Li., X. Xiao, and A. Sokolov, 1995: An interactive transient global emission model for nitrous oxide N_2O. *World meteorological organization report*, **WMO/Td-No.**, 205–208.

Lovins, A. B., 2003: Assessing the future hydrogen economy. *Science*, **302 (226-229)**.

Mastepanov, M., C. Sigsgaard, E. J. Dlugokencky, S. Houweling, L. Ström, M. P. Tamstorf, and T. R. Christensen, 2008: Large tundra methane burst during onset of freezing. *Nature*, **456 (7222)**, 628–30, doi:10.1038/nature07464.

McCormick, J. R. and K. Flärdh, 2012: Signals and regulators that govern *Streptomyces* development. *FEMS microbiology reviews*, **36 (1)**, 206–31, doi:10.1111/j.1574-6976.2011.00317.x.

Meyers, T. P., M. E. Hall, S. E. Lindberg, and K. Kim, 1996: Use of the modified bowen-ratio technique to measure fluxes of trace gases. *Atmospheric Environment*, **30 (19)**, 3321–3329, doi:10.1016/1352-2310(96)00082-9.

Miguélez, E. M., C. Hardisson, and M. B. Manzanal, 1999: Hyphal Death during Colony Development in *Streptomyces antibioticus* : Morphological Evidence for the Existence of a Process of Cell Deletion in a Multicellular Prokaryote. *The Journal of Cell Biology*, **145 (3)**, 515–525.

Monson, R. K., S. P. Burns, M. W. Williams, A. C. Delany, M. Weintraub, and D. a. Lipson, 2006: The contribution of beneath-snow soil respiration to total ecosystem respiration in a high-elevation, subalpine forest. *Global Biogeochemical Cycles*, **20 (3)**, 1–13, doi:10.1029/2005GB002684.

Monson, R. K., P. C. Harley, M. E. Litvak, M. Wildermuth, a. B. Guenther, P. R. Zimmerman, and R. Fall, 1994: Environmental and developmental controls over the seasonal pattern of isoprene emission from aspen leaves. *Oecologia*, **99 (3-4)**, 260–270, doi:10.1007/BF00627738.

Novelli, P. C., a. M. Crotwell, and B. D. Hall, 2009: Application of gas chromatography with a pulsed discharge helium ionization detector for measurements of molecular hydrogen in the atmosphere. *Environmental science & technology*, **43 (7)**, 2431–6.

Novelli, P. C., P. M. Lang, K. A. Masarie, D. F. Hurst, R. Myers, and J. W. Elkins, 1999: Molecular hydrogen in the troposphere: Global distribution and budget. *Journal of Geophysical Research*, **104 (D23)**, 30,427–30,444, doi: 199910.1029/1999JD900788.

Oke, T. R., 1978: *Boundary layer climates.* 2d ed., University Press, Cambridge, 435 pp.

Phillips, S. C., R. K. Varner, S. Frolking, J. W. Munger, J. L. Bubier, S. C. Wofsy, and P. M. Crill, 2010: Interannual, seasonal, and diel variation in soil respiration relative to ecosystem respiration at a wetland to upland slope at Harvard Forest. *Journal of Geophysical Research*, **115**, 18 PP., doi:201010.1029/2008JG000858.

Pielke Sr., R. a., 1984: *Mesoscale meteorological modeling.* Academic Press, Orlando, Florida, 612 pp.

Porter, J. N., J. J. Wilhelm, and H. D. Tresner, 1960: *Actinomycetes* from Soils Method for the Preferential Isolation of *Actinomycetes* from Soils. *Applied*, **8 (3)**, 174.

Prescott, J. F., 1991: *Rhodococcus equi*: an animal and human pathogen. *Clinical microbiology reviews*, **4 (1)**, 20–34.

Prinn, R. G., et al., 2000: A history of chemically and radiatively important gases in air deduced from ALE/GAGE/AGAGE. *Journal of Geophysical Research*, **105 (D14)**, 17 751–17 792, doi:10.1029/2000JD900141.

Rahn, T., 2002: Concentration and δD of molecular hydrogen in boreal forests: Ecosystem-scale systematics of atmospheric H_2. *Geophysical Research Letters*, **29 (18)**, 10–13, doi:10.1029/2002GL015118.

Raich, J. W. and W. H. Schlesinger, 1992: The global carbon dioxide flux in soil respiration and its relationship to vegetation and climate. *Tellus*, **44B**, 81–89.

Rao, D., 2012: Exploring the microbe-mediated soil H_2 sink : A lab-based study of the physiology and related H_2 consumption of isolates from the Harvard Forest LTER. Bachelor of science thesis, report 84, Massachusetts Institute of Technology, MIT Center for Global Change Science, 92 pp.

Raupach, M. R., 1981: Turbulence in and Above Plant Canopies : The Situation under Consideration. *Ann. Rev. Fluid MEch.*, **13**, 97–129.

Rhee, T. S., 2006: The overwhelming role of soils in the global atmospheric hydrogen cycle. *Atmospheric Chemistry and Physics*, **6 (6)**, 1611–1625, doi:10.5194/acp-6-1611-2006.

Rolph, G. D., 2012: Real-time Environmental Applications and Display sYstem (READY),http://ready.arl.noaa.gov.

Sanderson, M. G., W. J. Collins, R. G. Derwent, and C. E. Johnson, 2003: Simulation of Global Hydrogen Levels Using a Lagrangian Three-Dimensional Model. *Journal of Atmospheric Chemistry*, **46**, 15–28.

Savage, K. E. and E. A. Davidson, 2001: Interannual variation of soil respiration in two New England forests variation in soil respiration at the Harvard the interannual variation in net ecosystem exchange measured for this. *Global Biogeochemical Cycles*, **15 (2)**, 337–350.

Savage, K. E. and E. a. Davidson, 2003: A comparison of manual and automated systems for soil CO_2 flux measurements: trade-offs between spatial and temporal resolution. *Journal of Experimental Botany*, **54 (384)**, 891–899, doi: 10.1093/jxb/erg121.

Scherr, N. and L. Nguyen, 2009: *Mycobacterium* versus *Streptomyces*–we are different, we are the same. *Current opinion in microbiology*, **12 (6)**, 699–707, doi: 10.1016/j.mib.2009.10.003.

Schink, B., 1997: Energetics of syntrophic cooperation in methanogenic degradation . Energetics of Syntrophic Cooperation in Methanogenic Degradation. *Microbiol. Mol. Biol. Rev.*, **61 (2)**.

Schmidt, U., 1974: Molecular hydrogen in the atmosphere. *Tellus*, **26 (1-2)**, 78–90, doi:10.1111/j.2153-3490.1974.tb01954.x.

Schrempf, H., 2008: *Streptomycetaceae* : Life Style, Genome, Metabolism and Habitats. *Encyclopedia of Life Sciences.*, **(July)**, 1–7, doi: 10.1002/9780470015902.a0020393.

Schuler, S. and R. Conrad, 1990: Soils contain two different activities for oxidation of hydrogen. *FEMS Microbiology Ecology*, **73 (1)**, 77–83, doi:10.1111/j.1574-6968.1990.tb03927.x.

Schuler, S. and R. Conrad, 1991: Hydrogen oxidation activities in soil as influenced by pH, temperature, moisture, and season. *Biology and Fertility of Soils*, **12 (2)**, 127–130, doi:10.1007/BF00341488.

Simmonds, P. G., et al., 2000: Continuous high-frequency observations of hydrogen at the Mace Head baseline atmospheric monitoring station over the 1994-1998 period. *Journal of Geophysical Research*, **105 (D10)**, 12 105–12 121.

Smeulders, M. J., J. Keer, R. A. Speight, and H. D. Williams, 1999: Adaptation of *Mycobacterium smegmatis* to Stationary Phase. *J. Bacteriol.*, **181 (1)**, 270.

Smith-Downey, N. V., J. T. Randerson, and J. M. Eiler, 2006: Temperature and moisture dependence of soil H_2 uptake measured in the laboratory. *Geophysical Research Letters*, **33 (14)**, 1–5, doi:10.1029/2006GL026749.

Smith-Downey, N. V., J. T. Randerson, and J. M. Eiler, 2008: Molecular hydrogen uptake by soils in forest, desert, and marsh ecosystems in California. *Journal of Geophysical Research*, **113 (G3)**, 1–11, doi:10.1029/2008JG000701.

Steinbacher, M., a. Fischer, M. Vollmer, B. Buchmann, S. Reimann, and C. Hueglin, 2007: Perennial observations of molecular hydrogen (H_2) at a suburban site in Switzerland. *Atmospheric Environment*, **41 (10)**, 2111–2124, doi: 10.1016/j.atmosenv.2006.10.075.

Straight, P. D. and R. Kolter, 2009: Interspecies chemical communication in bacterial development. *Annual review of microbiology*, **63**, 99–118, doi: 10.1146/annurev.micro.091208.073248.

Stull, R. B., 1988: *An Introduction to Boundary Layer Meterology*. Publishers, Kluwer Academic, 666 pp.

Takai, S., S. Ohbushi, K. Koike, S. Tsubaki, H. Oishi, and M. Kamada, 1991: Prevalence of virulent *Rhodococcus equi* in isolates from soil and feces of horses from horse-breeding farms with and without endemic infections. *Journal of clinical microbiology*, **29 (12)**, 2887–9.

Tromp, T. K., R.-L. Shia, M. Allen, J. M. Eiler, and Y. L. Yung, 2003: Potential environmental impact of a hydrogen economy on the stratosphere. *Science*, **300 (5626)**, 1740–2, doi:10.1126/science.1085169.

Ueda, K., 2000: Wide Distribution of Interspecific Stimulatory Events on Antibiotic Production and Sporulation Among *Streptomyces* species. *The Journal of Antibiotics*, **53 (9)**, 979–982.

Warwick, N. J., 2004: Impact of a hydrogen economy on the stratosphere and troposphere studied in a 2-D model. *Geophysical Research Letters*, **31 (5)**, 2–5, doi: 10.1029/2003GL019224.

Wentworth, W. E., S. V. Vasnin, S. Stearns, and C. Meyer, 1992: Pulsed discharge helium ionization detector. *Chromatographia*, **34 (5-8)**, 219–225, doi: 10.1007/BF02268349.

Wilczak, J. M., S. P. Oncley, and S. A. Stage, 2001: Sonic anemometer tilt correction algorithms. *Boundary-Layer Meteorology*, **99**, 127–150.

Winther-Jensen, B., O. Winther-Jensen, M. Forsyth, and D. R. Macfarlane, 2008: High rates of oxygen reduction over a vapor phase-polymerized pedot electrode. *Science*, **321**.

Xiao, X., et al., 2007: Optimal estimation of the soil uptake rate of molecular hydrogen from the Advanced Global Atmospheric Gases Experiment and other measurements. *Journal of Geophysical Research*, **112**, 15 PP., doi: 200710.1029/2006JD007241.

Yonemura, S., S. Kawashima, and H. Tsuruta, 1999: Continuous measurements of CO and H_2 deposition velocities onto an andisol: uptake control by soil moisture. *Tellus B*, **51 (3)**.

Yonemura, S., M. Yokozawa, S. Kawashima, and H. Tsuruta, 2000: Model analysis of the influence of gas diffusivity in soil on CO and H_2 uptake. *Tellus*, **52B**, 919–933.